Design and characterization of catalysts with isolated metal sites

Osadchii, Dmitrii

DOI
10.4233/uuid:dc5f29f8-7d53-4a3c-83ee-a4d562fbe843

Publication date
2020

Document Version
Final published version

Citation (APA)
Osadchii, D. (2020). *Design and characterization of catalysts with isolated metal sites*. [Dissertation (TU Delft), Delft University of Technology]. https://doi.org/10.4233/uuid:dc5f29f8-7d53-4a3c-83ee-a4d562fbe843

Design and characterization of catalysts with isolated metal sites

Dmitrii Yurievich OSADCHII

Design and characterization of catalysts with isolated metal sites

Dissertation

for the purpose of obtaining the degree of doctor

at Delft University of Technology

by the authority of the Rector Magnificus Prof.dr.ir. T.H.J.J. van der Hagen,

Chair of the Board for Doctorates

to be defended publicly on

Wednesday 11 March 2020 at 15:00 o'clock

by

Dmitrii Yurievich OSADCHII

Master of Science in Chemistry, Novosibirsk State University, Russia

born in Novosibirsk, USSR

This dissertation has been approved by the promotors:
Prof.dr. F. Kapteijn and Prof.dr. J. Gascon Sabate

Composition of the doctoral committee:

Rector Magnificus	chairperson
Prof.dr. F. Kapteijn	Delft University of Technology, promotor
Prof.dr. J. Gascon Sabate	Delft University of Technology and King Abdullah University of Science and Technology, promotor

Independent members:

Prof.dr. A. Urakawa	Delft University of Technology
Prof.dr. E.A. Pidko	Delft University of Technology
Prof.dr. J.W. Niemantsverdriet	Eindhoven University of Technology / Syngaschem BV
Prof.dr. P. Van Der Voort	Ghent University, Belgium
Prof.dr. M.V. Fedin	International Tomography Center SB RAS, Russian Federation

The research reported in this thesis was conducted in the Catalysis Engineering group of the Chemical Engineering department, Faculty of Applied Sciences (TNW) of the Delft University of Technology.

This research was funded from the Dutch National Science Foundation (NWO-CW) / VIDI Grant Agreement n. 723.012.107, MetMOFCat.

To those who dare

To those who make it true

Table of Contents

1

Design of catalysts: the challenge of one-step methanol production

The main obstacles and challenges in the development of potential catalysts for the direct conversion of methane to methanol are highlighted. In the second part of this chapter, different characterization methods in the field of heterogeneous catalysis are discussed. The objective of the thesis project concludes this chapter.

1.1. Preface

Development of catalysts for sustainable energy conversion is one of the core areas of research in modern applied chemistry. Among the great variety of catalytic processes reported up to date, a significant part has never been applied industrially or finds only limited applications due to the inefficient use of energy and resources on the current stage of its development. Process engineering plays a great role here, however, the core of every catalytic process is the catalyst itself, and catalyst optimization remains a broad research field, that demands the combined efforts of synthetic chemists, chemical engineers, spectroscopists, and specialists in theoretical and computational chemistry.

In this combined effort, spectroscopic characterisation plays the role of a witness, bearing testimony of species present and the processes happening during the catalyst operation, as well as the role of a judge, evaluating the theoretical models and predictions. The proper use of these powerful tools demands the understanding of physical principles behind each spectroscopic technique, the limits of its applicability and the approaches to interpret the information it provides. As a result, the reasonable combination of spectroscopic techniques can provide a priceless insight in understanding of the catalyst behaviour and the approaches for its further development.

The main three characteristics that define how good is the catalyst are its activity, selectivity and stability. Spectroscopic characterization can be a useful tool for all these three aspects in the catalyst development. The studies considering the improvement of activity and selectivity of heterogeneous catalyst usually effectively deal with the modification of the catalyst's structural properties, its composition or the reaction conditions.

The main focus of this thesis lies on reflecting the role of spectroscopic characterization in catalyst design and development. The use of the combination of characterization techniques allows investigating the structure of the catalyst's active site (Chapters 2-4) and the transformations of the catalyst support under different synthesis conditions (Chapters 4-5). In Chapters 2-3 of this dissertation we can see how the adequate combination of characterization methods gives insight into the nature of catalytic activity of the first MOF-based catalysts for mild methane oxidation. To select the proper characterization tools one has to know the background of the investigated catalytic process and has to understand how similar materials and systems have been studied before. Thus, the basics of and previous studies on methane oxidation are discussed in detail in the first part of

Chapter 1. In Chapters 4-5 the application of X-ray based techniques, in particular X-ray Photoelectron Spectroscopy (XPS), for characterization of heterogeneous catalysts is discussed. The advantages and applicability of these techniques are described in the second part of Chapter 1.

1.2. Methane valorisation

Finding new sources for production of energy and valuable chemical products is one of the most important areas of chemical research to provide sustainable development of technology. For about 150 years crude oil has been one of the main sources of energy and materials for mankind. However, gradual depletion of the overall oil reserves rises the demand in improving the efficiency of the current oil extraction and processing technologies as well as the intensified use of alternative sources of hydrocarbons. In addition to this, the concern of global climate changes due to the enormous amounts of CO_2 produced by the society inspires the search for less CO_2 emitting energy sources. Here, large natural supplies of methane (main component of natural gas) have attracted significant attention for its utilization. Methane, the most simple organic molecule, has lower CO_2 emissions per generated energy unit compared to oil distillates and coal. After the invention of Fischer-Tropsch process and development of technologies for large-scale transportation of gas, the world's consumption of methane has grown significantly. Currently natural gas finds broad applications as fuel as well as a starting material for chemical synthesis.

Unfortunately, modern technologies of methane processing are facing a number of intrinsic drawbacks that limit their efficiency. Nowadays all industrial pathways for production of fuels and chemicals from methane require the generation of synthesis gas (a mixture of hydrogen and carbon monoxide) as an intermediate step. Current technologies of syngas production operate at high temperatures (700-1250 °C) and moderate pressures (1-30 bar).[1-3] By applying different forms of Fischer-Tropsch process, synthesis gas can be further converted to methanol or to hydrocarbons. Although these indirect routes have progressed substantially in terms of commercial development, they are economically viable only on a very large scale. Remote locations of natural gas sources and its high flammability results in a complicated and expensive process of gas transportation. Due to these reasons many small gas fields are still not commercially attractive for industrial utilization, and in many cases their development ends up with flaring.

Syngas production represents a high energy- and resource-consuming process, which requires massive financial investments.[4] This stimulates the search of new processes in which methane is activated and converted to a valuable chemical in a single step. Among the most desirable processes here would be the direct conversion of methane to methanol, one of the holy grails in catalysis. Today methanol finds numerous applications in processes for its utilization as a fuel and as a starting material in chemicals synthesis (including such large scale processes as (MTO, MTG, MTH etc.). At normal conditions methanol is a non-corrosive stable liquid, that is significantly easier to store and transport than methane. All these advantages allowed to suggest the concept of “the methanol economy”, that considers methanol as the key compound for energetics of the future.[5] However, no processes for the one-step conversion of methane to methanol have been implemented in industry yet, making direct production of methanol one of the greatest challenges in the modern catalysis.

The main reason of this challenge is the outstanding stability of methane molecule. Non-polar C-H bonds of this highly symmetric molecule have bond energy of 438.8 kJ/mol, exceptional for organic chemistry. It should also be noted that C-H bond in methanol is significantly less stable (373.5 kJ/mol), thus making it difficult to avoid overoxidation and to achieve high methanol selectivity. Another equally important challenge is the activation and regeneration of the oxidant. The most abundant oxidant is dioxygen, but due to its triplet ground state it cannot react directly with hydrocarbons and needs to be converted into the reactive species either chemically or physically.

In this chapter the current progress in overcoming the three major challenges of direct methane-to-methanol conversion (C-H bond activation, oxidant activation and regeneration, methanol selectivity) is highlighted and promising routes for the development of catalysts for this process are suggested.

1.2.1. C-H bond activation

Controlled functionalization of methane has always been considered difficult due to very high energy gap between HOMO and LUMO of this molecule.[6] Non-catalytic methane oxidation usually occurs via cascade of radical reactions. There is no proven way to control the selectivity of such process, and the main product is usually CO_2. Investigation of methane activation at high temperatures (500–800 °C) had shown, that in these conditions it predominantly occurs via homolytic C–H bond cleavage, e.g. via generation

of radicals.[7] Operation at low pressures can enhance the process selectivity towards partial oxidation products, but in this case the main product is formaldehyde, more stable than methanol in gaseous phase.[8] Hence, high-temperature methane oxidation routes are not only energy costly, but also meet crucial problems of product selectivity.

Alternatively, great opportunities for C-H bond activation are offered by catalysis. Research on H-D exchange on hydrocarbons, started in the 1960's, evolved into several different families of transitional metal-based catalysts able to break methane C-H bond. According to Shilov,[9] all reported mechanisms of C-H bond activation can be sub-divided into three main classes: true activation, fake activation and Fenton-type activation.

In case of the **true activation** the metal centre (M) of the catalyst directly interacts with the C-H bond, and a new σ M-C bond is formed as a result. It implies that the catalyst active centre should contain coordinatively unsaturated metal species (otherwise methane molecule will not be able to access it). Formation of M-C bond and cleavage of methane C-H bond in this case is controlled by the transfer of electron density from the metal (occupied $d\pi$ orbital) to the C-H bond (empty σ^* orbital) and by the back donation from C-H bond (occupied σ orbital) to the metal (empty $d\sigma$ orbital). Based on the balance between charge transfer and back donation, the C-H bond activation can be nucleophilic (mainly via donation from metal), electrophilic (mainly via back donation), or ambiphilic (both processes have similar contribution).[10]

Depending on the manner of C-H bond coordination, true activation mechanism can be subdivided into two classes: substitution and insertion. The **insertion mechanism** takes place if the C-H bond coordinates to the single metal centre (M) on the first step of the reaction and transforms into M-CH_3 species without significant interaction of outgoing proton with the ligands of the metal centre. Depending on the metal centre, the insertion can proceed via the **electrophilic activation**, when the outgoing proton is removed by the free anionic groups in solution, or via the **oxidative addition**, when the C-H bond is broken by the 2*e* backdonation from the metal centre, forming the hydride M-H species. The latter case can be considered a purely nucleophilic activation and is possible only in case of the electron-rich transition metal centres in low oxidation states (e.g. Rh(I), Ir(I)). On the contrary, for the electrophilic activation the electron-deficient transitional metal centre, preferably in high oxidation state, is required. Due to the high oxidation state of the metal centre, these catalysts can withstand polar media such as water or strong acids. This stability enables the use of

strong oxidants, contrary to species that undergo oxidative addition where only weak or no oxidants are applicable.

Substitution mechanisms of C-H bond activation usually represent a version of electrophilic activation, where the electron-deficient metal centre is coordinated by ligand(s) with basic properties. In this case the proton that is generated during M-CH_3 bond formation interacts with the basic site, which helps shifting the equilibrium towards the C-H bond breakage. Effectively this represents a σ-bond metathesis reaction. In heterogeneous catalysis such active sites are usually referred to as Lewis acid/base pairs, and this concept is commonly used to describe processes on metal oxide surfaces, in zeolites, etc.

The concept of **fake activation** mechanism is usually involved when direct interaction of metal centre with methane molecule is not possible (usually due to active site geometry), and C-H bond activation proceeds via the interaction with its ligands only. In the majority of studied catalytic systems the ligands are oxygen atoms or oxygen-based species. It is important to mention that most of the reported catalytic systems for partial methane oxidation feature *electrophilic* (*i.e.* electron-deficient) oxygen species.[11] According to Baerends *et al*,[12-13] hydrogen atom abstraction from methane molecule in these cases can proceed through the interaction of methane's σ_{CH} orbital with either σ^* or π^* orbital of the metal-oxygen complex (σ-channel or π-channel mechanism, respectively). The preference towards one or another mechanism and the overall activity of the active centre in this case is controlled by the spin state of the complex and by the effects of surrounding ligands.

C-H bond can also be activated by interaction with free radicals (*e.g.* OH, OOH, *etc.*), which can be generated physically (high temperature, high frequency irradiation) or chemically in so-called **Fenton type catalytic processes**. In this case neither metal centre nor its ligands interact directly with the C-H bond. Highly reactive radical species formed by these catalysts readily react with alkanes, the reaction is highly exothermic and favours overoxidation products.

One can see that different classes of catalysts able to activate and break the C-H bond of methane are known up to date. However, this does not necessarily mean that all these catalysts are suitable for catalytic oxidation of methane to methanol. C-H bond activation is only one step in the whole catalytic process, which should, generally speaking, also include the steps of oxidant activation, reaction of activated methane and oxidant, desorption

of product (methanol) and regeneration of the active centre. Even one missing step will not allow the catalytic cycle to be closed. In the following parts of this chapter we will discuss which characteristics should the catalyst possess to favour each of these steps.

1.2.2. Oxidant activation and product preservation

Despite the major differences in various catalytic processes for partial methane oxidation reported so far, the following steps of the catalytic cycle are common for all catalysts facilitating either true or fake methane activation:

1) Transformation of the catalyst centre into its active form by interaction with the solvent, with some activating species, or with the oxidant;
2) Interaction of methane with the active centre (coordination, C-H bond activation);
3) Catalytic reaction of activated methane with oxidant species (may require an additional preliminary step of oxidant activation on the active centre);
4) Desorption of the catalytic reaction product;
5) Regeneration of the active catalytic centre and regeneration of the oxidant.

Depending on the exact reaction mechanism, some of the steps might proceed simultaneously via concerted rearrangements in the active centre, but all these steps are required in order to close the catalytic cycle. Particular attention should be paid to the product removal step, which should guarantee the minimal side interaction of product (methanol) with oxidant in order to prevent overoxidation, and to the regeneration step, which is required to run the reaction in a catalytic manner.

The variety of reported catalytic processes for methane oxidation involves the use of highly reactive oxidants, which can relatively easily interact with the activated methane molecule or M-CH_3 complex. The first example of methane activation in solution (catalytic enhancement of H-D exchange between CH_4 and D_2O-AcOD media) was shown on Pt(II) salts in 1969.[14] Later the H_2PtCl_4 – H_2PtCl_6 – H_2O – AcOH system was proven to catalyse the oxidation of alkanes to alkyl chlorides.[15] Further investigation of this system has shown, that alkanes are activated on Pt(II) centres while Pt(IV)

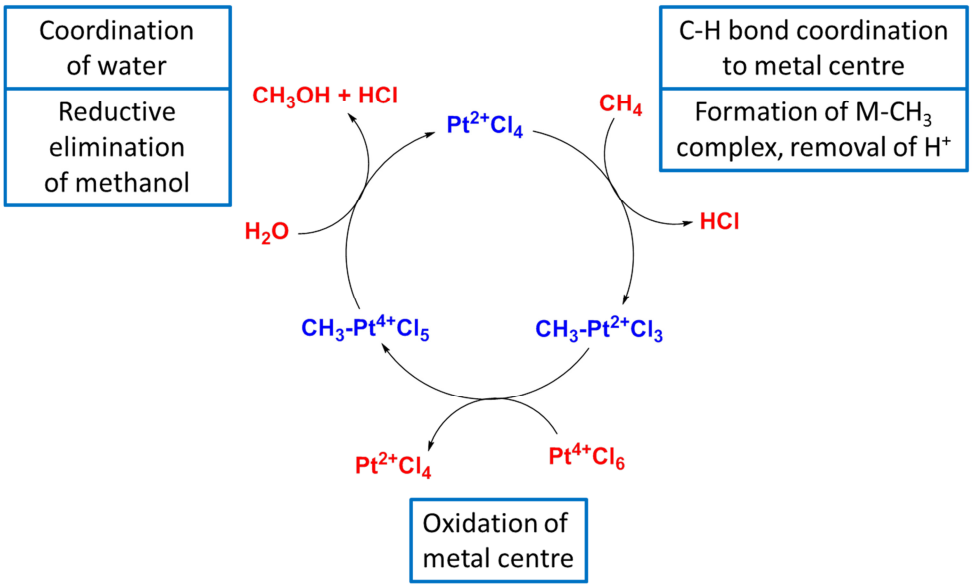

Figure 1. Methane oxidation over Pt(II)/Pt(IV) catalytic system.

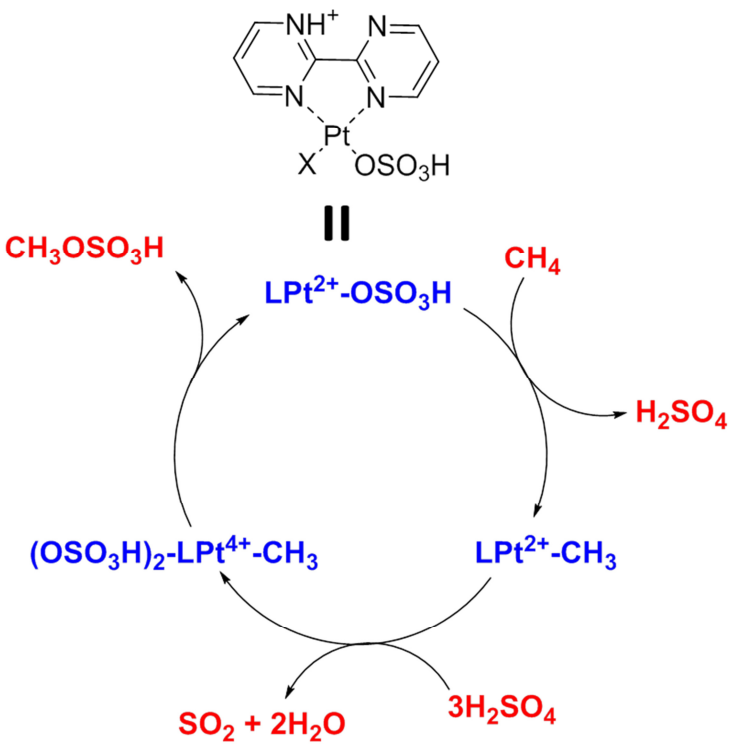

Figure 2. Methane oxidation over Periana's catalytic system.

serves as an oxidant (Fig.1).[9] The Pt(II)-CH_3 complex formed after methane activation is oxidised with Pt(IV) to the Pt(IV)-CH_3 complex, that undergoes reductive elimination with formation of CH_3Cl (or methanol in case of reaction with water). Use of acidic media was necessary to stabilize Pt species in high oxidation state. Another reason for the use of acidic conditions was protection of the reaction product: formation of methyl ester with acetic acid prevents methanol from overoxidation.

Since the possibility of methane activation was shown, a number of reported catalytic systems, capable of methane oxidation (based on complexes of Rh, Pd, Pt, Au, Hg, Tl), has grown significantly.[9, 16-18] Continuous improvement of the described catalytic systems has resulted in development of a few highly active and selective catalysts of this type, among which the most effective is so-called "Periana's catalyst".[19] This system represents 2,2'-bipyrimidine-platinum complex, able to oxidize methane to methyl bisulphate in oleum at 220 °C with 81% selectivity and 90% methane conversion. Further hydrolysis of the ester obtained gives methanol with 70% yield. Chemically this process is similar to Pt(II)/Pt(IV) system, but with SO_3 serving as an oxidant for the Pt(II)-CH_3 complex (Fig. 2).[16]

Catalytic properties in terms of selectivity and yield make Periana's system suitable for industrial process. Nevertheless, this system is still far from real application because of several disadvantages, common for this type of catalysts:

1) Problems with stability. Active species capable of methane activation, *e.g.* Pt(II) complexes, are easily reduced to metallic state and should be reoxidized to close the catalytic cycle. Such reoxidation usually demands utilization of very strong oxidants, *e.g.* SO_3 or/and Pt(IV).[15-16] It necessitates to develop a co-catalyst for regeneration of the oxidant by other available and inexpensive oxidants, usually dioxygen.

2) Harsh reaction conditions. For stabilization of active cationic species highly-acidic reaction media are used, as formation of hydroxo complexes generally leads to catalyst deactivation. Many catalysts are sensitive to amounts of water in the reaction mixture.

3) Problems with product recovery. The process is performed in highly acidic conditions (sulphuric, acetic, trifluoracetic acids), resulting in the formation of esters of methanol. This helps preventing product overoxidation, but at the same time it introduces an additional step to the overall process.

4) Environmental problems due to utilization of strong oxidants and highly-acidic conditions.

5) Economically unfavourable use of homogeneous noble metal complexes and harsh conditions.

Recent research progress shows some possibilities to overcome these limitations. The search for co-catalysts for regeneration of the Pt(II)/Pt(IV) catalyst system has shown that upon addition of $CuCl_2$ the system is able to perform methane oxidation even without initial addition of Pt(IV) complexes.[20] It was proposed that in highly acidic media Cu(I) species (obtained by oxidation of Pt(0) to Pt(II) by Cu(II)) can react with molecular oxygen, forming Cu(II) hydroperoxide species $Cu(OOH)^+$.[18] In acidic conditions copper(II) hydroperoxides are expected to be strong oxidants, able to oxidize Pt(II) to Pt(IV) (Fig. 3). Attractive approach for heterogenezation of Periana's catalyst by using covalent triazine frameworks (CTFs) has been proposed.[21-22] CTFs contain pyridinic and triazinic groups in their structure, which are suitable for coordination of isolated Pt centres. The resulting catalyst possesses Pt species in coordination environment similar to Periana's catalyst and is characterized by high stability and activity, close to that of homogeneous counterpart.

Alternative methane oxidation processes often utilize H_2O_2, O_3, N_2O and *tert*-butyl hydroperoxide as reactive oxygen donors in these schemes. Other substances like HNO_3, H_2SO_4, NaClO and $NaClO_2$ have also been applied. However, all these processes suffer from similar disadvantages: the oxidant is either too expensive or too difficult to handle in a safe manner for the environment. This requires implementation of additional steps for oxidant separation from the reaction mixture and development of an additional cycle for oxidant regeneration, which significantly increases the capital costs of the overall process.

In this sense, molecular oxygen O_2 would be the most desirable oxidant due to its high abundance, low cost and relatively low reactivity of its main by-product (H_2O). The main difficulty of applying O_2 directly for the selective oxidation of hydrocarbons is associated with the triplet ground state of the oxygen molecule. According to Wigner's spin selection rule,[23] the total spin of reactants should be equal to the total spin of products in the chemical reaction. Methane molecule has singlet ground state (S = 0) and oxygen is a triplet (S = 1), which means that reaction between them cannot give methanol and water (both S = 0) as products.[24] In principle, this limitation

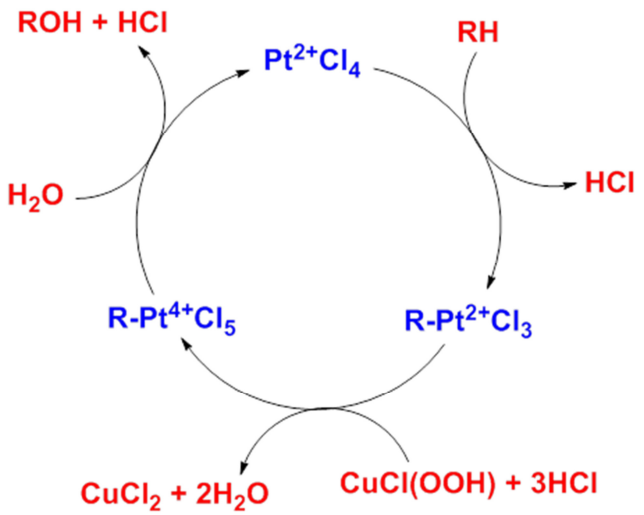

Figure 3. Alkane oxidation over a catalytic Pt-Cu system.

could be overridden if O_2 is excited into a singlet state. In practice excitation of dioxygen molecule to such singlet states requires high temperatures or other high energy sources (plasma, high electric fields, *etc.*), which usually leads to poor product selectivity. Alternative approaches involve catalytic activation of O_2 by transition metal centres, which can facilitate the spin inversion of triplet oxygen either by single electron transfer or via intersystem crossing by spin orbit coupling. This reaction can result in different intermediate species, and the redox potential of these intermediate species depends heavily upon pH or effective acidity of the reaction media. In general, one electron reduction of oxygen is favoured in highly protic media.

One of the most prominent examples of catalytic systems able to selectively oxidize methane to methanol using molecular dioxygen are zeolite-based systems. In 1995 it was shown, that under treatment of Fe-containing zeolite ZSM-5 at 900 °C and its following activation with N_2O at 250 °C highly-active long-living oxygen species (so-called “α-oxygen”) are formed, readily reacting with organics.[25] Reaction of such species with methane at only 25 °C easily converted it to surface-bound methoxy species. Investigation of α-oxygen generation and its activity towards methane oxidation was also performed on Cu-containing ZSM-5. It was shown, that active oxygen species are also generated in reaction of thermally activated Cu-ZSM-5 with N_2O. Furthermore, treatment of Cu-ZSM-5 at 500 °C in oxygen also leads to formation of active copper-oxygen species.[26] Such reaction does not occur in case of Fe-ZSM-5. At 125 °C these species interact with methane, also

forming surface-bound methoxy groups. Unfortunately, the strong binding of these species does not allow obtaining methanol directly. Heating of the sample leads to its oxidation prior to desorption, resulting in CO_2 as the main product already at 250 °C. Another route is hydrolysis of chemisorbed methoxy species with consequent extraction of methanol, giving methanol with greater than 90% selectivity and overall methane conversion of 80%. Later investigations showed that water steam can be used as well for removal of methanol from the catalyst.[27-28] However, the necessity to have separate regeneration and extraction steps after each catalytic cycle makes this technology less commercially attractive. Attempts to perform the reaction in a continuous mode (*i.e.* by feeding methane, O_2 or N_2O, and steam at the same time) so far showed either low methane conversion or low methanol selectivity.[29-30]

The discussed examples show two main sides of the oxidant activation challenge: the oxidant should become suitable for reaction with activated methane molecule but at the same time its further reaction to methanol should be prevented. Economic and ecological considerations make dioxygen the most preferable oxidant. However, due to the triplet ground state of this molecule, it should first be converted into singlet spin state species to be able to react with methane. Methanol should not be adsorbing too strongly to the active catalyst centre and preferably should easily leave the catalytic site after the reaction. One of the common strategies to minimize the overoxidation of methanol is converting it into more bulky compounds (*e.g.* esters), but an additional step of methanol regeneration from these compounds needs to be introduced in this case.

1.2.3. Enzymes and enzyme-inspired catalysts for methane oxidation

Another type of catalytic systems, able to selectively oxidize methane to methanol, is found in nature. Natural enzymes, monooxygenases, were proven to perform methane oxidation with high activity and 100% selectivity towards methanol under mild aqueous conditions.[31-32] Two types of such enzymes are known to date – heme monooxygenases of the Cytochrome P450 type and non-heme methane monooxygenases (MMOs) (Fig. 4). In turn, two different classes of MMOs were found in various methanotrophic bacteria: soluble and particulate methane monooxygenases (sMMOs and pMMOs, respectively). pMMOs are present in all methanotrophic organisms, but are isolated hard and thus not well studied yet. sMMOs are produced

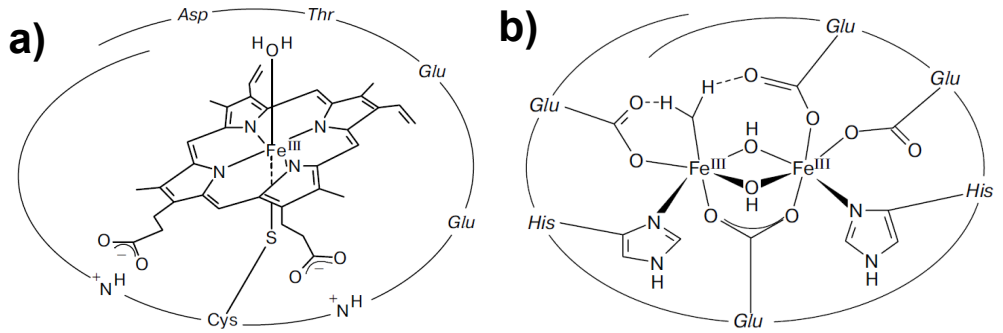

Figure 4. Active centre structure of a) Cytochrome P450 and b) soluble methane monooxygenase in oxidized (ferri) state (adopted from Shteinman *et al.*[31]).

only by a few methanotrophic species and only under specific conditions. sMMOs and cytochrome P450 can be isolated relatively easily, and for these enzymes their structure and mechanism of catalytic appearance is relatively well investigated.

In P450, the enzyme active centre is a heme complex of iron(III), coordinated to the cysteine group of the enzyme at one side of the porphyrin ring and with a coordinated water molecule at the other side (Fig. 4a). On both sides of the ring the enzyme structure forms hydrophobic pockets, suitable for methane binding, where the reaction takes place. After capture of the methane molecule in a hydrophobic pocket, the coordinated water is removed and Fe(III) is reduced to Fe(II) by electron transfer from the reducing agent. The Fe(II)-heme complex interacts with molecular oxygen, forming a haemoglobin-resembling complex. After several transition states it transforms into high valence ferryl complex Fe(IV)=O, that oxidizes methane to methanol (Fig. 5).

The active centre of sMMO is a binuclear iron complex, connected to the protein via four glutamate (Glu) and two histidine (His) groups. One of the carboxylic groups of Glu always serves as the bridge between the iron atoms. Additional bridges (up to 3) are formed during the catalytic cycle from other carboxylic groups and exogenous hydroxide or aqua ligands. In contrast to the active centre of cytochrome P450, with only one coordination site for formation of oxygen-containing intermediates, in sMMO there are four inner coordination sites that participate during the catalytic cycle. In the resting oxidized state (ferri-state) these sites are occupied by two bridging OH groups (Fig. 4b). The active site contains a hydrophobic substrate-binding cavity of about 185 Å in volume. Substrate binding in this

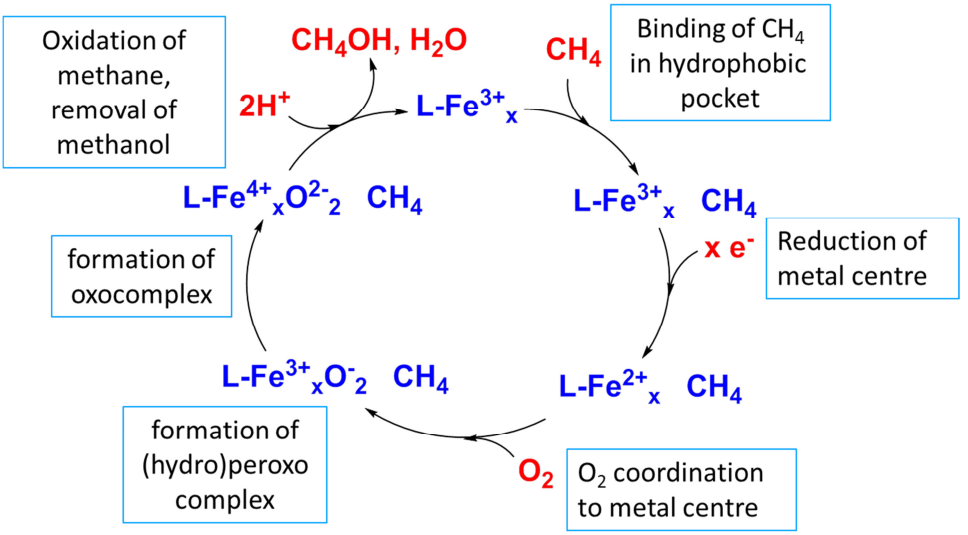

Figure 5. Generalized scheme of enzymatic methane oxidation

hydrophobic pocket initiates rapid two-electron reduction of the iron(III) cluster to iron(II), forming the reduced ferro-state. In the ferro-state both hydroxo bridges are broken and both iron atoms become five-coordinated, that gives two coordination sites for binding of O_2. Interaction with dioxygen leads to the formation of peroxodiiron(III) complex (intermediate P), that is spontaneously converted to bis-μ-oxo-Fe(IV)$_2$ complex (intermediate Q). Q interacts with methane and oxidizes it to methanol.

It should be mentioned that regeneration of sMMO active site (reduction of oxidized ferri-state into ferro-state) involves the two-electron donor chain mechanism, which requires additional components of sMMO – reductase MMOR and coupling protein MMOB.[33] MMOR reduces the oxidized Fe(III)-Fe(III) site, utilizing NAD(P)H as a source of electrons and protons, and MMOB controls interaction between MMOR and the main hydroxylase component. The presence of these components is essential for the catalytic activity of sMMO in natural conditions. However, it was shown that methane oxidation to methanol could be performed even without these components when H_2O_2 is used as oxidant instead of O_2.[34] This brings new insights into development of catalytic systems for methane oxidation.

Although in case of pMMO the exact structure of its active centre and the mechanism are still not confirmed, it is established that the pMMO structure includes one binuclear copper site and two mononuclear sites (one of them contains copper, the atom of another one is debatable). It was shown that the binuclear site is most likely the active centre for methane oxidation.[32]

One of the copper atoms is coordinated by two imidazole groups from two histidine units, and the other by imidazole and amino groups of one histidine unit with a Cu – Cu distance of ≈ 2.6 Å. Treatment of the enzyme with H_2O_2 does not change this distance.[35] It means no change of oxidation state takes place. A model bis-μ-oxocomplex of copper (Cu_2O_2 complexes) has shown the shortest Cu – Cu distance of ≈ 2.8 Å. This is supposed to be the closest to the real pMMO active centre. Additional theoretical calculations claim that the highest activity would be observed in case of mixed-valence complex bis-μ-oxo-Cu(II)Cu(III), that should be able to abstract the H-atom from methane.

According to the description given for P450 and sMMO, some general features of enzymatic methane oxidation can be distinguished. In case of enzymatic oxidation the methane C-H bond is not directly coordinated to a metal centre. In both cases the reaction cycle starts with approaching of methane to the active site, but the active metal centre serves for activation of the oxidant (dioxygen), not the C-H bond. Oxidation of metal complexes of the active centre results in the formation of active complexes with metal in a high-valence state, thermodynamically able to oxidize methane. Methane is coordinated to this metal-oxygen complex via an outer sphere mechanism and oxidized to methanol. The effective removal of the product is achieved via interaction with specific functional groups of the enzyme structure preventing overoxidation. This route is significantly different from the inner-sphere methane oxidation mechanism discussed before and draws significant attention. The advantages of these systems – direct utilization of dioxygen as oxidant, no need to use highly acidic conditions, inexpensive metals of the active centre – make the development of an industrial catalyst in this direction attractive.

There is a variety of homogeneous mono-, bi- and trinuclear complexes of iron and copper that has been applied for methane oxidation.[35-37] However, most of these systems are unable to bind molecular oxygen to use it as an oxidant. Oxidation of methane takes place only with the use of hydrogen peroxide in case of some iron-containing complexes. Some of these catalysts show high selectivity towards methanol, but its activity is usually low. In case of copper model complexes, only weak C-H bonds can be oxidized. One of the catalysts with the highest methane oxidation activity represents binuclear N-bridged diiron(IV) phtalocyanine complex, mimicking cytochrome P450 active site.[37-38] This system is able to catalyze the oxidation of methane to acetic acid by H_2O_2 in water at 25–60 °C with 30-50% yield. The presence of the peroxoiron complexes Fe(III)–OOH and

ferryl species Fe(V)=O was detected during the reaction, showing the similarities with the reaction pathway of monooxygenases.[39] However, a methanol selectivity of 50% and higher was shown only in case of very low-active phtalocyanine-based catalysts.[40] Another issue is the stability of these catalysts because of the macrocyclic ligand decomposition under the reaction conditions.

One of the reasons of the low activity in case of such molecular complexes could be flexibility of the utilized ligands. Insufficient rigidity of the structure allows conversion of resulting complexes in conformations far from desired for methane oxidation.[41] In several cases immobilization of active centres on an appropriate support led to improvement of its catalytic properties.[42] Effect of stabilization of active centres on the catalytic properties was successfully shown in case of zeolite-based catalysts. Fe-and Cu-modified zeolite ZSM-5(30) shows 90% selectivity towards methanol at 10% methane conversion with H_2O_2 in water.[43] The observed turnover frequency of more than 14 000 h^{-1} is over three orders of magnitude higher than any previously reported. Investigation of the catalyst has proved the formation of diferric active site, containing one ferryl (Fe(IV)=O) and one Fe-hydroperoxy (Fe-OOH) component. It should be noted, that in case of ZSM-5(30) with only Fe^{3+} sites the methanol selectivity was only about 10%, whereas the introduction of Cu^{2+} does not have any influence on catalyst activity but improves its selectivity towards methanol greatly. Authors claim that Cu^{2+} species are able to bind hydroxyl radicals, present in the reaction mixture because of H_2O_2 decomposition, and thus prevent product overoxidation.

Based on these results, it can be concluded that H_2O_2 could successfully replace molecular oxygen as an oxidant for enzyme-mimicking mild methane oxidation catalysts. H_2O_2 can directly react with organics. From a practical point of view, the main limitation there is the relatively high price of H_2O_2 (currently more expensive than methanol), although the development of new efficient catalysts for H_2O_2 production from H_2 and O_2 could make these technologies more economically feasible.[44-45]

1.2.4. Strategy for design of mild methane oxidation catalyst

Based on the examination of different natural and artificial catalytic systems for oxidation of methane to methanol one can formulate the following features of the successful catalyst for mild methane oxidation:

- Isolated active species. Spatial separation of catalyst active sites would decrease the chance of methanol readsorption after reaction and its overoxidation. Thus, single mono-, di- or trimeric metal sites are preferred over supported metal clusters or nanoparticles;
- Stability. The catalyst should withstand the reaction conditions and should be efficiently regenerated after each catalytic cycle without degradation;
- Heterogeneity and porosity. Heterogeneous catalysts are preferred over homogeneous for most of industrial applications. To maximize the utilization of the catalyst surface, the catalyst should be porous;
- Hydrophobicity. To facilitate the approaching of methane molecule to the catalyst active site as well as the removal of methanol molecules after the reaction, the catalyst support should preferably be hydrophobic.

Considering the studies of the active sites of MMOs and the advances in zeolite-based catalysts for methane oxidation, Fe and Cu are going to be the first choice as metals for active sites of catalysts for methane-to-methanol conversion. However, other transitional metals used in catalysts for oxidative conversion of hydrocarbons (Cr, Co, Os, *etc.*) should also be considered.

Although dioxygen is the most favorable oxidant from commercial point of view, its activation still requires high temperatures or harsh reaction conditions, thus limiting the range of applicable catalyst types. From this point of view, the use of hydrogen peroxide could be beneficial as it can react with organics already in mild aqueous conditions. Heterogeneous catalysts for methane oxidation with oxygen or other strong oxidants, reported so far, are usually intrinsically hydrophilic inorganic materials. However, a broad range of hydrophobic organic and metal-organic porous polymers with tunable porosity (COFs, CTFs, MOFs, *etc.*) could be applied for methane oxidation with H_2O_2 (of course, if the material proves to be stable in H_2O_2 solutions). Such material should stabilize well the isolated active metal sites, assuring that they do not leach into the solution or agglomerate on the catalyst surface as nanoparticles, which would lead to the unselective Fenton-type reactivity. Developing a catalyst that meets these requirements would open a promising pathway for implementation of a methanol economy.

One can see that the crucial part in the proposed design of mild methane oxidation catalyst is the stabilization of well-defined isolated active species. This implies the use of advanced synthesis methods but also advanced characterization techniques to distinguish the desired species and thoroughly characterize their properties. In the next sub-chapter we will discuss which characterization strategy and which methods should be the most suitable for this research area.

1.3. X-Ray techniques for characterization of heterogeneous catalysts

Thorough characterization of catalysts before, after and during the catalytic experiment has an utmost importance for understanding of the processes happening in the catalytic cycle. In order to have the full overview of the processes that take place on the surface of heterogeneous catalyst one should be able to identify, quantify and correlate

- The products generated during the catalytic reaction,
- The active centres of the catalysts – their composition, electronic and geometric structure,
- The reactive intermediates formed through the interaction of active centres with the reactants – their composition and structure.

In most cases one single technique cannot provide the necessary information on all these components of the catalytic system, so the state-of-the-art combination of methods is necessary for the conclusive characterization of the catalyst and for the understanding of its behaviour in the reaction conditions. Modern chromatography and mass-spectrometry techniques enables reliable *operando* quantification of reagents and products with very low detection limits. However, characterization of the active site and reactive intermediates generally represents a far more difficult task, that demands the development of individual analysis approach for nearly every new catalytic system. Below the problems typically arising in these studies are generalized.

Firstly, the analysis under true reaction conditions (*operando*) is still challenging for the majority of characterization methods due to the practical limitations of the equipment and methods themselves. Many spectroscopic techniques require low temperature or high vacuum conditions, or are just difficult to be applied at high pressures and temperatures required for the reaction. Although examples of advanced *in-situ* and *operando* setups and experimental cells for common spectroscopic techniques appear more and

more often in literature,[46-48] design and development of such equipment is challenging and non-trivial task, that is still far from serial production in many cases. Alternatively, the common practice of *ex-situ* analysis of catalyst after reaction can provide *post factum* some insight on the catalyst behaviour. However, this approach gives only limited information and is hardly applicable to several catalytic systems as the transfer of catalyst from the reaction to the analysis conditions can cause significant changes in its structure and composition.

Secondly, in many cases it becomes difficult to separate and identify the changes in experimental spectra arising from the transformation of catalytically active species, from the generated reaction products and intermediates, and from spectator species. This problem becomes particularly pronounced for the carbon-based catalysts, where the signals arising from possible changes of the carbon matrix itself overlap with the evidences of transformations on the catalytically active sites and with signals from the reaction products. There is no single method that can provide all necessary information on the structure, composition and chemical state of the catalyst active species, so the state-of-the-art combination of techniques is necessary for the conclusive characterization of the catalyst and understanding of its behaviour in the reaction conditions. However, the proper choice of techniques allows to get the relevant information in the most efficient way. Choosing the methods for analysis of the heterogeneous catalyst, the researcher should take the following considerations:

- As soon as most of the processes related to the catalyst performance take place on the surface of the catalyst, the methods with high surface sensitivity are preferred (however, bulk methods should be used to characterize the difference between the surface and the bulk phase of the catalyst);
- The method should provide high signal-to-noise ratio, preferably with narrow line widths, allowing to identify a broad variety of species and to detect subtle changes in the line shapes and positions;
- In case of non-crystalline materials with significantly disordered distribution of active sites on the surface the local structural methods, providing information on the closest surroundings of the active species, are preferred;
- In case of multielement samples or low concentrations of elements of interest in the samples the element-specific techniques are

preferred (this allows to investigate separately the features of each element species in the sample with minimal interference).

Below we will discuss the most common and informative techniques for characterization of heterogeneous catalysts active sites.

1.3.1. XPS

Most of the currently applied surface-sensitive spectroscopic techniques can be loosely divided into

- Techniques taking the advantage of directing an incident beam at very small angles to the sample surface, assuring that only the top layers of the sample are analysed;
- Techniques utilizing the radiation with very short mean free path in the analysed material;
- Techniques involving treatment of the sample surface with specific reagents and focusing specifically on the surface-reagent interactions.

All these approaches are widely used (often in combination) in numerous spectroscopic techniques. However, the majority of these methods are still not very common and require complex and expensive equipment. In this respect, one of the most abundant, widely used, well-developed methods for surface characterisation of composition and chemical state of catalysts is X-ray photoelectron spectroscopy (XPS). The technique is based on a well-studied photoelectric effect: the sample is irradiated with X-ray beam (usually with energy of 1-2 keV), that causes emission of electrons from the sample. The energy of this beam is sufficient to remove electrons from the deep-lying core energy levels. The energies of these discrete levels are characteristic for every element, so by measuring the kinetic energies of emitted electrons one can determine the elemental composition of the sample. Furthermore, exact positions of energy levels depend on the oxidation state and surrounding of an atom, so XPS also brings information on the chemical state of the elements. Due to relatively short mean free paths of electrons in solid state materials (1-20 nm) only electrons from surface and sub-surface atoms are detected, making XPS a (sub)surface analysis technique.[49] The narrow line width of X-ray radiation as well as the availability of advanced electron detection systems allow registering narrow photoelectron lines and performing quantitative chemical analysis of the surface species.

Currently XPS is widely used for the characterization of heterogeneous catalysts, and various modifications of the XPS equipment and the method itself (including *ex-situ* and *in-situ* catalytic experiments) have been reported up to date. However, the possibilities of this method for the routine analysis of catalysts are often underestimated. In particular, XPS analysis of carbon- or organic-based catalysts reported in literature often suffers from two opposite tendencies: authors either do not describe the changes in C*1s* or O*1s* spectra at all or use inadequately high number of peaks for fitting the experimental spectra. Obviously, characterization of catalysts that mainly consist of carbon with minor addition of some other elements, and especially characterisation of these catalysts after reaction, often represents a challenge. Signals from the catalyst matrix, the organic reaction products trapped in the pores or agglomerated on the surface of the catalyst as well as the possible contamination of the surface by adventitious carbon make the characteristic lines of carbon and oxygen a puzzle, that is often very difficult to interpret. However, a systematic and accurate XPS analysis of the samples in combination with reasonable use of other characterization techniques make XPS a valuable tool for catalyst characterization.

1.3.2. XAS

Techniques where X-rays are used both as the incident beam and as the detected signal (XRD, EXAFS, SAXS, *etc.*) are widely used for structural characterization of the materials. However, common X-ray diffraction (XRD) analysis can only be informative for materials possessing long-range order in their structure. However, catalyst active centres, especially in case of isolated metal sites, are usually too small and not distributed in ordered manner throughout the sample. XRD often becomes not informative for such samples, and other techniques, disclosing information on the local surrounding geometry for certain type of atoms, are required. In these cases, X-ray absorption spectroscopy (XAS) techniques become the best choice as they are element-specific and provide local structural information.

XAS studies the effects which take place when electrons from deep-lying core orbitals are excited to valent energy levels or even higher by X-ray irradiation of appropriate energy. By changing the energy of the incident X-ray beam and measuring the intensity of X-ray which passed through the sample one can obtain the X-ray absorption spectra (in this case the measurement is performed in *transmission mode*). Alternatively, one can measure the intensity of X-ray radiation generated from the interaction of the

incident X-ray beam with the sample; in this case the measurement is performed in *fluorescence mode*.

X-ray absorption spectra consist of intense absorption edges of complex structure. Excitation of electrons from the most deep-lying *1s* orbital gives rise to so-called *K*-edge, excitation from *2s* and *2p* orbitals – to *L*-edge, *etc*. Each element has characteristic energies of its X-ray absorption edges, so by choosing the right window of X-ray energies one can study each element of the sample separately.

Each *K*-edge XAS spectrum consists of the following regions:

1) Pre-edge, which represents transition of electrons from *1s* to the valent orbital (*3d* in case of 1st row transitional metals);
2) X-ray Absorption Near-Edge Structure (XANES), also known as NEXAFS (Near-edge X-ray Absorption Fine Structure), which represents transitions to the higher-lying empty orbitals. Usually these levels are overlapping and form a continuum with increasing energy;
3) Extended X-ray Absorption Fine Structure (EXAFS), observed at higher energies, which represents scattering of core electrons emitted from the atom on the neighbouring atoms.

The energies of the pre-edge and the edge are increasing at higher oxidation states of the element, thus providing informative tool for analysis of element valency in the sample. The shape of the pre-edge and the edge can differ a lot for different compounds of the same element. In particular, the intensity of the pre-edge depends on the geometry of the element surrounding: more centrosymmetric structure results in lower intensity of pre-edge, and *vice versa*. This opens broad possibilities for identification of local geometry and composition even in case of non-crystalline species, either by modelling or by using “fingerprint” spectra from the reference compounds.

Examination of the EXAFS region provides the distances between the atoms of the selected element and the neighbouring atoms, which helps identification of its local structure. Careful fitting of EXAFS spectra by using reference crystallographic data allows to identify the neighbouring elements and their coordination numbers.

One can see that combination of XPS and XAS provides important information, especially valuable for characterization of heterogeneous catalysts: XPS gives information on surface composition and chemical

states of the elements, and XAS provides element-specific structural information. Various modifications of these methods (small angle XAS, *operando* XPS) allow investigation of composition, chemical state and geometry of surface species in conditions close to the reaction conditions for a variety of catalytic systems and processes. However, in some cases this combination still might be not informative enough, so each particular catalytic system requires the individual selection of methods that will suit the best.

1.3.3. Selection of characterization methods for methane oxidation catalysts with isolated metal sites

Investigation of the catalysts with isolated metal sites is often challenging as better isolation of sites requires lower concentration of active species. As a consequence, detecting the species and resolving different chemical states by means of spectroscopy becomes challenging. Potential solution could be preparation of samples with higher concentration of active metal. However, this might lead to formation of new types of species or to agglomeration of active metal to nanoparticles. In this case the primary goal of spectroscopic characterization becomes the ability to distinguish isolated sites from nanoparticles.

Different spectroscopic techniques have different size limitations on detecting small particles. Powder XRD analysis usually allows identifying phases with particle size only above ~4 nm. TEM is often very helpful for control over sample homogeneity and, depending on a contrast between the support and the active species, allows to observe particles of ~1 nm in size. However, for catalysts with isolated sites the presence of non-incorporated clusters even smaller than 1 nm can have influence on catalytic performance. In this case XAS characterization becomes particularly valuable as it describes the closest atomic surrounding for atoms of particular element. Fitting of EXAFS data using the structural parameters of reference bulk phases allows to identify whether short metal-metal bonds are present in the sample or not. By fitting one can also obtain the average coordination number for these bonds, which allows to estimate the cluster size.

Even if the active metal is well dispersed in the sample, it is important to know in which form it is present: is it incorporated in the structure of the support or adsorbed on its surface, for example. In this case vibrational spectroscopy methods (IR spectroscopy, Raman spectroscopy) can provide

valuable insights. Comparison of the spectra from samples with active metal to the spectra from pristine support material will show which bonds are affected due to active metal introduction.

If the active metal is present in several oxidation states on the surface, XPS can be an informative tool for quantitative characterization of its surface composition. However, it should be noted that in most cases it is difficult to distinguish different types of species in the same oxidation state with XPS (*e.g.* metal oxide and isolated metal ions in complexes).

Another important aspect in characterization of isolated sites is determining their spin state, which directs the reactivity of active species. Electronic paramagnetic resonance (EPR) becomes the primary method in this case, as it provides information on the number of unpaired electrons in the system and types of interaction between them. If paramagnetic particles are present in the samples, the signal from them distorts the whole spectra, which is also helpful for identification of active metal phases in the sample.

For Fe-based systems Mössbauer spectroscopy provides additional broad opportunities for characterization of iron phases, present in the sample, their oxidation states and electron spin states. However, for the detailed analysis the samples should either contain a high concentration of Fe or should be prepared using Fe precursors enriched with the ^{57}Fe isotope.

Although both synthesis and characterisation of catalysts with isolated sites can be challenging, combination of structural methods (XRD, TEM, XAS), vibrational spectroscopy (IR, Raman), analysis of chemical states (XPS) and electron spin states (EPR, Mössbauer spectroscopy) can provide sufficient information for comprehensive characterisation of catalyst active sites.

1.4. Thesis outline

The main challenge addressed in this thesis is the development of methods for synthesis and characterization of heterogeneous catalysts with isolated metal sites with an emphasis on the mild oxidation of methane. Several different catalytic systems were studied. For each system the appropriate combination of characterization methods was chosen in order to study in detail the nature of its active sites or to optimize its properties by modification of synthesis procedure.

The above-mentioned research led to four research chapters, which focus on the design of catalysts for mild methane oxidation (Chapters 2-3) and application of X-ray based techniques for characterization of heterogeneous

catalysts (Chapters 4-5). After this introductory **Chapter 1** the following topics are addressed in the next chapters:

- **Chapter 2** describes the development of first catalyst for mild methane oxidation with H_2O_2 based on metal organic framework (MOF) MIL-53(Al) with incorporated isolated Fe sites. Optimization of the electrochemical MOF synthesis procedure leads to the catalysts with improved performance in selective methanol production compared to conventional hydrothermal synthesis. Extensive spectroscopic characterization shows that structural and magnetic features of the active sites in electrochemically-synthesized catalysts are similar to those of sMMO enzyme.
- In **Chapter 3** the strategies for further improvement of MIL-53(Al,Fe) catalysts for mild methane oxidation are studied. The effects of using functionalized linkers, different metal cations and modification of the reaction conditions are discussed. In addition, the attempt to develop a catalyst for mild methane oxidation with H_2O_2 based on covalent triazine frameworks (CTFs) is presented. The reasons of difference in performance between MOF- and CTF-based catalysts are discussed and directions for further catalyst design are proposed.
- **Chapter 4** shows the applicability of X-ray based techniques (XPS and XAS) for characterization of carbon-based heterogeneous catalysts. Three Case studies focus on three different systems, namely carbon nanotubes, nitrogen-doped amorphous carbons with cobalt sites, and a nitrogen-containing polymer with nickel sites. The benefits and pitfalls of using these techniques, as well as practical details of sample preparation and analysis, are discussed in the chapter.
- **Chapter 5** deals with optimization of the synthesis procedure of CTFs in order to make them suit better for applications in catalysis. Series of CTFs were prepared by varying the ratio between different monomers, synthesis temperature, synthesis time, catalyst for CTF formation, and the amount of the catalyst. Systematic XPS characterization of nitrogen sites in the samples was combined with their textural characterization. The results show how changing synthesis parameters influences the interplay between CTF formation and decomposition, affecting the properties of the resulting materials.

All chapters have been written as (parts of) individual publications and can be read independently. Therefore, some overlap may be present.

1.5. References

1. Aasberg-Petersen, K.; Dybkjær, I.; Ovesen, C. V.; Schjødt, N. C.; Sehested, J.; Thomsen, S. G., Natural gas to synthesis gas - Catalysts and catalytic processes. *Journal of Natural Gas Science and Engineering* **2011,** *3* (2), 423-459.
2. Havran, V.; Duduković, M. P.; Lo, C. S., Conversion of methane and carbon dioxide to higher value products. *Industrial and Engineering Chemistry Research* **2011,** *50* (12), 7089-7100.
3. Choudhary, T. V.; Choudhary, V. R., Energy-efficient syngas production through catalytic oxy-methane reforming reactions. *Angewandte Chemie - International Edition* **2008,** *47* (10), 1828-1847.
4. Holmen, A., Direct conversion of methane to fuels and chemicals. *Catalysis Today* **2009,** *142* (1), 2-8.
5. Olah, G. A., Beyond oil and gas: The methanol economy. *Angewandte Chemie - International Edition* **2005,** *44* (18), 2636-2639.
6. Schwarz, H., Chemistry with methane: Concepts rather than recipes. *Angewandte Chemie - International Edition* **2011,** *50* (43), 10096-10115.
7. Otsuka, K.; Wang, Y., Direct conversion of methane into oxygenates. *Applied Catalysis A: General* **2001,** *222* (1-2), 145-161.
8. Hargreaves, J. S. J.; Hutchings, G. J.; Joyner, R. W., Control of product selectivity in the partial oxidation of methane. *Nature* **1990,** *348* (6300), 428-429.
9. Shilov, A. E.; Shul'pin, G. B., Activation of C-H bonds by metal complexes. *Chemical Reviews* **1997,** *97* (8), 2879-2932.
10. Ess, D. H.; Goddard, W. A.; Periana, R. A., Electrophilic, ambiphilic, and nucleophilic C-H bond activation: Understanding the electronic continuum of C-H bond activation through transition-state and reaction pathway interaction energy decompositions. *Organometallics* **2010,** *29* (23), 6459-6472.
11. Rybak-Akimova, E. V., Mechanisms of Oxygen Binding and Activation at Transition Metal Centers. In *Physical Inorganic Chemistry: Reactions, Processes, and Applications*, **2010**, pp 109-188.
12. Gopakumar, G.; Belanzoni, P.; Baerends, E. J., Hydroxylation catalysis by mononuclear and dinuclear iron oxo catalysts: A methane monooxygenase model system versus the fenton reagent Fe IVO(H 2O) 5 2+∇. *Inorganic Chemistry* **2012,** *51* (1), 63-75.
13. Kazaryan, A.; Baerends, E. J., Ligand field effects and the high spin-high reactivity correlation in the h abstraction by non-heme Iron(IV)-oxo complexes: A dft frontier orbital Perspective. *ACS Catalysis* **2015,** *5* (3), 1475-1488.

14. Gol'dshleger, N. F. T., M. B.; Shilov, A. E.; Shteinman, A. A., Activation of saturated hydrocarbons. Deuterium-hydrogen exchange in solutions of transition metal complexes. *Zhurnal Fizicheskoi Khimii* **1969,** *43*, 2174-2175.

15. Gol'dshleger, N. F. E. k., V. V.; Shilov, A. E.; Shteinman, A. A., Reactions of alkanes in solutions of platinum chloride complexes. *Zhurnal Fizicheskoi Khimii* **1972,** *46*, 1353-1354.

16. Periana, R. A.; Bhalla, G.; Tenn Iii, W. J.; Young, K. J. H.; Liu, X. Y.; Mironov, O.; Jones, C. J.; Ziatdinov, V. R., Perspectives on some challenges and approaches for developing the next generation of selective, low temperature, oxidation catalysts for alkane hydroxylation based on the CH activation reaction. *Journal of Molecular Catalysis A: Chemical* **2004,** *220* (1), 7-25.

17. Hammond, C.; Conrad, S.; Hermans, I., Oxidative methane upgrading. *ChemSusChem* **2012,** *5* (9), 1668-1686.

18. Chepaikin, E. G., Oxidative functionalization of alkanes under dioxygen in the presence of homogeneous noble metal catalysts. *Journal of Molecular Catalysis A: Chemical* **2014,** *385*, 160-174.

19. Periana, R. A.; Taube, D. J.; Gamble, S.; Taube, H.; Satoh, T.; Fujii, H., Platinum catalysts for the high-yield oxidation of methane to a methanol derivative. *Science* **1998,** *280* (5363), 560-564.

20. Lin, M.; Shen, C.; Garcia-Zayas, E. A.; Sen, A., Catalytic shilov chemistry: Platinum chloride-catalyzed oxidation of terminal methyl groups by dioxygen [13]. *Journal of the American Chemical Society* **2001,** *123* (5), 1000-1001.

21. Palkovits, R.; Antonietti, M.; Kuhn, P.; Thomas, A.; Schüth, F., Solid catalysts for the selective low-temperature oxidation of methane to methanol. *Angewandte Chemie - International Edition* **2009,** *48* (37), 6909-6912.

22. Bavykina, A. V.; Olivos-Suarez, A. I.; Osadchii, D.; Valecha, R.; Franz, R.; Makkee, M.; Kapteijn, F.; Gascon, J., Facile Method for the Preparation of Covalent Triazine Framework coated Monoliths as Catalyst Support: Applications in C1 Catalysis. *ACS Applied Materials and Interfaces* **2017,** *9* (31), 26060-26065.

23. Wigner, E., Uber die Erhaltungssatze in der Quantenmechanik. *Nachrichten der Akademie der Wissenschaften in Gottingen. II. Mathematisch-Physikalische Klasse* **1927,** *2a*, 375.

24. Liu, X.; Ryabenkova, Y.; Conte, M., Catalytic oxygen activation versus autoxidation for industrial applications: a physicochemical approach. *Physical Chemistry Chemical Physics* **2015,** *17* (2), 715-731.

25. Sobolev, V. I.; Dubkov, K. A.; Panna, O. V.; Panov, G. I., Selective oxidation of methane to methanol on a FeZSM-5 surface. *Catalysis Today* **1995,** *24* (3), 251-252.

26. Groothaert, M. H.; Smeets, P. J.; Sels, B. F.; Jacobs, P. A.; Schoonheydt, R. A., Selective oxidation of methane by the bis(μ-oxo)dicopper core stabilized on ZSM-5 and mordenite zeolites. *Journal of the American Chemical Society* **2005,** *127* (5), 1394-1395.

27. Alayon, E. M.; Nachtegaal, M.; Ranocchiari, M.; van Bokhoven, J. A., Catalytic conversion of methane to methanol over Cu–mordenite. *Chem. Commun.* **2012,** *48* (3), 404-406.

28. Pappas, D. K.; Martini, A.; Dyballa, M.; Kvande, K.; Teketel, S.; Lomachenko, K. A.; Baran, R.; Glatzel, P.; Arstad, B.; Berlier, G.; Lamberti, C.; Bordiga, S.; Olsbye, U.; Svelle, S.; Beato, P.; Borfecchia, E., The Nuclearity of the Active Site for Methane to Methanol Conversion in Cu-Mordenite: A Quantitative Assessment. *Journal of the American Chemical Society* **2018,** *140* (45), 15270-15278.

29. Ipek, B.; Lobo, R. F., Catalytic conversion of methane to methanol on Cu-SSZ-13 using N2O as oxidant. *Chem. Commun.* **2016,** *52* (91), 13401-13404.

30. Dinh, K. T.; Sullivan, M. M.; Narsimhan, K.; Serna, P.; Meyer, R. J.; Dincă, M.; Román-Leshkov, Y., Continuous Partial Oxidation of Methane to Methanol Catalyzed by Diffusion-Paired Copper Dimers in Copper-Exchanged Zeolites. *Journal of the American Chemical Society* **2019,** *141* (29), 11641-11650.

31. Shteinman, A. A., The role of metal-oxygen intermediates in biological and chemical monooxygenation of alkanes. *Russian Chemical Bulletin* **2001,** *50* (10), 1795-1810.

32. Balasubramanian, R.; Rosenzweig, A. C., Structural and mechanistic insights into methane oxidation by particulate methane monooxygenase. *Accounts of Chemical Research* **2007,** *40* (7), 573-580.

33. Merkx, M.; Kopp, D. A.; Sazinsky, M. H.; Blazyk, J. L.; Müller, J.; Lippard, S. J., Dioxygen Activation and Methane Hydroxylation by Soluble Methane Monooxygenase: A Tale of Two Irons and Three Proteins. *Angewandte Chemie International Edition* **2001,** *40* (15), 2782-2807.

34. Andersson, K. K.; Froland, W. A.; Lee, S. K.; Lipskomb, J. D., Dioxygene independent oxygenation of hydrocarbons by methane monooxygenase hydroxylase component. *New J. Chem.* **1991,** *15*, 411-415.

35. Shilov, A. E.; Shteinman, A. A., Methane hydroxylation: A biomimetic approach. *Russian Chemical Reviews* **2012,** *81* (4), 291-316.

36. Roduner, E.; Kaim, W.; Sarkar, B.; Urlacher, V. B.; Pleiss, J.; Gläser, R.; Einicke, W. D.; Sprenger, G. A.; Beifuß, U.; Klemm, E.; Liebner, C.;

Hieronymus, H.; Hsu, S. F.; Plietker, B.; Laschat, S., Selective Catalytic Oxidation of C-H Bonds with Molecular Oxygen. *ChemCatChem* **2013,** *5* (1), 82-112.

37. Kitajima, N.; Moro-oka, Y., Copper-Dioxygen Complexes. Inorganic and Bioinorganic Perspectives. *Chemical Reviews* **1994,** *94* (3), 737-757.

38. Sorokin, A. B.; Kudrik, E. V.; Bouchu, D., Bio-inspired oxidation of methane in water catalyzed by N-bridged diiron phthalocyanine complex. *Chem. Commun.* **2008,** (22), 2562-2564.

39. Afanasiev, P.; Kudrik, E. V.; Millet, J. M. M.; Bouchu, D.; Sorokin, A. B., High-valent diiron species generated from N-bridged diiron phthalocyanine and H2O2. *Journal of the Chemical Society. Dalton Transactions* **2011,** *40* (3), 701-710.

40. Raja, R.; Ratnasamy, P., Direct conversion of methane to methanol. *Applied Catalysis A: General* **1997,** *158* (1-2), L7-L15.

41. Trukhan, V. M.; Gritsenko, O. N.; Nordlander, E.; Shteinman, A. A., Design and synthesis of new models for diiron biosites. *Journal of Inorganic Biochemistry* **2000,** *79* (1-4), 41-46.

42. Khenkin, A. M.; Belotra, V. S.; Stepanova, M. L., Methane oxidation by O2 under mild conditions in the presence of iron supported catalyst. *Catalysis Today* **1992,** *13* (4), 689-690.

43. Hammond, C.; Jenkins, R. L.; Dimitratos, N.; Lopez-Sanchez, J. A.; Ab Rahim, M. H.; Forde, M. M.; Thetford, A.; Murphy, D. M.; Hagen, H.; Stangland, E. E.; Moulijn, J. M.; Taylor, S. H.; Willock, D. J.; Hutchings, G. J., Catalytic and mechanistic insights of the low-temperature selective oxidation of methane over Cu-promoted Fe-ZSM-5. *Chemistry - A European Journal* **2012,** *18* (49), 15735-15745.

44. Edwards, J. K.; Solsona, B.; Ntainjua N, E.; Carley, A. F.; Herzing, A. A.; Kiely, C. J.; Hutchings, G. J., Switching off hydrogen peroxide hydrogenation in the direct synthesis process. *Science* **2009,** *323* (5917), 1037-1041.

45. Moreno, I.; Dummer, N. F.; Edwards, J. K.; Alhumaimess, M.; Sankar, M.; Sanz, R.; Pizarro, P.; Serrano, D. P.; Hutchings, G. J., Selective oxidation of benzyl alcohol using in situ generated H 2O2 over hierarchical Au-Pd titanium silicalite catalysts. *Catalysis Science and Technology* **2013,** *3* (9), 2425-2434.

46. Bentrup, U., Combining in situ characterization methods in one set-up: looking with more eyes into the intricate chemistry of the synthesis and working of heterogeneous catalysts. *Chemical Society Reviews* **2010,** *39* (12), 4718-4730.

47. José A. Rodriguez, J. C. H., Peter J. Chupas, *In-situ Characterization of Heterogeneous Catalysts*. John Wiley & Sons, Inc.: **2013**; p 496.

48. Zhang, Y.; Fu, D.; Xu, X.; Sheng, Y.; Xu, J.; Han, Y. F., Application of operando spectroscopy on catalytic reactions. *Current Opinion in Chemical Engineering* **2016,** *12*, 1-7.

49. Kerkhof, F. P. J. M.; Moulijn, J. A., Quantitative analysis of XPS intensities for supported catalysts. *The Journal of Physical Chemistry* **1979,** *83* (12), 1612-1619.

2

Isolated Fe sites in Metal Organic Framework catalyse the direct conversion of methane to methanol

Hybrid materials bearing organic and inorganic motives have been extensively discussed as playgrounds for the implementation of atomically resolved inorganic sites within a confined environment, with an exciting similarity to enzymes. Here, we present the successful design of a site-isolated mixed-metal Metal Organic Framework that mimics the reactivity of soluble methane monooxygenase enzyme and demonstrates the potential of this strategy to overcome current challenges in selective methane oxidation. We describe the synthesis and characterisation of an Fe-containing MOF that comprises the desired antiferromagnetically coupled high spin species in a coordination environment closely resembling that of the enzyme. An electrochemical synthesis method is used to build the microporous MOF matrix while integrating the atomically dispersed Fe active sites in the crystalline scaffold. The model mimics the catalytic C-H activation behavior of the enzyme to produce methanol, and shows that the key to this reactivity is the formation of isolated oxo-bridged Fe units.

This chapter is based on the following publication:
Isolated Fe sites in Metal Organic Framework catalyse the direct conversion of methane to methanol
D. Osadchii, A. I. Olivos Suarez, Á. Szécsényi, G. Li, M. A. Nasalevich, I. A. Dugulan, P. Serra Crespo, E. J. M. Hensen, S. L. Veber, M. V. Fedin, G. Sankar, E. A. Pidko, J. Gascon, *ACS Catalysis (2018), 8, 6, 5542.*

2.1. Introduction

Targeting the exquisite reactivity and selectivity that methane monooxygenase enzymes display for the conversion of methane to methanol requires the design of a chemical model able to combine characteristics both from the organic and inorganic materials fields. New organic-inorganic synthetic solids, such as metal organic frameworks (MOFs), offer a much higher degree of synthetic control and may become ideal solids for the synthesis of model methane activation catalysts (Fig. 2.1).[1] The current design of active sites in MOF-based catalysts is dominated by homogeneous catalysis and coordination chemistry strategies where the classical limitations of the respective approaches are not yet overcome.

Researchers have tried to emulate similar enzyme-like active sites within well-defined molecular ligand architectures and synthetic solids to address the challenge[2] to selectively activate methane.[3] In nature, the methane monooxygenase enzymes (MMOs) are able to directly and selectively oxidise methane to methanol (Fig. 2.1a) under mild aqueous conditions.[4] In the soluble version of the MMOs, the active site is a dimeric Fe species in the hydroxylase subunit (Fig. 2.1b). Two additional components mediate an electron transfer chain to reduce the Fe(III)-Fe(III) antiferromagnetically coupled, high spin, dimeric site to a Fe(II)-Fe(II) active species that effectively activates oxygen to produce a high valent metal-oxo intermediate. This highly oxidative intermediate is responsible for the activation of the C-H bond in methane via hydrogen abstraction.[5-6] Worth noticing is that the sMMO relies on the redox accessibility of the Fe dimer: the reduction step toward Fe(II)-Fe(II) species and the high valent Fe(IV)-Fe(IV). It has been proven that the hydroxylase component retains catalytic activity when the 2-electron donor chain is substituted by H_2O_2, thus proving the independence of these two events.[7] Notably, the high selectivity of this system is ensured by the encapsulation of methane in the nonpolar environment of the reaction centre that promotes the rebound mechanism and by the non-covalent interactions with the protein matrix that help product removal to prevent side-reactions.[6] In spite of these great efforts, catalysts designed on basis of the enzyme still need to overcome two major milestones, namely to avoid dissociation of the iron dimeric species after the catalytic cycle and to fully reproduce the magnetic properties of the Fe(III)-Fe(III) dimer, postulated to be crucial on reactivity.[8] Since the pioneering work of Panov,[9] zeolites have received a great deal of attention.[10-13]

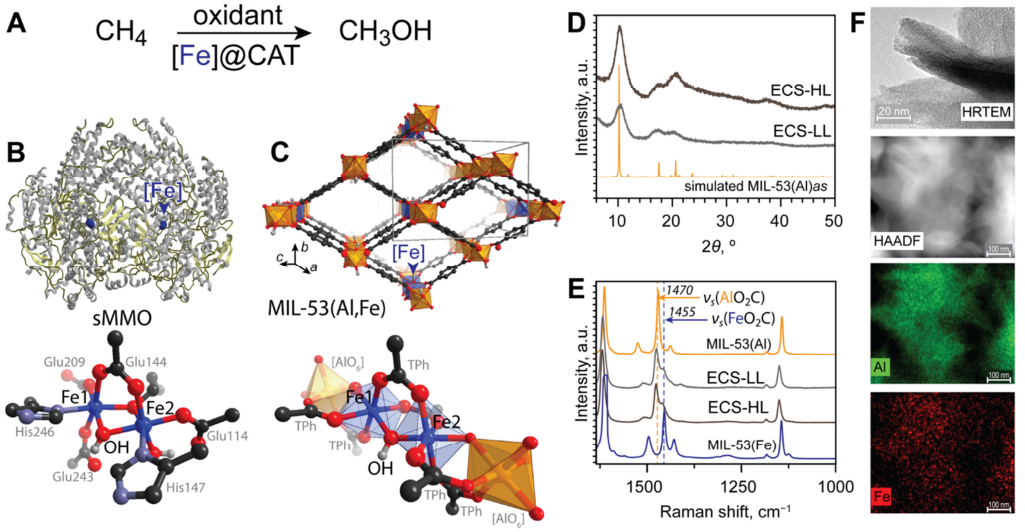

Figure 2.1. MOF mediated direct methane oxidation. (**a**) Reaction scheme for the direct catalytic methane oxidation. (**b**) Structure of sMMO hydroxylase (MMOH, PDB accession code 1MTY) enzyme, where each $\alpha_2\beta_2\gamma_2$ dimer contains two diiron active sites (blue spheres and ball and stick representation). (**c**) The MIL-53(Al,Fe) catalyst with the ball and stick representation of a site-isolated Fe within the MIL-53 octahedral [AlO_6] chain. (**d**) X-ray diffraction (XRD) analysis of the electrochemically synthesized (ECS) samples compared to the simulated XRD patterns of the (as synthesized) MIL-53(Al) structure. (**e**) Raman spectra of ECS samples compared to the pure MIL-53(Al) and MIL-53(Fe) phase (laser wavelength 785 nm, integration time 60 s). (**f**) Representative HRTEM and HAADF-STEM of ECS MIL-53(Al,Fe) catalysts with low Fe loading (-LL). The abbreviation -HL is used to denote materials with a high Fe loading (> 5 wt %).

However, the intrinsic hydrophilic nature and the relatively poor degree of tuneability in most pure inorganic matrices, including zeolites, lead to ill-defined active sites and to strong adsorption of methanol inside the zeolite pores, thus effectively creating stoichiometric reactants rather than catalysts. As demonstrated in this report, these drawbacks can be circumvented by making use of hybrid materials. Here, we report that the controlled incorporation of isolated Fe units into an Al-based MOF results in methane oxidation catalysts that display a high activity and selectivity.

2.2. Isolating catalytic active sites

Targeting the isolation of Fe_{oxo} sites in an environment resembling that of the enzymatic systems within a MOF structure, we selected the MIL-53(Al) structure as the support matrix because it is built from well-defined chains of non-redox active AlO_6 octahedra connected via trans-bridging OH ions and carboxylate moieties from the bridging 1,4-benzene-dicarboxylate linkers

(Fig. 2.1c).[14] We speculated that such a metal-oxo chain structure should be able to accommodate isolated Fe species with a coordination environment close to that in the sMMO active site.[15] Furthermore, unlike other bulk porous materials commonly used as catalyst supports, the micropores of MIL-53 are constructed from hydrophobic organic linkers that should favour the rapid desorption of methanol from the reactive centre in an aqueous environment.

We followed two different synthetic pathways for the incorporation of Fe atoms into the MIL-53(Al) framework: 1) post-synthetic cation exchange using hydrothermally synthesised MIL-53(Al) and $FeCl_3$ solutions (samples denoted as HTS); and 2) the in situ Fe incorporation via the addition of $FeCl_3$ aliquots during electrochemical synthesis of MIL-53(Al) from an Al-electrode and a terephthalic acid solution (samples denoted as ECS).[16] The efficiency of the post-synthetic cation exchange procedure was found to depend strongly on the solvent and temperature used. Successful incorporation of Fe into MIL-53(Al) with preservation of the MOF structure could be achieved only when the cation exchange was carried out in DMF at low temperature (80 °C). In this case, total Fe incorporation values ranging from 0.15 to 2 weight percent (wt %) could be achieved. Post-synthetic modification at higher temperature (120 °C) allowed incorporating amounts of Fe as high as 16.6 wt %, however at the expense of extraframework α-Fe_2O_3 formation (Fig. 2.2b, 2.14). Electrochemical synthesis, on the other hand, offered a greater control over Fe incorporation in the range from 0.3 to 5.5 wt % by only varying the concentration of Fe precursor (see Appendix for details). Following this method, we were able to achieve a highly homogeneous distribution of Fe sites within the lattice of MIL-53, as evidenced by the results of extensive physicochemical characterisation (*vide infra*, Fig. 2.1d-f, 2.2-2.3, 2.5, 2.12; Table 2.1). Broad XRD peaks of ECS samples indicate the formation of very small MOF nanoparticles that cluster with each other.[16-17] The agglomeration of these small crystals also eliminates the breathing in the material,[18] so that the ECS materials reside in the large pore form in a wide range of temperatures and pressures.

2.3. Methane reactivity

The hybrid HTS and ECS materials were tested for catalytic methane oxidation in water using H_2O_2 as oxidant under mild reaction conditions, in a procedure similar to that previously employed for pure inorganic Fe-zeolite catalysts.[13] While at higher temperatures (> 80 °C) the MIL-53(Al,Fe)

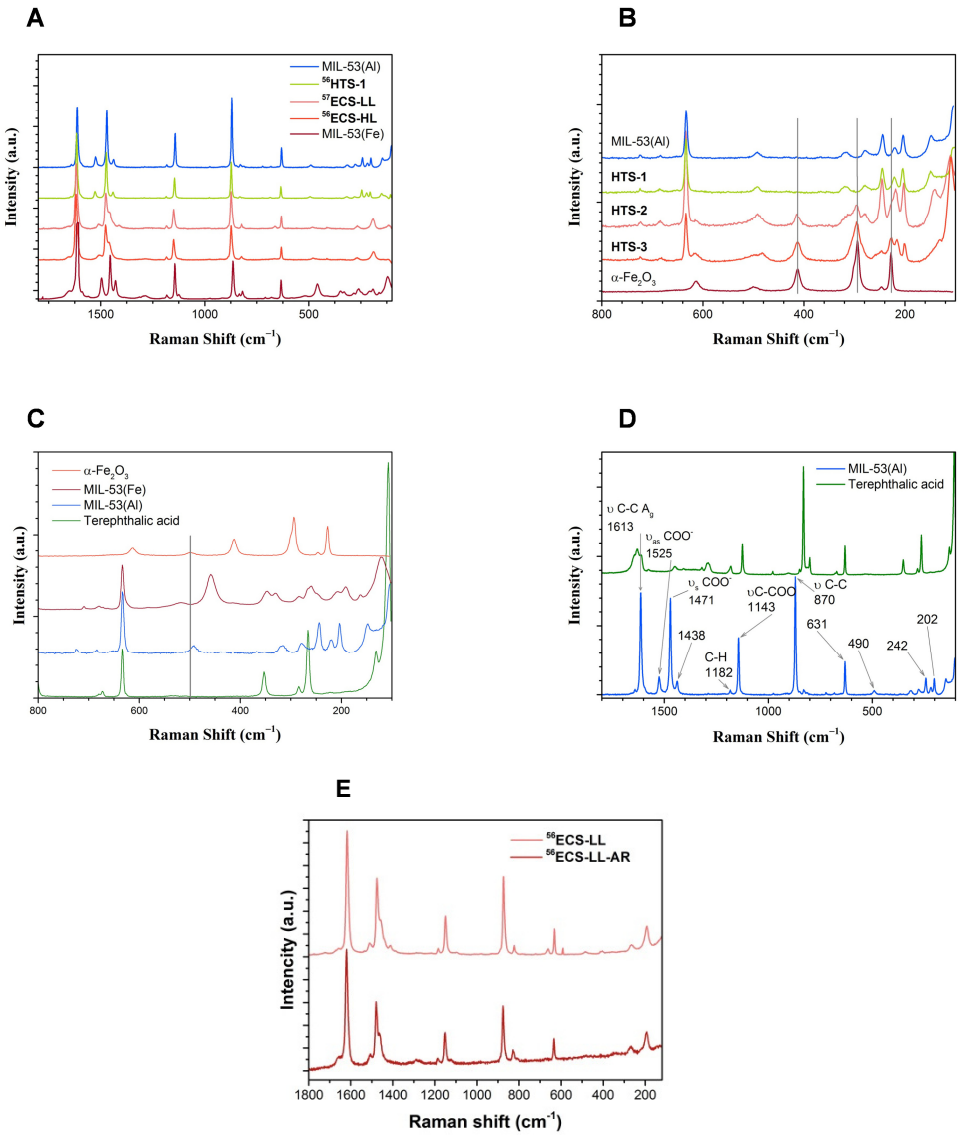

Figure 2.2. Raman spectra of MIL-53(Al,Fe) samples. **(a) HTS-1** and ECS series with reference MIL-53(Al) and MIL-53(Fe), **(b)** Fe@MIL-53(Al) samples (HTS series) compared to α-Fe_2O_3, **(c)** difference of Raman shift from the Fe-O bond in α-Fe_2O_3 [19-20] and MIL-53(Fe), **(d)** assignation of the Raman signals arising from terephthalic acid,[21] and **(e)** Raman spectra of **^{56}ECS-LL** sample before (*top*) and after (*bottom*) reaction.

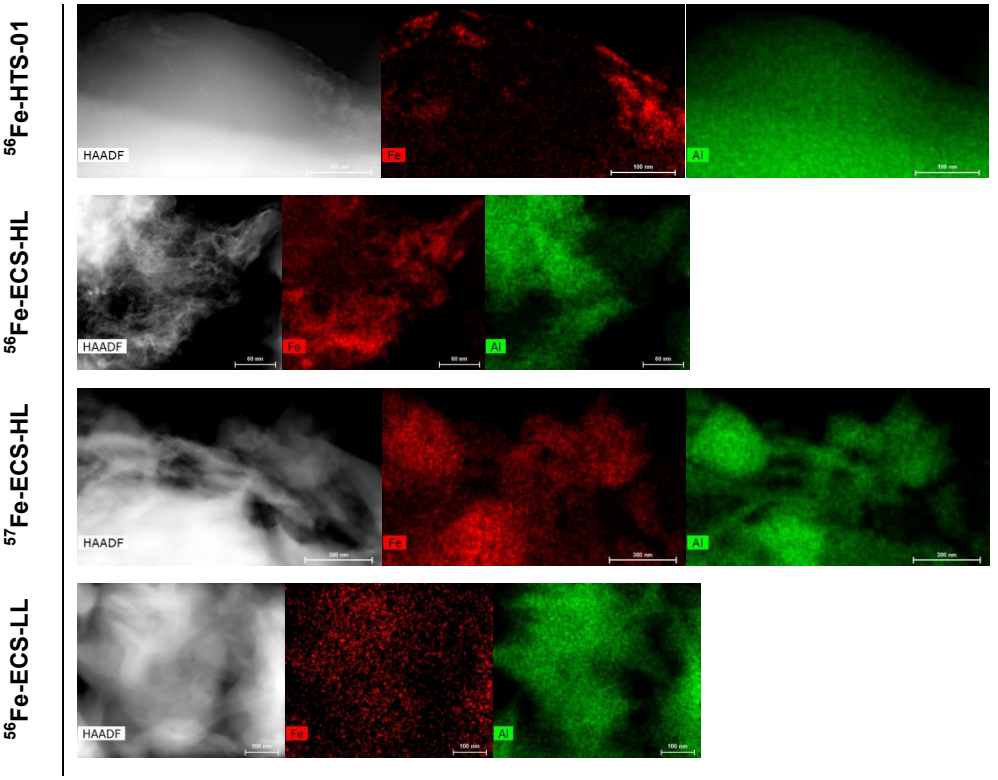

Figure 2.3. Representative STEM-HAADF grayscale images and EDS mapping of Fe and Al of the HTS and ECS series catalysts.

catalysts were not stable in aqueous H_2O_2, reactions performed at temperatures below 60 °C showed the selective formation of methanol along with traces of over-oxidation products. Analysis of the liquids (by ^{1}H NMR) and of the gaseous head space of the reaction (GC) did not show other products than methanol, methyl peroxide, formic acid and CO_2. Products arising from C-C coupling were not observed. In all tests, the optimal selectivity could be obtained at short reaction times (approx. 1 h), and after 2 h of reaction the activity decreases seemingly as consequence of the prevailed metal mediated H_2O_2 decomposition. Under the optimised conditions, reactions performed with the same catalysts but in lower amounts (Fig. 2.4c-d, 2.11) result in higher TONs, that can indicate high diffusional limitations within the MOF catalysts.

The stability of the HTS catalysts with high Fe content (**HTS-2** and **HTS-3**, 5.4 and 16.6 Fe wt % respectively) turned out to be an issue. Fe leaching into the solution was observed, along with the formation of a higher amount

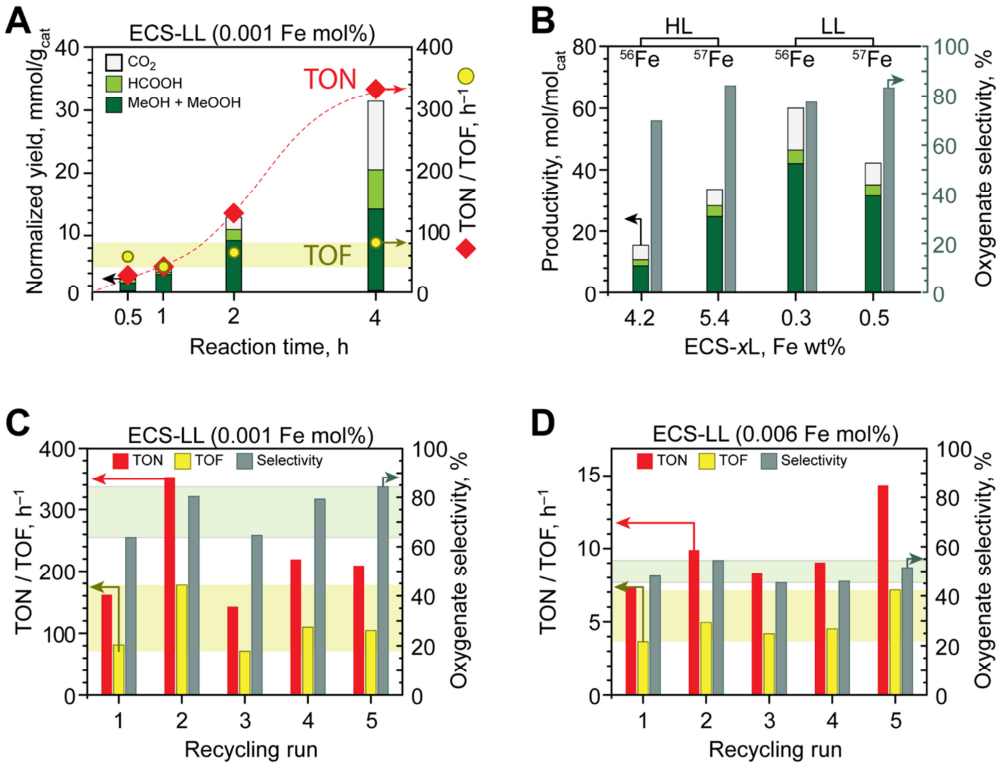

Figure 2.4. Catalytic oxidation of methane to methanol with H_2O_2 by MIL-53(Fe,Al). (**a**) Time-evolution of oxidation products and the respective values of TOF and TON during methane to methanol oxidation in the presence of low-concentrations of **ECS-LL** catalyst. (**b**) The influence of Fe content (wt %) in the **ECS-xL** catalysts on the productivity and oxygenate selectivity at 2 hr reaction time of methane to methanol oxidation. Catalytic performance of **ECS-LL** after consecutive recycling steps with a low (**c**) and high (**d**) catalyst loading (Fe mol%).

of side products and the presence of dissolved linker in solution, arising from the partial digestion of the framework. Fe incorporation through post synthetic ion exchange may result in the formation of large Fe clusters either as integral part of the framework or as extra-framework species (even when those could not be observed by XRD). Indeed, analysis of all Fe containing samples by Raman and Fe *K*-edge extended X-ray absorption spectroscopies (EXAFS) revealed the presence of α-Fe_2O_3 in highly loaded samples obtained via post-synthetic ion exchange (Fig. 2.2b, 2.14-2.15; Table 2.2).

To our delight, the formation of such extra-framework species is suppressed for every sample synthesised through the electrochemical route, even when reaching Fe loadings as high as 5.4 wt %. Characterization of samples after

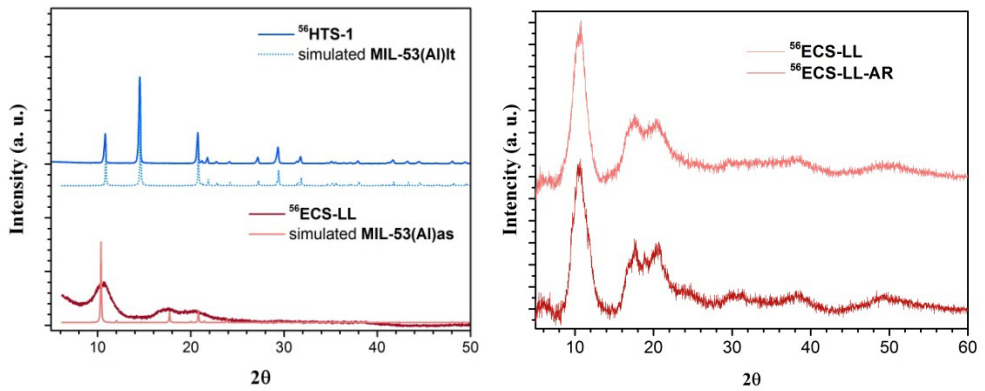

Figure 2.5. Experimental and simulated powder XRD patterns for **HTS-1** and **^{56}ECS-LL** (*left*), and powder XRD patterns of **^{56}ECS-LL** sample before and after reaction (*right*).

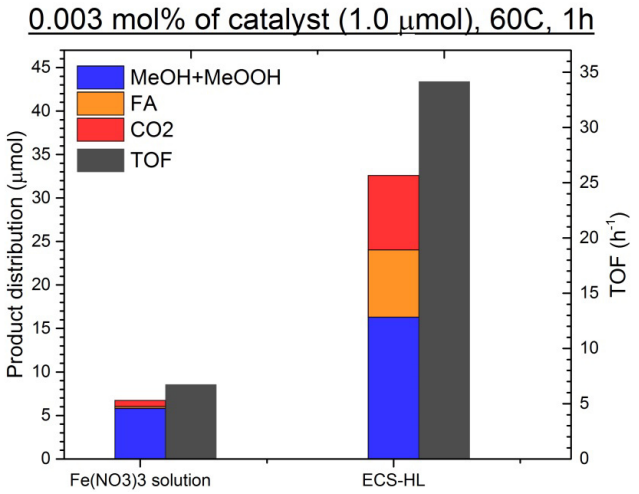

Figure 2.6. Comparison of product distribution and TOF for **^{57}ECS-HL** and reference $Fe(NO_3)_3$ solution at 0.1 mM of iron in the reaction mixture.

catalytic testing by means of Raman (Fig. 2.2e), XRD (Fig. 2.5), EPR (Fig. 2.21) and CO_2 adsorption measurements (Table 2.1) shows that electrochemically-synthesised catalysts are stable in the reaction conditions, and iron species reside in the MOF structure without formation of Fe_2O_3. Compared to a reference Fe^{3+} solution, ECS-HL catalyst shows at least 4 times higher activity at the same concentration of iron in the reaction mixture (Fig. 2.6). In general, the ECS samples display a higher activity than those obtained through post-synthetic ion exchange, with TOFs in the order

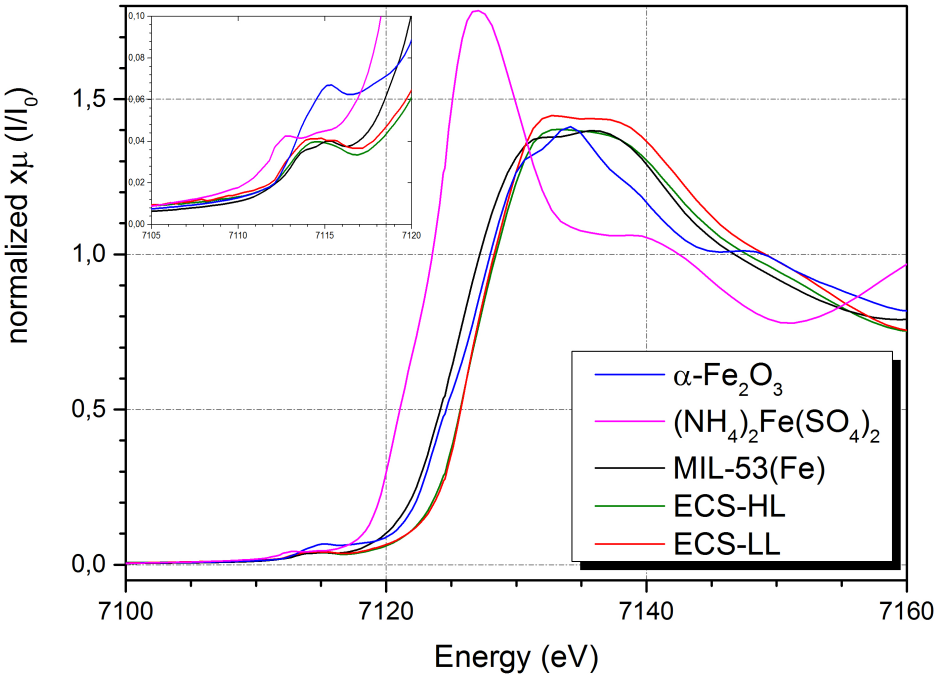

Figure 2.7. Fe *K*-edge XANES spectra for MOF samples and Fe references.

of 90 h^{-1} and selectivities to oxygenates of ca. 80% (Fig. 2.4a). A comparison between both ECS and HTS samples in terms of particle morphology (TEM) and Fe distribution (HAADF-STEM and energy dispersive X-ray spectroscopy (EDX), Fig. 2.3) reveals a smaller particle size along with a high Fe dispersion for the ECS catalysts. In addition, in the Raman spectra of these samples, the symmetric and asymmetric carboxylate vibrations are the result of the combination of carboxylates attached to either Fe or Al (Fig. 2.1e), strengthening the conclusion of a better dispersion of the Fe atoms within the framework.

2.3. Unravelling the chemical nature of the catalytic active sites

In order to reveal the chemical state and local structure of Fe species in the MOF catalysts they were characterized using XAS technique. Fe *K*-edge XANES spectra show that iron is present in 3+ oxidation state in all samples (according to the edge position at ~7126 eV). Low intensity of the pre-edge feature indicates octahedral coordination of Fe within the MOFs (Fig. 2.7). Further information on the state of Fe in the catalysts was obtained by fitting

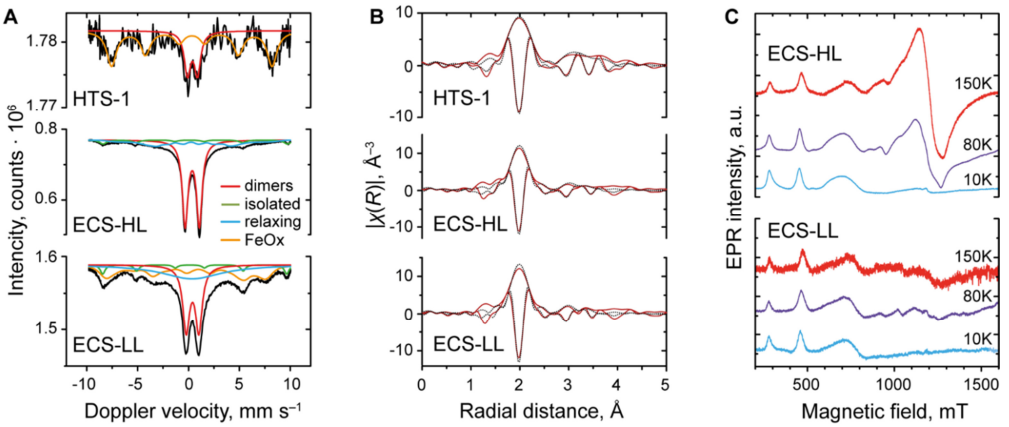

Figure 2.8. Spectroscopic characterisation of Fe single site. **(a)** Mössbauer spectra of the **HTS-1**, **^{57}ECS-HL**, and **^{57}ECS-LL** catalysts in zero field at 4.2 K. The experimental data is represented by back solid lines and the corresponding fitted components are represented by coloured lines. **(b)** Fourier transform of EXAFS Fe *K*-edge experimental (red solid line) and fitted (black dots) data for **HTS-1**, **ECS-HL**, and **ECS-LL** over the *k* range 3-11 Å^{-1}. **(c)** variable-temperature *Q*-band (ν_{mw} ≈ 33.2-33.8 GHz) continuous wave (CW) EPR spectra of ^{57}Fe enriched **^{57}ECS-HL** and **^{57}ECS-LL** at *T* = 10-150 K. All spectra are normalised to the signal of monomeric Fe(III) at ≈ 460 mT.

the EXAFS spectra of the **HTS-1**, **ECS-LL** and **ECS-HL** samples using models including one, two and three Fe atoms at the octahedral chain of the MIL-53(Al) crystal structure (Fig. 2.8b and Fig. 2.16). The obtained fitting parameters suggest that Fe sits in an octahedral coordination in the structure of **HTS-1** and both ECS samples (Fig. 2.8b, 2.17; Table 2.3). The first peak in the R-space is best fitted by two shells, two O atoms at 1.95-1.96 Å and four O atoms at slightly longer distance (2.01-2.03 Å) corresponding to the first coordination sphere around the iron sites. In this model, we assign the 4 O atoms at the equatorial positions to those arising from the two carboxylate-bridging ligands. The apical oxygen atoms are assigned to the expected shorter bridging Fe-μ-O-Fe bonds. All measured samples show a feature between R ~ 2.9 to 4.0 Å that can be fitted with a combination of different scattering shells arising from the neighbouring carbons (carboxylates from the terephthalic linker) and two metal centres from the octahedral chain. However, the large uncertainty in Debye-Waller factors for these shells indicate a wide range of Fe-ligand bond lengths and it cannot account for the different species considered in our three models. Thus, XAS analysis suggests that Fe-sites are possibly best described as either isolated Fe centres or multi-Fe segments dispersed evenly through the Al-based octahedral chain, but it cannot unambiguously interpret the

second coordination sphere and discriminate between Al or Fe neighbours (Al-O-Fe-O-Al, Al-O-Fe-O-Fe or Fe-O-Fe-O-Fe moieties).

The magnetic and structural properties of the catalysts were further assessed by a combined study of electron paramagnetic resonance (EPR) and Mössbauer spectroscopy. Because of the low Fe loading, in order to improve the quality of the Mössbauer analysis, we prepared additional samples using enriched (95.4%) ^{57}Fe. While it proved impossible to fully reproduce the **HTS-1** synthesis when starting from ^{57}Fe, the electrochemically synthesised samples **^{57}ECS-LL** (0.5 Fe wt %) and **^{57}ECS-HL** (5.4 Fe wt %) were synthesised and tested in catalysis, demonstrating similar performance to their non-enriched counterparts. From the EPR *X/Q*-band experiments, it is clear that the HTS samples contain mostly oligomeric Fe species. Indeed, the Mössbauer spectra of the non-enriched **^{56}HTS-1** could be fitted with two components: a dominant magnetic iron FeO_x cluster and a significantly smaller component, corresponding to a doublet with a *QS* of 0.98 mm·s^{-1} and an isomer shift of 0.38 mm·s^{-1}, typical for high spin Fe(III) located in a non-centrosymmetric environment (Fig. 2.8a, Table 2.4).[22] In contrast, the degree of dispersion that is observed in the ECS samples is remarkable. An apparent domination of a single atom species can be observed in EPR experiments at 10 K for all four ECS samples. The observed *X*- and *Q*-band spectra at 10 K were reasonably fitted with the same set of parameters for an isolated high-spin Fe(III) (Fig. 2.18). Notably, there is a broad temperature-dependent signal near the central *Q*-band field (~1200 mT), very intense at T = 150 K for samples with higher Fe concentration, but also visible for the low Fe content ECS catalysts. The shape and position of this signal (g-factor ≈ 2.0) are similar to those in pure Fe(III) MIL-53(Fe) (Fig. 2.19), and zero-field is not detected, suggesting the presence of an extended magnetic Fe(III) network. A drastic decrease of this signal (virtually reaching zero at 10 K) with temperature indicates antiferromagnetic exchange between even number of Fe(III) centres. Remarkably, the estimated Fe(III)-Fe(III) exchange coupling J ~ 100-120 cm^{-1} (Fig. 2.20; $H_{ex} = JS_1S_2$) has the same order of magnitude as those previously found for oxo-bridged Fe(III)-Fe(III) dimers in hemerythrin and *E. coli* ribonucleotide reductase (J = 270 and 220 cm^{-1}, respectively).[23-24] Thus, the broad EPR signal with $g \approx 2.00$ is most reasonably assigned to Fe(III) dimers resembling those in biological systems and additionally coupled by inter-dimer exchange. In Mössbauer spectroscopy there are no silent Fe species as in EPR and the inter-nuclear magnetic coupling is restricted to lower distances. Thus, the resulting

spectra are always composed of all the different species and magnetic hyperfine coupling is mostly observed for interconnected Fe centres. Remarkably, for all the ECS samples, the Mössbauer spectra at 4.2 K are composed of a dominant doublet component with $QS \approx 1.4\text{-}1.2$ mm·s^{-1} and $IS = 0.4$ mm·s^{-1} (Fig. 2.8a; Table 2.4) with a small component for single Fe(III) atoms. From the doublet at 4.2 K with no magnetic hyperfine structure and, together with the observed EPR temperature dependent signal, it is reasonable to assign the composition of Fe sites in the ECS samples to a combination of isolated, monomeric Fe(III) sites and antiferromagnetic coupled dimeric Fe(III)-Fe(III) species.

2.4. Reaction mechanism

To gain a better understanding of the nature and stability of these catalytic sites, we performed periodic density functional theory (DFT) calculations. Comparison of stability of iron species, incorporated in MIL-53(Al) framework, with extraframework iron clusters show, that species embedded in the MOF structure are significantly more stable (see Fig. 2.24, Table 2.12). Formation of extraframework Fe species is thermodynamically unfavourable; on the contrary, mixed-metal MIL-53(Al,Fe) show considerable stabilization compared to pure MIL-53(Al) and MIL-53(Fe) phases. Calculations for monomers, dimers, trimers and tetramers of iron in MIL-53(Al) structure show that antiferromagnetically coupled dimeric species are the most stable of them. These results perfectly agree with our EPR and Mössbauer characterization data and further prove the concept of isolated iron active sites, incorporated in the MOF structure.

The reactivity was modelled on isolated Fe species comprising dimeric Fe-Fe centres and single monomeric Fe centres embedded in the MIL-53(Al) structure. For comparison and to understand the origin of the low stability of pure MIL-53(Fe) (see Section 2.6.2), the respective model was also included in the computational analysis.

The analysis of various possible reaction paths allowed us to propose a reaction mechanism schematically illustrated in Fig. 2.9a. Fig. 2.9b summarises the results of the DFT calculations and shows the representative structures of the key intermediates involved in the activation of H_2O_2 and methane during the catalytic process. For all models, the catalytic cycle starts with the activation of H_2O_2 by an Fe site in the MIL-53 structure **1**. The most favourable route involves the replacement of one of

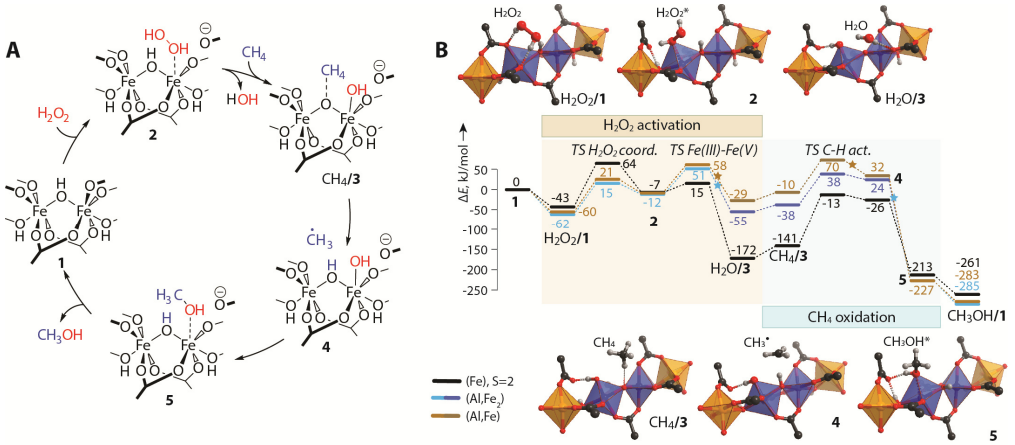

Figure 2.9. Catalytic reaction mechanism. (a) The proposed mechanism of methane to methanol oxidation with H_2O_2 over the dimeric Fe site in MIL-53(Al,Fe) and **(b)** the DFT-computed minimum-energy reaction path diagrams (including spin-transitions indicated with stars) for the catalytic process over different Fe-containing MIL-53 models.

the carboxylate ligands from the metal node by a hydrogen peroxide molecule. The open carboxylate moiety in **2** is stabilised via hydrogen bonding with a bridging hydroxyl group and contains several electrophilic O sites that, in turn, lead to different pathways for reactivity (see Section 2.6.11). When the number of Fe metal nodes through the framework chain is high and their corresponding carboxylate units are decoordinated, the framework stability is compromised, most likely leading to dissolution of the solid. In samples with sufficiently isolated Fe sites, the subsequent homolytic dissociation of the O-O bond (**2** → H_2O/**3**) results in the formation of a terminal Fe-OH species that in the case of the MIL-53(Fe) is very stable (-172 kJ·mol^{-1}). The concomitant abstraction of an H atom from the bridging hydroxyl group to form H_2O (H_2O/**3** + CH_4 → H_2O + CH_4/**3**) proceeds with a considerable lower energy barriers for isolated Fe sites ($\Delta E^{\ddagger}$ = 80 and 76 *vs* 128 kJ·mol^{-1} for single Fe(III), Fe(III)-Fe(III) species and MIL-53(Fe) respectively). The formal oxidation state of one Fe centre in the active site increases from (III) to (V). Subsequent homolytic dissociation of the C-H bond by the bridging O site in Fe-(μ-O)-Fe (or Fe-(μ-O)-Al for the single Fe species) of the activated iron site (CH_4/**3** → **4**) yields an OH group and a CH_3 radical which recombines with the terminal OH ligand to form adsorbed methanol (**4** → **5**). Alternatively, reaction with O_2 favours the formation of methyl hydroperoxide (Fig. 2.23)**.** The catalytic cycle is closed and the octahedral iron-carboxylate environment of the active species is restored via

the migration of the coordinated methanol to the pore of the MIL-53 (**5** → CH_3OH/**1**).

Computational results show that both monomeric and dimeric Fe species in MIL-53(Al) structure can catalyse oxidation of methane with H_2O_2. However, lower energy barriers in case of antiferromagnetically coupled dimers as well as their higher stability in the reaction conditions indicate that these species have the highest impact to the overall activity of the catalysts.

2.5. Conclusions

Based on the extensive spectroscopic characterisation provided here, we conclude that isolated, antiferromagnetically coupled, high spin, Fe sites are required to attain a substantial catalytic activity. Control experiments performed using pure phase MIL-53 materials based on redox metals such as Cr or Fe revealed dissolution of the frameworks under the optimal reaction conditions along with the formation of typical Fenton chemistry products, demonstrating that incorporation of extended Fe-containing moieties within the framework would result in considerable leaching and that the use of a non-redox scaffold is key to obtaining a high catalyst stability, as demonstrated upon recycling of the ECS-LL catalysts (results shown in Fig. 2.4c and 2.4d).

Up to date, many Fe_2O complexes, trimers and bigger clusters have been characterized.[25] However, the development of accurate models to describe and mimic the oxo-bridging Fe dimer expressed in enzymes has proven difficult.[26] Most of these examples can achieve to describe one of the intermediates of the MMO catalytic cycle, especially the highly oxidant intermediate **Q**.[27] However, after C-H bond activation, most of them dissociate into monomeric species,[28] acting as stoichiometric reagents rather than as catalytic sites. As already pointed out by Baerends *et al.*,[8] a factor to consider when designing biomimetic or bioinspired oxidation catalysts is the ligand field strength. Current models are mostly based on N-rich ligand architectures, which do not fully resemble the carboxylate-bridging diiron sMMO active site and typically yield low spin species rather than the high spin configuration present in the sMMO, with important implications on reactivity.[8] In contrast to these examples, the MOF based catalysts are, to the best of our knowledge, the first example of isolated Fe dimers that sit on an O-based structure and generate the desired antiferromagnetically coupled high spin species active in the catalytic hydroxylation reaction.

Our findings demonstrate that MOFs are excellent platforms for the development of model catalysts mimicking full enzymatic cycles and open new possibilities for fundamental studies of direct oxidative activation of CH_4. We anticipate that the implementation of additional functionalities to allow for the simultaneous activation of oxygen may pave the way to the development of industrially relevant MOF based catalysts.

2.6. Appendix

2.6.1. Synthesis

2.6.1.1. Hydrothermal synthesis of MIL-53(Al)

MIL-53(Al) was synthesised following the procedure previously described in the literature.[29] In a typical synthesis, 2 g terephthalic acid are added to a solution of 8 g $AlCl_3 \cdot 6H_2O$ in 30 mL deionized water and placed in a stainless steel autoclave fitted with a Teflon insert. The autoclave is set under static heating (220 °C) for 72 h. After cooling down, the powder is filtered with a 0.45µm nylon filter and the solid is recovered and suspended in 20 mL DMF and let under static heating (130 °C) overnight. After cooling down, the powder is again recovered and the residues of DMF are washed with methanol at 70 °C for 5 h. After recovering of the powder is let dry in air at 100 °C.

2.6.1.2. HTS. Post synthetic ion exchange

In a typical procedure, 400 mg MIL-53(Al) are suspended into a DMF solution of the desired $FeCl_3 \cdot 9H_2O$ concentration (this is calculated accordingly to equivalents of Al in the MOF). The mixture is sealed in a teflon fitted autoclave and set to the desired temperature (80 °C, or 120 °C) and let for 16 h. Extension of exchange time does not show an increase of the total Fe incorporation in the MOF and in high Fe concentrations condition leads only to the formation of α-Fe_2O_3. Exchange at 80 °C does not incorporate all the Fe added in solution, whereas for the exchange at 120 °C, all the added Fe is in the framework majorly as α-Fe_2O_3. After cooling down of the reaction mixture, the powder is recovered by filtration and washed with methanol at 70 °C for 5 h. After recovering, the powder is let dry in air at 100 °C.

2.6.1.3. ECS. Electrochemical synthesis of MIL-53(Al,Fe)

As already reported in the literature, the electrochemical synthesis was performed in batch mode.[16] The electrodes were aluminium metal plates with purity of 99.5%. In a typical synthesis, the electrodes are inserted between 2 PTFT holders isolating the electrode wiring to the potentiostat. The holders have a circular opening of 25 mm diameter to allow contact of the metal plate with the solution (4.9 cm^2). In a typical synthesis, 1.5 g terephthalic acid and 0.73 g NaCl are dissolved in 90 mL H_2O and

Table 2.1. Characterization of MIL-53(Al,Fe) catalysts with elemental analysis (Fe, Al, C, and H obtained from *Mikroanalytischen Laboratorium Kolbe*, with an uncertainty of 0.02 wt %) and CO_2 physisorption (Dubinin-Radushkevich equivalent surface areas and porous structure of the samples were measured using a *Micromeritics Tristar 3020* apparatus at 273 K after degassing under vacuum overnight at 423 K in *Micromeritics Vacprep 061* apparatus).

	C	H	Fe	Al	surface area	micropore volume
	wt%	wt%	wt%	wt%	$m^2 g^{-1}$	$cm^3 g^{-1}$
HTS-01	45.28	2.63	1.01	12.4	595	0.24 ± 0.05
ECS-HL	43.40	2.86	4.2	11.76	645	0.258 ± 0.007
ECS-LL	44.49	3.03	0.34	11.93	615	0.246 ± 0.005
ECS-LL-AR	41.78	3.05	0.44	12.01	530	0.213 ± 0.006
Ideal MIL-53(Al)	46.17	2.42		12.97		

10 mL DMF at room temperature. A solution of 0.191 g $FeCl_3$ in 9 mL H_2O and 1 mL DMF is prepared. The electrodes are immersed in the terephthalic solution, then the solution is heated to 80 °C and a current from 10 to 100 mA is applied through *Autolab PGSTAT302N* potentiostat. During the synthesis, aliquots of Fe^{3+} solution (10, 20 or 50 µL) are injected every 10 minutes so that the total Fe concentration in solution is maintained low during the synthesis. After completion, the synthesised powder is recovered by filtration and washed in 20 mL DMF under static heating (80 °C) overnight. After cooling down, the powder is again recovered and the residues of DMF are washed with methanol at 70 °C for 5 h. After recovering the powder is let dry in air at 100 °C.

2.6.1.4. Modification of the synthetic procedure starting with metallic ^{57}Fe

Metallic ^{57}Fe was dissolved under sonication with the minimum amount of aqueous concentrated HNO_3 (65 wt %, *Aldrich*). The resulting solution was centrifuged and the supernatant was titrated with ammonium hydroxide to increase the pH (~ 3) and just before the precipitation of the Fe^{3+} complex. MIL-53(Al,^{57}Fe) samples were synthesised by hydrothermal and electrochemical synthesis starting with the aqueous $^{57}Fe^{3+}$ solution instead of the inorganic Fe salt. Total Fe quantities were calculated as Fe equivalents to Al ratios accordingly and following the exact conditions mentioned above.

2.6.2. Catalytic experiments

The MIL-53(Al,Fe) samples were tested in the direct methane oxidation in liquid phase using water as reaction medium and H_2O_2 as oxidant. A 50 mL stainless steel autoclave fitted with a glass vessel insert (35 mL) and a heating jacket connected to recirculating oil bath was used. In a typical experiment, the desired amount of catalyst was weighed in a glass vessel insert, and 9.5 mL water was added and weighed consequently (weighing error 0.1 mg). The insert with the catalyst suspension in water was placed in the autoclave. Separately, 530 µL 50 wt/wt % H_2O_2 solution in water was weighed in a PE cap. The cup with H_2O_2 solution was transferred into the insert and was fitted to remain floating on top of the slurry. The closed reaction vessel was leak tested with N_2 up to 50 bar. After successful leak test the N_2 gas was evacuated and the autoclave was purged with methane up to 10 bar 3 times consecutively to remove impurities and to finally pressurize to 30.5 bar of methane for the reaction. The autoclave was heated to the desired temperature (40-60 °C), and mixing was started (700 rpm) when the temperature was stable. The stirring assures the beginning of the reaction because the mixing makes the cup with H_2O_2 drop, and after this H_2O_2 gets in contact with the catalyst. At the end of the experiment, the reaction was rapidly cooled to 10 °C with cooling jacket and cold finger. After cooling the gas phase was collected in 1 L gasbag and analysed by *Thermo Scientific Trace GC Ultra* with TCD detector (*vide infra*) to determine the total content of CO_2. After depressurizing the reactor was opened and the reaction mixture was filtered using a syringe filter with 0.2 µm nylon membranes. The filtered catalyst was dried on air, the filtered liquid phase was used for ^{1}H-NMR analysis of products and H_2O_2 titration.

Control experiments were performed in the absence of CH_4 or H_2O_2 for each catalyst. These control experiments did not show any considerable amounts of methane oxidation products both in the liquid and in the gaseous phase.

Additional control experiments in the absence of both CH_4 and H_2O_2 showed no traces of methanol from the catalyst synthesis.

Control experiments using the MIL-53(Fe) or MIL-53(Cr) under catalytic conditions (0.9 M H_2O_2 solution, 30 bar CH_4, 1 h at 60 °C) showed the collapse of the framework, total H_2O_2 consumption by the leached metal and several unidentified organic residues in solution, seemingly arising from the partial digestion of the MOF linker.

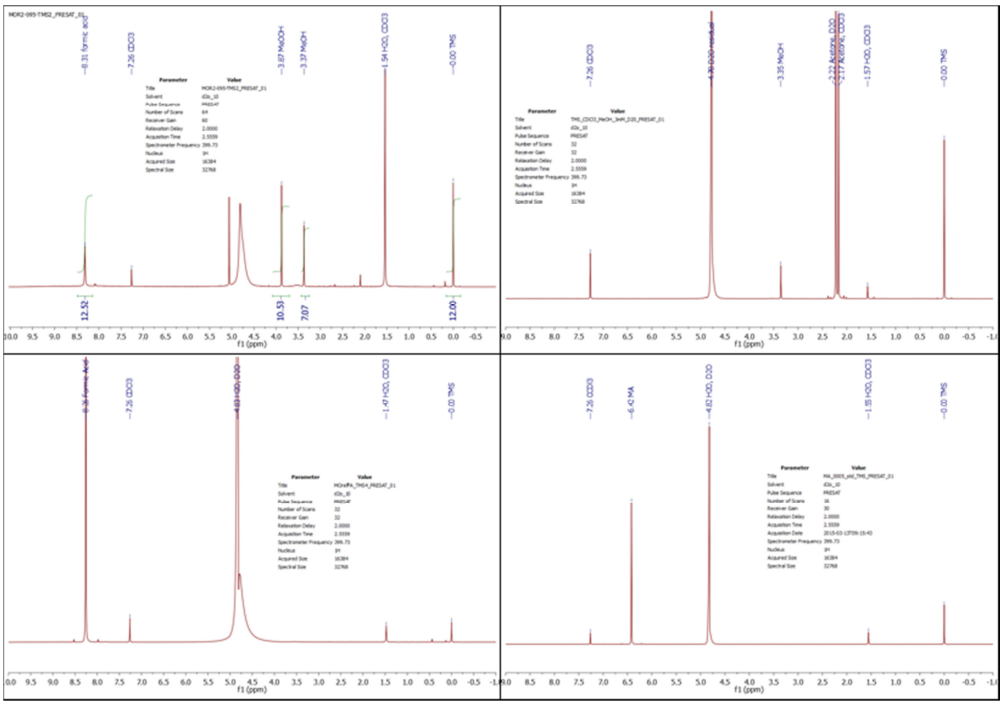

Figure 2.10. An example of the ^{1}H NMR spectra obtained in a catalytic run. Signals were assigned with the corresponding reference standard for each component in the same H_2O + D_2O mixture.

2.6.3. Analytical methods for catalytic quantification

2.6.3.1. NMR quantification

After catalysis, quantification of products in the liquid phase was carried out by ^{1}H-NMR spectroscopy using an external standard technique.[30] NMR spectra were acquired in *Agilent-400 MR DD2* NMR spectrometer and quantified by an external standard methods using glass capillary inserts. The standard is a glass sealed capillary (3 mm diameter) containing a ~0.01% tetramethylsilane (TMS) solution in $CDCl_3$ (*Eurisotope*). The exact area of the TMS signal in the external standard was calibrated for a water suppression pulse program with a series of reference solutions of maleic acid (*traceCERT, Aldrich*) in a mixture of *milli-Q* water and D_2O in 7:2 volume ratio (5 points calibration with 1-10 mM solutions of maleic acid). Calibration was carried out by the correlation of the external standard (maleic acid, MA) and the reference (TMS) peak areas in the NMR spectra (Fig. 2.10). Equal water suppression NMR program was used to quantify the experimental samples. In a typical NMR measurement, 700 µL liquid solution recovered after filtering of the catalyst is weighed, mixed with

200 µL D_2O and weighed again. The resulting solution is transferred into the NMR tube, and the external standard with TMS is placed inside. When the NMR spectrum is obtained, the peaks of methanol (*s*, δ = 3.36 ppm), MeOOH (*s*, δ = 3.89 ppm) and formic acid (*s*, δ = 8.4 ppm) are integrated and correlated to the MA standard calibration.

Calibration factors: K_{H1} = 0,316 ± 0,007 mM/a.u. (external standard #1);
K_{H2} = 0,327 ± 0,003 mM/a.u. (external standard #2);
K_{H3} = 0,348 ± 0,005 mM/a.u. (external standard #3).

2.6.3.2. GC quantification

Thermo Scientific Trace GC Ultra equipped with TCD detector was used for determination of CO_2 content in the gas phase after reaction. No gaseous components other than CH_4, CO_2, N_2 and O_2 were detected. Due to very high concentration of methane its quantification was not possible in most experiments. 7-point CO_2 calibration in a range of 200-1549 ppm was performed using 1549 ppm CO_2 in He and 99.999% He cylinders (*Linde Gas Benelux B.V.*). The flows were controlled using the *BRONKHORST HI-TEC* mass-flow controllers calibrated with *HORIBA STEC VP-2* film flowmeter unit.

In a typical measurement, the gas bag with the sample was connected to the inlet of the GC, and the outlet was connected to the custom-made (*GLOBAL analyser solutions*) microflow pump. Prior to the analysis GC lines were flushed with the gaseous sample flow of 0.5 mL/min for 5 min (measured with the *Agilent ADM1000* flowmeter connected to the outlet of the pump). The measurements were repeated 3 times.

Calibration factor: K_{CO2} = 0,0106 ± 0,0008 ppm/a.u.

2.6.4. TEM and SEM

SEM images were recorded without sputtering using a *JEOL JSM-6010LA* with a standard beam potential of 5-10 kV and an *Everhart-Thornley* detector. X-ray microanalysis (SEM/EDX) confirmed the elemental composition in the sample by scanning microscopy (SEM) coupled with a dispersive X-ray microanalysis system (EDX) with a Silicon-drift detector. Mapping analysis and element detection where analysed with *KLM* markers of the characteristic X-ray peak and a beam potential of 20 kV.

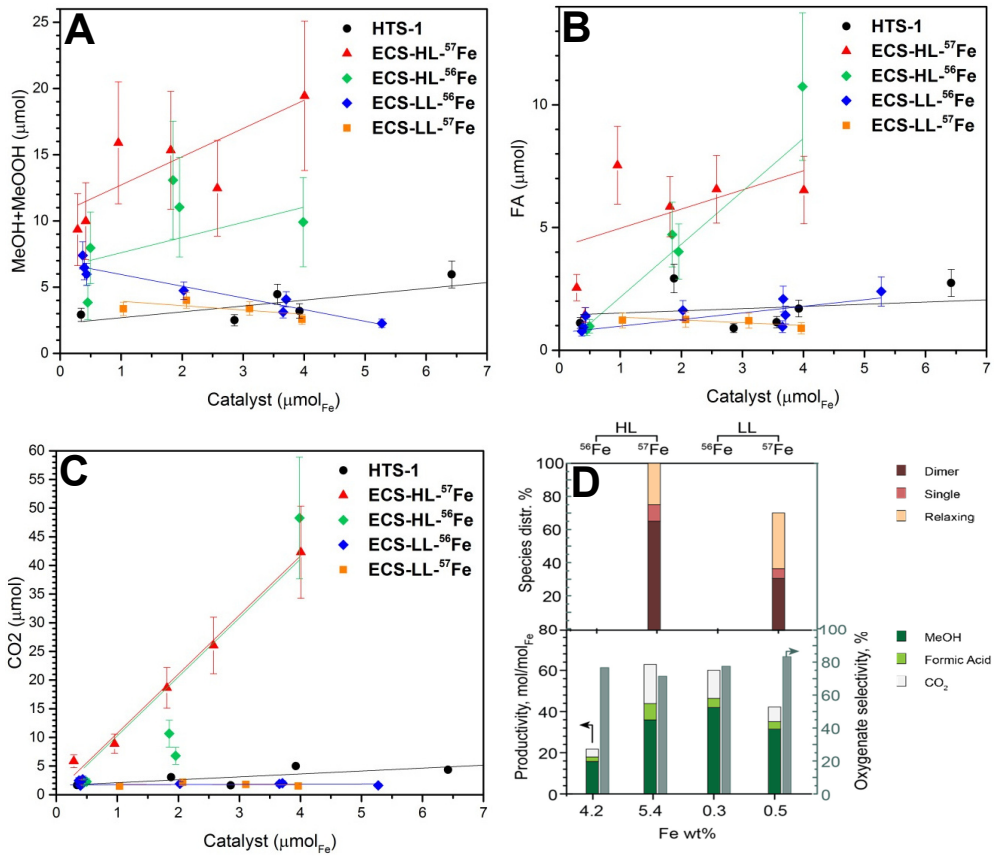

Figure 2.11. Evolution of **(a)** methanol and methyl hydroperoxide, **(b)** formic acid and **(c)** carbon dioxide oxidation products (μmol) at different iron loadings for electrochemically synthesized samples; **(d)** catalytic activity (*bottom*) and distribution of iron species according to Mössbauer characterization (*top*) for MIL-53(Al,Fe) ECS samples.

2.6.6. XRD

Diffractograms were recorded in Bragg-Brentano geometry in *Bruker D8 Advance* X-ray diffractometer equipped with a *Vantec* position sensitive detector and graphite monochromator. Measurements were performed at room temperature with monochromatic Co *Kα* radiation (λ = 0.179026 nm) in the 2θ range (10°-70°) at a scan rate of 0.2 s·deg^{-1}.

2.6.7. TGA

Experiments were performed using a *Mettler Toledo TGA/SDTA851e* instrument from room temperature to 700 °C with a ramping rate of 5 °C·min^{-1} under continuous flow of artificial air (100 mL·min^{-1}).

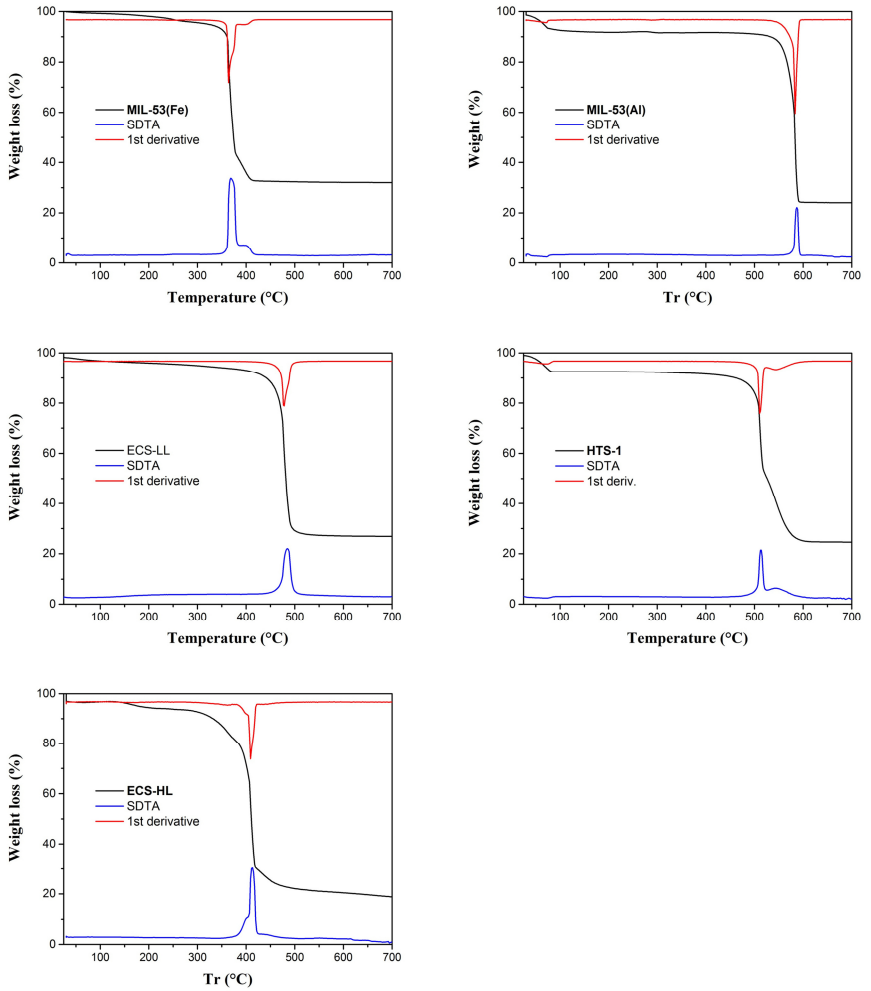

Figure 2.12. Thermogravimetric analysis of **ECS-HL** (*bottom left*), **ECS-LL** (*middle left*), and **HTS-1** (*middle right*) catalysts and the reference hydrothermally synthesised MIL-53(Fe) (*top left*) and MIL-53(Al) (*top right*).

2.6.5. Raman

Raman spectra were obtained with a *Renishaw inVia Reflex* confocal spectrometer using a 785 nm laser excitation. Laser power was in most cases set to 1 % and the sample was irradiated for 60 s. Measurements were carried in samples without any pre-treatment and exposed to normal conditions of air and humidity at room temperature. Spectra analysis was carried with *WIRE4.1* software without smoothing or baseline removal.

2.6.8. EXAFS

X-ray absorption experiments were performed at *DUBBLE* beam line *BM26A* in ESRF, Grenoble. The materials were studied using Fe *K*-edge. Energy calibration was achieved using metal foil as reference and the first peak in the first derivative of the metal foil XAS spectrum was calibrated to 7112 eV.[31] Calibration and data alignment was performed with *Athena* software by using values for reference compounds from *Hephaestus* software.[32] After averaging the spectra of the studied samples were normalized to a total absorption of unity and processed using the *Athena* data normalization and analysis package. For normalization, the spline *r*-background parameter was set to 1.0. The background subtraction was carried using a pre-edge range of -200 to -50 eV and a post-edge linear range of 60 to 830 eV. A spline range of k = 0 to k = 14.8 A^{-1} and k-weight of 3 was used to isolate the EXAFS (chi)function. The Fe *K*-edge EXAFS spectra were Fourier transformed over a k-range of k = 3 to k = 11 $Å^{-1}$.

2.6.8.1. EXAFS linear combination fitting

Fe *K*-edge EXAFS linear combination fittings were performed to determine the Fe components in high loading MIL-53(Al,Fe) samples. Hematite, FeOOH and the pure Fe MOF MIL-53(Fe) were used as standard components to fit the normalized Fe K-edge EXAFS spectra of the samples with the Athena linear combination fitting routine. Fits were performed in k-space in the range of 3-11 $Å^{-1}$. Coefficients of each component were constrained to have coefficients between 0 and 1 and that of their sum to 1.

2.6.8.2. EXAFS fitting of the MIL-53(Al,Fe) samples

Fitting of Fe *K*-edge EXAFS spectra was carried out by *Artemis* software.[32] The spectra of the different samples were fitted in *R*-space with a *R* range of 1 to 4.5 Å, and the fittings were done with a k-weight of 3. The Fourier transform and inverse Fourier transform was carried with a Δk of 1 and ΔR of 0. From the references fits we obtain the amplitude factor (S_0^2) 0.87 for α-Fe_2O_3 and 0.85 for pure iron phase MIL-53(Fe) (Fig. 2.13). In further fittings of the experimental samples S_0^2 = 0.85 was used.

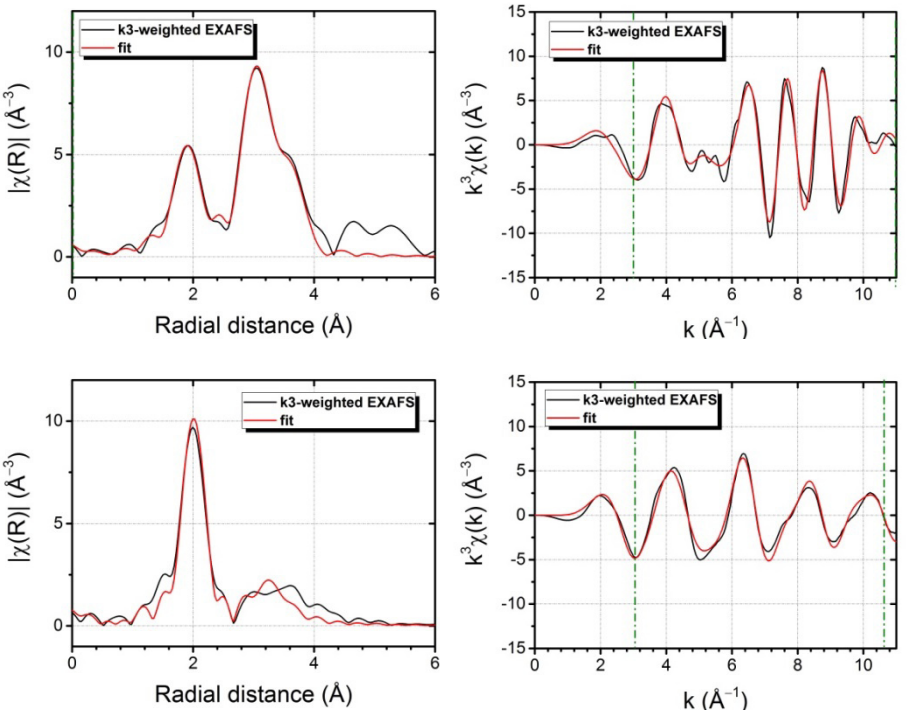

Figure 2.13. Reference materials. Top: Fitting of EXAFS spectrum for α-Fe_2O_3. Bottom: fitting of EXAFS spectrum for MIL-53(Fe).

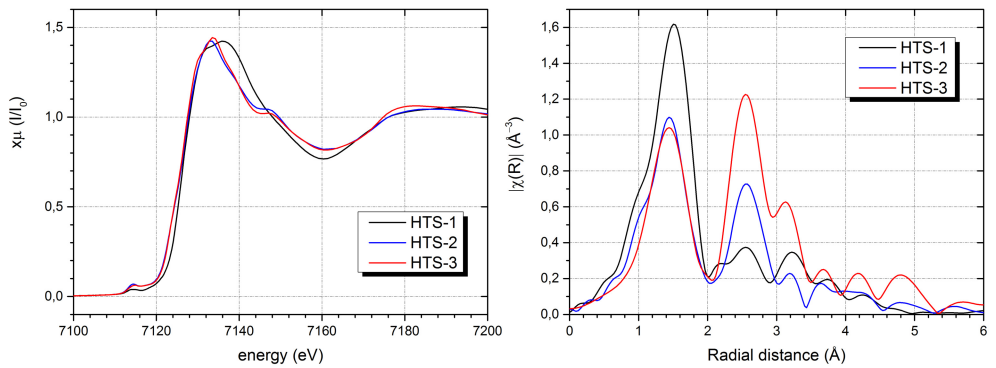

Figure 2.14. Fe *K*-edge XANES and FT EXAFS spectra for hydrothermally synthesized MIL-53(Al,Fe) samples (**HTS-1**, **HTS-2**, and **HTS-3** contain 1.0 wt %, 5.4 wt %, and 16.6 wt % Fe, respectively).

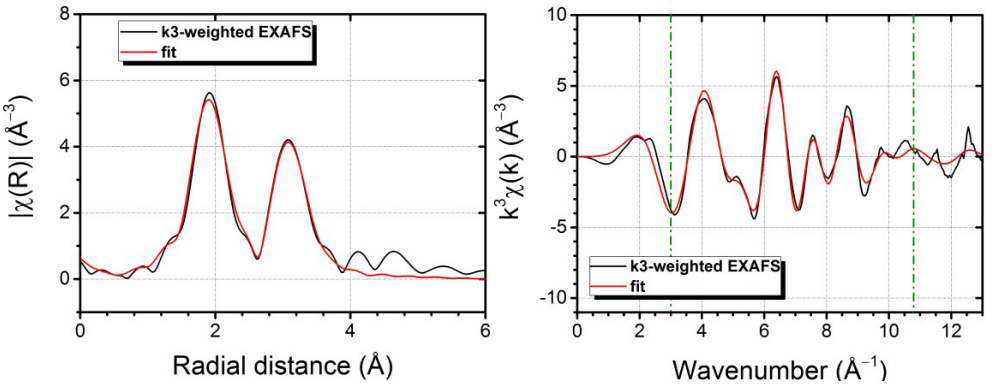

Figure 2.15. Fitting of FT EXAFS spectrum for sample **HTS-2** using α-Fe_2O_3 (hematite) structure parameters.

Table 2.2. EXAFS fitting results of the **HTS-2** sample.

	Model	Shell Number	Scat-terer	Coordination number N/-	Distance R/Å	Debye-Waller factor $\Delta\sigma^2$ / Å^2	R-factor
HTS-2	Fe_2O_3	1	O	3	1.91 ± 0.01	0.0060 ± 0.0008	0.0151651
		2	O	3	2.05 ± 0.01	0.008 ± 0.001	
		3	Fe	1	2.93 ± 0.01	0.0125 ± 0.0009	
		4	Fe	3	3.00 ± 0.01	0.0125 ± 0.0009	
		5	Fe	3	3.39 ± 0.01	0.0125 ± 0.0009	

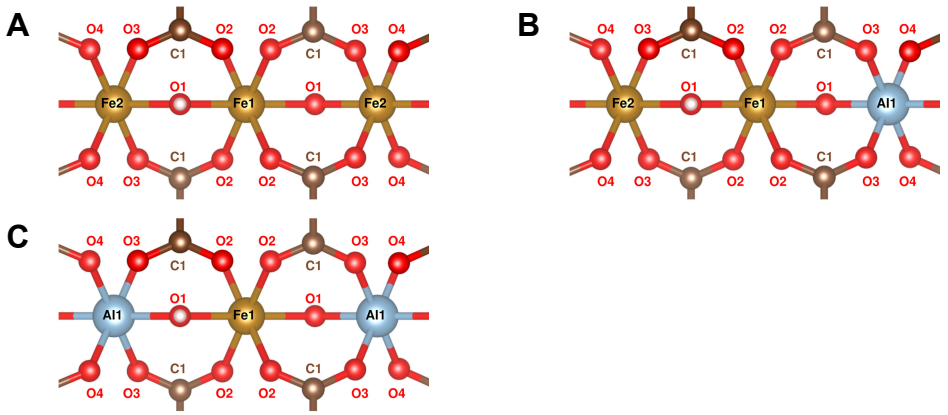

Figure 2.16. Models used for the fitting of Fe *K*-edge EXAFS spectra for MIL-53(Al,Fe) samples: **A**: Fe-O-Fe-O-Fe, **B**: Fe-O-Fe-O-Al, and **C**: Al-O-Fe-O-Al. The structures were plotted using VESTA software.[33]

Three models were tried for the fitting of Fe *K*-edge EXAFS spectra of MIL-53(Al,Fe) samples: 1) the Fe atom with two Fe neighbours in the MIL-53(Fe) structure (model A: Fe-O-Fe-O-Fe); 2) the Fe atom with one Fe and one Al neighbour in either the MIL-53(Al) or the MIL-53(Fe) structure (model B: Fe-O-Fe-O-Al); and 3) the Fe atom with two Al neighbours in the MIL-53(Al) structure (model C: Al-O-Fe-O-Al) (Figure 2.16 and Table 2.3).

All coordination numbers were fixed during the fitting. In the case of the **HTS-1** sample only the MIL-53(Fe) model gives a reasonable fit with meaningful parameters ($\sigma^2 > 0$). In the case of the ECS samples all models gave a reasonable fit, but with high uncertainty in the Debye-Waller factor. The most reliable fits for the ECS samples are obtained using MIL-53(Fe) as model. Thus, according to EXAFS, the Fe-O-Fe-O-Fe model gave the best fit, however, the large uncertainty of the obtained parameters and the variance observed in the bond length suggest that a mixture of the different Fe species (three models used for fitting) is present in the samples. Although the EXAFS fittings cannot unambiguously differentiate among monomers, dimers or bigger clusters, fittings with Fe_2O_3 proved reluctant to converge. In this scenario, XAS points to iron species that could be present in the form of small octahedric atom clusters that are well close to MIL-53(Fe) environment, and in agreement to Mossbauer and EPR spectra.

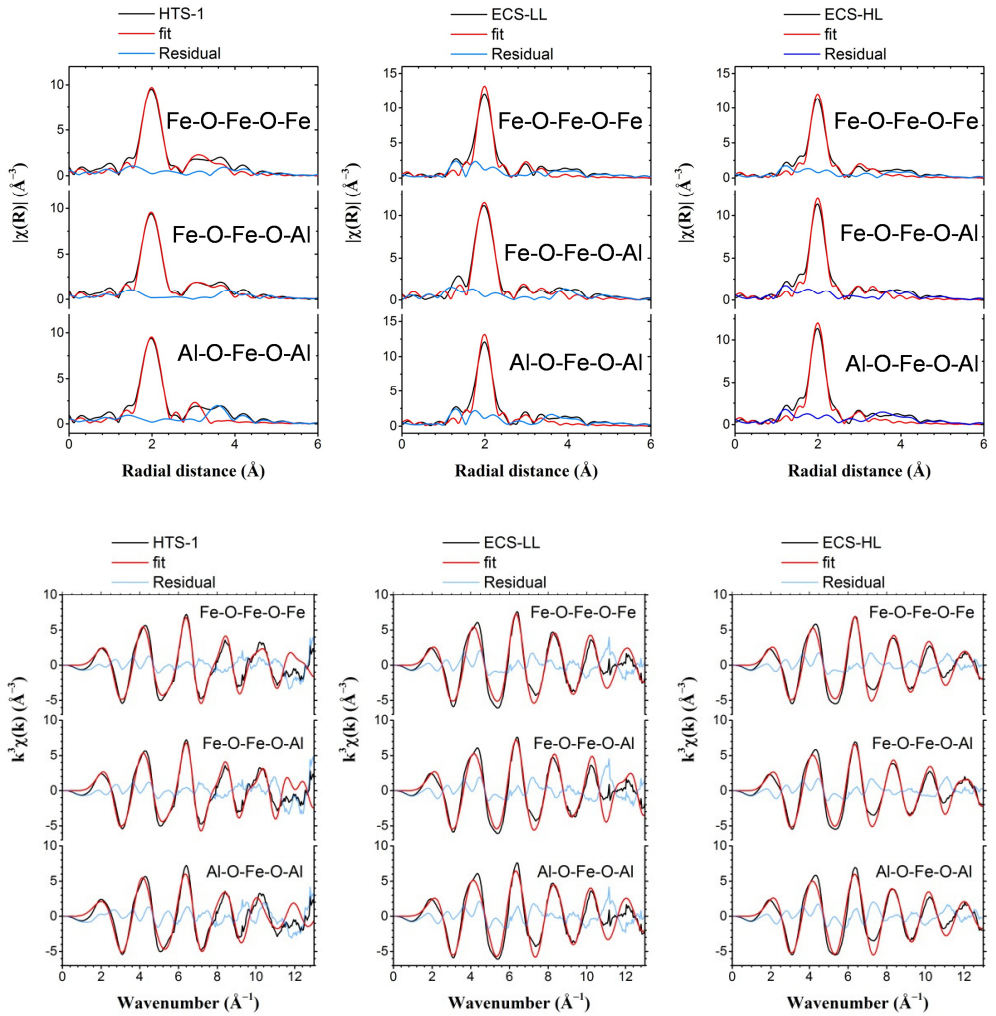

Figure 2.17. Fitting of FT EXAFS spectrum for MIL-53(Al,Fe) samples: **HTS-1** (left), **ECS-LL** (middle) and **ECS-HL** (right) using different models.

Table 2.3. EXAFS fitting results of the **HTS-1** and **ECS** series samples. Model legends correspond to figure 2.16; A: Fe-O-Fe-O-Fe, B: Fe-O-Fe-O-Al and C: Al-O-Fe-O-Al.

	Model	Shell Number	Scat-terer	Coordination number N/-	Distance R/Å	Debye-Waller factor $\Delta\sigma^2$ / Å^2	R-factor
HTS-1	A	1	O	2	1.95 ± 0.01	0.0039 ± 0.0009	0.0256500
		2	O	4	2.02 ± 0.01	0.0039 ± 0.0009	
		3	C	4	2.96 ± 0.04	0.007 ± 0.007	
		6	Fe	2	**3.41 ± 0.03**	**0.005 ± 0.003**	
	B	1	O	2	1.92 ± 0.01	0.0037 ± 0.0009	0.0221051
		2	O	4	2.03 ± 0.01	0.0037 ± 0.0009	
		3	C	4	2.95 ± 0.04	0.005 ± 0.006	
		6	Al	1	3.6 ± 0.1	0.003 ± 0.01	
		6	Fe	1	3.43 ± 0.08	0.001 ± 0.02	
	C	1	O	2	1.91 ± 0.02	0.002 ± 0.001	0.0410454
		2	O	4	2.02 ± 0.02	0.002 ± 0.001	
		3	C	4	3.02 ± 0.09	0.01 ± 0.03	
		6	Al	2	3.20 ± 0.06	0.006 ± 0.009	
ECS-LL	A	1	O	2	1.94 ± 0.01	0.0023 ± 0.0008	0.0469491
		2	O	4	2.01 ± 0.01	0.0023 ± 0.0008	
		3	C	4	2.97 ± 0.04	0.005 ± 0.005	
		6	Fe	2	**3.47 ± 0.06**	**0.012 ± 0.009**	
	B	1	O	2	1.94 ± 0.01	0.002 ± 0.001	0.0307670
		2	O	4	2.01 ± 0.01	0.002 ± 0.001	
		3	C	4	2.95 ± 0.04	0.005 ± 0.007	
		6	Al	1	3.44 ± 0.2	0.001 ± 0.009	
		6	Fe	1	3.45 ± 0.07	0.001 ± 0.009	
	C	1	O	2	1.94 ± 0.01	0.0023 ± 0.0008	0.0495379
		2	O	4	2.01 ± 0.01	0.0023 ± 0.0008	
		3	C	4	2.95 ± 0.06	0.008 ± 0.008	
		6	Al	2	3.4 ± 0.1	0.02 ± 0.02	
ECS-HL	A	1	O	2	1.94 ± 0.01	0.0030 ± 0.0007	0.0316240
		2	O	4	2.01 ± 0.01	0.0030 ± 0.0007	
		3	C	4	2.98 ± 0.03	0.006 ± 0.005	
		6	Fe	2	**3.44 ± 0.04**	**0.011 ± 0.006**	
	B	1	O	2	1.94 ± 0.01	0.0030 ± 0.0007	0.0298216
		2	O	4	2.02 ± 0.01	0.0030 ± 0.0007	
		3	C	4	2.97 ± 0.04	0.007 ± 0.006	
		6	Al	1	3.5 ± 0.2	0.003 ± 0.007	
		6	Fe	1	3.44 ± 0.08	0.003 ± 0.007	
	C	1	O	2	1.94 ± 0.01	0.0030 ± 0.0007	0.0397995
		2	O	4	2.01 ± 0.01	0.0030 ± 0.0007	
		3	C	4	2.96 ± 0.05	0.008 ± 0.008	
		6	Al	2	3.5 ± 0.4	0.04 ± 0.08	

Table 2.4. The Mössbauer fitted parameters of Fe-MOF samples, obtained at 4.2 K.

Sample/ Treatment	*IS* (mm·s^{-1})	*QS* (mm·s^{-1})	Hyperfine field (T)	*Γ* (mm·s^{-1})	Phase	Spectral contribution (%)
ECS-HL-^{56}Fe	0.39	1.02	-	0.72	Fe^{3+} (dimeric complex)[b]	58
	0.38	0.58	56.3	0.80	Fe^{3+} (isolated ions)[c]	8
	0.35	0.20	36.4*	0.76	Fe^{3+} (relaxing)[d]	34
HTS-1-^{56}Fe	0.38	0.98	-	0.74	Fe^{3+} (dimeric complex)[b]	28
	0.34	-0.02	49.0	1.15	Fe^{3+} (FeO_x clusters)	72
ECS-HL-^{57}Fe	0.37	1.40	-	0.66	Fe^{3+} (dimeric complex)[b]	68
	0.37	0.58	56.3	0.80	Fe^{3+} (isolated ions)[c]	8
	0.35	0.21	32.5*	0.76	Fe^{3+} (relaxing)[d]	24
ECS-LL-^{57}Fe	0.39	1.24	-	0.79	Fe^{3+} (dimeric complex)[b]	31
	0.37	0.47	56.2	0.57	Fe^{3+} (isolated ions)[c]	6
	0.35	-	-	7.10	Fe^{3+} (relaxing)[d]	30
	0.37	-1.23	44.5*	1.27	Fe^{3+} (FeO_x clusters)	33

Experimental uncertainties: Isomer shift: *I.S.* ± 0.01 mm s^{-1}; Quadrupole splitting: *Q.S.* ± 0.01 mm s^{-1}; Line width: *Γ* ± 0.01 mm s^{-1}; Hyperfine field: ± 0.1 T; Spectral contribution: ± 3%; *Average magnetic field; [a]Superparamagnetic iron oxide nanoparticles (clusters); [b]Dimeric high-spin Fe^{3+}–Fe^{3+} complexes, or Fe^{3+}–O chains composed of even numbered multiple atoms; [c]Isolated paramagnetic Fe^{3+} species with Fe-Fe ion distances greater than 15 Å; [d]Mössbauer line shape determined by the relaxed limit due to an increase in the number of neighbouring paramagnetic Fe-complexes, with uneven number of iron atoms.

Table 2.5. Structural, Mössbauer, and magnetic properties of selected diiron proteins[34] and MIL-53(Al,Fe) samples.

	Fe-μ-O, Å	Fe-O, Å	Fe…Fe, Å	-*J*, cm^{-1}	$\delta(IS)$, mm s^{-1}	*QS*, mm s^{-1}
M. Capsulatus (Bath) hydrolase		2.04	3.42	-32	0.5	1.05
oxyhemerythrin	1.76-1.8	2.17	3.20-3.24	-77	0.5	1.96
native RRB2	1.78-1.8	2.04-2.06	3.21-3.26	-108		
ECS-LL	1.94	2.01	3.47	-140	0.39	1.24
ECS-HL	1.94	2.01	3.44	-230	0.37	1.40

2.6.9. Mössbauer spectroscopy

Transmission ^{57}Fe Mössbauer spectra were collected at 4.2 K with a sinusoidal velocity spectrometer using a ^{57}Co(Rh) source. Velocity calibration was carried out at room temperature, using an *α*-Fe foil. The source and the absorbing samples were kept at the same temperature during the measurements. The Mössbauer spectra were fitted using the *Mosswinn 4.0* program.[35]

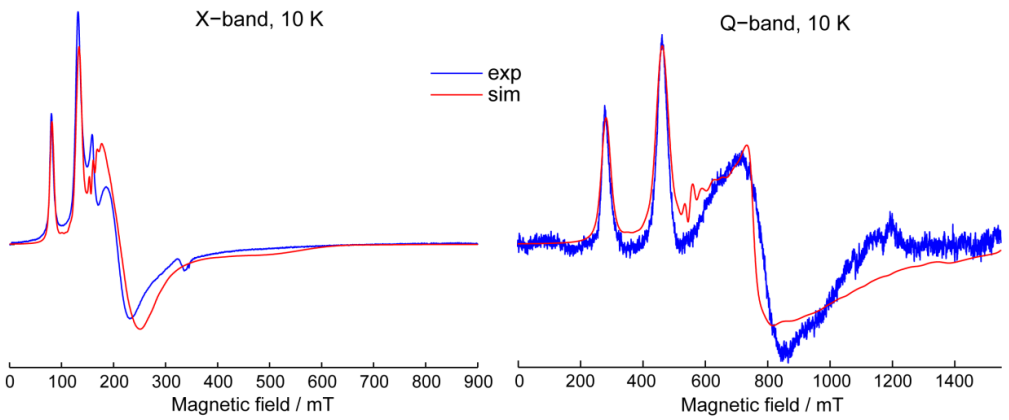

Figure 2.18. Fitting of the *X*- and *Q*-band CW EPR spectra of **^{57}ECS-LL** at 10 K using a model for isolated high-spin Fe^{3+}. Simulated curve (shown in red) was obtained using the following set of parameters for monomeric Fe^{3+} ion: S = 5/2, isotropic g = 1.95, D = 1.13 cm^{-1}, E = 0.18 cm^{-1}.

2.6.10. EPR

All EPR measurements were carried out in continuous wave (CW) mode at *X*-band (9 GHz) and *Q*-band (34 GHz) using a commercial spectrometer *Bruker ELEXSYS E580* equipped with an *Oxford flow* helium cryostat and temperature control system (T = 4-300 K). The powdered samples were placed in the quartz tubes and measured in a broad range of magnetic field 0-1.65 T at T = 10-80 K. Simulations were performed using *EasySpin* toolbox for *Matlab*.[36]

The magnitude of exchange coupling J within the antiferromagnetically-coupled Fe^{3+} network (*AF*-cluster) was roughly estimated following the temperature dependence of its line (broad feature with g ≈ 2.00, B_0 ≈ 1200 mT at *Q*-band) in **^{57}ECS-HL** and **^{56}ECS-HL**. The signals of monomeric (thus magnetically isolated) species present in the same EPR spectra were used as reference. We denote the magnetizations (second integrals of the corresponding EPR spectra) of the *AF*-cluster and monomeric Fe^{3+} centres as M_{AF} and M_{Fe}, respectively. Thus, Figure 2.20 shows their ratios, M_{AF}/M_{Fe}, calculated for the spectra shown in Figure 2.19 (**^{57}ECS-HL** and **^{56}ECS-HL**). To simulate the trend for *AF*-cluster, we used a model of two S = 5/2 spins coupled by antiferromagnetic exchange interaction J (spin-Hamiltonian $H_{ex} = JS_1S_2$). Such simulation allowed satisfactory agreement with experiment using the following parameters: J = 120 ± 35 cm^{-1}, n = 1.8 for **^{57}ECS-HL**,

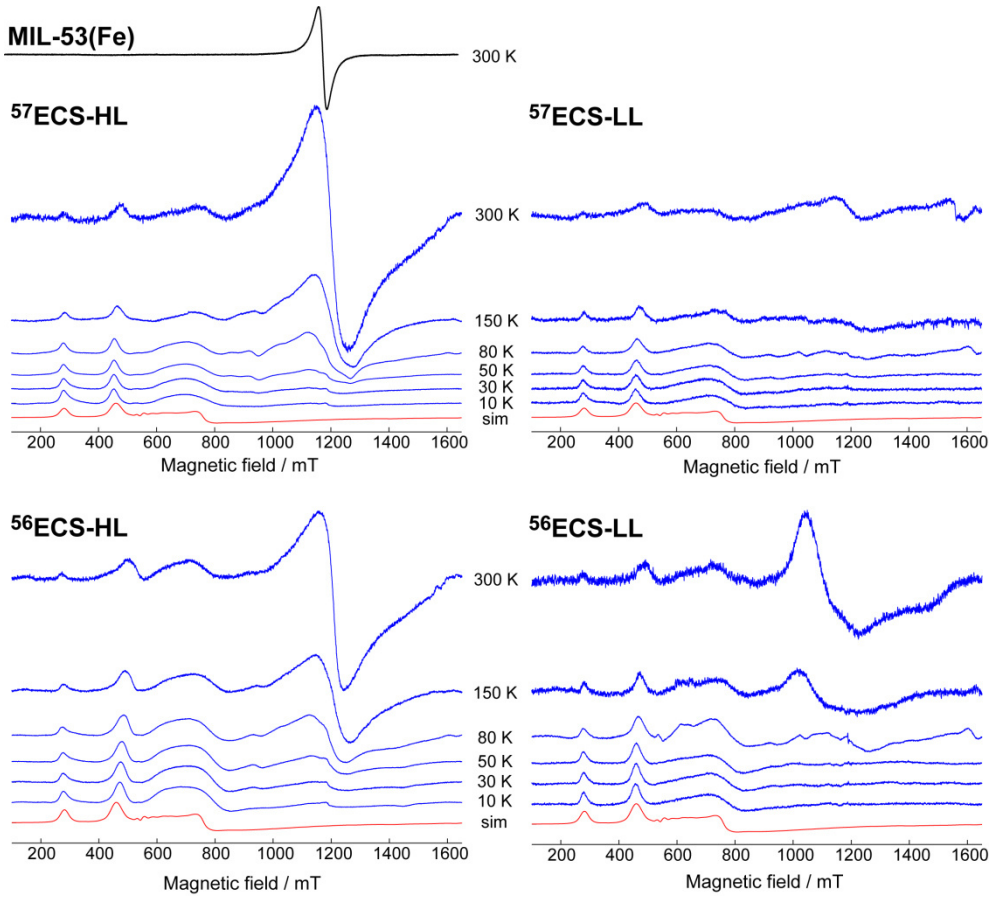

Figure 2.19. *Q*-band ($\nu_{mw} \approx$ 33.2-33.8 GHz) CW-EPR spectra vs. temperature for MIL-53(Fe), **^{57}ECS-HL**, **^{57}ECS-LL**, **^{56}ECS-HL** and **^{56}ECS-LL**. All spectra are normalized to the signal of monomeric Fe^{3+} at ≈ 460 mT (Simulated curve, shown in red).

and J = 100 ± 35 cm^{-1}, n = 1.0 for **^{56}ECS-HL**, where n is the ratio of *AF*-coupled dimers to monomers. Within the accuracy of this estimation, J values are closely the same for **^{57}ECS-HL** and **^{56}ECS-HL**.

Remarkably, although such estimation using EPR is rather crude, the orders of magnitude of the obtained J couplings are the same as those found previously for the oxo-bridged Fe^{3+}-Fe^{3+} dimers in hemerythrin and *E.coli* ribonucleotide reductase (J = 270 and 220 cm^{-1}, respectively).[23-24] This strongly supports the dimeric nature of isolated clusters and the closeness of their magnetic properties to those for Fe^{3+}-Fe^{3+} dimers in biological systems. Finally, parameter n provides the estimate of the relative content of

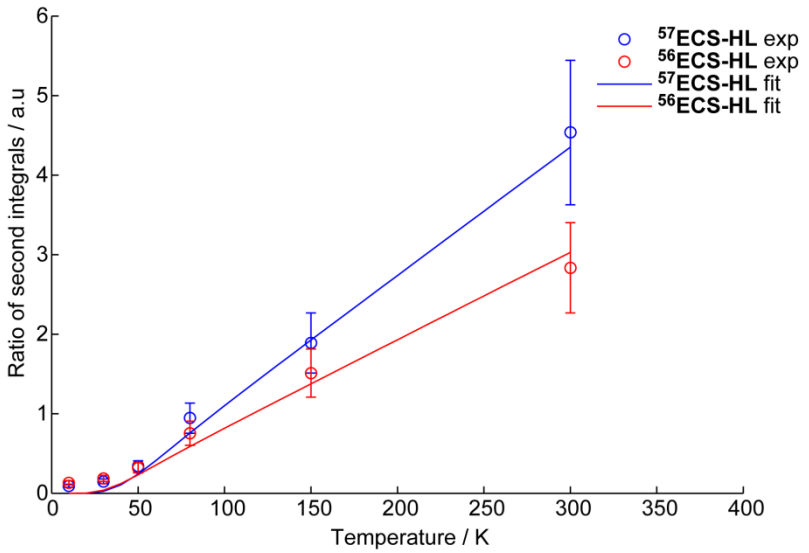

Figure 2.20. Ratio M_{AF}/M_{Fe} for **^{57}ECS-HL** and **^{56}ECS-HL** and the corresponding simulations, see the text for details.

dimers to monomers. Note that the number of Fe^{3+} species residing in dimers is twice larger than the number of dimers. Taking this into account, we find that the ratio of Fe^{3+} atoms in dimers relative to those in monomers is ≈ 78/12% for **^{57}ECS-HL** and ≈ 67/33% for **^{56}ECS-HL**. Such estimations reasonably agree with the Mossbauer data.

EPR measurements of sample **^{57}ECS-HL** before and after reaction (Fig. 2.21) do not show any significant changes in *Q*-band spectra, indicating that iron within this sample remains in the form of monomeric and dimeric species and does not generate iron oxide. This serves as an additional proof of stability of electrochemically-prepared MIL-53(Al,Fe) catalysts in the reaction conditions.

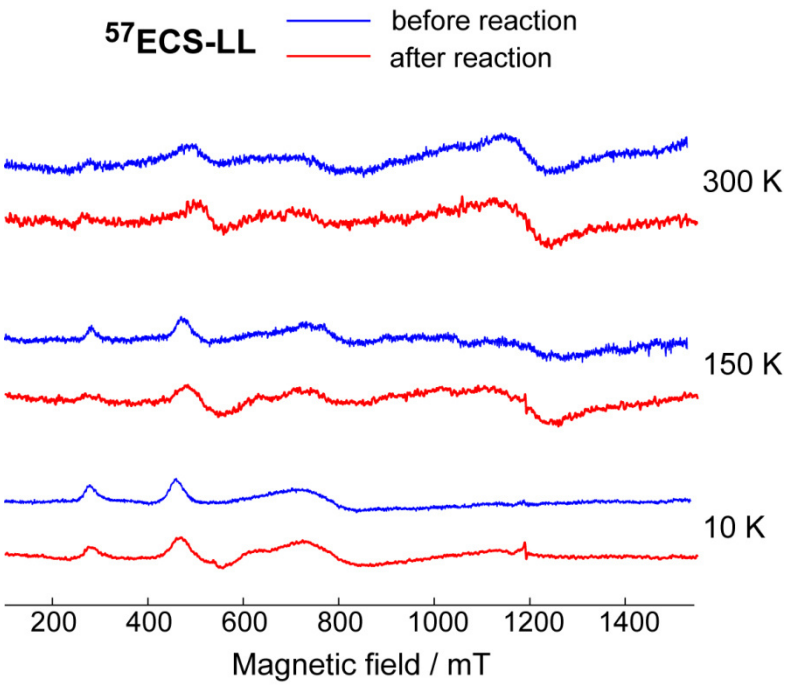

Figure 2.21. *Q*-band (ν_{mw} ≈ 33.2-33.8 GHz) CW-EPR spectra *vs*. temperature for **^{57}ECS-LL** before and after reaction.

2.6.11. Computational methods

The spin polarized periodic DFT calculations were carried out by the *Vienna Ab Initio Simulation Package* (*VASP*).[37] PBE exchange-correlation functional,[38] plane wave basis set with a cut-off energy of 400 and 450 eV for MIL-53(Al,Fe) and MIL-53(Fe) respectively and the projector augmented wave (*PAW*) method[39] were applied. To account for the van der Waals interactions Grimme's dispersion correction with Becke-Jonson damping (*DFT-D3(BJ)*) method was used.[40] Brillouin zone sampling was restricted to the Gamma point. Convergence was assumed to be reached when the forces on each atom were below 0.04 eV $Å^{-1}$. Geometry optimization was completed for all considered spin states.

To determine the transition state the nudged elastic band method (NEB)[41] was applied. The maximum energy geometry along the reaction path generated by the NEB method was further optimized using a quasi-Newton algorithm. In this procedure, only the extra-framework atoms were relaxed. Vibrational frequencies were calculated using the finite difference method (0.02 Å atomic displacements) as implemented in *VASP*. Transition state showed a single imaginary frequency corresponding to the reaction path.

During the calculations, the supercell approach was applied, which means that the basic unit cell was multiplied by an integer, in this case 12. All together the supercell contains 228 atoms. Firstly, the unit cell vectors of the models employed were optimized. The optimized parameters are: a=(20.917,0.000,0.000) b=(0.00,17.808,0.000) c=(0.000,0.000,12.216) and a=(20.133,0.000,0.000) b=(0.001,17.286,0.000) c=(0.097,-0.009,12.342) for the MIL-53(Al) and MIL-53(Fe) respectively. The cell parameters were kept constant during the subsequent geometrical and transition state calculations. One or two neighbouring Al atoms were substituted with Fe to obtain the models of MIL-53(Al,Fe) containing monomeric or dimeric Fe site.

2.6.11.1. Spin states

For monomeric Fe site the S = 5/2 high spin state was predicted to be the most stable electronic configuration. In the case of the MIL-53(Al,Fe) containing the Fe dimer (**1**), in agreement with the spectroscopic findings, DFT predicts the antiferromagnetically coupled high spin state to be the most stable species (Table 2.6). However, the ferromagnetically coupled high spin configuration (S = 5) is only 10 $kJ \cdot mol^{-1}$ higher in energy. Since the convergence of the antiferromagnetically coupled HS system is very

Table 2.6. Relative energies of the different spin states of the initial structure (**1**) of dimeric MIL-53(Al,Fe).

Spin state *S*	Energy kJ·mol^{-1}
0(open)	0
0(closed)	98
1	44
2	94
3	45
4	40
5	10

Table 2.7. Spin densities on the two Fe atoms of the Fe dimer for different spin states of the intermediates **1**, **2**, **CH_4/3** and **4**. The last column ***ΔE*** is the energy difference between the *S* = 0 spin state and the spin state marked in red and italic.

		***S* = 0**	***S* = 5**	***S* = 4**	***S* = 3**	***ΔE***
1	Fe1	4.02	*4.07*	2.80	4.01	-10
	Fe2	-4.02	*4.07*	4.00	1.15	
2	Fe1	4.01	*4.02*		3.96	-11
	Fe2	-3.966	*4.07*		1.15	
CH_4/3	Fe1	-3.035	3.20	*3.16*	1.81	-18
	Fe2	3.02	3.97	*3.17*	3.05	
4	Fe1	1.237	3.24	1.85	*1.60*	7
	Fe2	-2.016	4.02	4.01	*2.83*	
5	Fe1	3.127	*3.24*	1.85	1.60	-13
	Fe2	-3.956	*4.02*	4.01	2.83	

cumbersome, and it was shown by Baerends *et al*[42] that a weak exchange coupling does not influence the chemical reaction significantly, we did the modelling on the *S* = 5, 4 and 3 potential energy surfaces.

Besides Baerends' work we also did calculations on some of the minimum points in the *S* = 0 state (Table 2.7). The results were highly influenced by the initial guess (both structure, energy and spin density, see row 4 and 5 in Table 2.7), and in most cases the spin density was closest to the more stable one of the high spin states (*S* = 4 or 5) only with alternate spins on Fe (and surrounding) atoms. In these cases, its energy was consistently 10-20 kJ·mol^{-1} lower than the quintet or quartet states.

Table 2.8. Relative energies (in kJ·mol^{-1}) of the different spin states of the reaction intermediates (**1**, **CH_4/3** and **4**) of MIL-53(Fe).

S	1	CH_4/3	4
0	0		
1	25	-105	1
2	10	-131	-16
3	42		
4	39		
5	14	-136	-16
6	18		
7	-7		
8	-19	-117	14
9	2	-104	10
10	7	-89	44
18	96	-62	72
20	186		
25	309		
30	434		

The MIL-53(Fe) supercell contains 12 Fe atoms leading to the potential spin states ranging from 0 to 30. However, it turns out that in this case the electronic configurations containing mainly antiferromagnetically coupled Fe centres with low spin states (0-10) are preferable (Table 2.8). The energy differences of these spin states are within 60 kJ·mol^{-1}. After *S* = 10, the system's energy continuously increases with increasing the spin states and for *S* = 30 it is already more than 400 kJ·mol^{-1} higher in energy than that of *S* = 0. Based on these results, the reaction mechanism was calculated only on four randomly chosen lower spin states: *S* = 2, 8, 9 and 10.

2.6.11.2. Relative energies of the intermediates of the methane activation cycle

An alternative route was also considered for the activation of H_2O_2. Since the first coordination shell of Fe is fully saturated, for H_2O_2 to coordinate one bond of Fe has to be broken. This either can be the Fe-OCO-R bond as described in the paper, or the Fe-(μ-O) bond. In the latter case structure 2b is formed depicted on Fig. 2.22. This route is energetically much less favourable than braking the Fe-OCO-R bond (Table 2.9, entry 5).

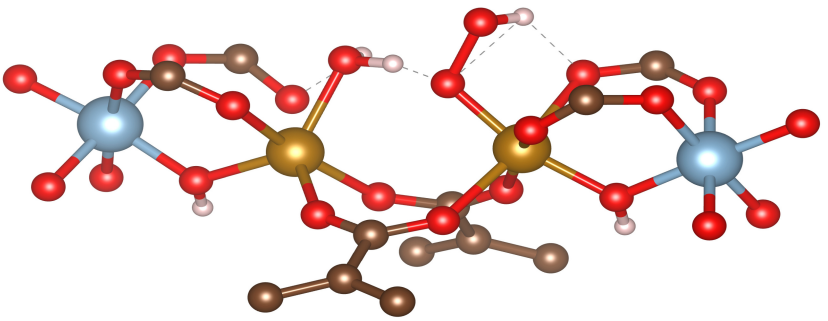

Figure 2.22. Local **s**tructure of **2b**. (Al: blue, Fe: yellow, O: red, C: brown and H: white)

Table 2.9. Relative energy (in $kJ \cdot mol^{-1}$) of the reaction intermediates in different spin states catalysed by the dimeric Fe site of MIL-53(Al,Fe).

	***S* = 5**	***S* = 4**	***S* = 3**
1	0	30	35
H_2O_2/1	-62	-36	-28
TS H_2O_2 coord.	15	46	54
2	-12	12	24
2b	19	44	87
TS $Fe^{(IV)}$-$Fe^{(IV)}$	51	61	106
H_2O/3	21	-55	-58
CH_4/3	39	-38	-43
TS C-H act.	73	38	72
4	31	24	68
5	-227	-214	-187
CH_3OH/1	-285	-265	-244

Table 2.10. Relative energy of the reaction intermediates in different spin states catalysed by the monomeric Fe site in MIL-53(Al,Fe).

	***S* = 5/2**	***S* = 3/2**	***S* = 1/2**
1	0	45	51
H_2O_2/1	-60	-23	-8
TS H_2O_2 coord.	21	53	
2	-13	24	50
TS $Fe^{(III)}$-$Fe^{(V)}$	58		
H_2O/3	34	-29	25
CH_4/3	50	-10	39
TS C-H act.	82	70	80
4	32	50	48
5	-233	-196	-177
CH_3OH/1	-283	-238	-227

Table 2.11. Relative energy (in $kJ \cdot mol^{-1}$) of the reaction intermediates in different spin states catalysed by MIL-53(Fe).

	***S* = 2**	***S* = 8**	***S* = 9**	***S* = 10**
1	0	-29	-8	-4
H_2O_2/1	-43	-82	-57	-59
TS H_2O_2 coord.	64			
2	-7	52	39	17
TS $Fe^{(III)}$-$Fe^{(V)}$	15			
H_2O/3	-172	-163	-134	-141
CH_4/3	-141	-127	-124	-99
TS C-H act.	-13	5	9	
4	-26	2	0	34
5	-213	-200	-206	-192
CH_3OH/1	-261	-257	-273	-241

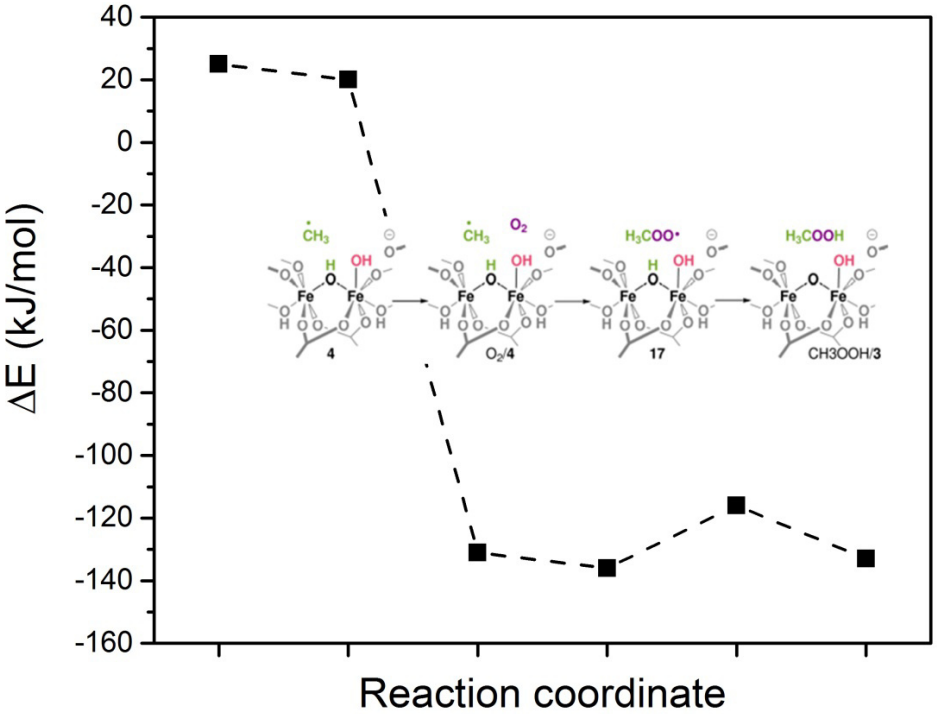

Figure 2.23. Proposed reaction mechanism of methyl hydroperoxide formation.

2.6.11.3. Stability of iron clusters in the MOF

Stability of lattice Fe substitution in MIL-53(Al) (framework Fe species): All calculations were done using a double super cell (24 metal atoms), in which Al atoms were consecutively substituted with Fe resulting in the formation of local Fe lattice clusters. The total spin was calculated by multiplying the local spin with the number of Fe atoms in the system. Based on the previous results for monomers and dimers the local spin was set to the high spin of Fe(III), which is 5/2. In case of the antiferromagnetically coupled calculations at first the non-spin polarized wave function was calculated and then it was used as the initial guess for the spin polarized calculations, where the total spin was set to 0 in case of even, and 5 in case of uneven number of Fe atoms, and the local spin was set with the *MAGMOM* to +5/2 and -5/2. Full geometry optimizations were carried out for all structures as described in the computational methods section.

Extraframework Fe species in MIL-53: Extraframework Fe-oxo species were inserted in the pore of the MIL-53(Al) MOF model resulting in neutral clusters with a formulae $Fe_{2x}O_{3x}$. The initial structures were constructed by

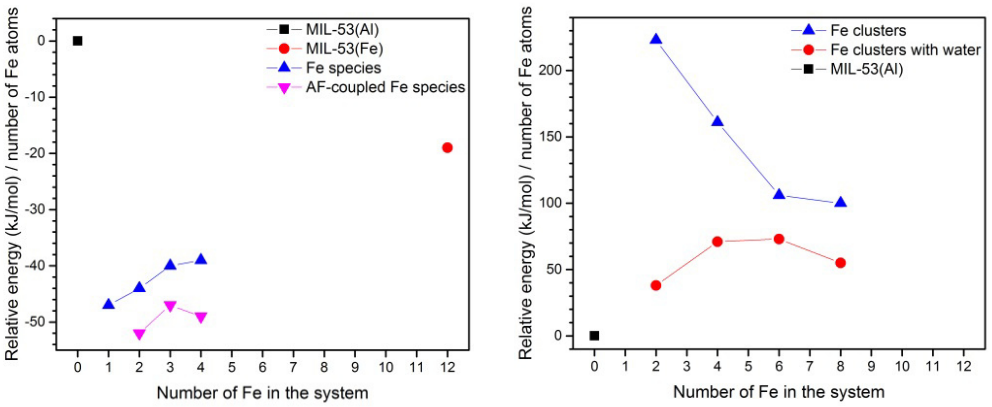

Figure 2.24. Stability of framework iron species (*left*) and extraframework iron clusters (*right*) in MIL-53(Al,Fe) catalysts

extracting molecular fragments from the octahedral (gamma) crystal of iron (III) oxide. For the H_2O-containing species, additional H_2O molecules were adsorbed to the Fe sites of the confined clusters to complete the coordination sphere of the Fe sites. In all calculations, the electronic state of the Fe centers was assumed to correspond to the high spin state. Geometries of all structures were optimized as described in the computational methods section.

The stabilities of the resulting Fe-containing structures were computed as the reaction energies for their formation from the pure-phase MIL-53(Al), α-Al_2O_3, α-Fe_2O_3 (the most stable crystals of Al_2O_3 and Fe_2O_3) and water with the following formula:

$$\Delta E = \frac{E_{xyz} + \frac{x}{12}E_{Al_2O_3} - \frac{x+y}{12}E_{MIL53(Al)} - \frac{x}{12}E_{Fe_2O_3}}{x}$$ for framework Fe species,

$$\Delta E = \frac{E_{xyz} - zE_{H_2O} - E_{MIL53(Al)} - \frac{x}{12}E_{Fe_2O_3}}{x}$$ for extraframework Fe species,

where x is the number of Fe atoms, y – number of Al atoms and z – number of H_2O molecules.

Our DFT calculations point to the substantial overall stabilization of the mixed-metal MIL-53 structure compared to the single-metal MIL-53(Fe) and MIL-53(Al) and separate oxide phase, indicating that such an isomorphous lattice substitution is indeed thermodynamically favorable. However, the associated energy gain (per Fe site) decreases with increasing the number of substituted Al ions, in other words, with increasing size of the Fe lattice

Table 2.12. This table shows the absolute and relative energies of calculated framework and extraframework Fe clusters in MIL-53(Al) MOF, and how many Fe and Al atoms and water molecules they contain. The relative values are calculated per Fe atom. For framework clusters both ferromagnetically coupled high spin (HS) and antiferromagnetically coupled high spin (AHS) states were calculated. MIL-53(Fe)* is in antiferromagnetically coupled low spin state.

	nr of Fe/ unit cell	nr of Al/ unit cell	nr of H_2O/ unit cell	E_{HS} (eV)	E_{AHS} (eV)	ΔE_{HS} (kJ/mol /nr of Fe)	ΔE_{AHS} (kJ/mol /nr of Fe)
α-Fe_2O_3	12	0		-224.53			
α-Al_2O_3	0	12		-231.45			
MIL-53(Al)	0	12		-1623.19		0	
H_2O				-14.23			
	Framework Fe clusters						
MIL-53(Al,Fe_1)	1	11		-1623.11		-47	
MIL-53(Al,Fe_2)	2	22		-3246.16	-3246.31	-44	-52
MIL-53(Al,Fe_3)	3	21		-3245.92	-3246.11	-40	-47
MIL-53(Al,Fe_4)	4	20		-3245.70	-3246.11	-39	-49
MIL-53(Fe)*	12	0			-1618.69		-19
	Extraframework Fe clusters						
Fe_2O_3/ MIL-53(Al)-1	2	12		-1656.00		223	
Fe_2O_3/ MIL-53(Al)-2	2	12		-1656.00		223	
Fe_2O_3/ MIL-53(Al)-3	2	12		-1655.99		223	
Fe_4O_6/ MIL-53(Al)-1	4	12		-1692.99		122	
Fe_4O_6/ MIL-53(Al)-2	4	12		-1691.13		167	
Fe_4O_6/ MIL-53(Al)-3	4	12		-1691.38		161	
Fe_6O_9/ MIL-53(Al)-1	6	12		-1728.85		106	
Fe_6O_9/ MIL-53(Al)-2	6	12		-1728.85		106	
Fe_8O_{12}/ MIL-53(Al)-1	8	12		-1764.61		100	
	Extraframework Fe clusters with water						
wFe_2O_3/ MIL-53(Al)-1	2	12	4	-1717.54		0	
wFe_2O_3/ MIL-53(Al)-2	2	12	4	-1716.84		34	

wFe_2O_3/ MIL-53(Al)-3	2	12	4	-1717.22	15
wFe_2O_3/ MIL-53(Al)-4	2	12	4	-1717.38	8
wFe_2O_3/ MIL-53(Al)-5	2	12	3	-1702.53	38
wFe_4O_6/ MIL-53(Al)-1	4	12	6	-1783.29	3
wFe_4O_6/ MIL-53(Al)-2	4	12	3	-1737.77	71
wFe_6O_9/ MIL-53(Al)-1	6	12	3	-1773.62	73
wFe_8O_{12}/Al-MIL-53-1	8	12	5	-1839.51	55

domain. Fe lattice sites are additionally stabilized through the antiferromagnetic coupling that allows decreasing the overall energy by *ca.* 10 kJ/mol making thus the dimeric configurations most stable among the structures considered. Nevertheless, we should note that these predicted energy differences are too small and could be influenced by the nature of the reaction environment during the synthesis resulting in a more heterogeneous site distributions in line with the experimental observations.

Importantly, our DFT calculations clearly show that the formation of extraframework Fe (EF-Fe) species inside MIL-53(Al) pores is thermodynamically unfavorable. For all EF-Fe-containing structures geometry optimization produced tetrahedrally-coordinated Fe species. Even when water molecules were introduced to complete the coordination sphere of the transition metal species, tetrahedral coordination of Fe sites was still preferred and in many cases water was desorbed from EF-Fe clusters to other sites inside the MIL-53 structure. The presence of water substantially stabilizes the EF-Fe-containing structures indicating that indeed the formation of clustered Fe sites can be expected for the synthesis carried out in the aqueous environment.

2.7. References

1. Nath, I.; Chakraborty, J.; Verpoort, F., Metal organic frameworks mimicking natural enzymes: a structural and functional analogy. *Chem. Soc. Rev.* **2016,** *45* (15), 4127-4170.
2. Labinger, J. A.; Bercaw, J. E., Understanding and exploiting C–H bond activation. *Nature* **2002,** *417* (6888), 507-514.
3. Zecchina, A.; Rivallan, M.; Berlier, G.; Lamberti, C.; Ricchiardi, G., Structure and nuclearity of active sites in Fe-zeolites: comparison with iron sites in enzymes and homogeneous catalysts. *Phys. Chem. Chem. Phys.* **2007,** *9* (27), 3483-99.
4. Sirajuddin, S.; Rosenzweig, A. C., Enzymatic oxidation of methane. *Biochemistry* **2015,** *54* (14), 2283-2294.
5. Tinberg, C. E.; Lippard, S. J., Dioxygen activation in soluble methane monooxygenase. *Acc. Chem. Res.* **2011,** *44* (4), 280-8.
6. Baik, M. H.; Newcomb, M.; Friesner, R. A.; Lippard, S. J., Mechanistic studies on the hydroxylation of methane by methane monooxygenase. *Chem. Rev.* **2003,** *103* (6), 2385-419.
7. Andersson, K. K.; Froland, W. A.; Lee, S. K.; Lipscomb, J. D., Dioxygen independent oxygenation of hydrocarbons by Methane Monooxygenase Hydroxylase Component. *New. J. Chem.* **1991,** *15* (6), 411-415.
8. Kazaryan, A.; Baerends, E. J., Ligand field effects and the high spin–high reactivity correlation in the H abstraction by non-heme iron(IV)–oxo complexes: A DFT frontier orbital perspective. *ACS Catal.* **2015,** *5* (3), 1475-1488.
9. Sobolev, V. I.; Dubkov, K. A.; Panna, O. V.; Panov, G. I., Selective oxidation of methane to methanol on a FeZSM-5 surface. *Catalysis Today* **1995,** *24* (3), 251-252.
10. Snyder, B. E. R.; Vanelderen, P.; Bols, M. L.; Hallaert, S. D.; Böttger, L. H.; Ungur, L.; Pierloot, K.; Schoonheydt, R. A.; Sels, B. F.; Solomon, E. I., The active site of low-temperature methane hydroxylation in iron-containing zeolites. *Nature* **2016,** *536* (7616), 317-321.
11. Narsimhan, K.; Iyoki, K.; Dinh, K.; Roman-Leshkov, Y., Catalytic oxidation of methane into methanol over copper-exchanged zeolites with oxygen at low temperature. *ACS Cent. Sci.* **2016,** *2* (6), 424-9.
12. Grundner, S.; Markovits, M. A. C.; Li, G.; Tromp, M.; Pidko, E. A.; Hensen, E. J. M.; Jentys, A.; Sanchez-Sanchez, M.; Lercher, J. A., Single-site trinuclear copper oxygen clusters in mordenite for selective conversion of methane to methanol. *Nature Communications* **2015,** *6*.
13. Hammond, C.; Forde, M. M.; Ab Rahim, M. H.; Thetford, A.; He, Q.; Jenkins, R. L.; Dimitratos, N.; Lopez-Sanchez, J. A.; Dummer, N. F.;

Murphy, D. M.; Carley, A. F.; Taylor, S. H.; Willock, D. J.; Stangland, E. E.; Kang, J.; Hagen, H.; Kiely, C. J.; Hutchings, G. J., Direct catalytic conversion of methane to methanol in an aqueous medium by using copper-promoted Fe-ZSM-5. *Angew. Chem. Int. Ed. Engl.* **2012,** *51* (21), 5129-33.

14. Loiseau, T.; Serre, C.; Huguenard, C.; Fink, G.; Taulelle, F.; Henry, M.; Bataille, T.; Ferey, G., A rationale for the large breathing of the porous aluminum terephthalate (MIL-53) upon hydration. *Chem. Eur. J.* **2004,** *10* (6), 1373-82.
15. Lee, S. J.; McCormick, M. S.; Lippard, S. J.; Cho, U. S., Control of substrate access to the active site in methane monooxygenase. *Nature* **2013,** *494* (7437), 380-384.
16. Martinez Joaristi, A.; Juan-Alcañiz, J.; Serra-Crespo, P.; Kapteijn, F.; Gascon, J., Electrochemical synthesis of some archetypical Zn2+, Cu2+, and Al3+metal organic frameworks. *Cryst. Growth Des.* **2012,** *12* (7), 3489-3498.
17. Beetz, M.; Zimpel, A.; Wuttke, S., Nanoparticles. In *The Chemistry of Metal–Organic Frameworks*, Wiley-VCH Verlag GmbH & Co. KGaA: **2016**, pp 491-521.
18. Neimark, A. V.; Coudert, F.-X.; Boutin, A.; Fuchs, A. H., Stress-Based Model for the Breathing of Metal−Organic Frameworks. *The Journal of Physical Chemistry Letters* **2010,** *1* (1), 445-449.
19. de Faria, D. L. A.; Venâncio Silva, S.; de Oliveira, M. T., Raman microspectroscopy of some iron oxides and oxyhydroxides. *J. Raman Spectrosc.* **1997,** *28* (11), 873-878.
20. Martin, T. P.; Merlin, R.; Huffman, D. R.; Cardona, M., Resonant two magnon Raman scattering in α-Fe2O3. *Solid State Commun.* **1977,** *22* (9), 565-567.
21. Arenas, J. F.; Marcos, J. I., Infrared and Raman spectra of ptalic, iophtalic and trephtalic aids. *Spectrochim. Acta A* **1980,** *36* (12), 1075-1081.
22. Solomon, E. I.; Lever, A. B. P., *Inorganic electronic structure and spectroscopy*. Wiley: New York, **1999**; Vol. Vol. I.
23. Dawson, J. W.; Gray, H. B.; Hoenig, H. E.; Rossman, G. R.; Schredder, J. M.; Wang, R.-H., Magnetic susceptibility study of hemerythrin using an ultrasensitive magnetometer. *Biochemistry* **1972,** *11* (3), 461-465.
24. Petersson, L.; Graslund, A.; Ehrenberg, A.; Sjoberg, B. M.; Reichard, P., The iron center in ribonucleotide reductase from Escherichia coli. *J. Biol. Chem.* **1980,** *255* (14), 6706-12.
25. Friedle, S.; Reisner, E.; Lippard, S. J., Current challenges of modeling diiron enzyme active sites for dioxygen activation by biomimetic synthetic complexes. *Chemical Society Reviews* **2010,** *39* (8), 2768.

26. Hohenberger, J.; Ray, K.; Meyer, K., The biology and chemistry of high-valent iron–oxo and iron–nitrido complexes. *Nat. Commun.* **2012,** *3*, 720.
27. Kodera, M.; Kawahara, Y.; Hitomi, Y.; Nomura, T.; Ogura, T.; Kobayashi, Y., Reversible O-O bond scission of peroxodiiron(III) to high-spin oxodiiron(IV) in dioxygen activation of a diiron center with a bis-tpa dinucleating ligand as a soluble methane monooxygenase model. *J. Am. Chem. Soc.* **2012,** *134* (32), 13236-9.
28. Xue, G.; Wang, D.; De Hont, R.; Fiedler, A. T.; Shan, X.; Munck, E.; Que, L., Jr., A synthetic precedent for the [FeIV2(mu-O)2] diamond core proposed for methane monooxygenase intermediate Q. *Proc. Natl. Acad. Sci. USA* **2007,** *104* (52), 20713-8.
29. Loiseau, T.; Serre, C.; Huguenard, C.; Fink, G.; Taulelle, F.; Henry, M.; Bataille, T.; Férey, G., A Rationale for the Large Breathing of the Porous Aluminum Terephthalate (MIL-53) Upon Hydration. *Chem. Eur. J.* **2004,** *10* (6), 1373-1382.
30. Bharti, S. K.; Roy, R., Quantitative 1H NMR spectroscopy. *TrAC Trend. Anal. Chem.* **2012,** *35*, 5-26.
31. Grunes, L. A., Study of the K Edges of 3d Transition-Metals in Pure and Oxide Form by X-Ray-Absorption Spectroscopy. *Phys. Rev. B* **1983,** *27* (4), 2111-2131.
32. Ravel, B.; Newville, M., ATHENA,ARTEMIS,HEPHAESTUS: data analysis for X-ray absorption spectroscopy using IFEFFIT. *J. Synchrotron Radiat.* **2005,** *12* (4), 537-541.
33. Momma, K.; Izumi, F., VESTA 3 for three-dimensional visualization of crystal, volumetric and morphology data. *J. Appl. Crystallogr.* **2011,** *44* (6), 1272-1276.
34. Dewitt, J. G.; Bentsen, J. G.; Rosenzweig, A. C.; Hedman, B.; Green, J.; Pilkington, S.; Papaefthymiou, G. C.; Dalton, H.; Hodgson, K. O.; Lippard, S. J., X-Ray absorption, Mossbauer, and EPR studies of the dinuclear iron center in the hydroxylase component of methane monooxygenase. *J. Am. Chem. Soc.* **1991,** *113* (24), 9219-9235.
35. Klencsar, Z., Mossbauer spectrum analysis by evolution algorithm. *Nucl. Instrum. Meth. B* **1997,** *129* (4), 527-533.
36. Stoll, S.; Schweiger, A., EasySpin, a comprehensive software package for spectral simulation and analysis in EPR. *J. Magn. Reson.* **2006,** *178* (1), 42-55.
37. Kresse, G.; Hafner, J., Ab-Initio molecular-dynamics for open-shell transition-metals. *Phys. Rev. B* **1993,** *48* (17), 13115-13118.
38. Perdew, J. P.; Burke, K.; Ernzerhof, M., Generalized gradient approximation made simple. *Phys. Rev. Lett.* **1996,** *77* (18), 3865-3868.

39. Blochl, P. E., Projector Augmented-Wave Method. *Phys. Rev. B* **1994,** *50* (24), 17953-17979.

40. Kresse, G.; Joubert, D., From ultrasoft pseudopotentials to the projector augmented-wave method. *Phys. Rev. B* **1999,** *59* (3), 1758-1775.

41. Jonsson, H.; Mills, G.; Jacobsen, K. W., Nudged elastic band method for finding minimum energy paths of transitions. In *Classical and Quantum Dynamics in Condensed Phase Simulations*, Berne, B. J.; Ciccotti, G.; Coker, D. F., Eds. **1998**, pp 385-404.

42. Belanzoni, P.; Bernasconi, L.; Baerends, E. J., O2 activation in a dinuclear Fe(II)/EDTA complex: spin surface crossing as a route to highly reactive Fe(IV)oxo species. *J. Phys. Chem. A* **2009,** *113* (43), 11926-11937.

3

Development and optimization of catalysts for mild methane oxidation

In this chapter a study to develop and further fine tune the properties of porous frameworks-based catalysts for mild methane oxidation is presented. The first part focuses on modifying catalytic properties of MIL-53(Al)-based catalysts by: 1) modification of the metal at the catalytic active center 2) modification of the substitution groups at the linker and 3) including additives in the reaction media. In the second part the use of porous organic polymers (POPs) as scaffolds to contain catalytic sites active in methane oxidation is studied. Based on these results, promising directions for further catalyst design are suggested.

3.1. Introduction

In Chapter 2 we have shown that metal-organic-based porous frameworks can be successfully used in the development of mild methane oxidation catalysts. The MIL-53(Al,Fe) catalyst, prepared by electrochemical synthesis, is able to oxidize methane to methanol in aqueous hydrogen peroxide solution with selectivity higher than 80% to oxygenates, TOF > 30 h^{-1}, showing stable catalytic performance for at least 5 catalytic runs. Although these results mark an important milestone in the development of MOF-based catalysts, it is obvious that improvement of the performance is needed. As it was mentioned in Chapter 2, the motivation to use MOFs as heterogeneous catalysts is the multitude of possibilities to fine-tune its geometric structure and functionalization of catalytic active sites they provide. Following this concept, in this chapter we investigate how the MIL-53(Al,Fe) system can be modified in order to improve its catalytic properties.

The common approach that allows the modification of MOFs is based on three strategies – 1) functionalization of organic linkers, 2) modification of inorganic nodes, or 3) inclusion of additional components in the MOF pores. [1-2] All these strategies can be performed either directly during the MOF synthesis or through post-synthetic exchange/modification of MOF building blocks.[3-6] Comparison of direct and post-synthetic approaches for the synthesis of mixed-metal MIL-53(Al,Fe) was performed in Chapter 2. It was shown that in case of post-synthetic ion exchange only a small amount of iron gets incorporated into the structure of MIL-53(Al), and the rest just forms iron oxide species in the MOF pores. On the contrary, direct introduction of the iron salt during the electrochemical MOF synthesis provides homogeneous mixed-metal samples with atomically dispersed iron species within the MOF structure and negligible formation of iron oxide. Following these results, we focused on approaches for the direct modification of MIL-53(Al) during its synthesis.

A part of this chapter is devoted to the optimisation of the parameters of liquid-phase methane oxidation reaction. To a certain extent this was already done in Chapter 2 (including the screening of different reaction times and temperatures). In this chapter we investigate the influence of pH and additional components in the reaction mixture on the catalytic performance of MIL-53(Al,Fe) catalysts.

Apart from MOFs, in this chapter we also study another type of porous framework: porous organic polymers, that are able to host isolated metal sites. In particular, we develop a methane oxidation catalyst based on

covalent triazine frameworks (CTFs) – porous organic frameworks well-known for their stability, adjustable porosity and presence of coordinating sites for transitional metals within their structure.[7] Comparing the results for MOFs and CTFs, we summarize and critically analyse the main possible directions for the further development of heterogeneous mild methane oxidation catalysts based on hybrid hosts.

3.2. Experimental section

3.2.1. Electrochemical synthesis of MOFs

The electrochemical synthesis procedure, which was described in detail in Chapter 2, is applied with minor modifications. In a typical synthesis, two aluminium electrodes are inserted in PTFT holders isolating the electrode wiring to *Autolab PGSTAT302N* potentiostat. The holders have a circular opening of 25 mm diameter to allow contact of the metal plate with the solution (4.9 cm^2). In a typical synthesis, 9 mmol linker and 0.73 g (12.5 mmol) NaCl are dissolved in 90 mL H_2O and 10 mL DMF at room temperature. A solution of 0.3 mmol transition metal salt in 9 mL H_2O and 1 mL DMF is prepared separately. The electrodes are immersed in the linker solution that is heated at 80 °C upon stirring, and a current of 20 mA is applied by the potentiostat for 4 h. During the synthesis, the transition metal solution is injected continuously using syringe pump (*Harvard Apparatus PHD 2000 RS-232*) with the speed of 0.042 mL/min while stirring. After completion, the synthesised powder is recovered by filtration and washed in 20 mL DMF under static heating (80 °C) overnight. After cooling down, the powder is again recovered and the residues of DMF are washed with methanol at 70 °C for 5 h. After recovering the powder is further dried in vacuum at 150 °C. All MOF samples reported in this work and details of their preparation are summarized in Table 3.1.

3.2.2. Synthesis of CTFs

The details of CTF catalysts preparation are summarized in Table 3.2. **CTF-10** is prepared solvothermally from 2,6-pyridinedicarbonitrile (further denoted as **pydn**), and CTF-12 is prepared from the mixture of **pydn** and 4,4'-biphenyldicarbonitrile (further denoted as **bpdn**) in a molar ratio of 1:2. In a typical synthesis, a quartz ampoule is charged with the corresponding nitriles and anhydrous metal chloride as catalyst in a molar ratio of nitriles:chloride = 1:5 inside the glovebox. The ampoule was flame sealed and heated to the desired temperature with a heating rate of 1 °C·min^{-1}, kept

Table 3.1. Metal precursors, metal content and textural properties of electrochemically synthesized MIL-53(Al)-based catalysts.

	Metal precursors	Elemental analysis	BET area, m^2/g	Total pore volume, cm^3/g	Micropore volume, cm^3/g
ECS-Fe-HL (ECS-HL)	Fe^0 dissolved in HNO_3	5.44 wt% Fe, 11.15 wt% Al	925	0.39	0.34
ECS-Fe-LL (ECS-LL)	Fe^0 dissolved in HNO_3	0.34 wt% Fe, 11.93 wt% Al	1405	0.59	0.52
ECS-Cr	$Cr(NO_3)_3•9H_2O$	2.3 wt% Fe, 11.8 wt% Al	1335	0.57	0.49
ECS-CrFe	$Fe(NO_3)_3•9H_2O$, $Cr(NO_3)_3•9H_2O$ (1:1 molar ratio)	0.72 wt% Fe, 1.00 wt% Cr, 11.20 wt% Al	1310	0.54	0.48
ECS-Co	$Co(acac)_3$	0.52 wt% Co, 13.42 wt% Al	1290	0.53	0.48
ECS-Cu	$Cu(CO_2CH_3)_2•2H_2O$	1.42 wt% Cu, 13.75 wt% Al	1110	0.47	0.41
NH2-Fe-HL	$FeCl_3•6H_2O$	3.56 wt% Fe, 12.6 wt% Al	125	0.09	0.04
NH2-Fe-LL	$FeCl_3•6H_2O$	0.68 wt% Fe, 12.8 wt% Al	200	0.11	0.07

Table 3.2. Synthesis conditions and textural properties of CTF-based catalysts.

	Precursors	Elemental analysis	BET area, m^2/g	Total pore volume, cm^3/g	Micropore volume, cm^3/g
CTF-10(Cu)	**pydn**:CuCl = 1:5	3.91 wt% Cu	1151	0.70	0.25
CTF-12(Zn)	**pydn**:**bpdn**:$ZnCl_2$ = 1:2:15	0.30 wt% Zn	1730	1.05	0.42
CTF-12(Zn)+Cu	$Cu(CH_3CN)_4PF_6$ (139 mg)	8.54 wt% Cu	1167	0.65	0.35
CTF-12(Zn)+Fe	$(NH_4)_2Fe(SO_4)_2•6H_2O$ (146 mg)	7.57 wt% Fe, 0.53 wt% Zn	925	0.44	0.33

at this temperature for 48 h and then cooled to room temperature. The product was consequently washed in 15 % HCl solution at 100 °C, in 15 % NH_4OH solution at 60 °C, in H_2O at 100 °C and finally in THF at 60 °C overnight. The resulting powder was dried under vacuum at 150 °C overnight.

3.2.3. Synthesis of CTF-12(Zn)-M catalysts

200 mg **CTF-12(Zn)** and 0.37 mmol metal salt were mixed in 20 mL methanol under constant stirring with reflux at 80 °C overnight. The resulting black solid was filtered, washed with methanol and dried in air at 80 °C.

3.2.4. Catalytic experiments

Catalytic tests and quantification of the reaction products was performed as reported in Chapter 2. In brief, 10 mL water was added together with the desired amount of catalyst in a 50 mL stainless steel autoclave fitted with a glass vessel insert (35 mL).

In a separate PE cap 530 µL 50 wt/wt % H_2O_2 solution in water was added and this cap was fitted to remain floating on top of the slurry. The closed reaction vessel was leak tested with N_2 up to 50 bar. After successful leak test the N_2 gas was evacuated and the autoclave was purged with methane 3 times consecutively to remove impurities and to finally pressurize to 30.5 bar methane for the reaction. The autoclave was heated to the desired temperature (60 °C) and mixing was started (700 rpm) when the temperature was stable. The stirring assures the beginning of the reaction because the PE cap drops when the stirrer starts moving and H_2O_2 gets in contact with the catalyst at that moment. After 1 h the reaction was rapidly cooled to 10 °C with cooling jacket and cold finger. The gas phase was collected and analysed by GC with TCD detector to determine the total content of CO_2. The catalyst was filtered from the liquid reaction mixture with 0.2 µm nylon membranes. From the liquid phase aliquots for ^{1}H-NMR and H_2O_2 titration were taken.

The experiments with Na_2SO_3 were performed under conditions similar to Hammond *et al.*[8], using a ratio of $[H_2O_2]/[Na_2SO_3] = 10$. The experiments at different pH were performed with the addition of the calculated amount of 0.05 M NaOH solution to the reaction mixture.

3.2.5. Spectroscopic characterization

DRIFTS spectra were recorded on a *Thermo Scientific Nicolet 8700* spectrometer at 423 K.

XRD was measured on a *BRUKER D8 ADVANCE* spectrometer using a Co *Kα* X-ray source (*λ* = 1.78897 Å).

N_2 physisorption was measured on a *micromeritics TriStar II* at 77 K. Prior to the measurement, the samples were weighed and degassed under N_2 flow at 423 K for 15 h.

A *JEOL JSM-6010LA* microscope was used for **SEM** and **EDS** characterization. For the measurements, the samples were placed on a carbon taped sample holder.

NMR spectra were acquired in an *Agilent-400 MR DD2* NMR spectrometer and quantified by an external standard method using glass capillary inserts (see Chapter 2).

All **EPR** measurements were carried out in continuous wave (CW) mode at *X*-band (9 GHz) and *Q*-band (34 GHz) using a commercial spectrometer *Bruker ELEXSYS E580* equipped with an Oxford flow helium cryostat and temperature control system (*T* = 4-300 K). The powdered samples were placed in the quartz tubes and measured in a broad range of magnetic field 0-1.65 T at *T* = 10-80 K. Simulations were performed using *EasySpin* toolbox for Matlab.

Elemental Analysis was performed by "*Mikroanalytischen Laboratorium Kolbe*", Germany.

3.3. Results and discussion

3.3.1. Linker functionalization

In case of MIL-53(Al,Fe) catalysts for methane oxidation, introduction of functional groups can be beneficial by either changing the properties of the active site or by providing a better access of the reactants to the active site. In the former case the most reasonable approach would be to introduce electron-donating or electron-accepting functionalities, in the latter case to make the linker more hydrophobic. In this chapter the opportunities and limitations of these strategies are discussed.

3.3.1.1. Hydrophobic linkers

Typical approaches to increase the hydrophobicity of the organic compound usually include its functionalization with halogen or alkyl groups. However, alkyl moieties can be reactive in methane oxidation conditions, so this type of functionalities should be avoided. In the row F – Cl – Br – I, halogens with higher atomic number form less stable bonds with organics, are prone to

substitution reactions, and can be oxidized more easily. Therefore, fluoride becomes the best substituent for improving the hydrophobic properties of methane oxidation catalyst.

Following this idea, we have tried to electrochemically synthesize MIL-53(Al,Fe) using commercially available tetrafluoroterephthalic acid as a linker. Unfortunately, no solid product was obtained. It should be noted that the synthesis of Al- or Fe-based MIL-53 structures with the tetrafluoroterephthalate linker has not been reported so far. The examples of tetrafluoroterephthalate-based MOFs found in literature usually contain heavy metal cations of periods 5 and 6,[9-12] indicating that synthesis of MIL-53(Al)-based MOF with tetrafluoroterephthalate is strongly hampered by sterical hindrance. So far, the best examples of fluorinated MIL-53 were reported by Biswas *et al.* who synthesized Al-based MOFs with the MIL-53 structure using mono- and difluoroterephthalate linkers.[13-14] However, the total pore volume in these MOFs is significantly lower than in the original MIL-53(Al), and it results in lower uptake of alkanes and aromatics compared to the non-functionalized analogue. According to this, we can conclude that strategies aiming to increase the hydrophobicity of the linker cannot significantly improve the catalytic performance of MIL-53(Al,Fe) catalysts.

3.3.1.2. Linkers with electron-donating groups

In order to study how the introduction of an electron-donating group influences the catalytic performance of MIL-53(Al,Fe) we have prepared amino-functionalized NH_2-MIL-53(Al,Fe) using 2-aminoterephthalic acid as a linker. Following a similar electrochemical synthesis procedure as in case of MIL-53(Al,Fe), we have obtained two amino-functionalized NH_2-MIL-53(Al,Fe) samples with iron loading of 0.68 and 3.56 wt.% of Fe, further denoted as **NH2-Fe-LL** and **NH2-Fe-HL**, respectively. The samples showed homogeneous distribution of iron in SEM and did not indicate any presence of iron oxide. When NH_2-MIL-53(Al) is prepared by hydrothermal synthesis, it adopts the narrow-pore conformation at normal conditions, showing very low pore volume and BET area in N_2 adsorption. However, in case of electrochemically synthesized **NH2-Fe-LL** and **NH2-Fe-HL** the samples were found to be porous. XRD patterns of these samples (Fig. 3.11a) indicated that they are in the large-pore conformation, similarly to electrochemically-synthesized MIL-53(Al,Fe) (Chapter 2, Fig. 2.1d). These results prove that electrochemical synthesis is beneficial for stabilizing the

large-pore conformation of the “breathing” MOFs, making them more suitable for applications in catalysis.

However, **NH2-Fe-LL** and **NH2-Fe-HL** have shown a significantly lower catalytic activity in methane oxidation than MIL-53(Al,Fe) catalysts. At the same molar loading of catalyst **NH2-Fe-LL** and **NH2-Fe-HL** demonstrate a 3 times and 6 times lower overall methane conversion compared to **ECS-Fe-LL** and **ECS-Fe-HL**, respectively (Fig. 3.1). This effect can be the result of two reasons. Firstly, the amino group reduces the pore volume, as it was observed in case of fluorinated MOFs.[13-14] MIL-53-type MOFs are so-called “breathing” frameworks, and in some cases introduction of bulky functional group can induce the transition of MOF from the narrow-pore to the large-pore conformation;[15] however, electrochemical synthesis generates highly defective MIL-53 that are present in the large-pore conformation at normal conditions,[16] so additional functionalities can only lower the space within the MOF. Secondly, hydrogen bonding between Fe-(μ-O)-M species and amino groups[17] within the structure of the MOF can make the catalyst active site inaccessible for methane molecules. Thirdly, the presence of electron-donating amino group can hamper the formation of iron species in high oxidation state (Fe^{IV}-Fe^{IV} or Fe^{V} species), necessary to oxidize methane. From this point of view, introduction of electron-accepting groups that cannot form H-bonds with the active site (nitro-, sulfo-, carboxylic groups) can be more beneficial for the catalyst improvement. However, these species have an even larger kinetic diameter than the amino group, so most probably this cannot lead to a significant improvement of the overall catalyst productivity.

The alternative solution to improve the mass transport within the MOF is the use of longer linkers, *e.g.* 2,6-naphtalenedicarboxylate and 4,4’-biphenyldicarboxylate, that are used in Al-based MOFs DUT-4 and DUT-5, respectively.[18] Unfortunately, these MOFs are chemically less stable than MIL-53(Al) and are prone to interpenetration that lowers the total pore volume.[19] However, rational design of catalysts based on these MOFs with appropriate choice of functional groups can result in new stable and highly-active catalysts for methane oxidation.

3.3.2. Influence of metal cation

MOFs with MIL-53 structure are known for several metals that have stable oxides in 3+ oxidation state (Al, Sc, Cr, Fe, etc). Electrochemical synthesis allows to synthesize mixed-metal MIL-53(Al,Fe) with homogeneously

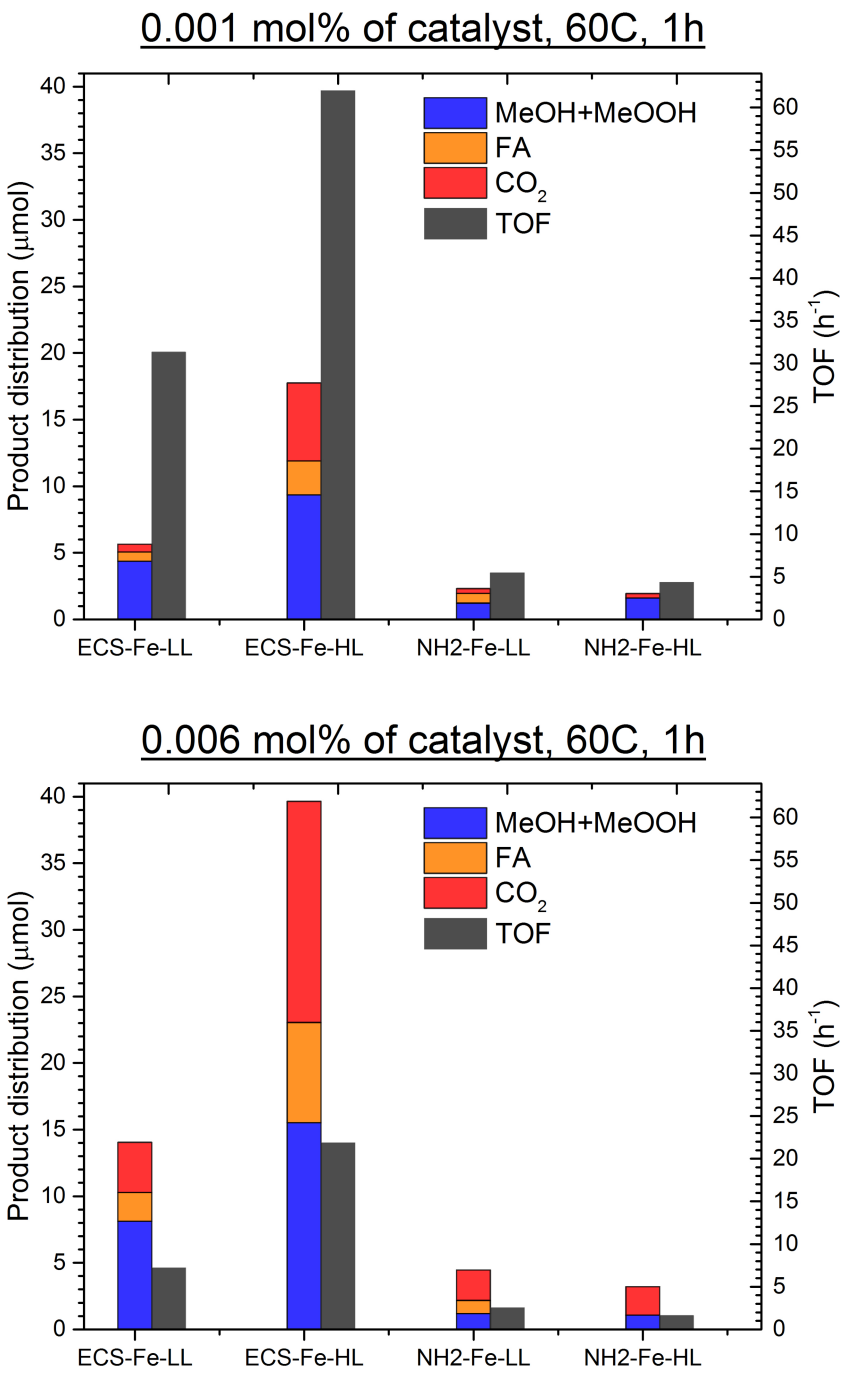

Figure 3.1. Amounts of products formed after 1 h at 60°C, 30.5 bar CH_4 with different NH_2-MIL-53(Al,Fe) and MIL-53(Al,Fe) catalysts at 0.03 mM (*top*) and 0.2 mM (*bottom*) Fe^{3+} in the reaction mixture.

distributed isolated iron sites in the MIL-53(Al) framework (see Chapter 2). The next logical step was to prepare mixed-metal MIL-53(Al,M) with other transitional metals using the advantages of electrochemical synthesis technique. Particularly interesting for catalytic applications was the introduction of Cr^{3+} and Co^{3+} as catalysts based on these metals have already been studied in a number of oxidative catalytic processes.[20-24] MIL-53 topology is not typical for cobalt MOFs, so successful incorporation of Co^{3+} in MIL-53(Al) structure makes an impact to the field of rational MOF engineering. Another promising pathway is introduction of Cu^{2+}, that forms active species in a number of zeolitic and enzymatic catalysts for methane oxidation. Due to the charge difference, direct incorporation of Cu^{2+} into MIL-53(Al) structure is challenging, but immobilization of Cu-complexes in the pores by chemical interaction [25-26] or using the “ship-in-a-bottle” strategy [3] can be a successful approach for further catalyst development.

MIL-53(Al,M) MOFs were synthesized following the protocol for MIL-53(Al,Fe) but with different sources of metals to be introduced in MIL-53(Al) structure (see Table 3.1). Below the main differences in the synthesis of these catalysts are discussed.

MIL-53(Al,Cr) (further referred as **ECS-Cr**) was successfully prepared using a chromium(III) nitrate solution. In order to investigate whether more than one type of metal cations can be introduced in MIL-53(Al) structure via electrochemical synthesis we have also prepared MIL-53(Al,Cr,Fe) sample (further referred as **ECS-CrFe**) by using the mixture of chromium(III) and iron(III) nitrates in 1:1 molar ratio.

The first attempt to prepare electrochemically MIL-53(Al,Co) using $[Co(NH_3)_6]Cl_3$ solution resulted in the material containing only traces of cobalt (Al/Co ratio = 428 according to EDS). However, the use of cobalt(III) acetylacetonate complex instead increases the Co loading in the resulting MOF more than 5 times (Al/Co ratio = 79 according to EDS; further referred as **ECS-Co**). The complexes of Co^{3+} with acetylacetonate are less stable and more bulky than ammonia complexes, so the use of $Co(acac)_3$ facilitates both the interaction of Co^{3+} with the framework and the trapping of Co-complex in the MOF pores.

For the synthesis of MIL-53(Al,Cu) (further referred as **ECS-Cu**) copper(II) acetate was used. Cu(II) forms relatively stable complexes with acetate ligands, so this precursor was chosen for the investigation of possibilities for incorporation of copper(II) in MIL-53(Al).

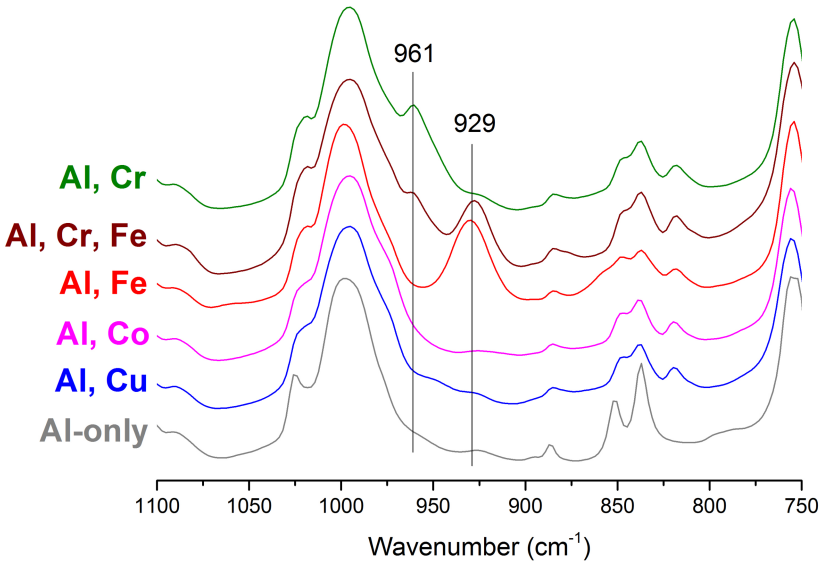

Figure 3.2. IR spectra of as-prepared MIL-53(Al,M) catalysts.

All MIL-53(Al,M) samples show a homogeneous distribution of metals in EDS (Fig. 3.9, 3.10), a high BET area and micropore volume (Table 3.1), and have an XRD pattern typical for electrochemically-synthesized MIL-53(Al) without any additional phases (Fig. 3.11b). In order to determine whether metal cations are incorporated in the MIL-53(Al) structure, the samples were characterized using DRIFTS (Fig. 3.2). The presence of (μ_2-OH) groups connected to two different metal cations in MIL-53 should result in new peaks in the range of 850-1000 cm^{-1} in the IR spectra.[27] In case of MIL-53(Al,Fe) a new peak at 929 cm^{-1}, that is not present for pure MIL-53(Al), appears. The IR study of **ECS-Cr** shows the new peak at 961 cm^{-1}, that can be attributed to Al(μ_2-OH)Cr moieties. Both these peaks are observed in case of **ECS-CrFe**, indicating that Cr and Fe can be co-incorporated.in MIL-53(Al). However, no additional peaks are present in IR spectra of **ECS-Co** and **ECS-Cu**, showing that in this case metal complexes are only trapped within the pores.

In order to further investigate the magnetic properties of **ECS-Cr** and **ECS-CrFe** these catalysts were characterized using EPR spectroscopy (Fig. 3.3). As well as in case of MIL-53(Al,Fe) (see Fig. 2.3), EPR spectra show signals from monomeric metal centres in MIL-53(Al) structure [28] and a strong temperature-dependent signal at a central magnetic field g ~ 2, that is attributed to antiferromagnetically-coupled dimers. The magnitude of

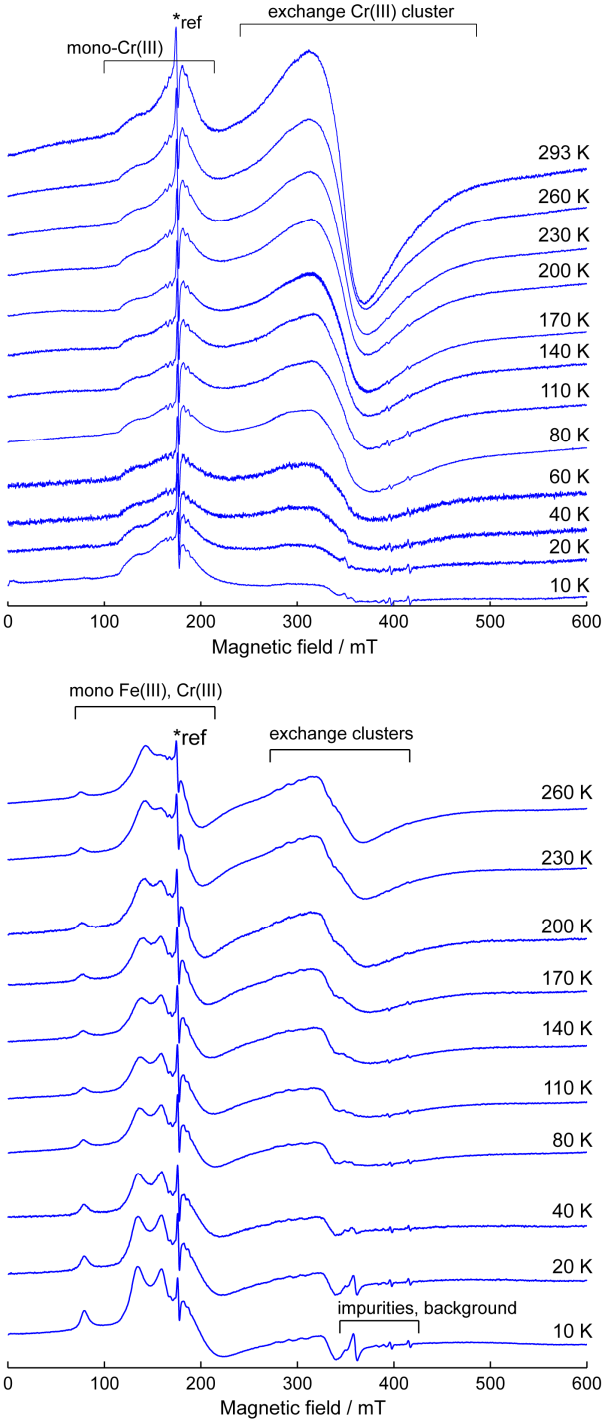

Figure 3.3. *X*-band EPR spectra of MIL-53(Al,Cr) (*top*) and MIL-53(Al,Cr,Fe) (*bottom*) at different temperatures. All spectra are normalized to the reference (*)

antiferromagnetic exchange coupling J was estimated to be $J_{eff} \sim 100 \pm 30$ cm^{-1} for both samples (Fig. 3.14), that perfectly matches with the results for MIL-53(Al,Fe) ([29], Chapter 2). Importantly, estimation of the ratio of Cr^{3+} in different types of centers for **ECS-Cr** shows that approximately 85-90% of Cr(III) ions reside in clusters, and only 10-15% – in monomers. This is markedly different from the results for **ECS-Fe-HL**, where the ratio of Fe^{3+} in monomers to Fe^{3+} in dimers was approximately 30:70, and it indicates that formation of antiferromagnetically-coupled dimers is significantly more favorable for chromium. Furthermore, simulation of EPR spectra for **ECS-CrFe** at 10 K as a superposition of monomeric Cr^{3+} and Fe^{3+} ions (Fig. 3.17) reveals that mono-Fe(III) ions are totally dominating over mono-Cr(III) ions. The rough estimation shows that only 3% of monomers are Cr(III), and 97% are Fe(III). According to this, most Cr^{3+} in **ECS-CrFe** resides as exchange coupled dimers, and most of Fe^{3+} remains as monomers.

All samples were tested as catalysts in the liquid-phase methane oxidation with H_2O_2. For all catalysts the experiments were performed at 60 °C for 1 h and with different catalyst loadings, ranging from 0.2 μmol to 2.6 μmol of metal (Cr, Cr+Fe, Fe, Co or Cu) in the reaction mixture.

Catalytic results (Fig. 3.4) show that Cr-containing samples **ECS-Cr** and **ECS-CrFe** produce the highest amounts of methanol per metal atom. Methanol productivity of **ECS-Cu** is close to the results for **ECS-Fe-HL**, but for **ECS-Co** it is significantly lower. For all catalysts production of methanol reaches a plateau at approximately 1 μmol (0.003 mol%) of catalyst in the reaction mixture, which can be the result of transport limitations within the MOF or overoxidation to CO_2 (Fig. 3.3, 3.12). **ECS-CrFe** and **ECS-Fe-HL** catalysts also show the highest production of formic acid and CO_2, but **ECS-Cr** produces substantially less over-oxidation products. **ECS-Co** generates only traces of formic acid, **ECS-Cu** does not form it at all. Nevertheless, both these catalysts produce CO_2, and its amount rapidly increases at higher catalyst loadings.

Catalytic results indicate that **ECS-CrFe** has the highest total methane conversion and **ECS-Cr** has the highest methanol selectivity, especially at high catalyst loadings (Fig. 3.13). However, reference experiments demonstrate that chromium nitrate has nearly the same activity in methane oxidation with H_2O_2 as **ECS-Cr** (Fig. 3.5). ICP analysis of filtered solutions after methane oxidation experiments shows that **ECS-Cr** and **ECS-CrFe** lose 62% and 50% of chromium, respectively, after 1 h in the reaction

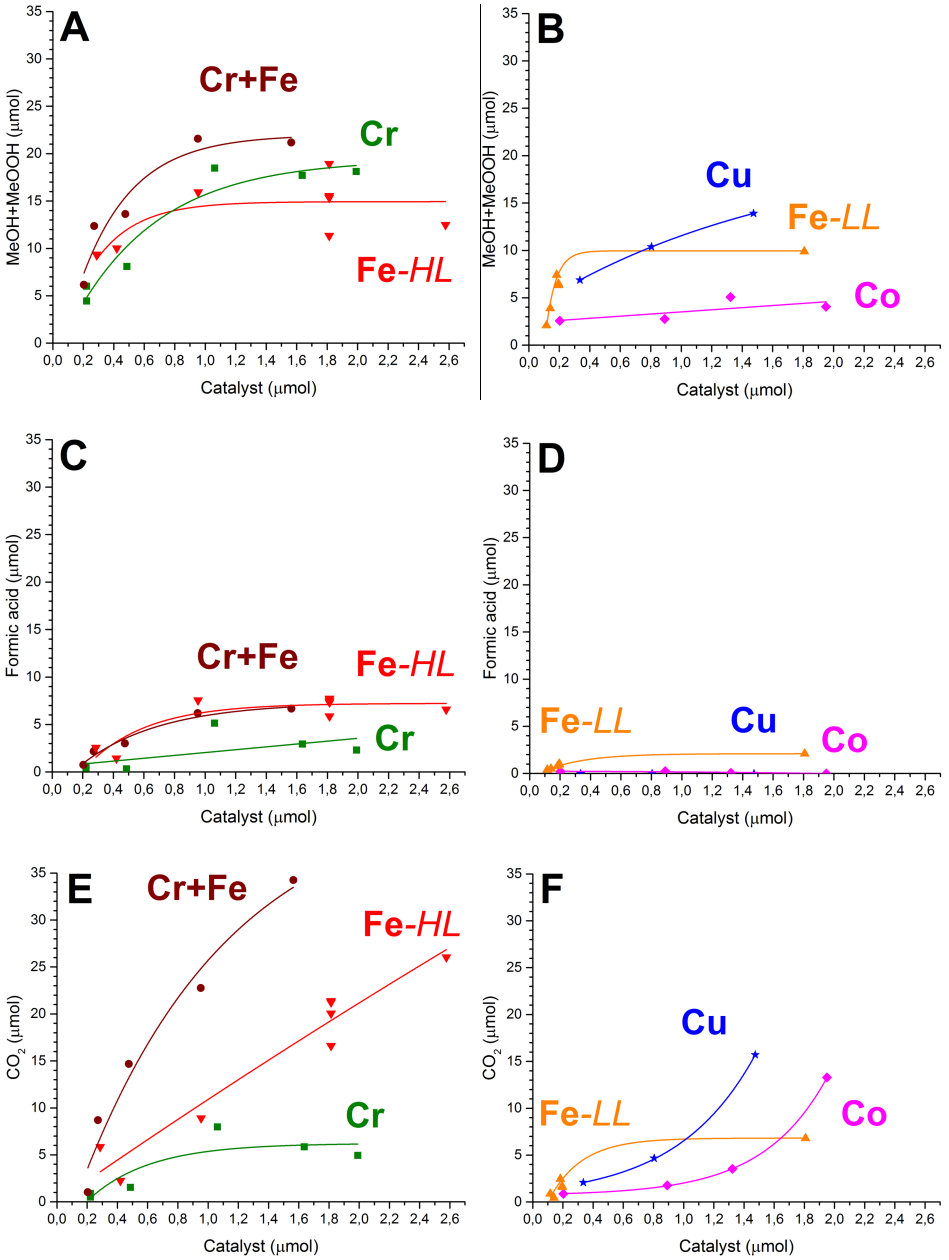

Figure 3.4. Amounts of (A, B) methanol and methyl hydroperoxide, (C, D) formic acid, and (E, F) CO_2 formed at different amounts of **ECS-Cr, ECS-CrFe, ECS-Fe-HL** (A, C, E), **ECS-Fe-LL, ECS-Co**, and **ECS-Cu** (B, D, F) after 1 h at 60 °C, 30.5 bar CH_4.

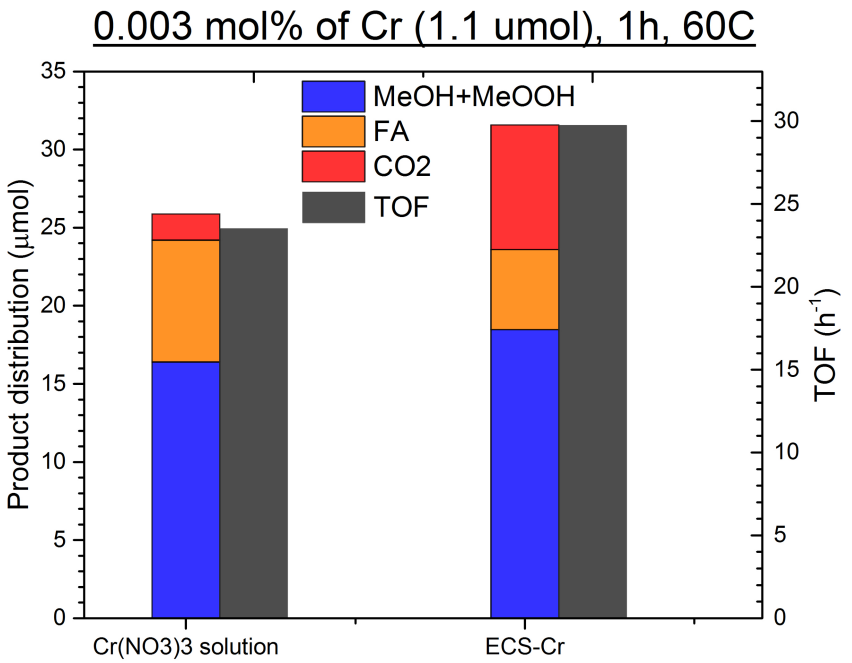

Figure 3.5. Amounts of products formed at 0.11 mM Cr^{3+} in the reaction mixture in case of **ECS-Cr** and reference $Cr(NO_3)_3$ solution after 1 h at 60 °C, 30.5 bar CH_4.

mixture (in case of **ECS-Fe-HL** less than 0.5% of Fe was lost in the same conditions). These results confirm insufficient stability of chromium species incorporated within MIL-53(Al) in H_2O_2 solutions. In this case activity of chromium-containing samples in methane oxidation should rather be attributed to formation of highly oxidative Cr^{6+} species in H_2O_2-containing media.[30] However, high selectivity towards methanol makes Cr-based catalysts promising for methane-to-methanol conversion, and finding the approaches for stabilization of active Cr species in the framework can be the further direction for development this topic.

3.3.3. Modification of the reaction conditions

One of the main concerns in the development of MOF-based catalysts for applications in aqueous media is usually the stability of the framework under reaction conditions. The framework stability determines whether the activity can be attributed to well-defined active sites within the MOF or to species formed during the framework decomposition. In case of methane oxidation with H_2O_2 using MIL-53(Al,Fe) catalyst, decomposition of the MOF can generate free Fe^{3+} ions in the solution, that should catalyse the production of free •OH radicals in the Fenton reaction [31] leading to non-selective oxidation

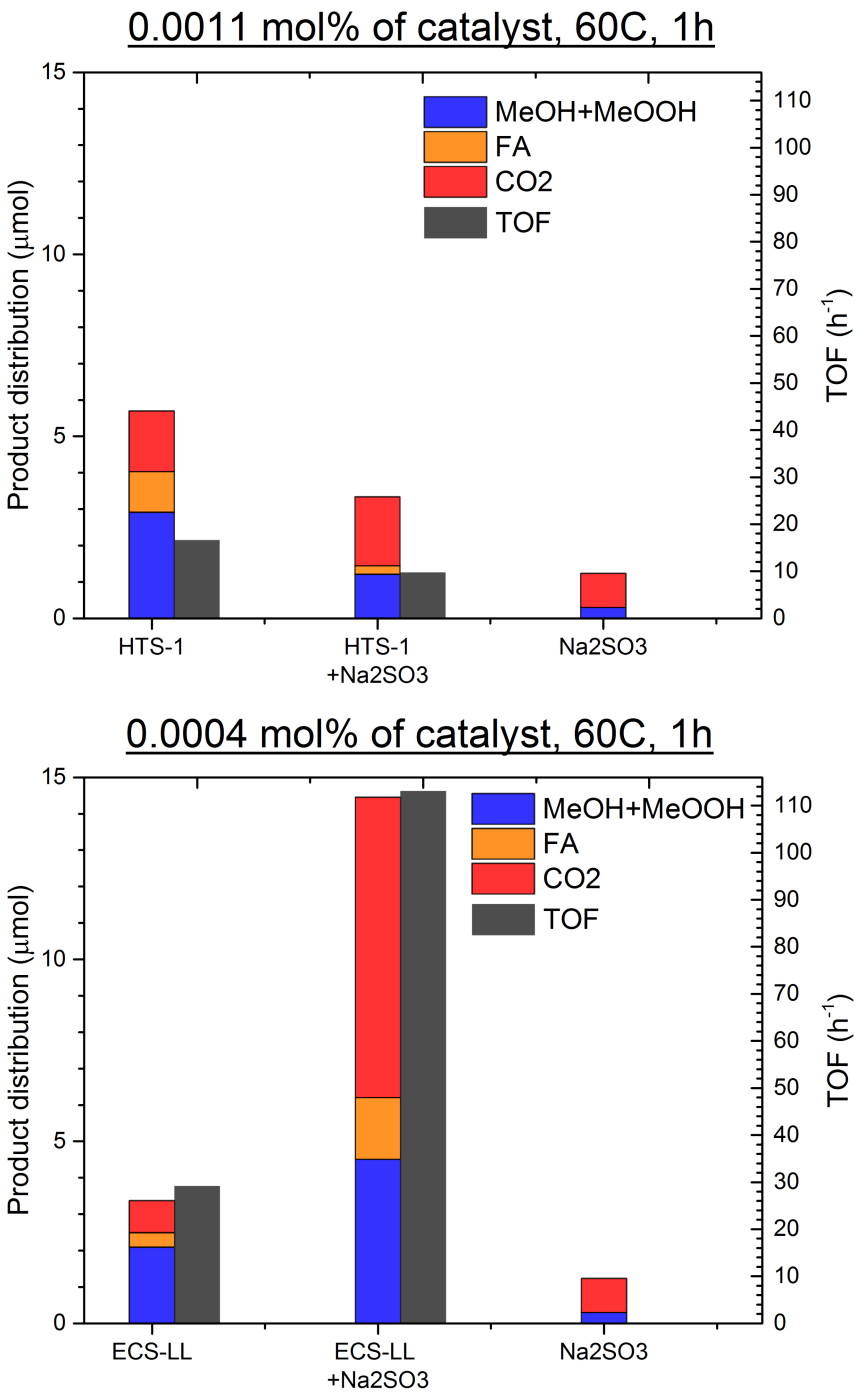

Figure 3.6. Amounts of products formed after 1 h at 60 °C, 30.5 bar CH_4 at 0.03 mM Fe^{3+} in case of **HTS-1** (*top*) and 0.01 mM Fe^{3+} in case of **ECS-LL** (*bottom*) catalysts upon addition of Na_2SO_3 ($[H_2O_2]/[Na_2SO_3]$ = 10).

processes. In the previous reports on ZSM-5 catalysts for mild methane oxidation with H_2O_2 the possibility of Fenton-type processes under reaction conditions was excluded by performing catalytic tests with the radical scavenger Na_2SO_3, that readily reacts with •OH radicals in solution.[8] When Fe^{3+} salt solution was used as a catalyst, the addition of Na_2SO_3 caused considerable decrease of activity in methane oxidation. However, in case of ZSM-5 catalyst Na_2SO_3 addition did not lead to any significant change in the overall productivity, indicating that the activity of this catalyst does not arise from the generation of free •OH radicals. The calculated reaction mechanism of methane oxidation with MIL-53(Al,Fe) (see Chapter 2) also does not imply Fenton-type processes, and estimating the impact of MOF decomposition products to the overall catalyst activity is important for the further catalyst development.

Following the results obtained for zeolites,[8] we performed methane oxidation experiments with Na_2SO_3 for MIL-53(Al,Fe) catalyst under similar reaction conditions (Fig. 3.6). For the preliminary tests we used catalysts **ECS-Fe-LL** and **HTS-1** (iron content 0.34 wt.% and 1.01 wt.%, respectively) in low catalyst loadings ([catalyst]/[H_2O_2] = $1.3 \cdot 10^{-5}$ and $3.6 \cdot 10^{-5}$, respectively). In case of **HTS-1** addition of Na_2SO_3 led to considerable decrease of the catalyst activity, indicating the significant role of free hydroxyl radicals in methane oxidation with this catalyst. This perfectly agrees with the characterization results that indicate the presence of Fe_2O_3 clusters in the pores of **HTS-1** (Fig. 2.2b, 2.8a), trapped in the pores of **HTS-1** as Fe_2O_3 works well as Fenton catalyst. However, in case of **ECS-Fe-LL** the addition of Na_2SO_3 increases the production of methanol more than two times. The overall methane conversion increases more than 3 times in this case. These effects were not observed for zeolite catalysts and were counter-intuitive as Na_2SO_3 was expected to remove highly reactive but unselective •OH species rather than generate even more reactive ones.

Reference experiments with Na_2SO_3 solution without catalyst did not show any noticeable methanol production. Looking for the possible explanation, one can think of either direct interaction of SO_3^{2-} with the catalyst or formation of species that affect the catalyst behaviour. As SO_3^{2-} is a weak acid anion, high concentrations of these species increase the pH of solution. The calculated reaction mechanism reported in Chapter 2 suggests the presence of non-coordinated carboxylic groups in the reaction active site on stages **2 – 5** (see Figure 2.9), so basic conditions can be beneficial for stabilizing these species. Following this, we performed catalytic experiments

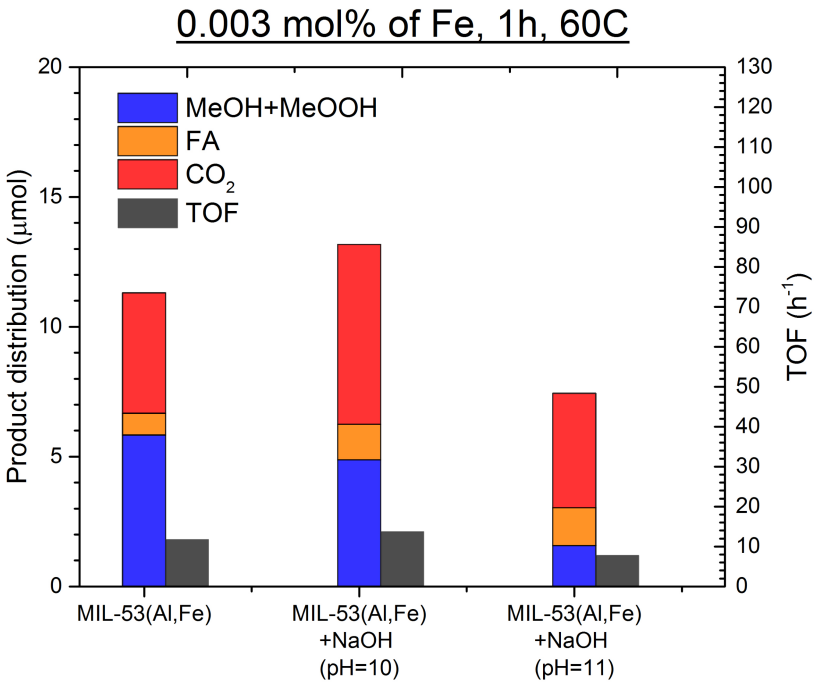

Figure 3.7. Amounts of products formed after 1 h at 60 °C, 30.5 bar CH_4 with MIL-53(Al,Fe) catalyst at 0.1 mM Fe^{3+} in the reaction mixture upon addition of NaOH.

at different pH with ECS MIL-53(Al,Fe) catalyst (1.22 wt % Fe). In these experiments the pH was controlled by addition of 0.05 M NaOH solution to the reaction mixture. However, the results show that at higher pH the catalyst activity decreases (Fig. 3.7).

Alternatively, one can think of the reactivity of SO_4^{2-} anion, the product of SO_3^{2-} oxidation. It is known that at high concentrations of H_2SO_4 and H_2O_2 highly reactive peroxomonosulfuric acid H_2SO_5 can be formed. H_2SO_5 is a strong oxidiser that readily reacts with organics. However, initial concentration of Na_2SO_3 in the reaction mixture is only 0.1 M so one can expect only traces of H_2SO_5. This can indicate that MIL-53(Al,Fe) catalyses the formation of H_2SO_5 in H_2O_2 solution, that was not observed in case of ZSM-5 catalysts and can be promising for further development of MOF-based methane oxidation catalyst.

Interaction of MIL-53(Al,Fe) catalyst with Na_2SO_3 significantly increases the methane conversion and suggests the new pathway for development of MOF-based catalysts for methane oxidation (*e.g.* by using the sulfonated MOFs [32]). However, an increased pH has a negative effect on the catalyst reactivity and should be avoided.

3.3.4. CTF-based catalysts

MOFs offer significant advantages for the development of heterogeneous catalysts with isolated metal sites for mild methane oxidation. However, other types of porous frameworks also show considerable potential for catalysis. The field of porous organic polymers (POPs) has greatly expanded in the recent decades, offering numerous types of purely organic frameworks with various functional groups within their structure, suitable for coordination of transitional metals. Among the types of polymers promising for applications in catalysis are covalent triazine frameworks (CTFs). Similar to MOFs, these materials offer adjustable porosity and functionalization, but also substantially higher chemical stability, that makes them a suitable platform for development of mild methane oxidation catalysts.

One of the first examples of POP-based catalysts for methane oxidation was developed by Palkovits *et al*. [33] as a heterogeneous mimicking of the renowned Periana catalyst.[34] By coordinating platinum chloride complexes to pyridine-functionalized CTF, the authors obtained an active and stable catalyst, that is able to produce methyl bisulfate from methane with selectivity higher than 75% and TON > 250 after 2.5 h of reaction in oleum at 215 °C. The catalyst can be recycled at least 5 times without any loss of activity. Remarkable stability and satisfying activity of this catalyst motivated us to develop Cu- and Fe-containing CTF-based catalysts for oxidation of methane with H_2O_2.

The CTF that was used by Palkovits *et al*. for their work, further denoted as **CTF-10(Zn)**, was prepared from 2,6-pyridinedicarbonitrile by trimerization of nitrile groups in solvothermal conditions with molten $ZnCl_2$ (Lewis acid catalyst) at 400 °C in a sealed ampoule. The obtained microporous material consists of pyridinic and triazinic aromatic rings that are suitable for coordination of transition metals. Although it contained traces of zinc that could not be removed, the isolated active platinum sites were successfully immobilized on the nitrogen functional sites of the CTF.

Following a similar synthetic strategy, we have modified the synthesis procedure to prepare CTF materials with improved characteristics for our purposes:

1. To improve the transport of reagents and products in the catalyst pores we prepared the new mesoporous **CTF-12(Zn)** from the mixture of 2,6-pyridinedicarbonitrile and 4,4'-biphenyldicarbonitrile. The bigger size of 4,4'-biphenyldicarbonitrile allows to obtain the larger size pores in the structure of the resulting material.

2. To exclude the influence of non-removable Zn traces we have prepared the new **CTF-10(Cu)** from 2,6-pyridinedicarbonitrile using CuCl as a catalyst. Similar to $ZnCl_2$, copper(I) chloride is widely applied in organic synthesis as a Lewis acid, and its use in CTF synthesis allows to directly prepare the CTF catalyst with coordinated copper active sites.

By coordinating iron and copper salts to **CTF-12(Zn)** we have prepared the catalysts **CTF-12(Zn)-Fe** and **CTF-12(Zn)-Cu**, respectively. All CTF catalysts, including **CTF-10(Cu),** exhibited a homogeneous metal distribution, a high thermal stability and a significant mesoporosity. XPS characterization of **CTF-10(Cu)** and **CTF-12(Zn)-Cu** shows that Cu species within the structure of CTFs are different from the initial copper salts and should be attributed to the coordinated copper species.

All CTF catalysts were tried in methane oxidation experiments at 60 °C for 1 h. Surprisingly, experiments with **CTF-12(Zn)-Fe** led to complete dissolution of the catalyst. ^{1}H NMR indicates the presence of products of CTF decomposition (*e.g.* pyridine-based compounds) in the solution. The possible explanation of this phenomenon is the Lewis acidity of Fe^{3+} that can catalyse the opening of triazine rings in CTF structure.

In case of **CTF-10(Cu)** and **CTF-12(Zn)-Cu** the catalysts were stable in the reaction conditions. However, they demonstrated a significantly lower methanol production and selectivity than the MOF-based catalyst MIL-53(Al,Cu) (Fig. 3.8). The reason of it lies in the difference between the copper species in CTFs and in more active catalytic systems. Cu-containing enzyme pMMO, Cu-containing zeolites and MIL-53(Al,Cu) include high-spin Cu^{2+} species, that have been recognized as the active sites for methane oxidation. However, coordination of Cu^{2+} to nitrogen-containing electron-donating ligands (pyridine, amines, etc.) leads to low-spin species, which are significantly less suitable for the activation of methane. This observation significantly limits the application of POPs for the development of methane oxidation catalysts as many classes of POPs contain intrinsic nitrogen functionality. However, chemical modification of POPs by introducing functional groups that form high-spin complexes with transition metals can be beneficial approach for development of POP-based methane oxidation catalysts.

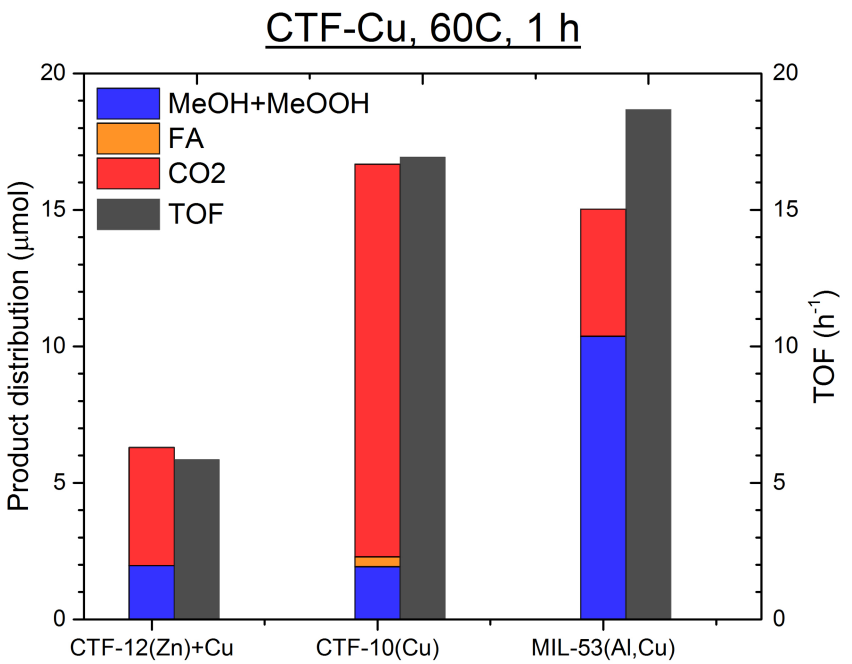

Figure 3.8. Amounts of products formed after 1 h at 60 °C, 30.5 bar CH_4 with **CTF-10(Cu), CTF-12(Zn)-Cu,** and MIL-53(Al,Cu) catalyst at 0.1 mM Cu^{2+} in the reaction mixture.

3.4. Conclusions

In this chapter we have investigated and evaluated different strategies for the development of MOF- and POP-based catalysts for mild methane oxidation with H_2O_2. Our results allow us to select the most promising pathways for further catalyst design.

The use of nitrogen-containing ligands for immobilization of Cu and Fe catalytic active sites leads to low-spin complexes, that have negative effect on the catalyst activity and selectivity towards methanol. This fact significantly limits the application of POPs as methane oxidation catalysts because most of the water-stable POPs are synthesized through C-N bond formation. However, functionalization of POPs with other functional groups that are favourable for high-spin complex formation (*e.g.* O-containing) potentially can solve this problem. From this point of view, stable O-containing MOFs are promising systems for catalytic methane oxidation.

This concept works well for electrochemically-synthesized MIL-53(Al) catalysts with incorporated Fe^{3+} species. The promising pathway for further development of these catalysts imply the use of other stable Al-based MOF types with larger pore size in order to improve the transport of products and reagents within the MOF structure. Another approach for improvement of the catalyst activity demands the introduction of electron-accepting groups in the MOF structure. These groups can stabilize the highly-oxidized Fe^{4+} species necessary for methane oxidation, increasing the total conversion of methane.

Electrochemical incorporation of other M^{3+} cations (Cr^{3+}, Ga^{3+}, Sc^{3+}, *etc*.) in MIL-53(Al) can further broaden the family of mixed-metal MIL-53 frameworks. Following this strategy, MIL-53(Al,Cr) and MIL-53(Al,Cr,Fe) MOFs were successfully synthesized. Although methane oxidation experiments with Cr-based MOFs demonstrated noticeable activity and selectivity towards methanol, low stability of these samples in H_2O_2 limits their applications in catalysis. However, finding approaches for stabilization of Cr-based active species can potentially result in new type of catalysts for selective methane oxidation to methanol.

Unfortunately, the development of MOF-based catalyst with active centers based on divalent cations (*e.g*. Cu^{2+}) is more challenging because far less water-stable MOFs based on M^{2+} cations are known up to date. A few highly stable examples [35] are constructed from linkers with coordinating nitrogen groups, that are unfavourable for generation of high-spin active centres. However, inclusion of stable high-spin M^{2+} complexes in the MOF pores can be beneficial for this type of catalysts.

The strategy aiming to improve the methane oxidation activity of MIL-53(Al)-based catalysts by making the framework more hydrophobic (*e.g*. by using fluorinated derivatives of terephthalic acid as linkers) has no prospect of success because the replacement of hydrogen atom for fluorine decreases the pore volume, eliminating the advantage of a higher hydrophobicity. However, this approach can be useful for MOFs with larger pore sizes. Introduction of electron-accepting functional groups into the MOF structure can also have positive effect on catalyst activity, but one has to be sure that these additional functionalities do not block the active site due to hydrogen bonding or other effects.

3.5. Appendix

3.5.1. SEM-EDS analysis

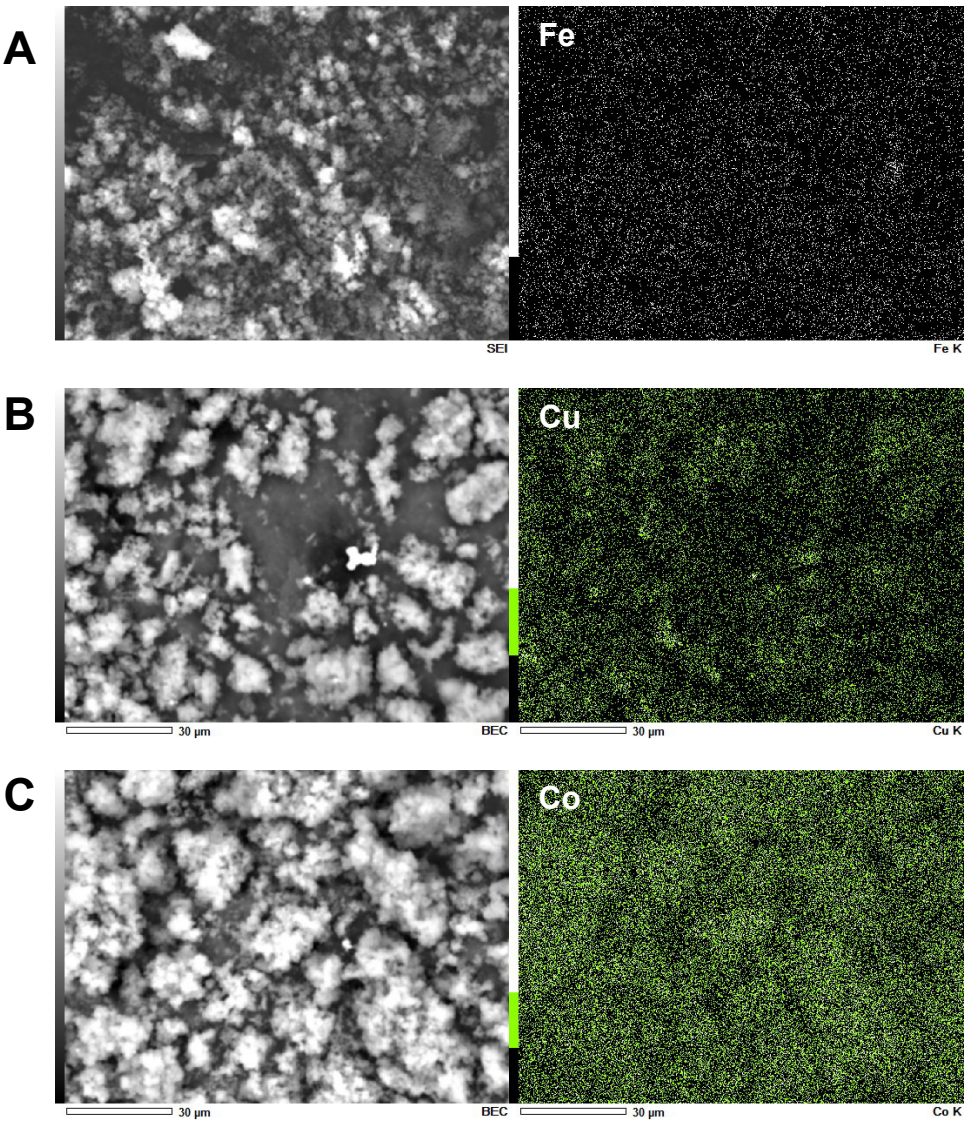

Figure 3.9. SEM images (*left*) and EDS mapping (*right*) of Fe for **NH2-HL** (A), Cu for MIL-53(Al,Cu) (B) and Co for MIL-53(Al,Co) (C).

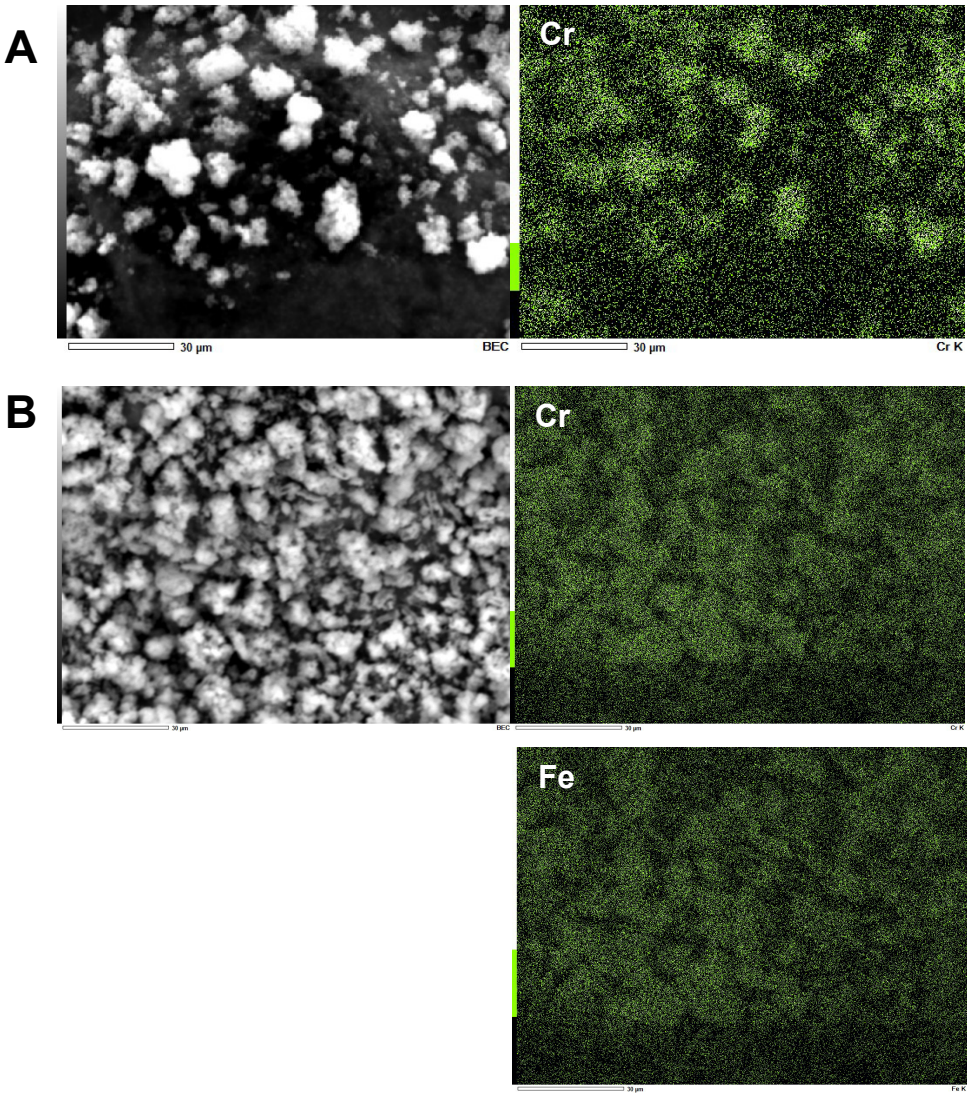

Figure 3.10. SEM images (*left*) and EDS mapping (*right*) of Cr and Fe for MIL-53(Al,Cr) (A) and MIL-53(Al,Cr,Fe) (B).

3.5.2. XRD analysis

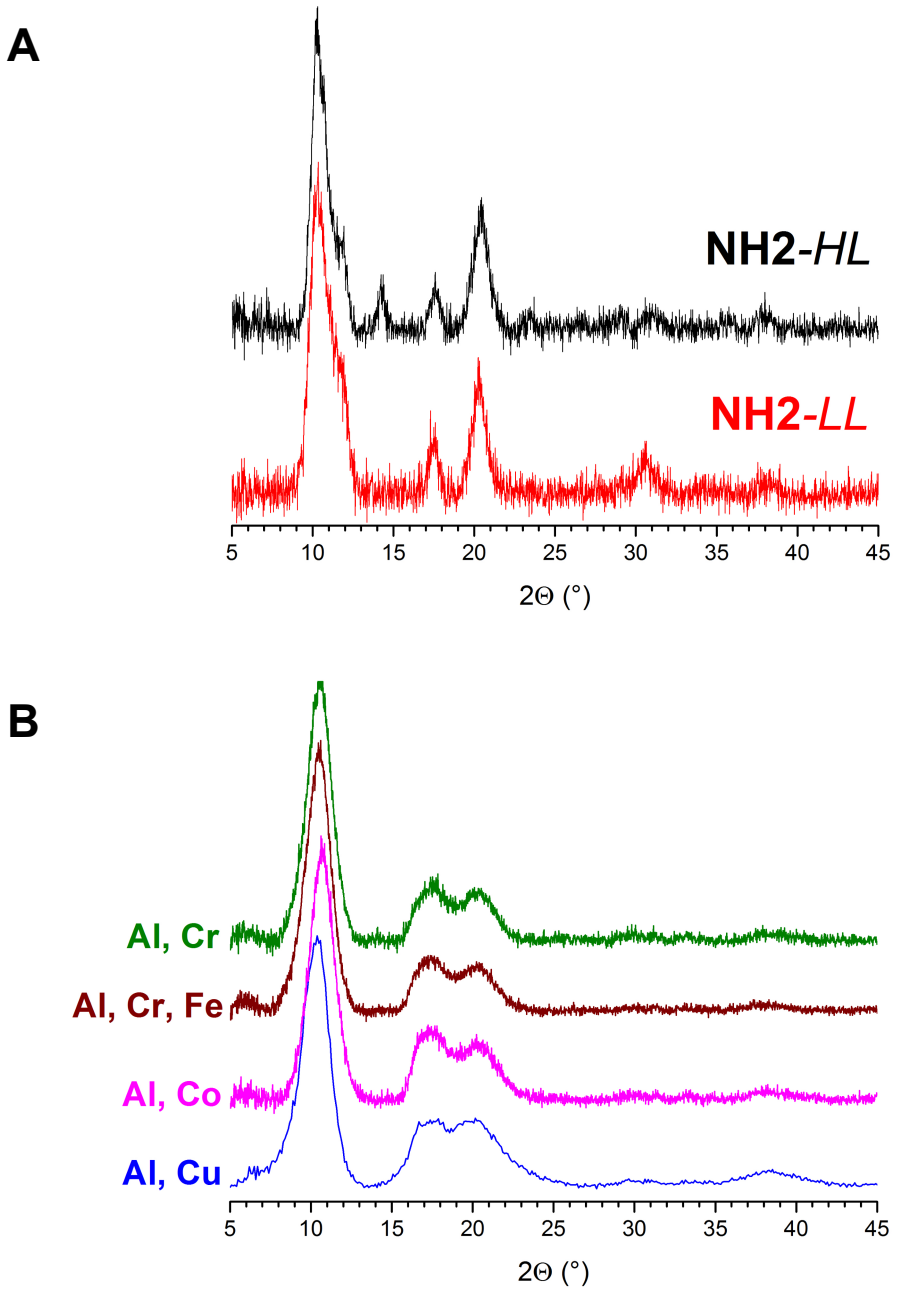

Figure 3.11. XRD patterns for (A) **NH2-HL** and **NH2-LL,** (B) MIL-53(Al,Cr), MIL-53(Al,Cr,Fe), MIL-53(Al,Co) and MIL-53(Al,Cu).

3.5.3. Raman spectroscopy

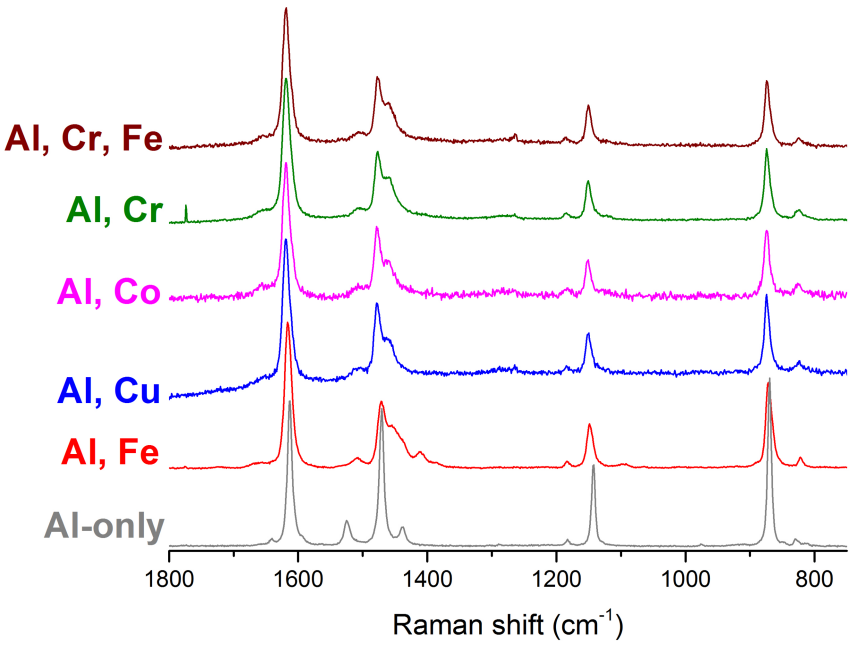

Figure 3.12. Raman spectra for electrochemically-synthesized MIL-53(Al,Cr,Fe), MIL-53(Al,Cr), MIL-53(Al,Co) MIL-53(Al,Cu), MIL-53(Al,Fe)-HL and hydrothermally-synthesized MIL-53(Al).

3.5.4. Catalysis results

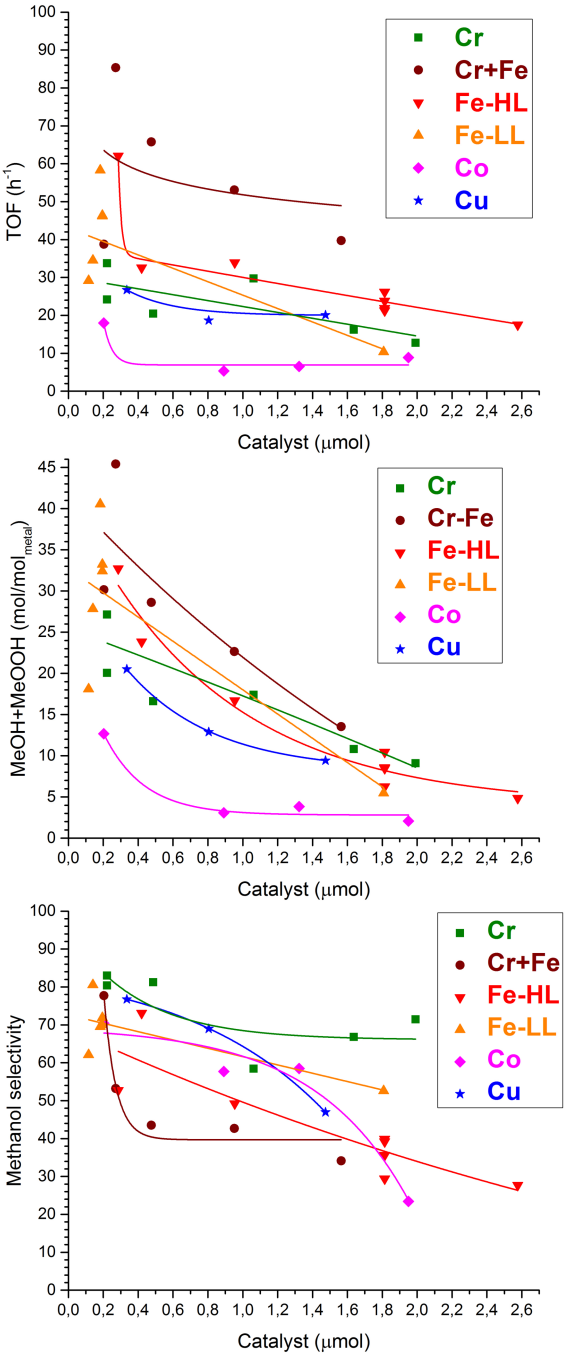

Figure 3.13. TOFs (*top*), methanol productivity (*middle*) and methanol selectivity (*bottom*) for MIL-53(Al,Cr,Fe), MIL-53(Al,Cr), MIL-53(Al,Co), MIL-53(Al,Cu) and MIL-53(Al,Fe) catalysts.

3.5.5. EPR analysis

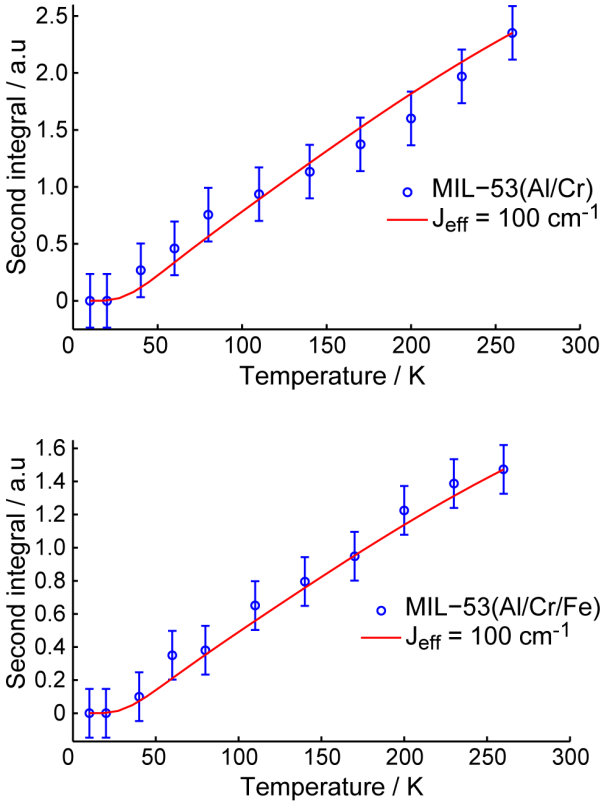

Figure 3.14. The intensity of EPR signal of exchange-coupled cluster in MIL-53(Al,Cr) (*top*) and MIL-53(Al,Cr,Fe) (*bottom*) vs. temperature. The data points are obtained based on *X*-band data (Fig. 3.3). Red curve shows the simulation using Boltzman fit with $J \sim 100$ cm^{-1}.

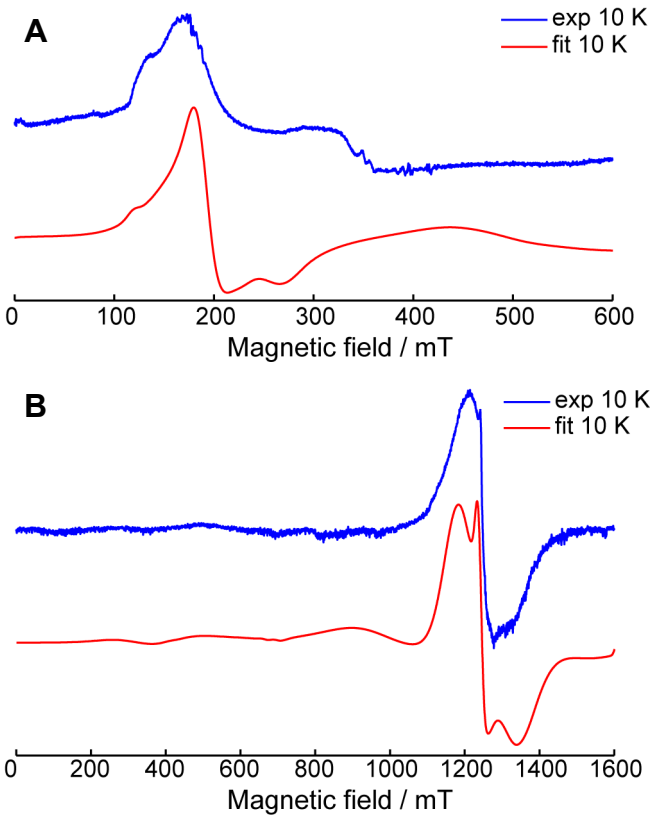

Figure 3.15. Experimental spectra (*blue*) and simulation (*red*) of EPR signals from mono-Cr(III) ions of MIL-53(Al,Cr) at (A) *X*- and (B) *Q*-bands. The parameters of Cr(III) ions are close to the reported values,[28] but are not exactly the same. D = 8.3 GHz (0.28 cm^{-1}), E = 0.8 GHz (0.027 cm^{-1}), g = 1.976.

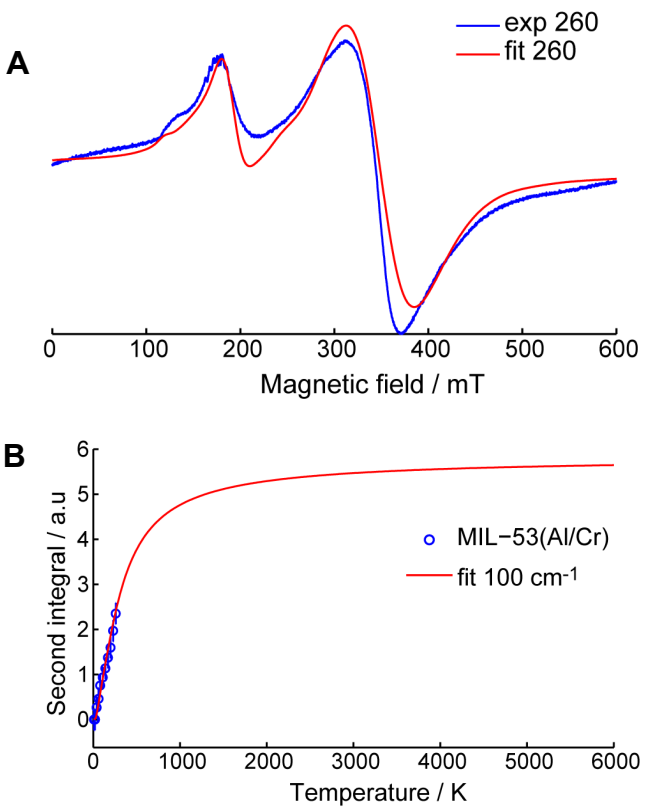

Figure 3.16. (A) Experimental spectrum (*blue*) and simulation (*red*) of *X*-band EPR spectrum of MIL-53(Al,Cr) at 260 K using two components – mono-Cr(III) (signal around 170 mT) and Cr(III)-Cr(III) dimer (signal around 350 mT). (B) Boltzman extrapolation (*red*) of theoretical curve shown in Fig. 3.14 to infinite temperatures. At infinite temperatures the curve saturates and the magnetization becomes proportional just to a number of spins.

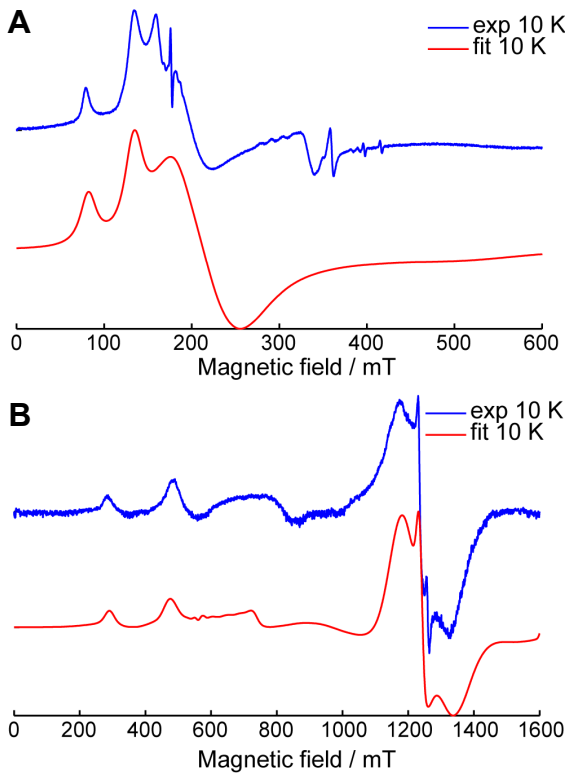

Figure 3.17. Experimental spectrum (*blue*) and simulation (*red*) of EPR signals from mono-Cr(III) + mono-Fe(III) ions of MIL-53(Al,Cr,Fe) at (A) *X*- and (B) *Q*-bands. The contributions from Cr(III) and Fe(III) are 0.03 and 0.97, respectively. The parameters of signal from Cr(III) ions are the same as those in Fig. 3.15 above. The parameters of Fe(III) are the same as those used by us previously for MIL-53(Al,Fe), viz. D = 1.13 cm^{-1}, E = 0.18 cm^{-1}, g = 1.95.

3.6. References

1. Gascon, J.; Corma, A.; Kapteijn, F.; Llabrés i Xamena, F. X., Metal Organic Framework Catalysis: Quo vadis? *ACS Catalysis* **2014,** *4* (2), 361-378.
2. Corma, A.; García, H.; Llabrés i Xamena, F. X., Engineering Metal Organic Frameworks for Heterogeneous Catalysis. *Chemical Reviews* **2010,** *110* (8), 4606-4655.
3. Juan-Alcañiz, J.; Gascon, J.; Kapteijn, F., Metal-organic frameworks as scaffolds for the encapsulation of active species: State of the art and future perspectives. *Journal of Materials Chemistry* **2012,** *22* (20), 10102-10119.
4. Kim, M.; Cahill, J. F.; Fei, H.; Prather, K. A.; Cohen, S. M., Postsynthetic Ligand and Cation Exchange in Robust Metal-Organic Frameworks. *Journal of the American Chemical Society* **2012,** *134* (43), 18082-18088.
5. Lescouet, T.; Kockrick, E.; Bergeret, G.; Pera-Titus, M.; Aguado, S.; Farrusseng, D., Homogeneity of flexible metal-organic frameworks containing mixed linkers. *Journal of Materials Chemistry* **2012,** *22* (20), 10287-10293.
6. Nasalevich, M. A.; Becker, R.; Ramos-Fernandez, E. V.; Castellanos, S.; Veber, S. L.; Fedin, M. V.; Kapteijn, F.; Reek, J. N. H.; Van Der Vlugt, J. I.; Gascon, J., Co@NH2-MIL-125(Ti): Cobaloxime-derived metal-organic framework-based composite for light-driven H2 production. *Energy and Environmental Science* **2015,** *8* (1), 364-375.
7. Kuhn, P.; Thomas, A.; Antonietti, M., Toward tailorable porous organic polymer networks: A high-temperature dynamic polymerization scheme based on aromatic nitriles. *Macromolecules* **2009,** *42* (1), 319-326.
8. Hammond, C.; Jenkins, R. L.; Dimitratos, N.; Lopez-Sanchez, J. A.; Ab Rahim, M. H.; Forde, M. M.; Thetford, A.; Murphy, D. M.; Hagen, H.; Stangland, E. E.; Moulijn, J. M.; Taylor, S. H.; Willock, D. J.; Hutchings, G. J., Catalytic and mechanistic insights of the low-temperature selective oxidation of methane over Cu-promoted Fe-ZSM-5. *Chemistry - A European Journal* **2012,** *18* (49), 15735-15745.
9. Al-Terkawi, A. A.; Scholz, G.; Emmerling, F.; Kemnitz, E., Mechanochemical Synthesis, Characterization, and Structure Determination of New Alkaline Earth Metal-Tetrafluoroterephthalate Frameworks: Ca(pBDC-F4)·4H2O, Sr(pBDC-F4)·4H2O, and Ba(pBDC-F4). *Crystal Growth and Design* **2016,** *16* (4), 1923-1933.
10. Chen, B.; Yang, Y.; Zapata, F.; Qian, G.; Luo, Y.; Zhang, J.; Lobkovsky, E. B., Enhanced near-infrared-luminescence in an erbium tetrafluoroterephthalate framework. *Inorganic Chemistry* **2006,** *45* (22), 8882-8886.

11. Defuria, M. D.; Zeller, M.; Genna, D. T., Removal of Pharmaceuticals from Water via π-π Stacking Interactions in Perfluorinated Metal-Organic Frameworks. *Crystal Growth and Design* **2016,** *16* (6), 3530-3534.

12. MacNeill, C. M.; Day, C. S.; Marts, A.; Lachgar, A.; Noftle, R. E., Synthesis, crystal structure and properties of novel isostructural two-dimensional lanthanide-based coordination polymers with 2,3,5,6-tetrafluoro- 1,4-benzenedicarboxylic acid. *Inorganica Chimica Acta* **2011,** *365* (1), 196-203.

13. Biswas, S.; Couck, S.; Denysenko, D.; Bhunia, A.; Grzywa, M.; Denayer, J. F. M.; Volkmer, D.; Janiak, C.; Van Der Voort, P., Sorption and breathing properties of difluorinated MIL-47 and Al-MIL-53 frameworks. *Microporous and Mesoporous Materials* **2013,** *181*, 175-181.

14. Biswas, S.; Rémy, T.; Couck, S.; Denysenko, D.; Rampelberg, G.; Denayer, J. F. M.; Volkmer, D.; Detavernier, C.; Van Der Voort, P., Partially fluorinated MIL-47 and Al-MIL-53 frameworks: Influence of functionalization on sorption and breathing properties. *Physical Chemistry Chemical Physics* **2013,** *15* (10), 3552-3561.

15. Devic, T.; Horcajada, P.; Serre, C.; Salles, F.; Maurin, G.; Moulin, B.; Heurtaux, D.; Clet, G.; Vimont, A.; Grenéche, J. M.; Le Ouay, B.; Moreau, F.; Magnier, E.; Filinchuk, Y.; Marrot, J.; Lavalley, J. C.; Daturi, M.; Férey, G., Functionalization in flexible porous solids: Effects on the pore opening and the host-guest interactions. *Journal of the American Chemical Society* **2010,** *132* (3), 1127-1136.

16. Martinez Joaristi, A.; Juan-Alcañiz, J.; Serra-Crespo, P.; Kapteijn, F.; Gascon, J., Electrochemical synthesis of some archetypical Zn 2+, Cu 2+, and Al 3+ metal organic frameworks. *Crystal Growth and Design* **2012,** *12* (7), 3489-3498.

17. Stavitski, E.; Pidko, E. A.; Couck, S.; Remy, T.; Hensen, E. J. M.; Weckhuysen, B. M.; Denayer, J.; Gascon, J.; Kapteijn, F., Complexity behind CO2 capture on NH2-MIL-53(Al). *Langmuir* **2011,** *27* (7), 3970-3976.

18. Senkovska, I.; Hoffmann, F.; Fröba, M.; Getzschmann, J.; Böhlmann, W.; Kaskel, S., New highly porous aluminium based metal-organic frameworks: Al(OH)(ndc) (ndc = 2,6-naphthalene dicarboxylate) and Al(OH)(bpdc) (bpdc = 4,4′-biphenyl dicarboxylate). *Microporous and Mesoporous Materials* **2009,** *122* (1-3), 93-98.

19. Marshall, R. J.; Lennon, C. T.; Tao, A.; Senn, H. M.; Wilson, C.; Fairen-Jimenez, D.; Forgan, R. S., Controlling interpenetration through linker conformation in the modulated synthesis of Sc metal-organic frameworks. *Journal of Materials Chemistry A* **2018,** *6* (3), 1181-1187.

20. Das, B. K.; Clark, J. H., A novel immobilised cobalt() oxidation catalyst. *Chem. Commun.* **2000,** (7), 605-606.

21. Feenan, J. J.; Anderson, R. B.; Swan, H. W.; Hofer, L. J. E., Chromium Catalysts for Oxidizing Automotive Exhaust. *Journal of the Air Pollution Control Association* **1964,** *14* (4), 113-117.

22. Pope, D.; Walker, D. S.; Moss, R. L., Preparation of cobalt oxide catalysts and their activity for CO oxidation at low concentration. *Journal of Catalysis* **1977,** *47* (1), 33-47.

23. Subrahmanyam, C.; Louis, B.; Rainone, F.; Viswanathan, B.; Renken, A.; Varadarajan, T. K., Catalytic oxidation of toluene with molecular oxygen over Cr-substituted mesoporous materials. *Applied Catalysis A: General* **2003,** *241* (1), 205-215.

24. Yim, S. D.; Chang, K.-H.; Nam, I.-S., Deactivation of Chromium Oxide Catalyst for the Removal of Perchloroethylene (PCE). In *Studies in Surface Science and Catalysis*, Spivey, J. J.; Roberts, G. W.; Davis, B. H., Eds. Elsevier: **2001**, pp 173-180.

25. Bloch, E. D.; Britt, D.; Lee, C.; Doonan, C. J.; Uribe-Romo, F. J.; Furukawa, H.; Long, J. R.; Yaghi, O. M., Metal insertion in a microporous metal-organic framework lined with 2,2′-bipyridine. *Journal of the American Chemical Society* **2010,** *132* (41), 14382-14384.

26. Bunchuay, T.; Ketkaew, R.; Chotmongkolsap, P.; Chutimasakul, T.; Kanarat, J.; Tantirungrotechai, Y.; Tantirungrotechai, J., Microwave-assisted one-pot functionalization of metal-organic framework MIL-53(Al)-NH2 with copper(ii) complexes and its application in olefin oxidation. *Catalysis Science & Technology* **2017,** *7* (24), 6069-6079.

27. Nouar, F.; Devic, T.; Chevreau, H.; Guillou, N.; Gibson, E.; Clet, G.; Daturi, M.; Vimont, A.; Grenèche, J. M.; Breeze, M. I.; Walton, R. I.; Llewellyn, P. L.; Serre, C., Tuning the breathing behaviour of MIL-53 by cation mixing. *Chem. Commun.* **2012,** *48* (82), 10237-10239.

28. Mendt, M.; Jee, B.; Stock, N.; Ahnfeldt, T.; Hartmann, M.; Himsl, D.; Pöppl, A., Structural phase transitions and thermal hysteresis in the metal-organic framework compound MIL-53 as studied by electron spin resonance spectroscopy. *Journal of Physical Chemistry C* **2010,** *114* (45), 19443-19451.

29. Osadchii, D. Y.; Olivos-Suarez, A. I.; Szécsényi, Á.; Li, G.; Nasalevich, M. A.; Dugulan, I. A.; Crespo, P. S.; Hensen, E. J. M.; Veber, S. L.; Fedin, M. V.; Sankar, G.; Pidko, E. A.; Gascon, J., Isolated fe sites in metal organic frameworks catalyze the direct conversion of methane to methanol. *ACS Catalysis* **2018,** *8* (6), 5542-5548.

30. Miscellaneous uses for hydrogen peroxide technology. In *Applications of Hydrogen Peroxide and Derivatives*, Jones, C. W.; Clark, J. H., Eds. The Royal Society of Chemistry: **1999**, pp 231-256.

31. Hayyan, M.; Hashim, M. A.; Alnashef, I. M., Superoxide Ion: Generation and Chemical Implications. *Chemical Reviews* **2016,** *116* (5), 3029-3085.

32. Goesten, M. G.; SzÃ©csÃ©nyi, Ã.; De Lange, M. F.; Bavykina, A. V.; Gupta, K. B. S. S.; Kapteijn, F.; Gascon, J., Sulfonated Porous Aromatic Frameworks as Solid Acid Catalysts. *ChemCatChem* **2016,** *8* (5), 961-967.

33. Palkovits, R.; Antonietti, M.; Kuhn, P.; Thomas, A.; Schüth, F., Solid catalysts for the selective low-temperature oxidation of methane to methanol. *Angewandte Chemie - International Edition* **2009,** *48* (37), 6909-6912.

34. Periana, R. A.; Taube, D. J.; Gamble, S.; Taube, H.; Satoh, T.; Fujii, H., Platinum catalysts for the high-yield oxidation of methane to a methanol derivative. *Science* **1998,** *280* (5363), 560-564.

35. Burtch, N. C.; Jasuja, H.; Walton, K. S., Water stability and adsorption in metal-organic frameworks. *Chemical Reviews* **2014,** *114* (20), 10575-10612.

4

X-ray techniques for characterization of carbon-based catalysts

In this chapter benefits and pitfalls of using X-ray Photoelectron Spectroscopy (XPS) for characterization of heterogeneous catalysts are discussed. Three Case studies demonstrate applicability of XPS for characterization of different types of carbon-based catalysts and materials (carbon nanotubes, nitrogen-doped amorphous carbons with cobalt sites, and a nitrogen-containing polymer with nickel sites). Based on these examples, a general strategy for characterization of carbon-based catalysts is described and details of sample preparation and analysis with XPS are discussed.

This chapter is based on the following publications:

Metal–Organic Framework Mediated Cobalt/Nitrogen-Doped Carbon Hybrids as Efficient and Chemoselective Catalysts for the Hydrogenation of Nitroarenes.
X. Sun, A.I. Olivos-Suarez, L. Oar-Arteta, E. Rozhko, D. Osadchii, A. Bavykina, F. Kapteijn, J. Gascon, *ChemCatChem (2017), 9, 10, 1854.*

Single Cobalt Sites in Mesoporous N-Doped Carbon Matrix for Selective Catalytic Hydrogenation of Nitroarenes.
X. Sun, A.I. Olivos-Suarez, D. Osadchii, M.J.V. Romero, F. Kapteijn, J. Gascon, *J. Catal. (2018), 357, 20.*

Covalent organic frameworks as supports for a molecular Ni based ethylene oligomerization catalyst for the synthesis of long chain olefins.
E. Rozhko, A. Bavykina, D. Osadchii, M. Makkee, J. Gascon, *J. Catal. (2017), 345, 270.*

4.1 Introduction

Carbon-based materials play an indispensable role in various fields of science and technology, but characterization of their chemical states still remains challenging in many cases. For a broad range of amorphous carbonaceous materials on the edge of organic and inorganic chemistry the characterization toolbox set is not large enough as chemical states of carbon turn out to be similar for many spectroscopic tools. X-ray photoelectron spectroscopy (XPS) enables characterizing chemical states of carbon and other elements simultaneously. Due to its surface sensitivity and relative incidence XPS has become one of the most common and important characterization methods, especially in heterogeneous catalysis. However, due to the limitations of this method, it is important to adequately combine XPS with other characterization techniques.

In this chapter the approaches to use XPS for characterization of carbon-based catalysts are discussed. The material is organised in a form of Case studies, describing different types of heterogeneous catalysts which mainly consist of carbon. Starting from relatively simple, purely carbon-based materials (carbon nanotubes) in Case study I, we expand it to the field of nitrogen-doped carbons with various cobalt species (Case study II) and nitrogen-containing organic polymers with coordinated nickel active sites (Case study III). The increasing complexity of the investigated systems allows to show in detail which information could be obtained solely from XPS and which arises from multidimensional characterization of samples.

Case study I discusses the details of sample preparation and XP spectra analysis in routine XPS characterization, using commercial carbon nanotubes as an example. Careful fitting of C*1s* and O*1s* lines with reasonable parameters allows to describe quantitatively the nature of surface species in this sample.

Case study II is devoted to heterogeneous catalysts for selective reduction of nitroarenes into the corresponding amines.[1-3] One of the recent successful approaches to obtain stable and active hydrogenation catalysts consists in preparing it by pyrolysis of nitrogen-containing cobalt complexes or metal-organic frameworks (MOFs) in inert atmosphere.[3-4] In these conditions the initial material transforms into the N-doped carbon (NC) with embedded cobalt species. However, the nature of their actual active sites still remains debatable because cobalt in the samples resides in a range of different forms including cobalt nanoparticles and atomically dispersed cobalt species.[4-5] An additional problem in characterization of these

catalysts is that most of cobalt is not accessible to the reaction media due to its encapsulation by graphite shells, which are formed under the synthesis conditions. In order to investigate separately the properties of these cobalt species, the series of model Co@NC catalysts were prepared by pyrolysis of Co-containing MOF ZIF-67 (cobalt(II) 2-methylimidazolate), following the reported synthesis procedure.[4] Extensive XPS characterization of different Co@NC catalysts in combination with TEM, XAS and other techniques shows how changes of pyrolysis temperature, cobalt acid leaching, dilution of cobalt and use of templating agents influences the ratio of cobalt and nitrogen species in the samples with effect on their catalytic activity.

Case study III describes heterogeneous Ni-based catalyst, mimicking diimine and iminopyridine complexes of nickel for ethylene oligomerization (EO) into C_4-C_{20} *α*-olefins.[6-7] The catalyst was prepared by coordination of a nickel salt to an imine-linked polymer network (IL-PON), which contains diiminopyridine moieties within its structure. Combination of XPS with TEM and XAS allows to study deeper the coordination environment of nickel in the catalyst, showing whether nickel is coordinated to nitrogen species of the framework, bonded to bromide ions of the precursor, or starts forming nickel oxide particles.

The Case studies in this Chapter show which information can XPS provide regarding the quantification of surface species of an element in different oxidation states and in the same oxidation state but in different chemical environment. In cases when the information that could be obtained solely from XPS is not sufficient, it is shown how combination of XPS with other methods could help distinguishing similar chemical states. Focusing on the details of sample preparation, XPS data acquisition procedure and data analysis, an overview is given of common problems researchers usually face and mistakes they make when performing XPS experiments and performing data analysis. The described observations and practical details can be valuable for the researchers in catalysis or spectroscopists working with similar types of materials.

4.2. Experimental

4.2.1. Synthesis of materials

4.2.1.1. Case study I

Commercial carbon nanotubes (Hyperion CS-02C-063-XD) were used as received for the analysis. The sample is further denoted as ***1*** (see Table 4.1).

4.2.1.2. Case study II

The detailed procedure of catalyst synthesis is described elsewhere.[8-9] In brief, series of Co@NC catalysts were synthesized by carbonization of metal-organic framework ZIF-67 under N_2 flow at 600, 700, or 800 °C (samples ***2, 3,*** and ***4,*** respectively; see Table 4.1). Acid-leached samples ***2a, 3a,*** and ***4a*** were prepared by immersing of corresponding Co@NC catalysts in 0.5 M hydrochloric acid solution for 24 h at ambient temperature, repeated three times. Catalyst ***6*** was prepared from bimetallic MOF ***5*** with Zn^{2+}/Co^{2+} molar ratio of 25. ***5*** was impregnated with tetramethyl orthosilicate (TMOS) and exposed to a wet N_2 stream in order to convert TMOS into SiO_2. Resulting material was pyrolyzed at 900 °C for 4 h under N_2 and further leached in 1 M sodium hydroxide solution for 24 h to remove the SiO_2 template.

4.2.1.2. Case study III

The detailed procedure of catalyst synthesis is described elsewhere.[10] In brief, the IL-PON support ***7*** was prepared by mixing 10 mL DMSO solutions of *2,6*-pyridinedicarboxaldehyde and *1,3,5*-tris(*4*-aminophenyl)benzene in molar ratio 3:2 upon addition of 1 mL 99.8% acetic acid. For the synthesis of ***8*** a mixture of 0.2 g ***7*** and 0.1 g nickel(II) bromide ethylene glycol dimethyl ether (DME•$NiBr_2$) in THF was stirred at 67 °C overnight and filtered.

4.2.2. Spectroscopic characterization

XPS measurements were performed on a *K-alpha Thermo Fisher Scientific* spectrometer using a monochromatic Al *Kα* X-ray source. The spectrometer is equipped with 180° double focusing hemispherical analyzer with 128-channel detector. In a typical experiment, the holder with the mounted samples was loaded into the sample loading chamber and set under vacuum to reach $2 \cdot 10^{-7}$ mbar. At this pressure, the sample holder was transferred into the analysis chamber and set to reach c.a. 10^{-8} mbar. The

Table 4.1. List of samples.

Sample	Description	Sub-chapter
1	Fresh MWCNT (Hyperion CS-02C-063-XD)	Case study I
2	Co@NC, prepared by pyrolysis of ZIF-67 at 600 °C	Case study II
2a	**2** after acid leaching	
3	Co@NC, prepared by pyrolysis of ZIF-67 at 700 °C	
3a	**3** after acid leaching	
4	Co@NC, prepared by pyrolysis of ZIF-67 at 800 °C	
4a	**4** after acid leaching	
5	Bimetallic Zn, Co MOF, isostructural to ZIF-67, with Zn^{2+}/Co^{2+} molar ratio of 25	
6	Mesoporous Co@NC, prepared from **5** with additional templating agent	
7	Imine-linked porous organic network	Case study III
8	**7** after coordination of Ni^{2+}	

X-ray gun was operated at 3 mA and 12 kV and the spot size was set to 400 μm. Precision spectra of the core photoelectron lines were registered with 0.1 eV energy step using constant analyzer pass energy of 50 eV. The measurements were performed at ambient temperature; the chamber pressure during the measurement was about 10^{-7} mbar. A flood gun was used for charge compensation.

Spectra were analyzed using the Thermo Avantage software package. Background subtraction was done using the setting “SMART” (based on the Shirley background with the additional constraint that the background should not be of a greater intensity than the actual data at any point in the region). The deconvolution of spectra was performed using a mixed Gauss-Lorentz function. Quantification was done using the Scoffield sensitivity factors. Difference in depth of analysis for different photoelectron lines was accounted using the *TPP-2M* method.[11]

X-ray absorption experiments were performed at *DUBBLE* beam line *BM26A* in ESRF, Grenoble. Co- and Ni-bearing materials (Case study II and Case study III, respectively) were studied using the corresponding Co *K*-edge and Ni *K*-edge. Energy calibration was achieved using metal foils as references. The first peak in the first derivative of the metal foil XAS spectrum was calibrated to 7709 eV for Co and to 8333 eV for Ni.[12]

Calibration and data alignment was performed using ATHENA program, obtaining values for reference compounds from HEPHAESTUS program.[13] After averaging, the spectra of the studied samples were normalized to a total absorption of unity and processed using the ATHENA data normalization and analysis package. For normalization, the spline *r*-background parameter was set to 1.0. The background subtraction was carried using a pre-edge range of -200 to -30 eV and a post-edge linear range of 50 to 985 eV. A spline range of k = 0 to k = 14.8 A^{-1} and k-weight of 3 was used to isolate the EXAFS (chi)function. The Co *K*-edge EXAFS spectra were Fourier transformed over a k-range of k = 3 to k = 11 $Å^{-1}$. Fitting of Co *K*-edge EXAFS spectra was carried out by ARTEMIS software.[13] The spectra of the different samples were fitted in *R*-space with an *R*-range of 1 to 4.5 Å, and the fittings were done with a k-weight of 3. The Fourier transform and inverse Fourier transform was carried with a Δk of 1 and ΔR of 0. From the references fits we obtain the amplitude reduction factor (S_0^2) equal to 0.77 ± 0.03 for cobalt foil, 0.73 ± 0.13 for CoO, and 0.80 ± 0.07 for $NiCl_2$•$6H_2O$. In further fittings of the experimental samples S_0^2 = 0.73 was used for Co *K*-edge EXAFS spectra and S_0^2 = 0.80 was used for Ni *K*-edge EXAFS spectra.

Transmission Electron Microscopy (TEM) images in Case study II were obtained by using a *Talos F200X microscope* (FEI, Hillsboro, OR, USA) at 200 kV. In Case study III TEM analysis was performed in a *JEOL JEM-1400-Plus* microscope operated at 120 keV with LaB6 emission filament.

In Case study II the concentrations of Co and N in the samples were measured by atomic adsorption spectroscopy (AAS) (*AAnalyst 200*, Perkin Elmer, USA) and elemental analysis (*Vario EL*, Elementar, Germany), respectively. In Case study III elemental composition of ***8*** was analyzed using *PerkinElmer Optima 5300* (torch:4300) instrument, with ICP-OES 5300DV.

X-ray diffraction (XRD) patterns were recorded in Bragg-Brentano geometry in *Bruker D8 Advance* X-ray diffractometer equipped with a Vantec position sensitive detector and graphite monochromator. Measurements were performed at room temperature with monochromatic Co *Kα* radiation (λ = 0.179026 nm).

4.3. Case Study I: Practical aspects of XPS analysis of carbon-based materials

4.3.1. Sample preparation for XPS measurements

Performing the XPS characterisation of carbon-based materials, one has to pay particular attention to the choice of support and sample preparation. Conducting carbon tapes, commonly used for supporting powder samples, can contribute into the registered C*1s* and O*1s* spectra of the samples. As a possible solution to this problem, one can avoid the use of carbon tape by direct embedding of the sample onto the metal holder surface. However, in this case it becomes crucial to assure good and uniform contact between the holder and the sample. Depending on the type of sample material, this can be achieved either by pressing the sample into the holder (or into the metal foil attached to the holder), or by preparing a thin layer of sample directly on the holder surface. However, these methods imply that samples supported in such way possess the same structure and composition as the bulk materials, that is not always the case.

Alternative approach accepts the use of carbon tape with additives of elements other than carbon and oxygen. In this case presence of photoelectron lines of these elements in survey XP spectra will indicate that signal from the tape influences the results, and the intensity of these lines will allow to estimate the contribution from the tape. One of the most common and suitable additives of this type is silicon. XP spectra of silicon possess only two lines, Si*2p* and Si*2s* (BE ≈ 102 eV and 154 eV, respectively), so it does not overlap with C*1s* and O*1s* directly. Furthermore, the low binding energy of Si*2p* and Si*2s* lines means that electrons emitted from these energy levels should have very high kinetic energy, resulting in deeper analysis zone for silicon compared to oxygen and carbon. This assures that the signal from the tape does not contribute anything to experimental spectra when Si*2p* and Si*2s* lines are not observed in the survey spectrum. Of course, this strategy does not work when the sample itself contains silicon or the content of silicon in the tape is low (below 1% at.), but is reasonably reliable in other cases.

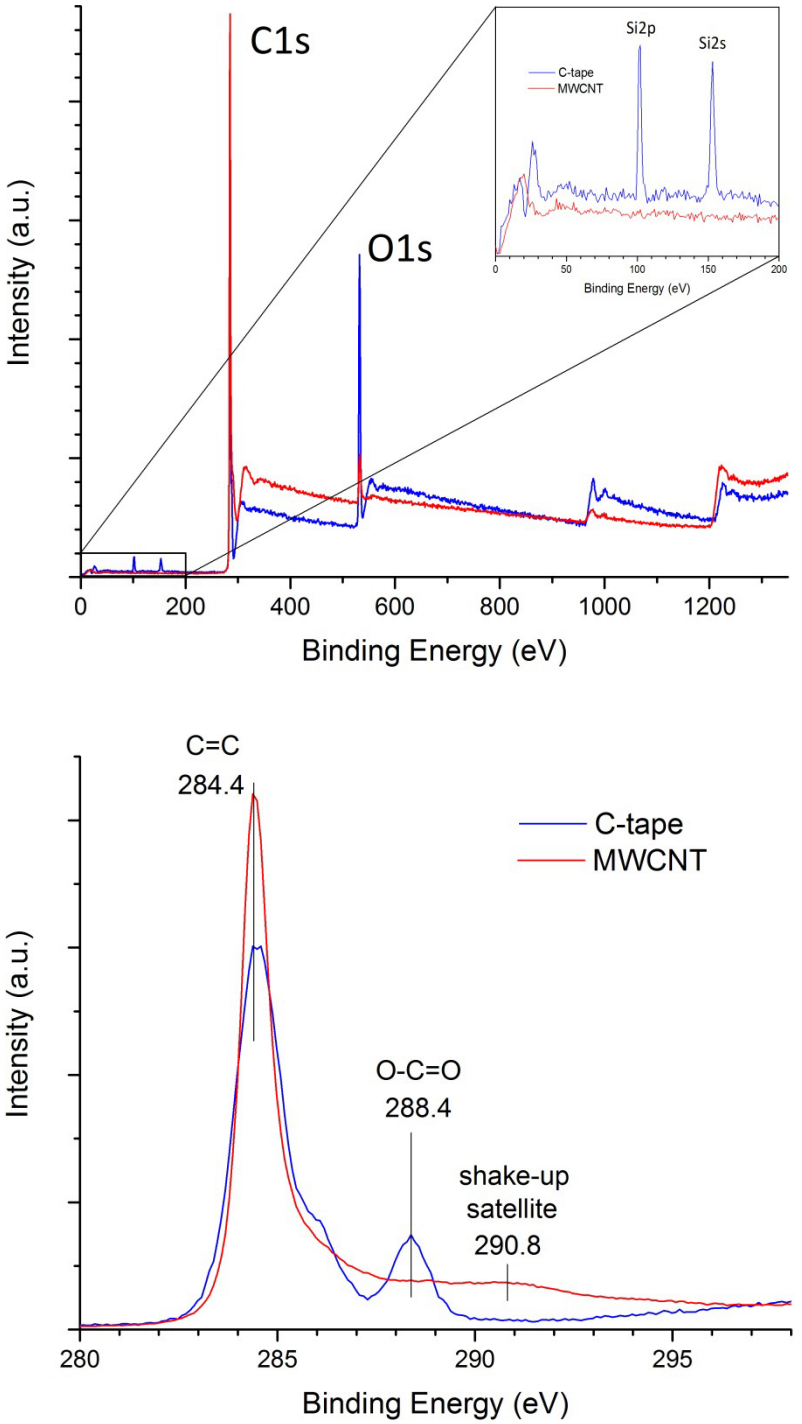

Figure 4.1. Survey (*top*) and C*1s* (*bottom*) XP spectra of the carbon tape support and supported carbon nanotubes.

Table 4.2. Surface composition of supportive tape and carbon nanotubes sample.

Element, at.%	Tape	Nanotubes
Carbon	74.6 ± 0.5	94 ± 2
Oxygen	22.1 ± 0.1	6 ± 2
Silicon	3.4 ± 0.6	-

In our XPS measurements we supported sample powder using double-faced conducting carbon tape with a silicon content of approx. 3% at. (NEM TAPE, Nisshin EM Co., Ltd.). Figure 4.1 shows survey and C*1s* spectra of the tape compared to the supported sample ***1***. Complete absence of photoelectron lines in the range 100-200 eV in case of ***1***, as well as significant differences in C*1s* line shape (more narrow main peak at ~284.4 eV, corresponding to C=C bonds, no pronounced peak of carboxylates at ~288.4 eV, noticeable broad shake-up satellite feature at ~290.8 eV) indicate that the sample layer is thick enough and the tape is not visible for XPS.

4.3.2. XP spectra analysis

In order to check the homogeneity of the supported sample and to assure the statistical significance of the results, it is recommended to measure each sample at several points on its surface. In case of ***1*** in some points the differential charging of surface was observed due to the non-uniform thickness of the sample layer in the analysis area. This leads to distortions in the shapes of XPS lines (broadening of lines or even additional peaks appearing in the spectra). If present, differential charging affects all lines in the same manner, which usually makes it easy to distinguish from the real chemical changes in the sample. In this case, such differentially-charged points were not used for the analysis.

XP survey spectra analysis indicates that surface of the sample consists only of carbon and oxygen (Fig. 4.1), and their ratio significantly differs from the values for the pure tape support (Table 4.2).

Precision C*1s* and O*1s* XP spectra of the sample are shown on Fig. 4.2 and 4.3. Detailed analysis allows to identify four main peaks in O*1s* line spectra at 530.6 eV, 531.8 eV, 533.5 eV, and 536.0 eV. According to literature,[14] these oxygen types were attributed to O-C=O species (carboxylic acid, anhydride, lactone, and ester groups), C=O species (carbonyl groups), C-O species (hydroxyl groups), and adsorbed water, respectively. During the fitting particular attention was paid to keeping the binding energy (BE) of

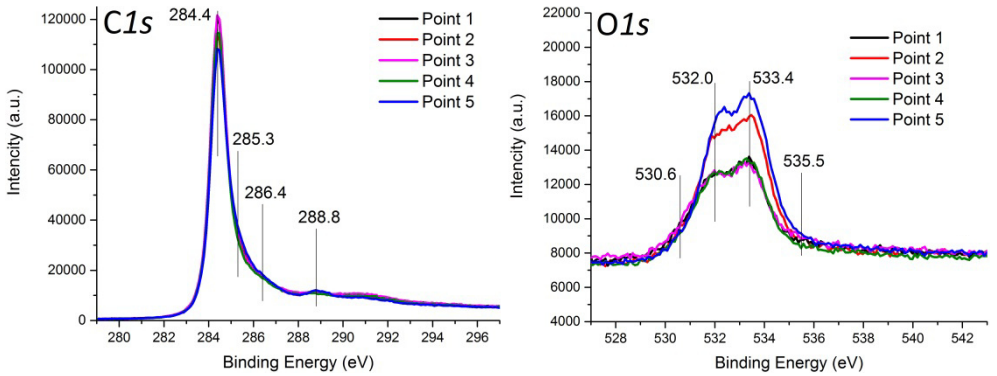

Figure 4.2. XP spectra of ***1***, measured at five different locations. Left: C*1s* spectra. Right: O*1s* spectra.

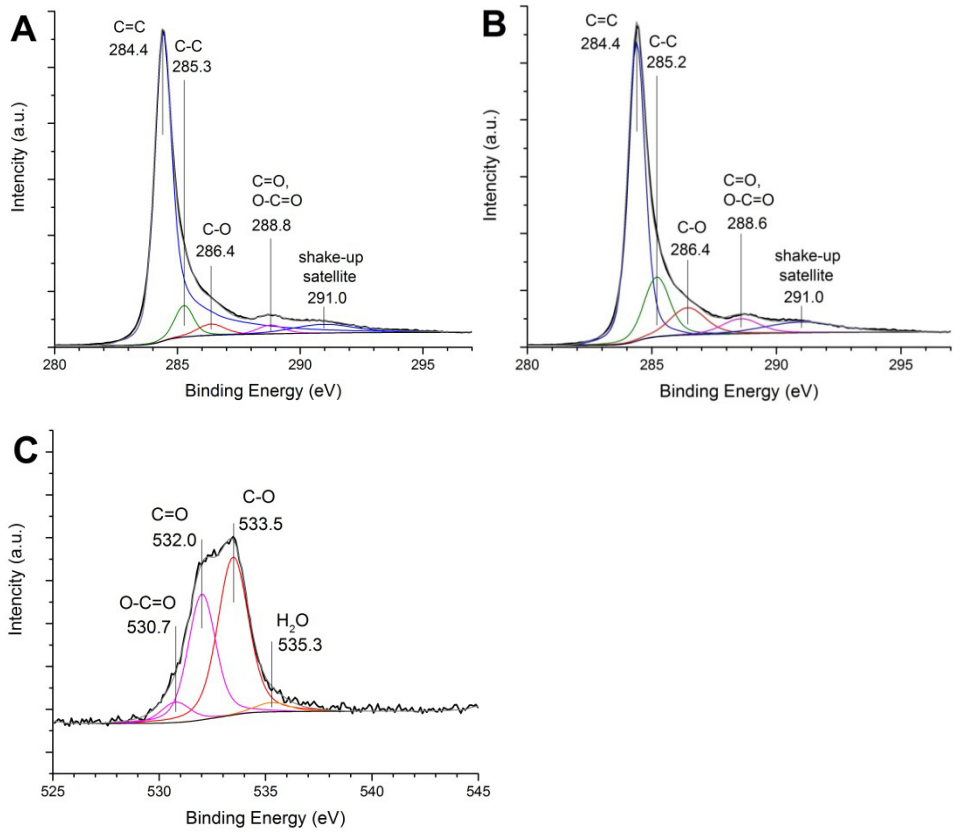

Figure 4.3. Deconvolution of XP spectra of ***1***: C*1s* spectrum fitted using *a*) asymmetric and *b*) symmetric shape of peak at 284.4 eV, and *c*) O*1s* spectrum.

Table 4.3. Fitting of O*1s* XP spectra of ***1***.

Surface species	**"O-C=O"**	**"C=O"**	**"C-O"**
BE, eV	530.6 ± 0.1	531.9 ± 0.1	533.45 ± 0.06
FWHM, eV	1.5 ± 0.1	1.6 ± 0.1	1.67 ± 0.03
Content, at%	0.3 ± 0.1	1.8 ± 0.4	2.3 ± 0.6

Table 4.4. Fitting of C*1s* XP spectra of ***1***.

Surface species		**"C=C"**	**"C-C"**	**"C-O"**	**"C=O"**
Asymmetric main peak	**BE, eV**	284.42 ± 0.01	285.30 ± 0.04	286.37 ± 0.03	288.78 ± 0.04
	FWHM, eV	0.84 ± 0.03	0.86 ± 0.04	1.3 ± 0.1	1.24 ± 0.03
	Content, at%	85.5 ± 3.5	4.5 ± 1.5	3.5 ± 0.8	2.0 ± 0.6
Content, at% (symmetric main peak)		63.4 ± 3.6	12.0 ± 2.2	7.0 ± 0.7	8.6 ± 3.8

peaks and their full width at half maximum (FWHM) nearly constant in all spectra, aiming to have an error less than 0.1 eV for each type of species (see Table 4.3).

C*1s* line spectra were fitted using four main peaks at 284.4 eV, 285.3 eV, 286.4 eV and 288.7 eV, corresponding to sp^2 carbon of nanotubes, sp^3 carbon of coke deposits, C-O and C=O species, respectively. However, for an adequate peak fitting one should remember that carbon nanotubes and other graphite-like types of carbon are conductive,[15] whereas sp^3 carbon species are not. Due to the high density of electron states near the Fermi level conductive materials are characterized by asymmetric peaks in XPS with a tail towards higher binding energies. In this case the use of symmetric Voight function for fitting can significantly distort the quantification results (Fig. 4.3 and Table 4.4), so these peaks should be carefully fitted using the asymmetric Doniach–Šunjić peak shape. The resulting fitting of C*1s* and O*1s* spectra shows good agreement in quantification of carbon and oxygen of C-O and C=O species on the surface (see Table 4.3 and Table 4.4).

In this case study we show the utmost importance of systematic analysis of all lines in the XPS measurements. Different photoelectron lines have different depth of analysis and sensitivity to certain species, so any conclusions based on the deconvolution of one line should agree with the results obtained from other lines in a quantitative manner.

4.4. Case Study II: Co@NC catalysts for selective hydrogenation of nitroarenes

Co@NC catalysts described in this case study can have multiple cobalt and nitrogen species, which often give peaks with very close binding energy in Co*2p* and N*1s* XP spectra, respectively. In order to differentiate these species, three groups of Co@NC samples were investigated with XPS:

1) Samples ***2, 3,*** and ***4,*** prepared by pyrolysis of ZIF-67 at different temperatures (600 °C, 700 °C, 800 °C, respectively);
2) Samples ***2a, 3a,*** and ***4a,*** prepared by acid leaching of ***2, 3,*** and ***4*** with HCl;
3) Sample ***6,*** prepared by pyrolysis of bimetallic zinc-cobalt analogue of ZIF-67 (sample ***5***) with low Co:Zn ratio and additionally introduced SiO_2 templates.

Different synthesis conditions change the ratios of different cobalt and nitrogen species in Co@NC samples, thus allowing to distinguish them in XP spectra. In this case study we discuss how the features of Co*2p* and N*1s* XP spectra reflect the changes onto surface and sub-surface layers of Co@NC catalysts. In combination with the results from XAS, TEM, and XRD, XPS gives insight into the nature of the cobalt species that have the greatest impact on the catalyst activity.

4.4.1. Effect of synthesis temperature and acid leaching

Previous studies on the pyrolysis of ZIF-67 have shown that higher pyrolysis temperatures lead to the formation of bigger nanoparticles of metallic cobalt, covered by a graphitic shell.[16] In order to study the effect of increasing size and concentration of Co nanoparticles on XP spectra of the corresponding samples, catalysts ***2, 3,*** and ***4*** were prepared by pyrolysis of ZIF-67 at 600 °C, 700 °C, and 800 °C, respectively.

To estimate how the distribution of cobalt in Co@NC samples changes at different pyrolysis temperatures it is important to compare the results of bulk elemental analysis with XPS quantification of surface elemental composition (see Table 4.5). Elemental quantification from XPS data was performed based on the analysis of precision spectra; it is not recommended to use survey spectra for quantification as their higher energy step can cause greater errors in the analysis results (especially for elements in low

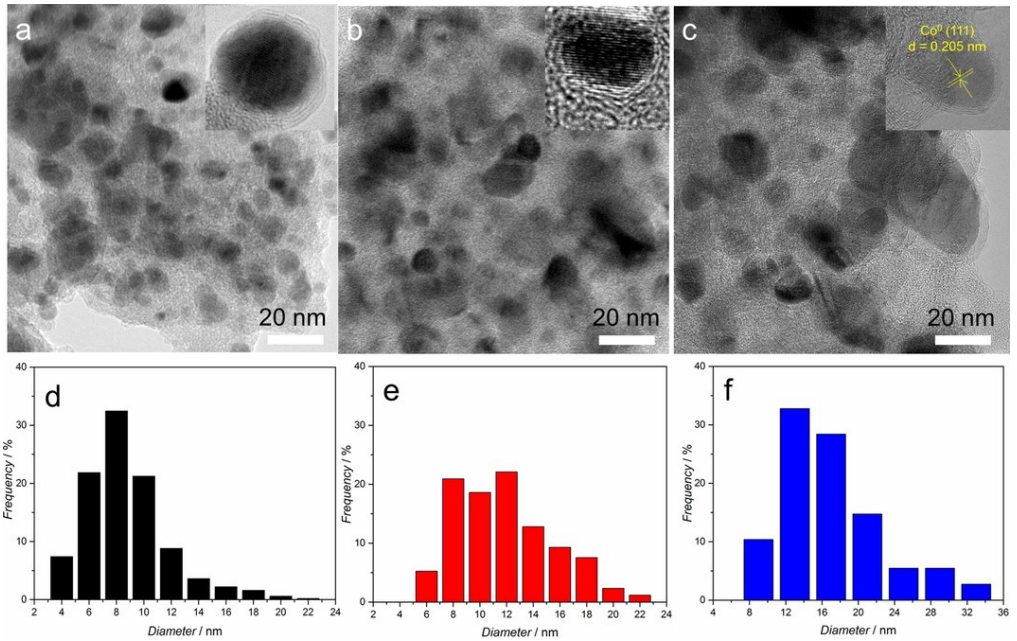

Figure 4.4. TEM images and corresponding size distribution of Co nanoparticles in ***2*** (a, d), ***3*** (b, e) and ***4*** (c, f). TEM images were obtained by using a *Talos F200X* microscope (FEI, Hillsboro, OR, USA) at 200 kV.

Table 4.5. Surface and bulk composition of Co@NC catalysts.

	XPS quantification				Elemental composition	
Material	C, wt%	O, wt%	Co, wt%	N, wt%	Co, wt% [a]	N, wt% [b]
2	64,7	16,4	10,7	8,2	31,0	7,8
3	71,4	11,8	10,0	6,8	32,9	3,7
4	79,5	9,8	6,1	4,5	37,4	2,4
2a	68,7	18,3	6,0	7,0	27,1	9,4
3a	76,1	13,1	4,8	5,9	19,4	5,4
4a	79,2	16,1	1,9	2,8	13,6	3,5

[a] Measured by atomic absorption spectroscopy (*AAnalyst 200*, Perkin Elmer, USA)
[b] Measured by elemental analysis (*Vario EL*, Elementar, Germany)

concentrations). As a consequence, precision spectra should be collected completely, including all possible satellites, to assure proper background subtraction and avoid understatement of the element content.

Both elemental analysis and XPS show that nitrogen content decreases at higher pyrolysis temperatures. Obviously, thermal degradation of organic part of ZIF-67 (2-methylimidasole linker) leads to formation of volatile C- and N-containing products, resulting in increasing loss of nitrogen in the samples. As a result, the total cobalt content should increase at higher pyrolysis temperatures, that agrees well with the results of elemental analysis. However, XPS indicates the opposite trend: the surface content of cobalt becomes lower at higher temperatures. This effect can be the result of two factors:

- Aggregation of cobalt species into bigger size particles, so that most of cobalt inside the particle becomes invisible for XPS analysis;
- Formation of layers of other compounds on the surface, covering the cobalt species.

TEM analysis of Co@NC samples indicates that both these processes take place: size of cobalt particles increases and the layer of highly ordered graphitic carbon grows on their surfaces at higher temperatures (Fig. 4.4). XRD analysis results additionally prove these observations (Fig. 4.17a). However, in order to see how the ratio between different cobalt and nitrogen species changes with pyrolysis temperature precision XP spectra of Co*2p* and N*1s* lines should be analysed.

From deconvolution of Co*2p* spectra two different types of cobalt were identified – metallic Co^0 at *BE*(Co$2p_{3/2}$) ≈ 778.2 eV and oxidized Co^{n+} species at *BE*(Co$2p_{3/2}$) ≈ 780.0 eV, followed by a broad satellite structure (Fig. 4.5). During the fitting the width of Co^0 peak was kept significantly more narrow than Co^{n+} peaks (≈ 1.2 eV and ≈ 2.7 eV, respectively), which is typically observed for transition metals and their compounds.[17] Remarkably, the ratio between these two forms of cobalt does not change significantly with pyrolysis temperature, and in all cases 70-85% of cobalt on surface remains oxidized (Table 4.6). Due to close BE values and complex satellite structures of different Co^{2+} and Co^{3+} compounds we cannot undoubtedly distinguish from Co*2p* spectra only whether this oxidized cobalt corresponds to atomically dispersed cobalt species, cobalt oxide particles or shells of cobalt oxide on the surface of metallic cobalt particles.

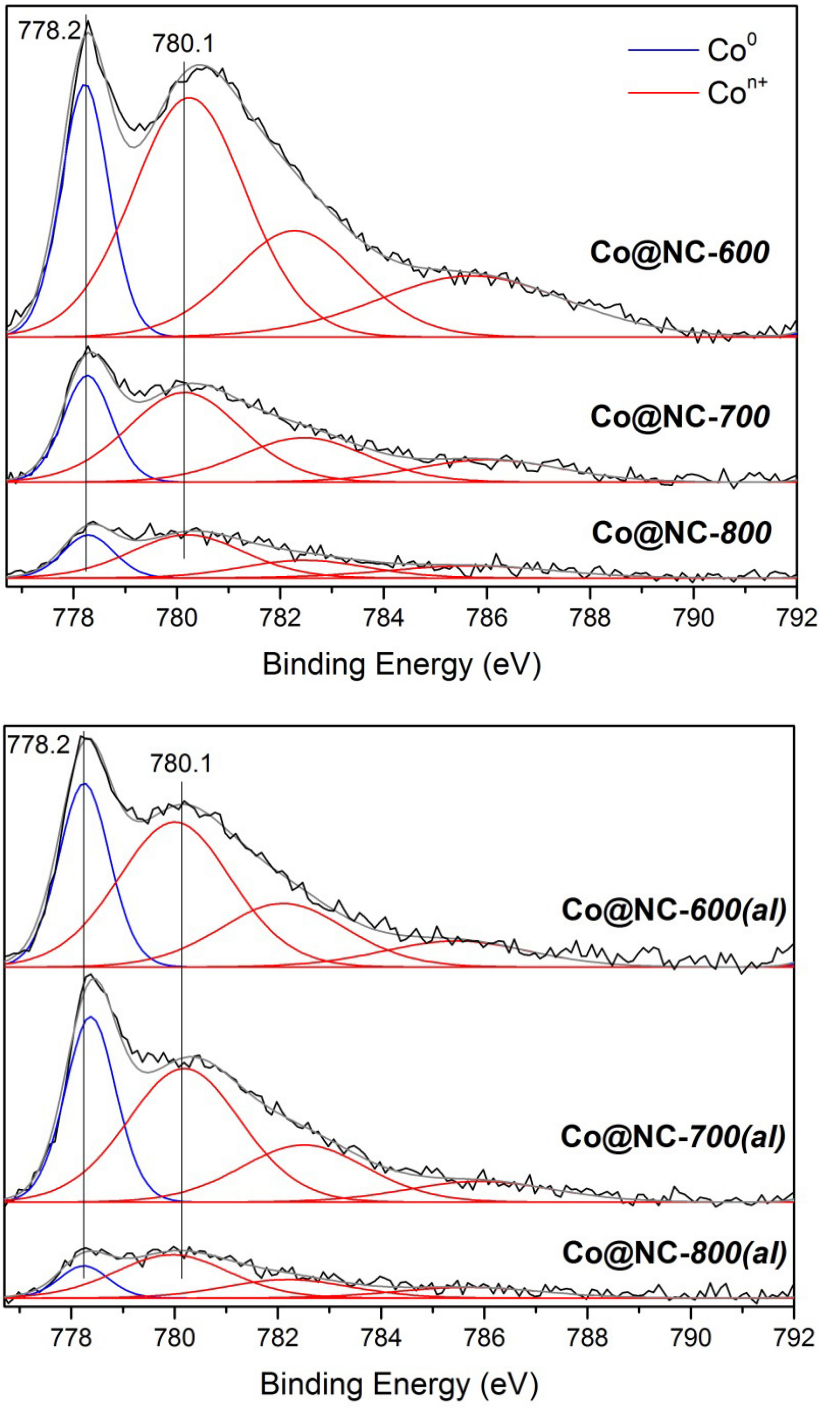

Figure 4.5. Deconvolution of Co$2p_{3/2}$ XP spectra for ***2, 3,*** and ***4*** (top), and ***2a, 3a,*** and ***4a*** (bottom).

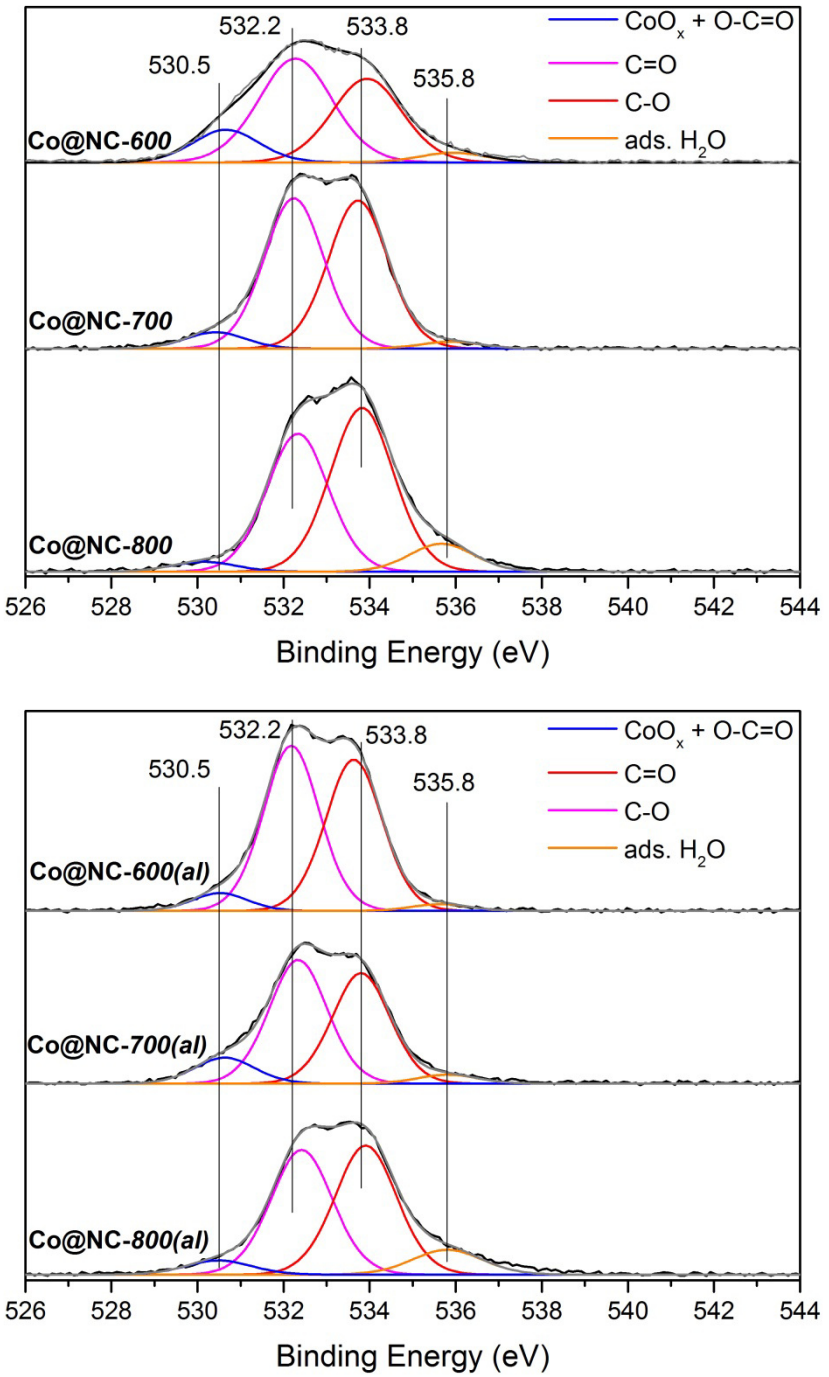

Figure 4.6. Deconvolution of O*1s* XP spectra for ***2, 3,*** and ***4*** (top), and ***2a, 3a,*** and ***4a*** (bottom).

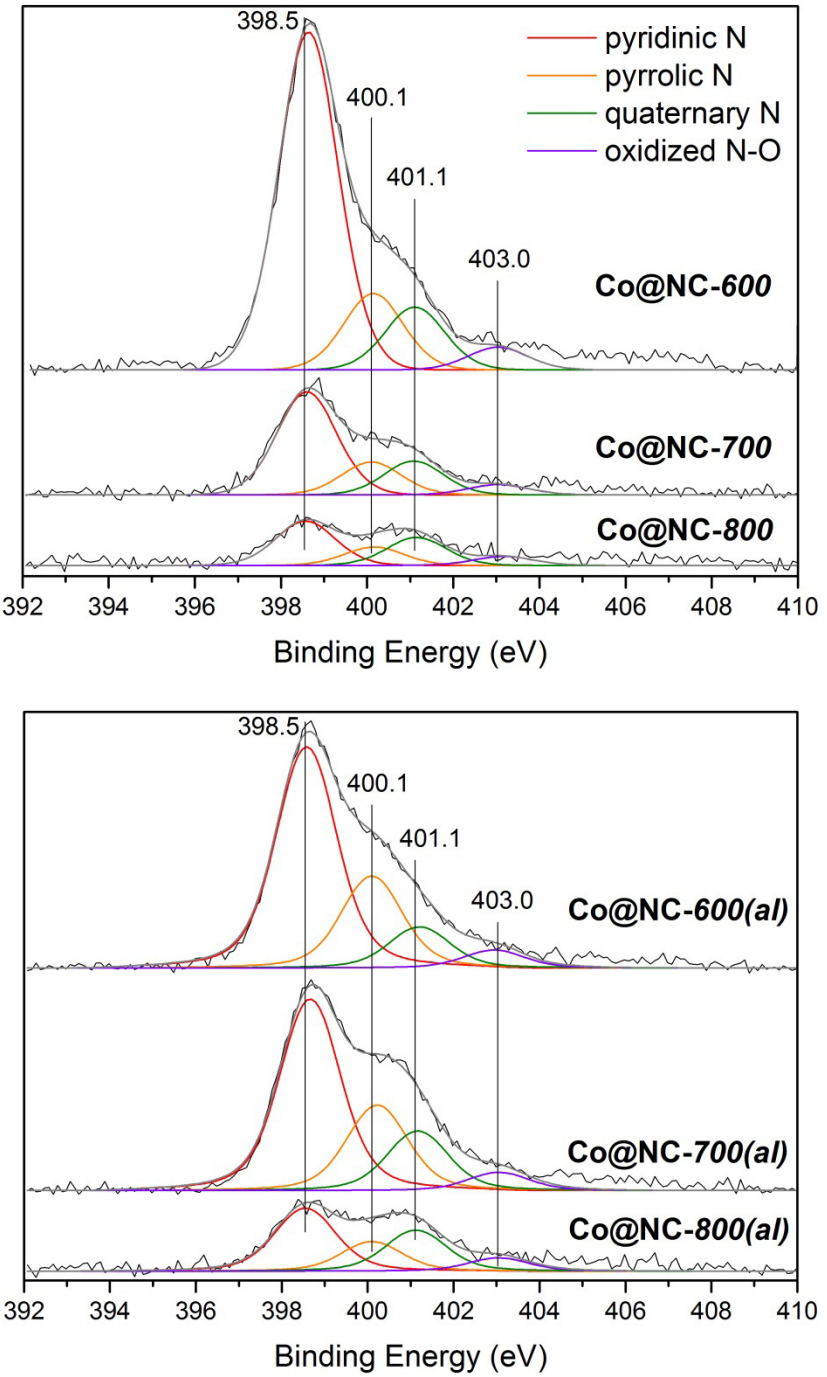

Figure 4.7. Deconvolution of N*1s* XP spectra for ***2, 3,*** and ***4*** (top), and ***2a, 3a,*** and ***4a*** (bottom).

Table 4.6. Surface content of nitrogen-based species determined by fitting of Co*2p* XP spectra.

Material	Co^0 at.% (778.2 eV)	Co^{n+} at.% (780.1 eV)
2	0.5	2.1
3	0.3	0.7
4	0.3	1.1
2a	0.3	1.0
3a	0.3	0.8
4a	0.1	0.3

Table 4.7. Surface content of oxygen-based species determined by fitting of O*1s* XP spectra.

Material	"O-C=O" + CoO_x at.% (530.5 eV)	"C=O" at.% (532.2 eV)	"C-O" at.% (533.8 eV)	Coordinated H_2O at% (535.8 eV)
2	1.9	6.7	5.1	0.6
3	0.9	8.0	7.9	0.4
4	0.5	7.0	8.5	1.4
2a	0.8	7.3	6.8	0.3
3a	1.1	4.9	4.3	0.4
4a	0.7	5.4	5.6	1.2

Table 4.8. Surface content of carbon-based species determined by fitting of C*1s* XP spectra (asymmetric peak shape for C=C species, symmetric peak shape for other species).

Material	"C=C" at.% (284.4 eV)	"C-C" at.% (285.3 eV)	"C-O/N" at.% (286.4 eV)	"C=O/N" at.% (289.0 eV)
2	35.9	19.2	13.2	6.6
3	34.1	23.7	13.2	7.6
4	31.1	24.9	15.5	8.9
2a	33.0	25.0	12.0	6.4
3a	52.6	17.9	6.0	6.0
4a	46.1	18.9	11.5	7.5

Table 4.9. Surface content of nitrogen-based species determined by fitting of N*1s* XP spectra.

Material	"pyridinic N" at.% (398.5 eV)	"pyrrolic N" at.% (400.0 eV)	"quaternary N" at.% (401.0 eV)	"N-O" at% (403.0 eV)
2	5.5	1.3	1.0	0.4
3	1.9	0.6	0.6	0.2
4	0.8	0.3	0.5	0.2
2a	4.0	1.7	0.7	0.3
3a	3.0	1.3	0.9	0.3
4a	1.1	0.5	0.7	0.2

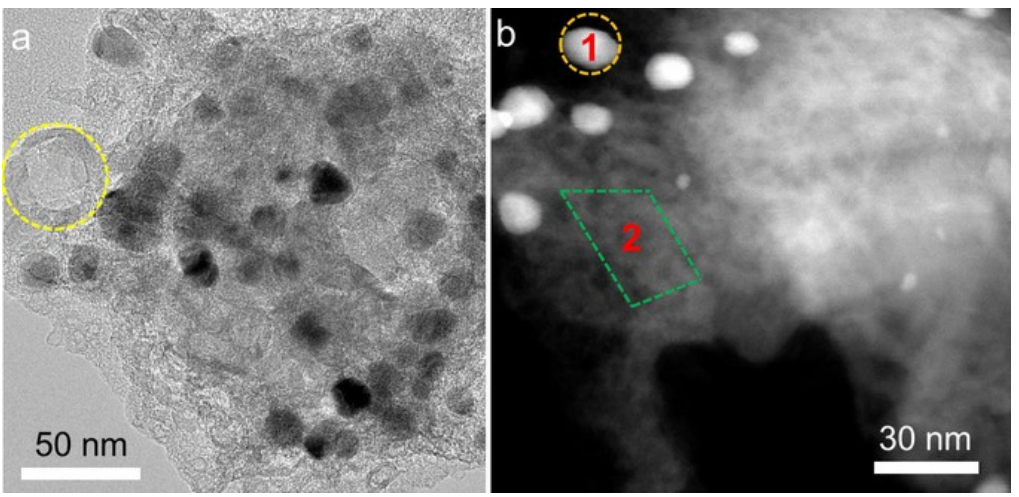

Figure 4.8. a) TEM and b) HAADF images of ***4a***. TEM images were obtained by using a Talos F200X microscope (FEI, Hillsboro, OR, USA) at 200 kV.

Deconvolution of O*1s* spectra gives four main peaks at 530.5 eV, 532.2 eV, 533.8 eV and 535.8 eV (Fig. 4.6). The second, the third and the fourth peak can be attributed to C-O, C=O species and adsorbed water, respectively. However, the first peak can correspond both to carboxylic species and to the oxygen of cobalt oxide. The area of this peak changes from 13% to 3% of total O*1s* line area when the pyrolysis temperature is increased from 600 °C to 800 °C, respectively (Table 4.7). Nevertheless, due to the uncertainty in concentration of surface carboxylic groups we cannot directly relate the decrease of this peak to decrease of CoO_x species content on the surface. Deconvolution of C*1s* line, in principle, could give more insights regarding the change of carboxylate concentration, but due to the gamut of

possible C-O- and C-N-containing surface species it becomes impossible to trustfully distinguish carboxylates from C*1s* line analysis in this case (Table 4.8).

Deconvolution of N*1s* lines of Co@NC-*T* catalysts allowed to identify four types of nitrogen species with binding energies around 398.5 eV, 400.0 eV, 401.0 eV and 402.9 eV (Fig. 4.7). According to literature,[18-20] they can be attributed to pyridinic-N, pyrrolic-N, quaternary-N and oxidized N-O species, respectively. It should be noted that "pyridinic-N" in this case refers not only to pyridine and its derivatives, but to majority of aromatic N-heterocycles with a basic lone pair of electrons on a nitrogen atom. As the lone electron pair of nitrogen is suitable for coordinating most transition metals, these species are expected to play an important role in stabilizing dispersed cobalt sites. In pyrrolic-N and quaternary-N species the lone electron pair of nitrogen is involved in aromatic conjugation or formation of C-N bonds and does not contribute significantly to coordination of dispersed metal species. Oxidized N-O species are able to form complexes with transition metals, but usually they are far less stable compared to complexes with pyridinic-N moieties. Thus, the ratio between different nitrogen groups on the material surface is an important factor that determines the concentration and stability of transition metal species coordinated to it.

In case of ***2*** pyridinic-N species are the dominant nitrogen species on the sample surface (approximately 70% of all nitrogen detected by XPS). However, increase of pyrolysis temperature leads to relatively fast decay of pyridinic-N content, whereas the amount of pyrrolic-N, quaternary-N and N-O species does not decrease that significantly (Table 4.9). This indicates that incorporation of nitrogen into graphitic layers is more favourable at higher temperatures. As a result, only 45% of surface nitrogen in ***4*** remains as pyridinic-N species. These results are in line with the observed tendency towards decomposition of atomically dispersed cobalt species and growth of Co^0 particles at higher pyrolysis temperatures; nevertheless, even after pyrolysis at 800 ^oC the major part of surface nitrogen is still in a form of pyridinic-N species, that shows high thermal stability of these moieties. Notably, the content of pyridinic-N is higher than the content of oxidized cobalt species for all samples.

XPS characterization of ***2, 3,*** and ***4*** indicates that although increase of pyrolysis temperature leads to growth of Co^0 particles and to decrease of nitrogen content in the material, significant concentration of oxidized cobalt species is still present on the surface. Unfortunately, XPS does not allow to distinguish different oxidized cobalt species directly. An alternative approach

that can allow to investigate separately the catalytic properties of isolated CoN_x species is the acid leaching of samples. Metallic cobalt and cobalt oxides dissolve in hydrochloric acid, but cobalt-nitrogen complexes are more stable in acidic media. Following this strategy, catalysts ***2a, 3a,*** and ***4a*** were prepared and characterized.

As expected, elemental analysis of acid leached catalysts shows that the total cobalt content decreases after the acid leaching, and the efficiency of cobalt removal increases for samples with higher pyrolysis temperature. However, TEM analysis shows that cobalt nanoparticles are still present in the samples (Fig. 4.8), and reflections of metallic cobalt phase can still be observed in XRD diffractograms (Fig. 4.17b). From TEM images it can be concluded that remaining cobalt nanoparticles are fully encapsulated by the layers of graphitic carbon, which protect these particles from the acid treatment. In this case only the partially covered particles can be removed, which is indicated by the presence of hollow carbon shells in TEM images of the leached samples.

XPS analysis of acid leached samples agrees well with the results of TEM characterisation. Co*2p* spectra for ***2a*** demonstrate that the surface content of Co^0 does not change much during the acid leaching, but the content of oxidized cobalt species decreases by half. This is also confirmed by the O*1s* spectra, which show a significant decrease of the metal oxide species content. This indicates that only Co^0 particles that were not fully encapsulated and were in contact with the atmosphere (so that the layer of oxidized cobalt could form on their surface) were dissolved by acid. At 800 ^oC and higher more cobalt particles become exposed due to enhanced decomposition of the original carbon support and particle agglomeration. As a result, the content of both Co^0 and Co^{n+} species substantially decreases. However, even at these temperatures dispersed cobalt species are still present in the carbon support, which is indicated by EDX analysis (see Fig. 4.19)

The ratio between different nitrogen species varies significantly before and after the acid leaching for different pyrolysis temperatures. One would expect that after removal of cobalt particles more nitrogen species would be accessible for XPS, so the nitrogen content should increase. This trend is observed for pyrrolic-N and quaternary-N species, but is not always observed for pyridinic-N species: for example, the content of pyridinic-N decreases by 30% after acid leaching in case of ***2a***. As the content of Co^{n+} is significantly lower than the content of pyridinic-N in XPS, the reason of this effect can be the different stability of coordinated and non-coordinated

pyridinic-N species. For some other types of pyridinic-N species (e.g. for phthalocyanine complexes) it has been reported that coordination of transitional metals increases the chemical stability of these compounds. In HCl solutions non-coordinated pyridine-N moieties can become protonated, forming hydrochloride salts, that can shift the position of the corresponding peak in XPS.

In order to figure out whether dispersed CoN_x species actually influence the overall activity of the catalysts or not, additional experiments with selective inhibition of these sites were performed. Thiocyanate ions (SCN-) form strong complexes with broad range of transitional metals and are widely used in homogeneous catalysis for inhibiting metal centres. Addition of NaSCN to the reaction mixture with ***4a*** catalyst in a molar ratio NaSCN:Co = 8.5 resulted in a decrease of hydrogenation activity from 62% to 39%. As the acid leached catalyst should not have any accessible Co^0 particles and CoO_x species, this result proves that significant part of the overall catalyst activity should be attributed to CoN_x centres.

In summary, in this series of experiments we have demonstrated that Co@NC catalysts possess several types of cobalt species (Co^0 particles, CoO_x and CoN_x centres), that all show activity in hydrogenation of nitroarenes. Different synthetic approaches such as pyrolysis at higher temperatures and acid leaching can change the ratio between them but do not allow to obtain only one type of species exclusively. Different Co and O species in these samples have close binding energies and strongly overlap with each other. In this case preparation of model samples with modified ratio of these species, supported by the adequate external analysis method(s) which allow to detect at least some of these species, can help quantification of the sample surface composition.

4.4.2. Effect of lower cobalt concentration and SiO_2-templating in MOF

An alternative approach for obtaining selectively the isolated cobalt species in N-doped carbon matrix without formation of cobalt nanoparticles is improving the dispersion of cobalt by lowering its content in the initial MOF material. The attractive strategy for this involves preparation of bimetallic MOFs, in particular, by diluting Co with Zn ions[21]. Zn-methylimidazolate MOF ZIF-8 is isostructural to ZIF-67, and it has already been shown that addition of both Co and Zn precursors in the synthesis mixture results in

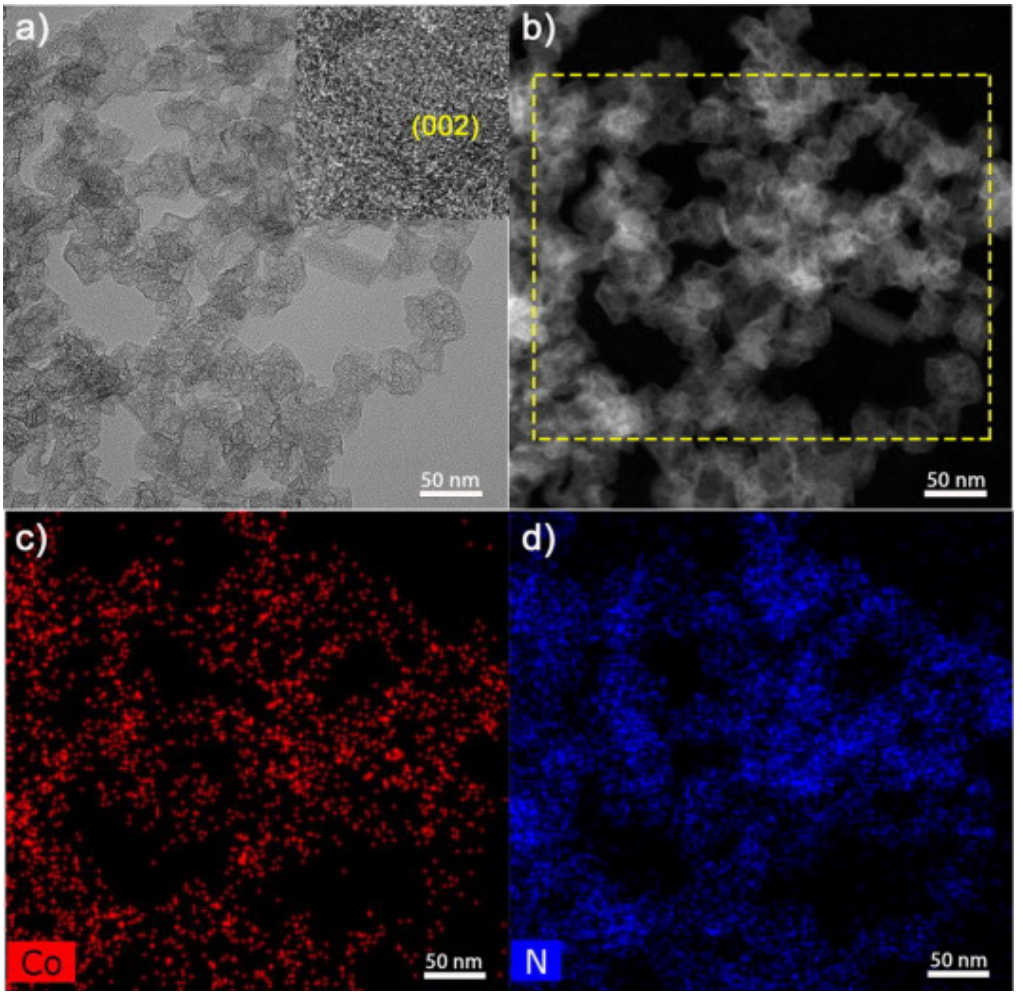

Figure 4.9. TEM analysis of ***6.*** *Top*: bright field (a) and dark field (b) TEM images. *Bottom*: element mapping image of Co (c) and N (d).

Table 4.10. Surface and bulk composition of ***6***.

	C, wt%	N, wt%	Co, wt%	Zn, wt%	Si, wt%	O, wt%	H, wt%
XPS quantification	70.6	6.3	1.1	0.9	0.9	20.2	-
Elemental analysis	49.6	15.0	3.5	2.8	1.6	-	3.7

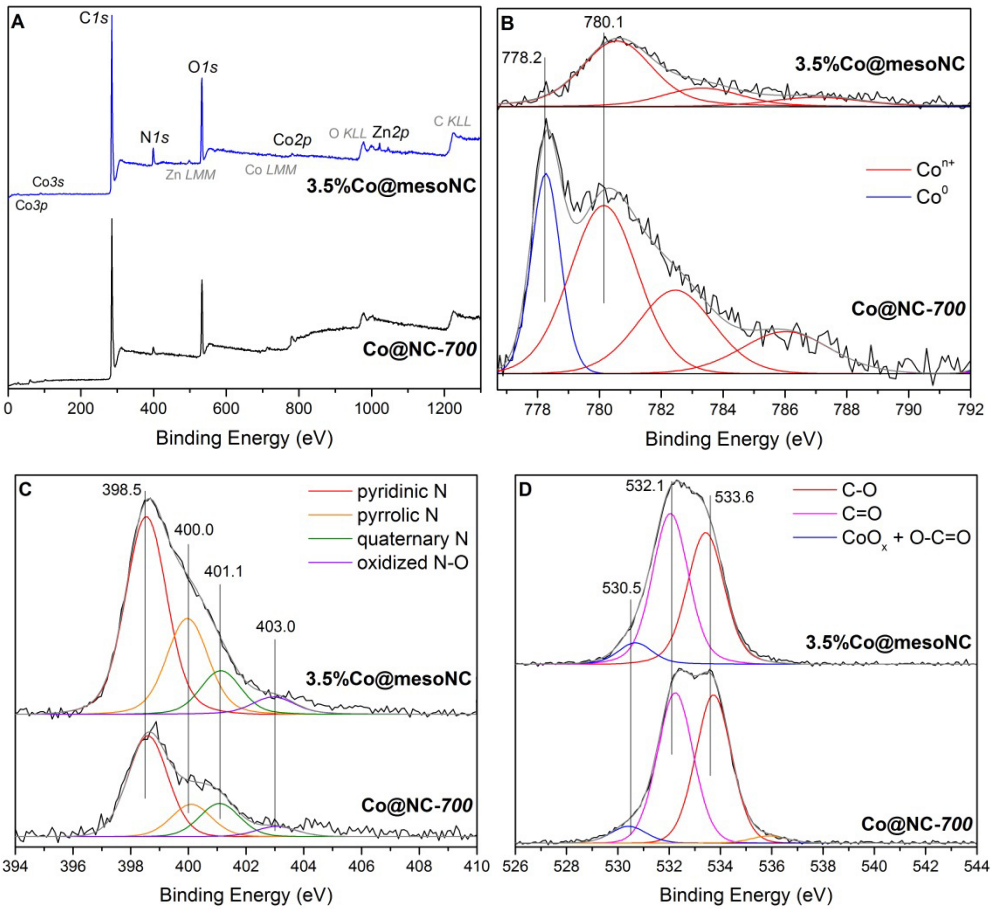

Figure 4.10. Comparison of XP spectra for catalysts ***6*** and ***3***: survey (*a*), Co*2p* (*b*), N*1s* (*c*) and O*1s* (*d*) XP spectra.

BIMZIF(Co,Zn) frameworks with homogeneous distribution of metals.[22] Volatility of metallic zinc (boiling temperature 907 °C) and inertness of ZnN_x species in nitroarene hydrogenation reactions assures that the presence of zinc has a negligible influence on the catalytic properties of the resulting materials. Thus, pyrolysis of bimetallic BIMZIF(Co,Zn) MOFs provides a promising pathway for synthesis of Co@NC catalysts with improved cobalt dispersion.

Earlier reports on pyrolysis of BIMZIF(Co,Zn) indicate that a material prepared from BIMZIF with a Zn:Co molar ratio of 20 has a significantly better dispersion of cobalt than Co@NC from pure ZIF-67; however, even in this case some small metallic Co nanoparticles were observed in the sample. In order to prevent the agglomeration of cobalt even further, an SiO_2-templating approach was applied. Pores of the MOF were filled with

tetramethyl orthosilicate (TMOS), which was further hydrolyzed to form SiO_2 nanoparticles in the pores. Such an SiO_2 template further impedes the formation of cobalt nanoparticles under pyrolysis conditions. Furthermore, leaching of SiO_2 with alkaline solution allows to create mesoporosity and to maintain a high specific surface area in the pyrolized samples, beneficial for mass transport of reactants and products within the catalyst.

Following this strategy, the bimetallic MOF sample ***5*** with Zn:Co molar ratio of 25 was impregnated with SiO_2, pyrolyzed and leached with an NaOH solution. According to the elemental analysis, the resulting material contains 15.0 wt% N and 3.5 wt% of Co, so it was further denoted as ***6***. It is worth mentioning that in case of samples prepared from pure ZIF-67 the content of N was less than 8 wt% after pyrolysis at 600°C, and it was further decreasing at higher pyrolysis temperatures. 2.8 wt% Zn and 1.6 wt% Si were also detected in ***6***, indicative of some residual Zn and Si in the sample even after high-temperature pyrolysis and NaOH washing. The high-resolution TEM (HR-TEM) image of ***6*** on Fig. 4.9 clearly demonstrates the presence of a layered graphitic carbon structure with a typical interplanar distance of 0.34 nm and the absence of any Co or Zn nanoparticles. EDX analysis further confirms high dispersion of Co and Zn in this sample.

XPS characterisation of ***6*** indicates that Co, N, Zn and Si are present on the catalyst surface (Fig. 4.10). However, the surface content of these elements, recalculated from XPS data, is 2-3 times lower than the elemental analysis results (Table 4.10). This observation can be explained by better removal of these elements from the surface than from the bulk of the material during the sample washing steps. Deconvolution of N*1s* spectra and quantification of the ratio between different surface species show that more than 55% of surface nitrogen belongs to pyridinic N-species, suitable for coordination of metal ions. Analysis of Co*2p* spectra indicates that only oxidized Co species are present in the sample. These findings agree well with the results from other analysis methods and prove that the use of silica-loaded ***5*** as a precursor for Co@NC catalysts increases their stability, leading to materials with a high nitrogen content and without any metallic Co nanoparticles.

4.4.3. Complementary XAS characterization

In order to investigate further the local environment of cobalt in ***6***, Co *K*-edge X-ray absorption spectroscopy (XAS) was applied. Parent ZIF-67*,* ***2, 4, 5,*** and ***6***, as well as Co foil and Co(II) phthalocyanine references were studied in detail both in XANES and EXAFS region. As expected,

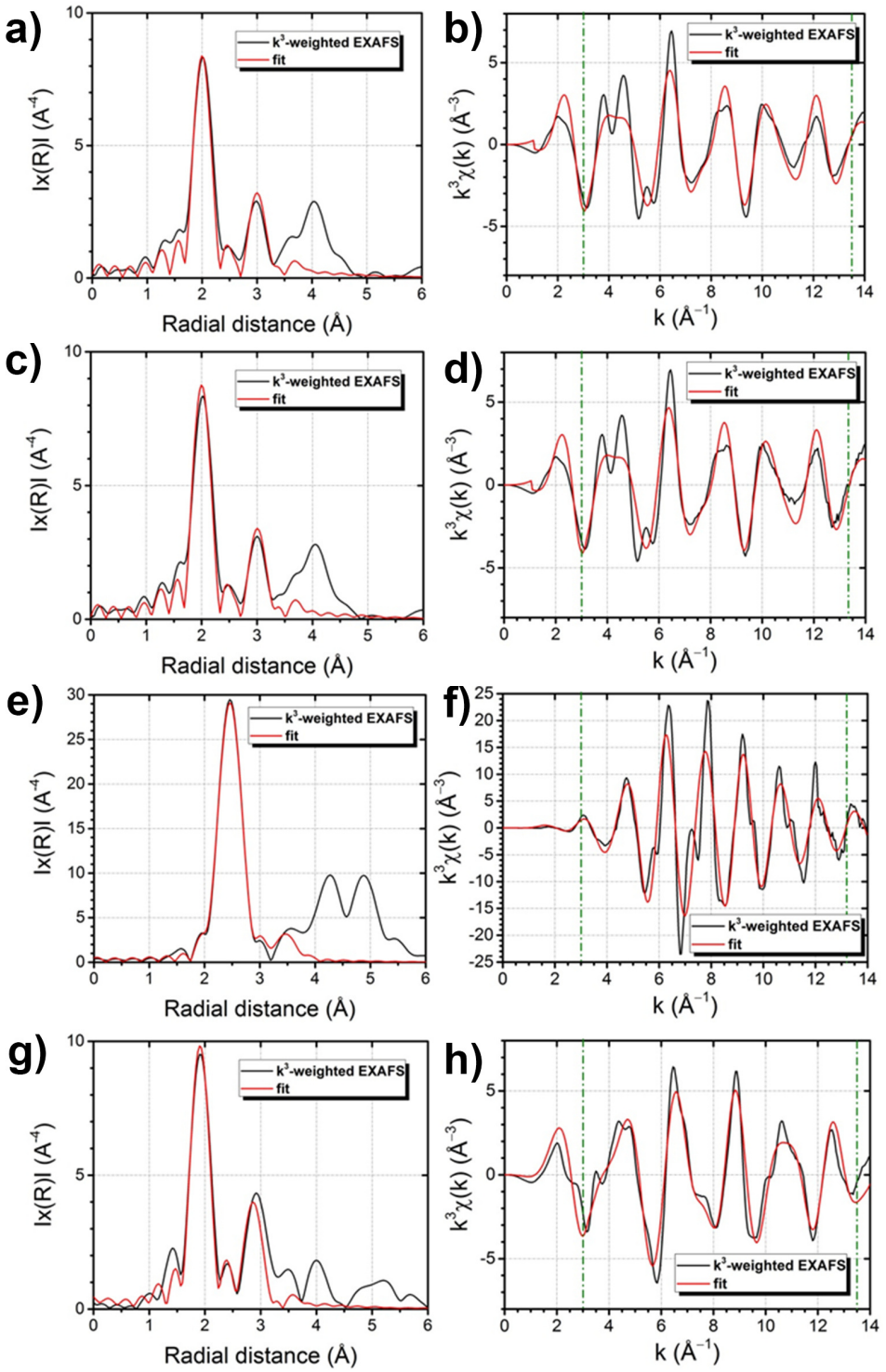

Figure 4.11. Phase-corrected plots of EXAFS spectrum fittings for ZIF-67 (a,b), ***5*** (c,d), ***2*** (e,f), and CoPc (g,h)

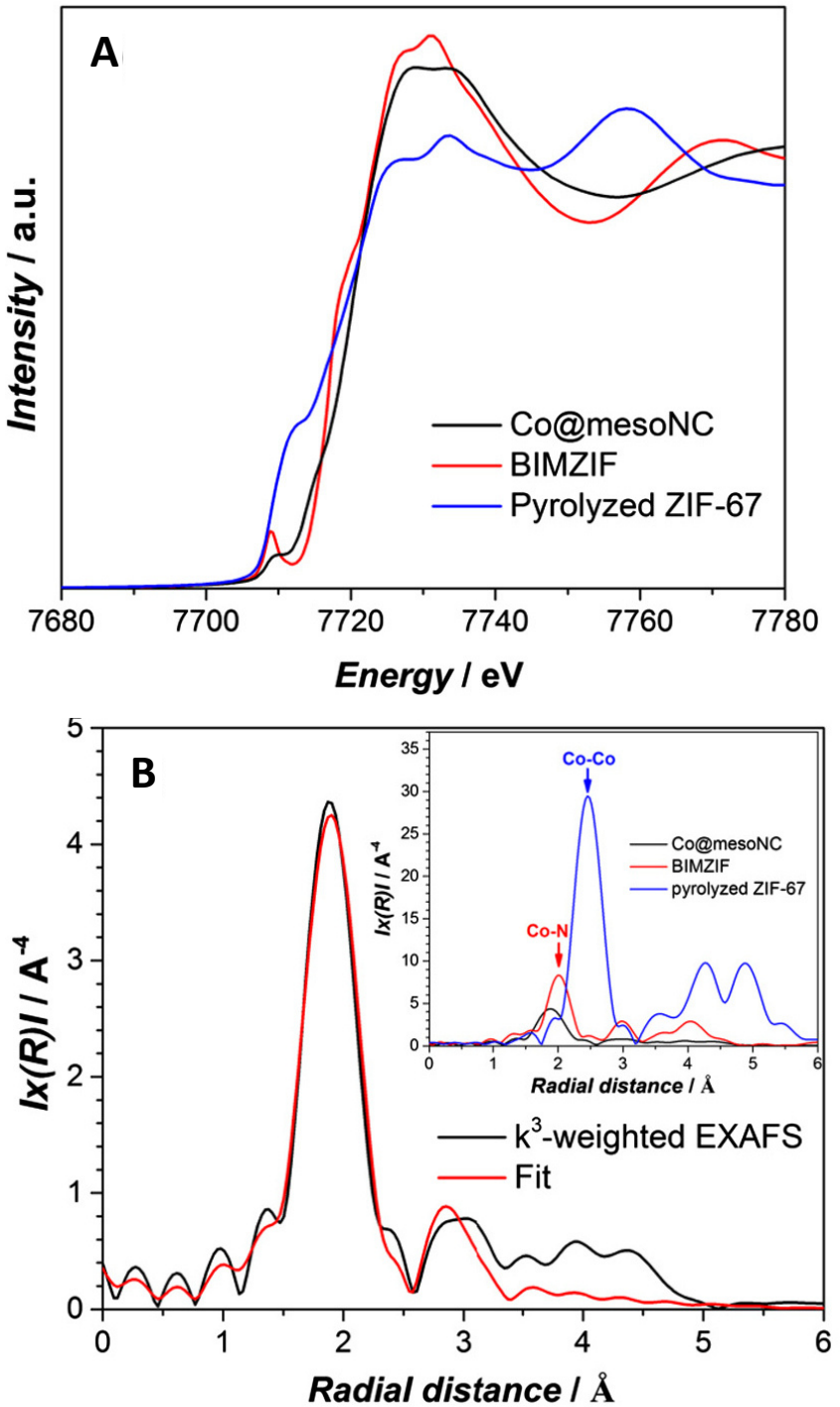

Figure 4.12. XAS characterization of ***2, 5*** and ***6***. (*a*) Co *K*-edge XANES spectra; and (*b*) Fitting of phase corrected k^3-weighted $\chi(k)$-function EXAFS spectra of ***6***, together with the phase corrected EXAFS spectra of ***2*** and ***5*** in the inset.

Table 4.11. EXAFS fitting results of the pyrolyzed ZIF-67 and Co@mesoNC samples.

Sample	Model	Shell Number	Scatterer	Coordination number N/-	Distance *R*/Å	Debye-Waller factor $\Delta\sigma^2$ / Å^2
2	A	1	Co	10.4 ± 1.4	2.493 ± 0.009	0.006 ± 0.001
		2	Co	5.2 ± 0.7	3.50 ± 0.04	0.011 ± 0.005
6	B	1	N	5.7 ± 1.1	1.89 ± 0.02	0.008 ± 0.002
		2	C	11.3 ± 2.3	2.84 ± 0.04	0.018 ± 0.005
		3	N-C	22.6 ± 4.5	3.03 ± 0.07	0.015 ± 0.010
	B*	1	N	4.06 ± 0.95	1.92 ± 0.02	0.006 ± 0.003
		2	C	8.1 ± 1.9	2.89 ± 0.04	0.015 ± 0.006
		3	N-C	16.2 ± 3.8	3.07 ± 0.06	0.021 ± 0.009
			O	1.1 ± 0.4	2.07 ± 0.05	0.006 ± 0.003
	C	1	N	5.2 ± 1.7	1.89 ± 0.03	0.008 ± 0.003
		2	C	10.4 ± 3.5	2.81 ± 0.27	0.054 ± 0.082
		3	Co	-0.4 ± 1.8	2.61 ± 0.09	0.013 ± 0.038

Co *K*-edge XANES and EXAFS spectra of ZIF-67 and ***5*** are nearly identical (Fig. 4.11, 4.12.a), proving that the presence of Zn in ZIF structure does not make any significant changes in the closest coordination environment of cobalt atoms. XANES spectra of both MOFs feature intense pre-edge peaks at 7709 eV, clearly revealing that the local symmetry around cobalt ions is not centrosymmetric and confirming the tetrahedral symmetry of the ZIF structure around central cobalt atoms.[23] The X-ray absorption edge energy (E_0) of 7717 eV suggest the presence of divalent Co in the original framework. XANES and EXAFS spectra of ***2*** and ***4*** are very similar to those of metallic Co foil (E_0 = 7709 eV), further proving that the majority of Co in these samples is present in metallic form.

However, XANES spectra of ***6*** are markedly different from the references (Fig. 4.12a). The energy of the X-ray absorption edge (E_0) at 7720 eV indicates that no metallic cobalt phase is present in the sample. The lower intensity of the pre-edge feature in ***6*** compared to that of the original BIMZIF suggests that the tetrahedral coordination environment of cobalt in the framework changed during the high-temperature pyrolysis process. The similar location of the white line (with a threshold energy of 7731 eV) and the marked differences of the continuous resonance shape between both samples (***5*** and ***6***) also confirm a drastic change in the local geometry around cobalt.[23] However, the shape of XANES spectra of bulk Co oxides also differ from spectra of ***6***, suggesting the different nature of these species.

2, ***5*** and ***6*** samples were also studied in EXAFS region. *R*-space fitting of Co *K*-edge EXAFS spectra from both ZIF-67 and BIMZIF yields a first coordination sphere at 1.99 Å ascribed to the Co-N bonds (insert of Figure 4.12b)[23-24]. After pyrolysis of ZIF-67, the first coordination sphere shifts to a larger bond distance (2.49 Å), typical for Co-Co distances in metal, and fitting of the spectra using only metallic Co model gives a very good agreement (see Table 4.11). Coordination numbers of Co-Co shells obtained from this fit are lower compared to the ideal hexagonal close-packed structure of metallic cobalt. This can indicate that cobalt is present in the form of small clusters without formation of large aggregates.

On the contrary, in case of ***6*** the first coordination sphere around Co is shifted to a lower distance (1.89 Å), closer to the values for the Co-N distance in cobalt(II) phthalocyanine (1.92 Å). However, fitting of ***6*** EXAFS spectra with CoPc model gives the best fit only with increased coordination numbers (5.7 instead of 4 for 1st shell Co-N). Considering that the *1s→3d* pre-edge feature looks similar to the one in distorted octahedral coordination environment, the coordination number of 6 becomes reasonable; however, one would expect the formation of CoN_4 rather than CoN_6 species during the pyrolysis process. As soon as the backscattering amplitudes of N and O are very close, we can propose the formation of square-planar CoN_4 complexes with additional O-containing species (e.g. H_2O) coordinated to Co in the axial position. Using the modified B model (B* model – CoPc with additional Co-O distance), we have obtained the best fit of the experimental data with coordination numbers close to 4 and 1 for Co-N and Co-O paths, respectively. Importantly, in the fittings of the EXAFS signal for ***6*** it was not possible to include any Co-Co scattering paths with reasonable parameters (Table 4.11). This proves that cobalt is atomically dispersed in the sample ***6***.

This case study shows us how the intrinsic limitations of XPS can affect the interpretation of experimental spectra. Chemically different species of the same element can often have very close binding energies (especially in the case of the same oxidation state and a similar chemical surrounding), which can make quantitative XPS analysis significantly more complicated, if not impossible. These issues could be resolved by combination of XPS with complementary techniques which can differentiate these species due to their structural, magnetic or other properties. In this case study XPS was very informative in analysis of nitrogen species and distinguishing Co^0 from Co^{2+}, but could not provide enough information to differentiate cobalt oxide particles from atomically dispersed CoN_x species. In this situation structural methods (XRD, TEM, EXAFS) proved to be very helpful, although the

results of surface XPS and bulk structural analysis should be compared cautiously to avoid misinterpretation.

4.5. Case Study III: Covalent Organic Frameworks as Supports for a Molecular Ni based Ethylene Oligomerization Catalyst

In this Case study we investigate the Ni-based catalyst for ethylene oligomerization ***8,*** which was prepared by reaction of Ni^{2+} precursor with the imine-linked polymer network ***7*** (see Fig.4.13). It is particularly important to determine whether nickel in ***8*** is coordinated to the framework as isolated atomically dispersed sites or it is present on the surface of ***7*** in a form of non-coordinated species (oxides, hydroxides, etc.). In order to study deeper the coordination environment of nickel in ***8*** catalyst the combination of XPS and XAS techniques was applied. This case study shows how the combination of these techniques can be used for characterization of the active site of transitional metal-based heterogeneous catalyst.

An informative approach in this case is the comparison of bulk (ICP-OES) and surface (XPS) elemental analysis results. Figure 4.14.a and Table 4.12 show the survey XPS spectra and the results of XPS quantification, respectively, for ***7*** and ***8***. Bulk elemental analysis states that total nickel content in ***8*** is 4.7 wt%, which is close to 4.4 wt% obtained from XPS quantification. This result indicates that nickel is homogeneously distributed throughout the catalyst. Absence of any Ni-containing nanoparticles on TEM images of ***8*** (Fig. 4.15) further confirms uniform nickel distribution.

In order to reveal the chemical state of Ni in the catalysts, high resolution spectra of N*1s* and Ni*2p* line were analysed (Fig. 4.14b and 4.14c). The Ni*2p* spectrum of ***8*** represents the line shape typical for Ni^{2+} compounds. The main Ni$2p_{3/2}$ peak at 855.1 eV definitely does not correspond to Ni(II) oxide NiO (main peak at 853.7 eV),[25] but is in the range of typical values for many Ni-O and Ni-N complexes.[26]

Fig. 4.14.b shows N*1s* line of ***7*** before and after introduction of Ni. The main peak of N*1s* line with binding energy of about 398.4 eV is clearly shifted to a higher binding energy (399.1 eV) in case of ***8***. This shift indicates the donation of electron density from N atoms, which is normally observed upon coordination of N-containing groups to metal ions.[27] Additional peaks with a higher binding energy (399.9 eV, 401.6 eV), which can be observed in the N*1s* line of ***7***, disappear after Ni coordination. These peaks can be attributed

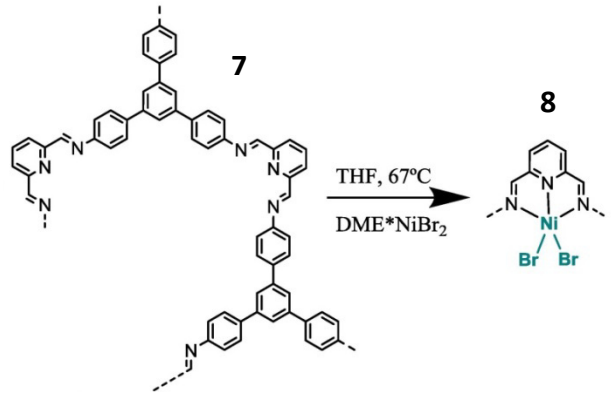

Figure 4.13. Synthesis of ***8*** through expected coordination of Ni^{2+} to the nitrogen species in ***7***.

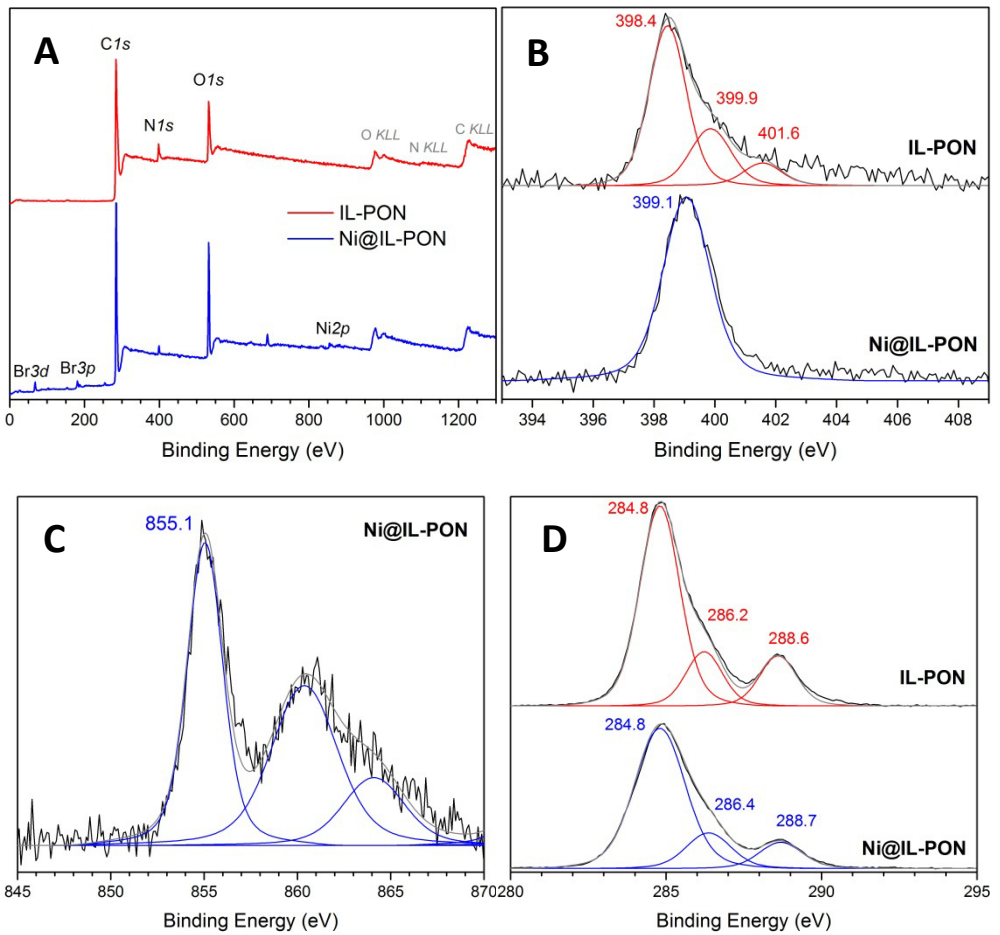

Figure 4.14. XP spectra of ***7*** and ***8***: survey (*a*), N*1s* (*b*), Ni$2p_{3/2}$ (*c*), and C*1s* (*d*).

Table 4.12. Surface composition of ***7*** and ***8***.

	Atomic percentage					Weight percentage				
	C	N	O	Ni	Br	C	N	O	Ni	Br
7	83.2	2.4	14.4	-	-	79.1	2.7	18.3		
8	76.3	2.0	18.4	1.1	2.2	61.9	1.8	19.9	4.4	12.1

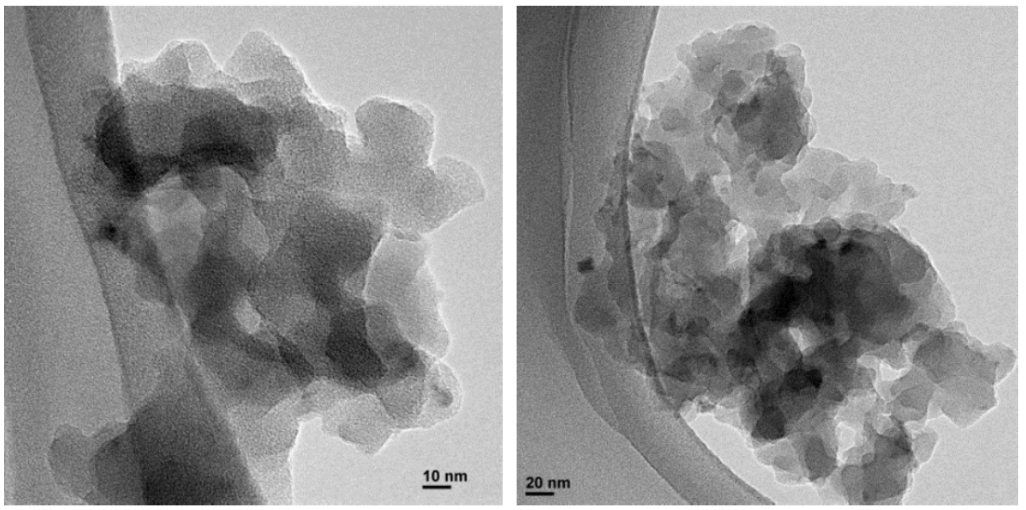

Figure 4.15. TEM images of ***8***.

to unreacted monomer and other non-framework species removed during the process of Ni introduction and washing. C*1s* and O*1s* spectra do not show any distinctive difference between ***7*** and ***8*.** Thus, we can conclude that XPS characterisation confirms coordination of nickel to the nitrogen sites of ***7*** and its homogeneous distribution within the catalyst.

Based on the atomic ratio of 1:2 between Ni and Br in ***8*** (see Table 4.12) one might think that nickel is coordinated to the framework in a form of $NiBr_2$ species, similar to schematic representation of ***8*** on Figure 4.13. However, solely XPS data are not sufficient to support this statement. In order to investigate further the coordination environment of nickel atoms in ***8***, the catalyst was characterized by XAS.

Fig. 4.16 shows the fitted Ni *K*-edge EXAFS spectra of ***8*** and of reference compounds $NiCl_2$•$6H_2O$ and DME•$NiBr_2$. For the fitting of DME•$NiBr_2$ EXAFS spectra the structure of a similar compound NiI_2•$(DME)_2$ was used as a model[28]. Iodine atoms of the initial NiI_2•$(DME)_2$ structure were replaced by

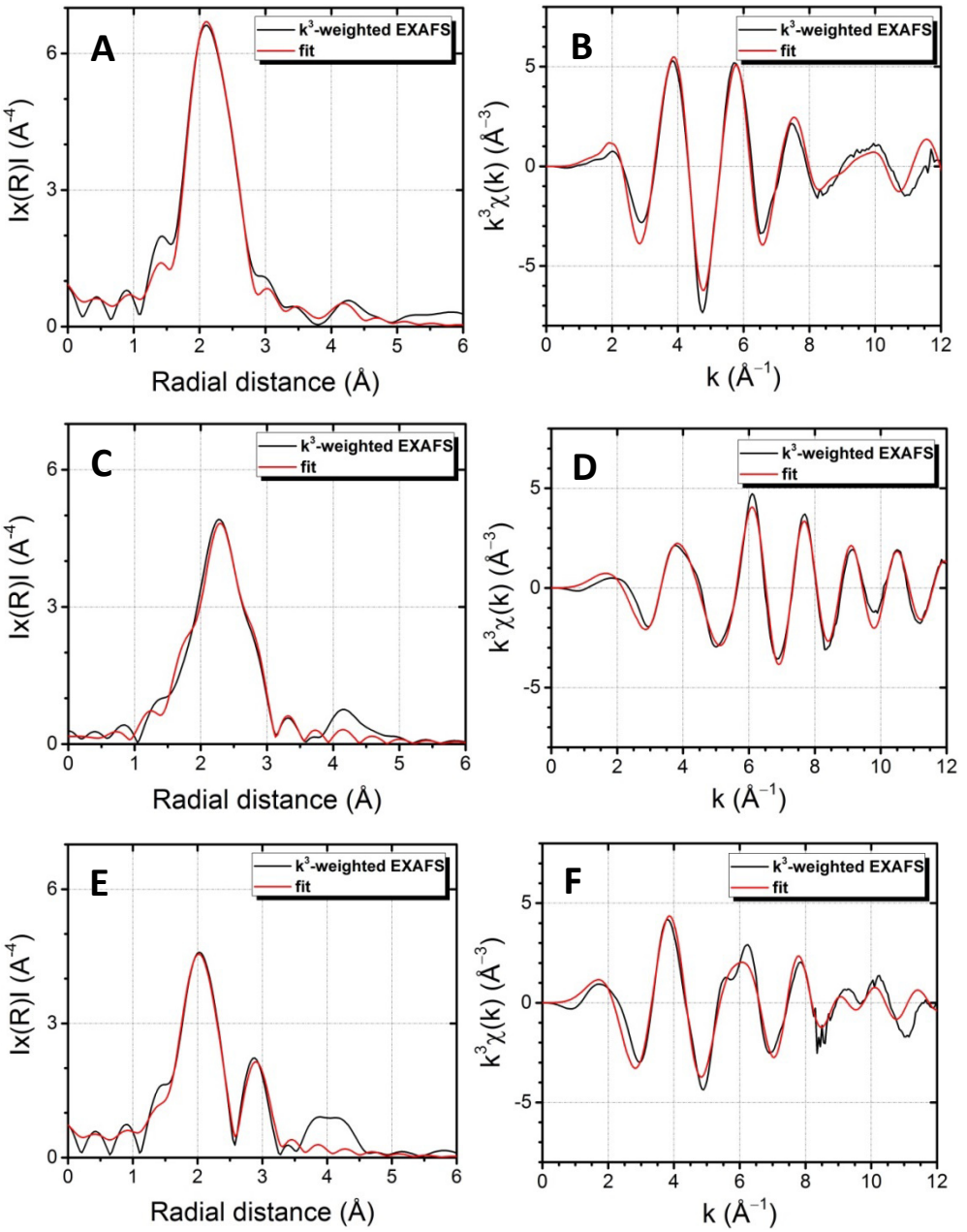

Figure 4.16. Phase-corrected plots of EXAFS spectrum fittings for $NiCl_2 \cdot 6H_2O$ (a,b), DME·$NiBr_2$ (c,d), and ***8*** (e,f; fitted using NiO model).

Table 4.13. EXAFS fitting results of DME·$NiBr_2$ and ***8***.

Sample	Model	Shell Number	Scat-terer	Coordination number N/-	Distance *R*/Å	Debye-Waller factor $\Delta\sigma^2$ / Å^2
DME•$NiBr_2$	$NiBr_2$•$(DME)_2$	1 2	O Br	4.9 ± 0.8 2.5 ± 0.4	2.03 ± 0.01 2.460 ± 0.007	0.013 ± 0.003 0.009 ± 0.001
8	$NiBr_2$•$(DME)_2$	1 2	O Br	9 ± 1 4.4 ± 0.6	2.05 ± 0.02 2.82 ± 0.03	0.016 ± 0.003 0.020 ± 0.003
	$NiBr_2N_3L$	1 2	N Br	13 ± 3 0.5 ± 1.4	2.09 ± 0.03 2.41 ± 0.05	0.018 ± 0.004 0.01 ± 0.02
	$Ni(OH)_2$	1 2	O Ni	7 ± 1 -2 ± 2	2.06 ± 0.02 3.13 ± 0.04	0.016 ± 0.004 0.013 ± 0.013
	NiO	1 2	O Ni	7 ± 1 1.2 ± 0.9	2.06 ± 0.01 2.89 ± 0.02	0.015 ± 0.003 0.008 ± 0.006

bromine and the potentials were recalculated in Artemis software before using them for fitting. Fitting of DME•$NiBr_2$ EXAFS spectra with non-fixed coordination numbers results in increase of coordination number in the first shell (4.9 ± 0.8), which implies possible coordination of additional ligands (*e.g.* water molecules) to nickel atoms (Table 4.13). Fitting also gives Ni-Br bond distance of 2.46 Å, which is shorter than in pure $NiBr_2$ (2.585 Å).

Fitting of EXAFS spectra for ***8*** was performed using the models of $NiBr_2$•$(DME)_2$, nickel(II) oxide NiO, nickel(II) hydroxide $Ni(OH)_2$, and diiminopyridine complex of $NiBr_2$ [29] (further denoted as $NiBr_2N_3L$), which structure is similar to the expected coordination of $NiBr_2$ to ***7***. Table 4.12 shows that only in case of the NiO model a good fit could be obtained with reasonable parameters ($\sigma^2 > 0$, without negative or too large coordination numbers and with realistic bond distances). It should be noted that Ni-Ni bond in this case has a coordination number of 1.2 ± 0.9 (instead of 12 in pure NiO structure). This indicates that nickel in ***8*** can be present in a form of dimers or small clusters, but not as bulk oxide particles. Introduction of additional Ni-Br distances into the fitting did not allow to obtain a good fit, indicating that most likely bromine is not present in the close proximity of nickel atoms but rather rests in the outer coordination sphere.

This case study shows the importance of choosing the reasonable combination of complementary methods for characterization of catalysts. Knowing the intrinsic limitations of methods and the scale they are applicable on, one can estimate their relevance for each particular type of samples and use the most informative ones to describe comprehensively

the relations between structural, electronic and catalytic properties of catalysts.

4.6. Conclusions

In these three Case studies it is demonstrated how an appropriate combination of characterization tools enables catalyst understanding at chemical and structural levels. In Case study I we were able to simultaneously quantify C and O species in nanotube catalysts with XPS. In Case study II XPS was used to differentiate N species and, in combination with other spectroscopic methods (XAS, TEM), to distinguish Co species in different oxidation states and coordination environment. In Case study III XPS could be used to confirm the coordination of Ni species to N sites in the polymer. A complementary EXAFS study showed that Ni is preferentially present in the form of oligomers and neither $NiBr_2$ species nor NiO particles are present in the catalyst.

Based on these Case studies, we can see that XPS is very informative for distinguishing species of a certain element in different oxidation states, but becomes less suitable for differentiation of species with the same oxidation state but different chemical environment. In this situation combining XPS with structure characterization methods (TEM, EXAFS, grazing incidence XRD, SAXS) is beneficial as they can provide the missing information due to different structural features of the species that appear similar in XPS. The Case studies show, that this characterisation strategy has a relatively broad range of applicability, as it is suitable for different types of carbon materials with various loading of metals. Combination of XPS with other methods (*e.g.* solid state NMR) might also provide similar information, but could be problematic due to magnetic properties of samples, relatively high cost and limited availability.

4.7. Appendix

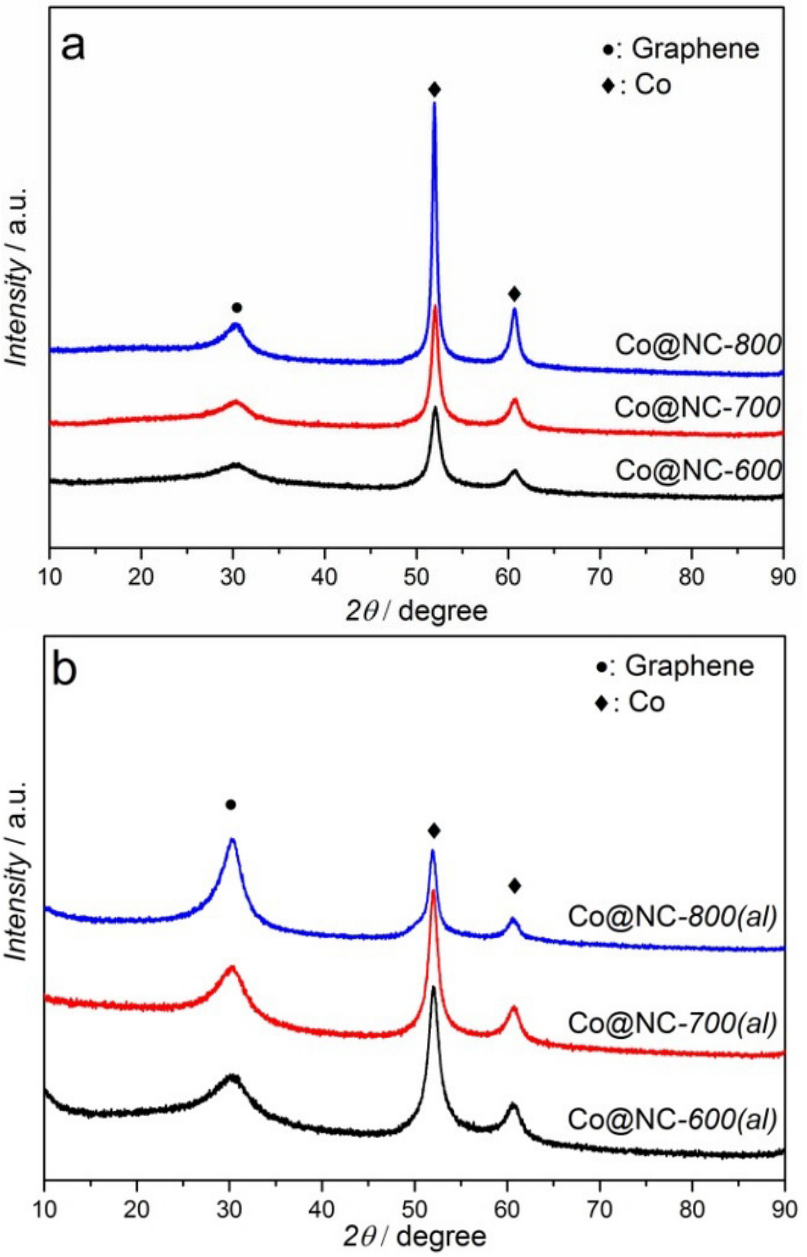

Figure 4.17. XRD patterns of Co@NC samples: *a*) ***2, 3, 4*** and *b*) ***2a, 3a, 4a***.

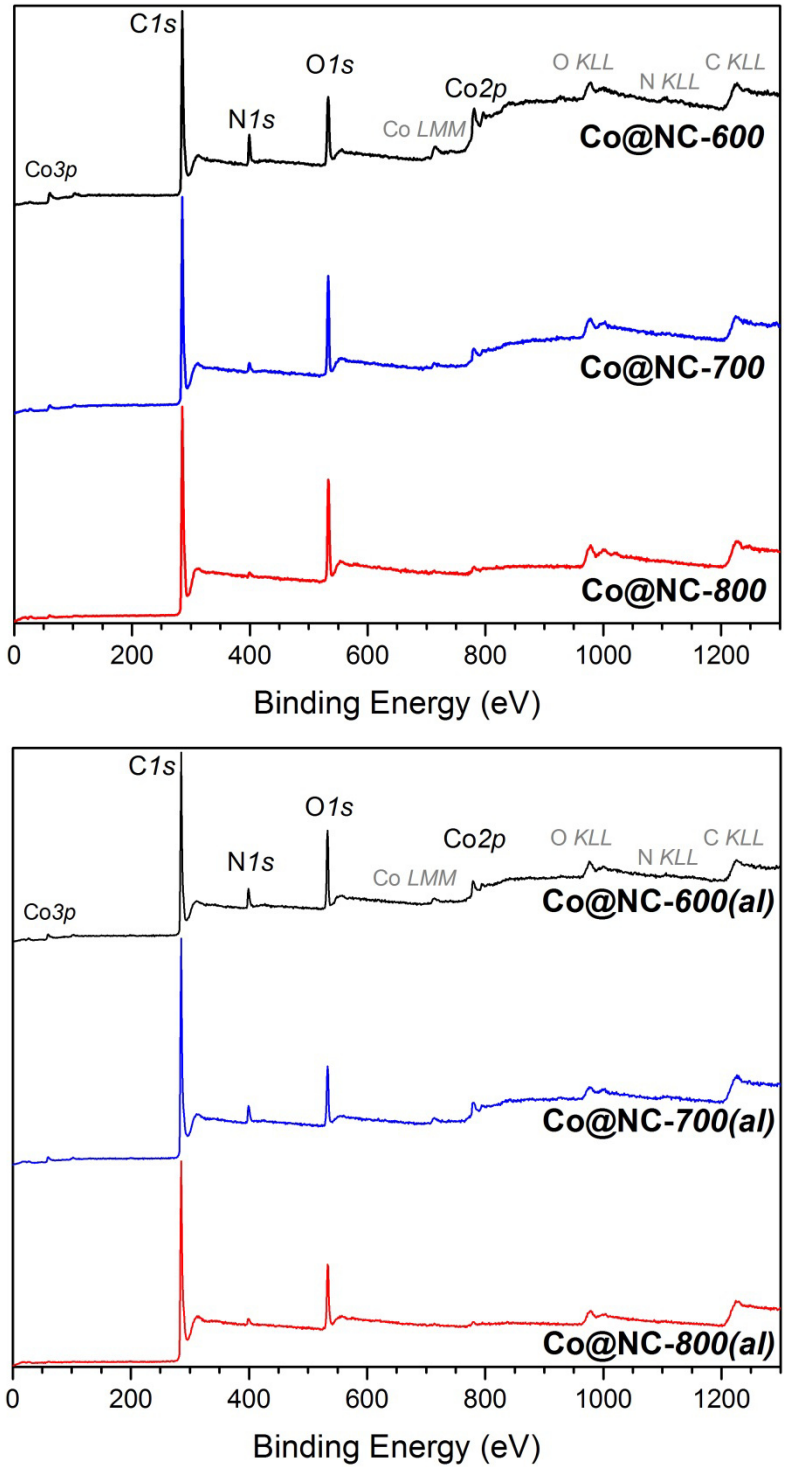

Figure 4.18. Survey XP spectra of Co@NC samples: ***2, 3, 4*** (*top*), and ***2a, 3a, 4a*** (*bottom*).

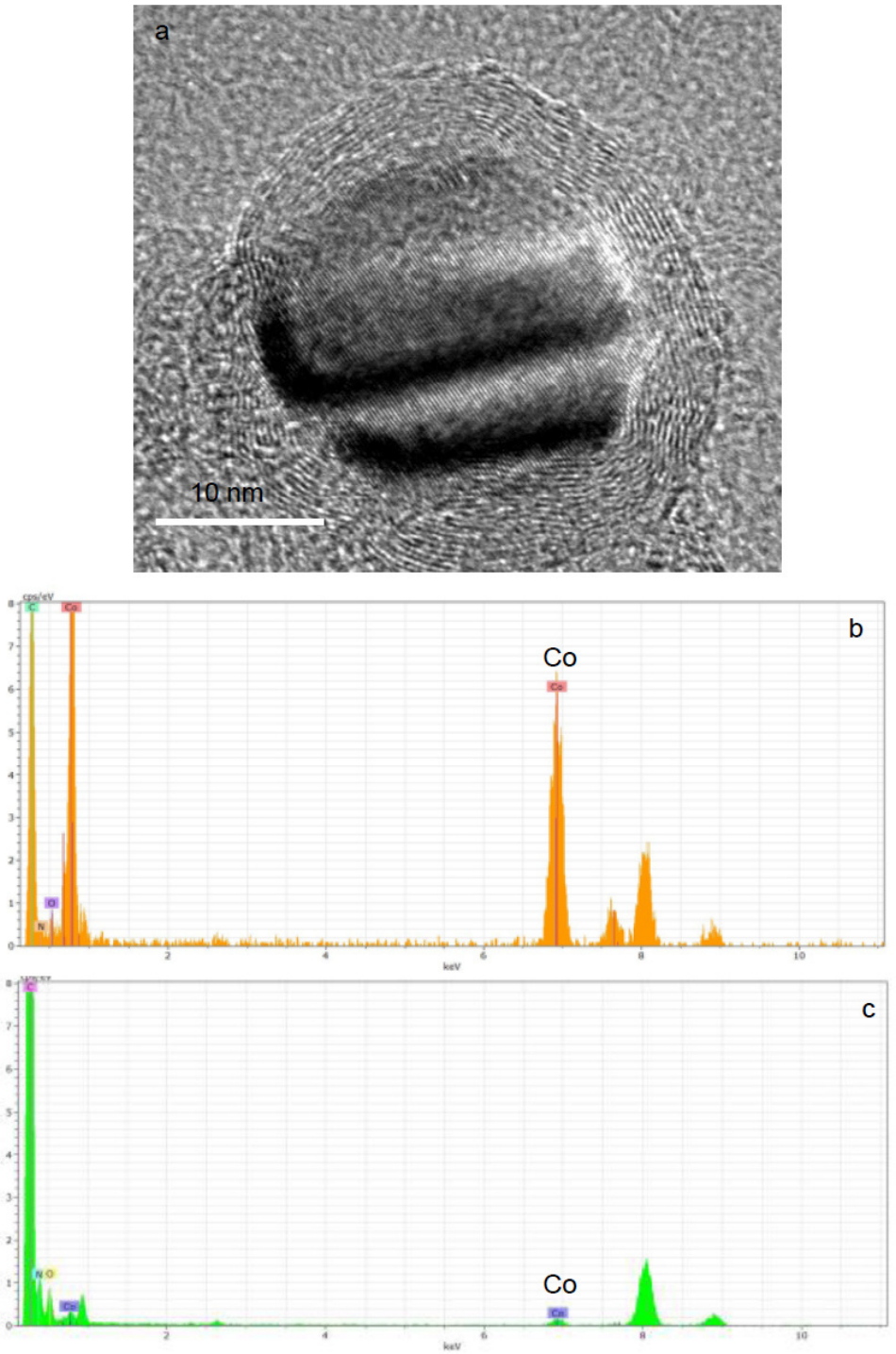

Figure 4.19. (*a*) HR-TEM of ***4a***, in which a Co crystallite encapsulated in a layered graphene shell can be clearly distinguished. EDXS analysis of ***4a*** from (*b*) area 1 and (*c*) area 2 in **Figure 4.8.b**.

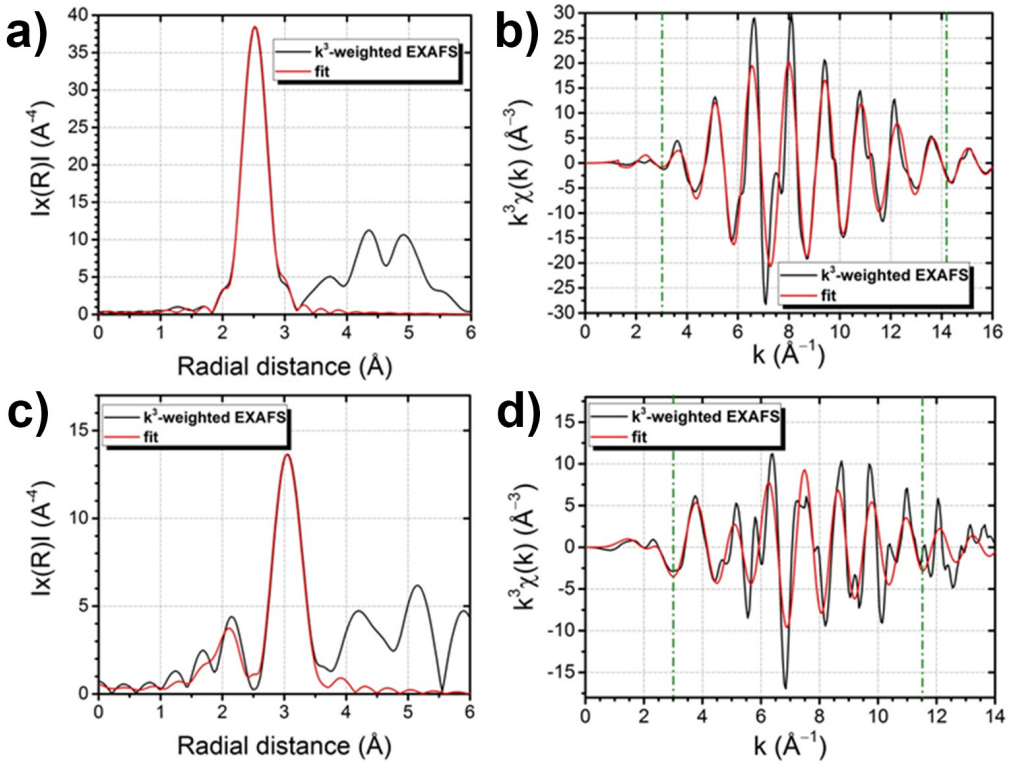

Figure 4.20. Reference materials. Phase-corrected plots of EXAFS spectrum fittings for Co foil (*a,b*) and CoO (*c,d*).

4.8. References

1. Corma, A.; Serna, P., Chemoselective hydrogenation of nitro compounds with supported gold catalysts. *Science* **2006,** *313* (5785), 332-334.
2. Jagadeesh, R. V.; Surkus, A. E.; Junge, H.; Pohl, M. M.; Radnik, J.; Rabeah, J.; Huan, H.; Schuñemann, V.; Brückner, A.; Beller, M., Nanoscale Fe2O3-based catalysts for selective hydrogenation of nitroarenes to anilines. *Science* **2013,** *342* (6162), 1073-1076.
3. Westerhaus, F. A.; Jagadeesh, R. V.; Wienhöfer, G.; Pohl, M. M.; Radnik, J.; Surkus, A. E.; Rabeah, J.; Junge, K.; Junge, H.; Nielsen, M.; Brückner, A.; Beller, M., Heterogenized cobalt oxide catalysts for nitroarene reduction by pyrolysis of molecularly defined complexes. *Nature Chemistry* **2013,** *5* (6), 537-543.
4. Wang, X.; Li, Y., Chemoselective hydrogenation of functionalized nitroarenes using MOF-derived co-based catalysts. *Journal of Molecular Catalysis A: Chemical* **2016,** *420*, 56-65.
5. Cheng, T.; Yu, H.; Peng, F.; Wang, H.; Zhang, B.; Su, D., Identifying active sites of CoNC/CNT from pyrolysis of molecularly defined complexes for oxidative esterification and hydrogenation reactions. *Catalysis Science & Technology* **2016,** *6* (4), 1007-1015.
6. Bianchini, C.; Giambastiani, G.; Luconi, L.; Meli, A., Olefin oligomerization, homopolymerization and copolymerization by late transition metals supported by (imino)pyridine ligands. *Coordination Chemistry Reviews* **2010,** *254* (5), 431-455.
7. Killian, C. M.; Johnson, L. K.; Brookhart, M., Preparation of linear α-olefins using cationic nickel(II) α-diimine catalysts. *Organometallics* **1997,** *16* (10), 2005-2007.
8. Sun, X.; Olivos-Suarez, A. I.; Oar-Arteta, L.; Rozhko, E.; Osadchii, D.; Bavykina, A.; Kapteijn, F.; Gascon, J., Metal–Organic Framework Mediated Cobalt/Nitrogen-Doped Carbon Hybrids as Efficient and Chemoselective Catalysts for the Hydrogenation of Nitroarenes. *ChemCatChem* **2017,** *9* (10), 1854-1862.
9. Sun, X.; Olivos-Suarez, A. I.; Osadchii, D.; Romero, M. J. V.; Kapteijn, F.; Gascon, J., Single cobalt sites in mesoporous N-doped carbon matrix for selective catalytic hydrogenation of nitroarenes. *Journal of Catalysis* **2018,** *357*, 20-28.
10. Rozhko, E.; Bavykina, A.; Osadchii, D.; Makkee, M.; Gascon, J., Covalent organic frameworks as supports for a molecular Ni based ethylene oligomerization catalyst for the synthesis of long chain olefins. *Journal of Catalysis* **2017,** *345*, 270-280.

11. Tanuma, S.; Powell, C. J.; Penn, D. R., Calculations of electron inelastic mean free paths. V. Data for 14 organic compounds over the 50–2000 eV range. *Surface and Interface Analysis* **1994,** *21* (3), 165-176.

12. Grunes, L. A., Study of the *K*-edges of *3d* transition metals in pure and oxide form by x-ray-absorption spectroscopy. *Physical Review B* **1983,** *27* (4), 2111-2131.

13. Ravel, B.; Newville, M., ATHENA, ARTEMIS, HEPHAESTUS: data analysis for X-ray absorption spectroscopy using IFEFFIT. *Journal of Synchrotron Radiation* **2005,** *12* (4), 537-541.

14. Beamson, G.; Briggs, D., *High Resolution XPS of Organic Polymers: The Scienta ESCA300 Database*. Wiley: **1992**.

15. Susi, T.; Pichler, T.; Ayala, P., X-ray photoelectron spectroscopy of graphitic carbon nanomaterials doped with heteroatoms. *Beilstein Journal of Nanotechnology* **2015,** *6*, 177-192.

16. Torad, N. L.; Hu, M.; Ishihara, S.; Sukegawa, H.; Belik, A. A.; Imura, M.; Ariga, K.; Sakka, Y.; Yamauchi, Y., Direct synthesis of MOF-derived nanoporous carbon with magnetic Co nanoparticles toward efficient water treatment. *Small* **2014,** *10* (10), 2096-2107.

17. Biesinger, M. C.; Payne, B. P.; Grosvenor, A. P.; Lau, L. W. M.; Gerson, A. R.; Smart, R. S. C., Resolving surface chemical states in XPS analysis of first row transition metals, oxides and hydroxides: Cr, Mn, Fe, Co and Ni. *Applied Surface Science* **2011,** *257* (7), 2717-2730.

18. Kapteijn, F.; Moulijn, J. A.; Matzner, S.; Boehm, H. P., Development of nitrogen functionality in model chars during gasification in CO2 and O2. *Carbon* **1999,** *37* (7), 1143-1150.

19. Pels, J. R.; Kapteijn, F.; Moulijn, J. A.; Zhu, Q.; Thomas, K. M., Evolution of nitrogen functionalities in carbonaceous materials during pyrolysis. *Carbon* **1995,** *33* (11), 1641-1653.

20. Stańczyk, K.; Dziembaj, R.; Piwowarska, Z.; Witkowski, S., Transformation of nitrogen structures in carbonization of model compounds determined by XPS. *Carbon* **1995,** *33* (10), 1383-1392.

21. Chen, Y. Z.; Wang, C.; Wu, Z. Y.; Xiong, Y.; Xu, Q.; Yu, S. H.; Jiang, H. L., From Bimetallic Metal-Organic Framework to Porous Carbon: High Surface Area and Multicomponent Active Dopants for Excellent Electrocatalysis. *Advanced Materials* **2015,** *27* (34), 5010-5016.

22. Yin, P.; Yao, T.; Wu, Y.; Zheng, L.; Lin, Y.; Liu, W.; Ju, H.; Zhu, J.; Hong, X.; Deng, Z.; Zhou, G.; Wei, S.; Li, Y., Single Cobalt Atoms with Precise N-Coordination as Superior Oxygen Reduction Reaction Catalysts. *Angewandte Chemie International Edition* **2016,** *55* (36), 10800-10805.

23. Hillman, F.; Zimmerman, J. M.; Paek, S.-M.; Hamid, M. R. A.; Lim, W. T.; Jeong, H.-K., Rapid microwave-assisted synthesis of hybrid zeolitic-

imidazolate frameworks with mixed metals and mixed linkers. *Journal of Materials Chemistry A* **2017,** *5* (13), 6090-6099.

24. Yin, P.; Yao, T.; Wu, Y.; Zheng, L.; Lin, Y.; Liu, W.; Ju, H.; Zhu, J.; Hong, X.; Deng, Z.; Zhou, G.; Wei, S.; Li, Y., Single Cobalt Atoms with Precise N-Coordination as Superior Oxygen Reduction Reaction Catalysts. *Angewandte Chemie International Edition* **2016,** *55* (36), 10800-10805.
25. Biesinger, M. C.; Payne, B. P.; Lau, L. W. M.; Gerson, A.; Smart, R. S. C., X-ray photoelectron spectroscopic chemical state Quantification of mixed nickel metal, oxide and hydroxide systems. *Surface and Interface Analysis* **2009,** *41* (4), 324-332.
26. Matienzo, J.; Yin, L. I.; Grim, S. O.; Swartz, W. E., X-ray photoelectron spectroscopy of nickel compounds. *Inorganic Chemistry* **1973,** *12* (12), 2762-2769.
27. Artyushkova, K.; Kiefer, B.; Halevi, B.; Knop-Gericke, A.; Schlogl, R.; Atanassov, P., Density functional theory calculations of XPS binding energy shift for nitrogen-containing graphene-like structures. *Chem. Commun.* **2013,** *49* (25), 2539-2541.
28. Crochet, A.; Fromm, Katharina M., Polyether Adducts of d-Block Metal Compounds as Starting Materials for New Cluster Compounds. *Zeitschrift für anorganische und allgemeine Chemie* **2010,** *636* (8), 1484-1496.
29. Gao, R.; Zhang, M.; Liang, T.; Wang, F.; Sun, W.-H., Nickel(II) Complexes Chelated by 2-Arylimino-6-benzoxazolylpyridine: Syntheses, Characterization, and Ethylene Oligomerization. *Organometallics* **2008,** *27* (21), 5641-5648.

5

Revisiting nitrogen species in covalent triazine frameworks

Covalent triazine frameworks (CTFs) are porous organic materials promising for applications in catalysis and separation due to their high stability, adjustable porosity and intrinsic nitrogen functionalities. CTFs are prepared by ionothermal trimerization of aromatic nitriles, however, multiple side reactions also occur under synthesis conditions, and their influence on the material properties is still poorly described. Here we report the systematic characterization of nitrogen in CTFs using X-ray photoelectron spectroscopy (XPS). With the use of model compounds, we could distinguish several types of nitrogen species. By combining these data with textural properties, we unravel the influence that the reaction temperature, the catalyst and the monomer structure and composition have on the properties of the resulting CTF materials.

This chapter is based on the following publication:
Revisiting nitrogen species in covalent triazine frameworks
D. Osadchii, A. I. Olivos Suarez, A. V. Bavykina, J. Gascon, *Langmuir (2017), 33, 50, 14278.*

5.1. Introduction

Porous organic frameworks (POFs) consist of organic monomers linked by covalent bonds and have recently found many applications in the fields of catalysis and separation.[1-2] Variation of the monomer units results in a wide range of materials with different pore size distributions and various functionalities. Owing to their high structural and functional tunability, POFs offer numerous advantages when compared to traditional inorganic materials. Thus, the development of new POF structures and their applications have been intensively researched over the last decade. Covalent triazine frameworks (CTFs) are among the most popular POF classes because they are composed of rigid conjugated aromatic networks with high thermal and chemical stability as well as very high porosity.[3] CTFs are synthesized from relatively cheap aromatic nitriles and are formed by Lewis acid-mediated nitrile trimerization[3-7] (Scheme 5.1), although alternative synthetic routes are also possible.[7-8]

Intrinsic nitrogen functionalities within the structure make CTFs very attractive materials for the coordination of metals,[9-13] as well as for selective adsorption.[4, 14-15] Since the first synthesis of CTFs using $ZnCl_2$ as catalyst,[3] several attempts have been made to rationalize and optimize their synthesis. Extensive studies of the ionothermal synthetic conditions have shown that the framework porosity strongly depends on the synthesis temperature and the amount of catalyst used to promote the nitrile trimerization.[3, 16-18] An increase of the polymer mesoporosity is observed with raising the synthesis temperature from 400 °C to 700 °C, although at the expense of structure regularity. This effect can be a result of two factors: i) irreversible C-C and C-N bond formation under Lewis-acid catalyzed conditions (e.g. Diels-Alder type reactions,[19] Scheme 5.2) and/or ii) carbonization of the material at high temperature. However, detailed studies have not been performed either on the nature of intermediate species or on the polymerization mechanism. Synthesis at lower temperature and extended time (300 °C for 7 days) prevents these side reactions, but leads to a mixture of aryl-triazine oligomers (ATOs)[20] with negligible to moderate porosity and surface area, rather than to a porous framework.

Most of the research dedicated to tuning the porosity by modifying the CTFs synthetic procedure has only been published on **CTF-1**, prepared from the monomer terephthalonitrile, **1** (Scheme 5.1a).[17, 21] Access to CTFs with different functionalities is crucial for their application. **CTF-10**, synthesized

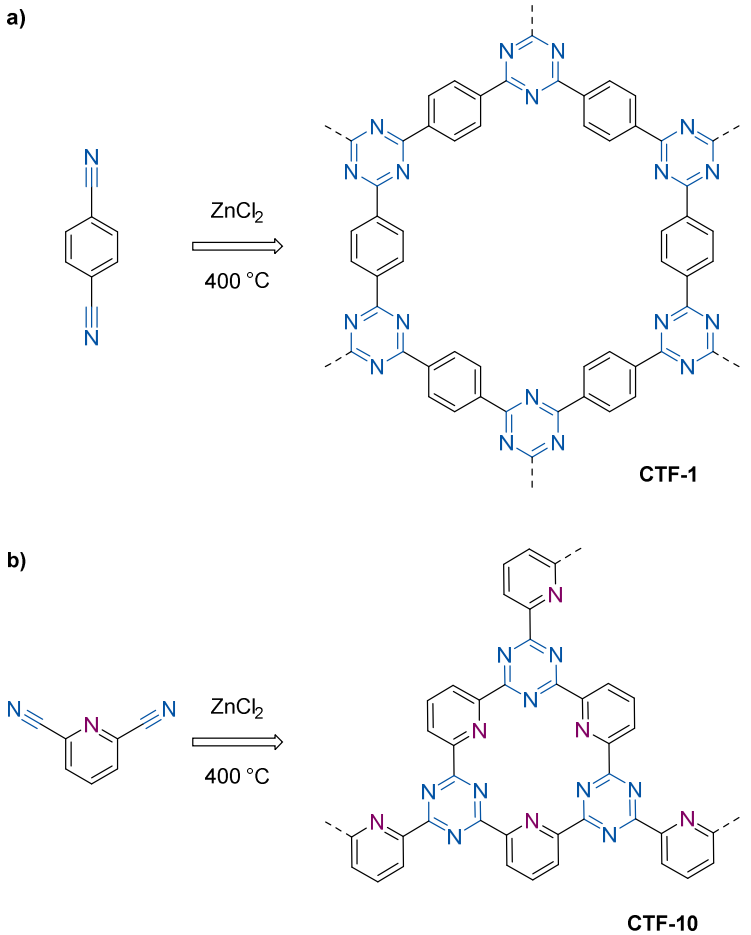

Scheme 5.1. Synthesis of CTFs from a) terephthalonitrile (**1**) and b) 2,6-pyridinedicarbonitrile (**2**) (idealized CTF structures).

from 2,6-pyridinedicarbonitrile (**2**), contains suitable pincer-like pyridinic-triazinic sites for metal coordination. The synthesis of **CTF-10** compared to that of **CTF-1** represents a more complicated process. Preferential zinc binding to the pyridine moieties promotes the activation of neighboring nitrile groups, causing back-donation from Zn d_{xz} and d_{yz} orbitals to the anti-bonding π^*-orbital of the nitrile (C≡N) group. This back donation can favor the trimerization reaction, as well as promote various side reactions. As a result of these additional side reactions, **CTF-10** has a significantly lower porosity than **CTF-1**.[18]

It should be noted that most of CTFs are amorphous dark materials with strong absorbance in the spectral range of many common spectroscopic

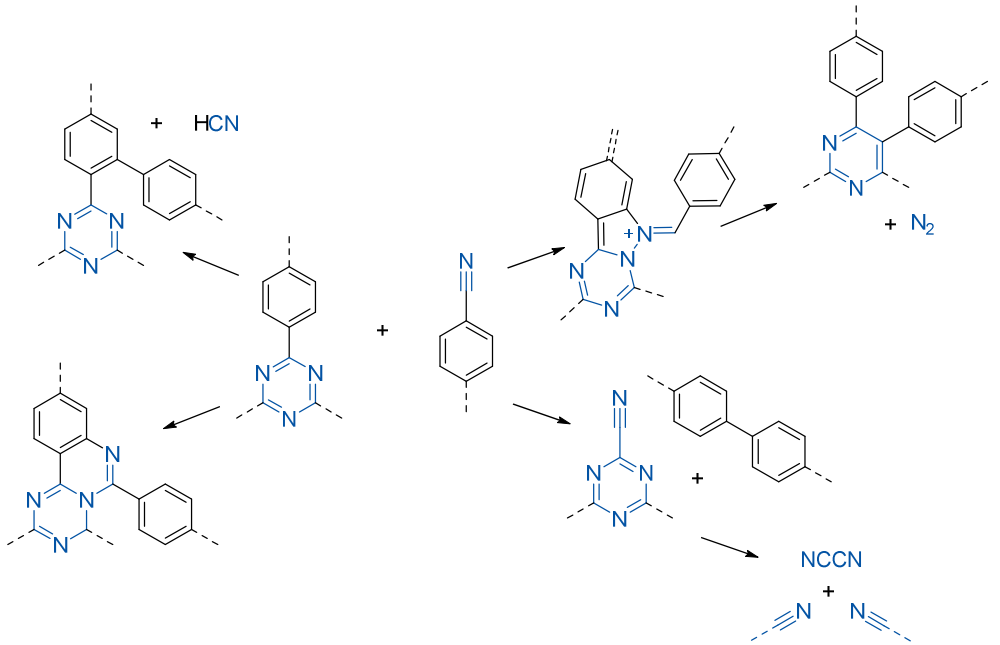

Scheme 5.2. Possible side reactions during the CTF synthesis at elevated temperatures.

techniques. These features make the characterization of these materials difficult and hamper a better understanding of their structural and chemical properties. In contrast, the ATOs usually display a yellow color and can be characterized by methods involving visible and ultraviolet light irradiation.[20] Although ATOs can be considered as model compounds for CTF characterization, synthesis of CTFs from ATOs is still accompanied by some degree of amorphization giving rise to a variety of new carbon and nitrogen species that cannot be easily characterized. Alternative spectroscopies that use higher energy (XAS, XPS)[10, 22] or are based on magnetic properties (CP-MAS solid-state NMR)[14-15, 21-22] become a common and useful tool for the challenging characterization of these materials. Moreover, due to the gamut of species present in the amorphous CTFs, interpretation of experimental data becomes challenging and demands in-depth study of the materials.

The relatively broad range of N*1s* binding energies makes X-ray photoelectron spectroscopy (XPS) a useful tool for characterization of species containing multiple nitrogen moieties in different electronic environments. XPS has already been successfully applied to a variety of carbon-nitrogen materials including carbon nitrides,[23] N-functionalized

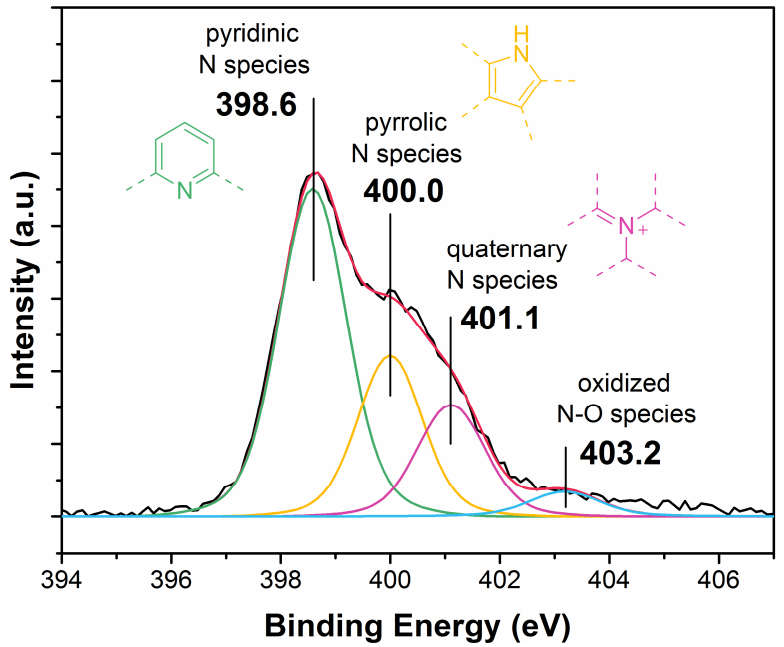

Figure 5.2. Deconvolution of the N1s spectrum of CTF-10 (ionothermal synthesis with 5 equivalents of $ZnCl_2$ at 500 ºC for 48 h) with a typical peak assignment according to the literature.

amorphous carbons,[24-26] N-doped carbon nanotubes and graphenes[27-28] and N-containing organic polymers.[29] However, non-systematic use of the method can provide only limited knowledge. As an example, the typical deconvolution[22] of the N*1s* spectrum for **CTF-10** (Fig. 5.1) merely relies on assignments reported in the literature for amorphous carbons.

In this work, we show the opportunities that XPS offers for characterization of CTFs. By using XPS together with characterization of the textural properties we critically review CTF ionothermal synthesis and highlight the impact that different monomers, synthesis temperature and catalysts have on the final properties of these solids. Through a correlated study of model compounds, we are able to assign a number of nitrogen species that until now have been elusive and assigned only on basis of nitrogen containing organic polymers and carbonaceous supports.

5.2. Experimental section

5.2.1. Synthesis of CTFs

The synthesis procedure for CTF materials was similar to the one reported by Kuhn *et al.*[3] Various dicarbonitrile monomers, trimerization catalysts

(inorganic Lewis acids) and reaction temperatures were used for different samples. All samples reported in this work and details of their preparation are summarized in Table 5.1. In a typical synthesis, a quartz ampoule was charged with the mixture of corresponding nitriles and an anhydrous metal salt in a molar ratio of nitriles:chloride = 1:5 inside the glovebox. The ampoule was flame sealed and heated to the desired temperature with a heating rate of 1 °C·min^{-1}, kept at this temperature for 48 h and then cooled to room temperature. The product was consequently washed in 15% HCl solution at 100 °C, in 15% NH_4OH solution at 60 °C, in H_2O at 100 °C and finally in THF at 60 °C overnight. The resulting powder was dried under vacuum at 180 °C overnight. The overall yield was typically in the range of 90-98%.

5.2.2. Synthesis of model compounds

Complexes **4-Cu** and **5-Cu** (Fig. 5.2) were prepared from commercially available 2,4,6-triphenyl-1,3,5-triazine (**4**) and 2,4,6-tris(2-pyrydyl)-1,3,5-triazine (**5**), respectively. In a typical synthesis, a mixture 1:1 molar ratio of the corresponding ligand and the tetrakis(acetonitrile)copper(I) hexafluorophosphate salt ($Cu(MeCN)_4PF_6$) was dissolved in methanol and set under reflux at 80 °C overnight. The resulting solids were filtered and dried in air at 80 °C.

5.2.3. Synthesis of Cu-CTF-10

496 mg CTF-10 and 250 mg copper(II) acetate monohydrate were mixed in 20 mL methanol under constant stirring with reflux at 80 °C overnight. The resulting black solid was filtered and dried in air at 80 °C.

5.2.4. X-ray photoelectron spectroscopy

XPS measurements were performed on a *K*-alpha Thermo Fisher Scientific spectrometer using a monochromatic Al *Kα* X-ray source. In a typical experiment, the sample powder was mounted on a double-faced conducting carbon tape (NEM TAPE, Nisshin EM Co., Ltd.), attached to a sample holder. The holder with the mounted samples was loaded into the sample loading chamber and set under vacuum to reach $2 \cdot 10^{-7}$ mbar. At this pressure, the sample holder was transferred into the analysis chamber and set to reach c.a. 10^{-8} mbar. The X-ray gun was operated at 3 mA and 12 kV and the spot size was set to 400 μm. Precision spectra of the core photoelectron lines were registered with 0.1 eV energy step using constant

Table 5.1. Synthesis conditions and textural properties of CTFs.

Sample[a]	2	2a	3	BET area, $m^2 g^{-1}$	Total pore volume, $cm^3 g^{-1}$	Micropore volume, $cm^3 g^{-1}$
CTF-10	1	0	0	905	0.40	0.35
CTF-10-1x	1	0	0	755	0.32	0.29
CTF-10a	0	1	0	895	0.39	0.35
CTF-10a-400	0	1	0	0	0	0
CTF-02	0	0	1	1880	1.55	0.25
CTF-11	1	0	1	1610	0.96	0.48
CTF-12	1	0	2	1730	1.05	0.42
CTF-12-10h	1	0	2	1510	0.85	0.42
CTF-12a	0	1	2	1940	1.24	0.34
CTF-12a-400	0	1	2	1030	0.45	0.38
CTF-12-400	1	0	2	1230	0.63	0.41
CTF-14	1	0	4	1720	1.24	0.17
CTF-10(Cu)[b]	1	0	0	1150	0.70	0.25
CTF-10(Sn)[c]	1	0	0	495	0.23	0.21

2

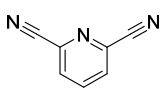

2,6-pyridinedicarbonitrile

2a

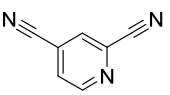

2,4-pyridinedicarbonitrile

3

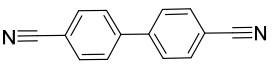

4,4'-biphenyldicarbonitrile

[a]Samples are denoted as CTF-XX-T(-400), where XX gives the stoichiometric ratios of linker mixtures used during synthesis. The suffix -400 is used for samples synthesized at 400 °C. Samples without this suffix were synthesized at 500 °C.

[b]Synthesized using CuCl as ionothermal Lewis acid catalyst.

[c]Synthesized using $SnCl_2$ as ionothermal Lewis acid catalyst.

analyzer pass energy of 50 eV. The measurements were performed at ambient temperature; the chamber pressure during the measurement was about 10^{-7} mbar. A flood gun was used for charge compensation.

All the measured spectra were corrected by setting the reference binding energy of carbon (C*1s*) at 285.0 ± 0.025 eV. Spectra were analyzed using the Thermo Avantage software package. Background subtraction was done using the setting "SMART" (based on the Shirley background with the additional constraint that the background should not be of a greater intensity than the actual data at any point in the region). The deconvolution of spectra was performed using a mixed Gauss-Lorentz function where the Lorentzian contribution was set to 20% for C*1s*, N*1s* and O*1s* and to 30% for Cu*2p*, Zn*2p*, Sn*2p*. Quantification was done using the Scoffield sensitivity factors. Difference in depth of analysis for different photoelectron lines was accounted using the *TPP-2M* method.[30]

5.2.5. Nitrogen adsorption measurements

N_2 adsorption measurements were performed using a Tristar II 3020 Micromeritics instrument at 77 K. Samples were activated under N_2 flow for at least 13 h at 150 °C. Pore size distribution, pore volume and surface area were calculated using Microactive Version 3.00 software.

5.3. Results and discussion

The N*1s* spectra of CTFs normally consist of a peak with BE ≈ 398.5 eV, usually attributed to "pyridine-like" aromatic nitrogen, and a broader shoulder at higher binding energy, considered arising from partial framework decomposition. Common deconvolution of the N*1s* line is given by a "pyridine-like" peak and three other peaks to fit the shoulder (Fig. 5.1). The designation of these peaks – "pyrrole-like" (BE ≈ 400 eV), "quaternary" (BE ≈ 401 eV) and "oxygenated (N-O)" (BE > 402 eV) nitrogen species – is based on the nomenclature used in the literature for N-doped carbons.[25] Coordination of metals to CTFs leads to increasing of the peak between 399.5 – 400 eV. This effect is often attributed to the interaction of the nitrogen binding sites of CTFs with metals. However, it was never unambiguously assigned to a metal-framework interaction.[10-12, 22]

To assign the different signals arising from N-species in the CTFs, we investigated some reference compounds. 2,4,6-triphenyl-1,3,5-triazine (**4**) and 2,4,6-tris(2-pyrydyl)-1,3,5-triazine (**5**) were chosen as model

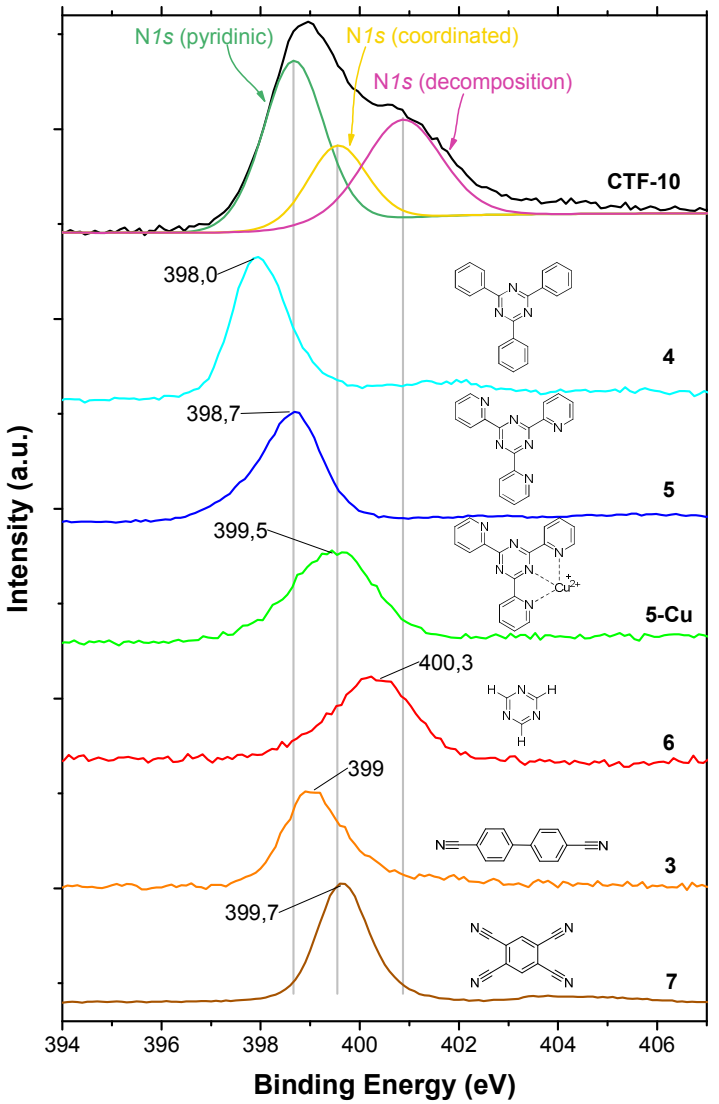

Figure 5.2. N*1s* XPS spectra of **CTF-10** compared to that of the model compounds: phenyl substituted triazine (**4**)**,** pyridine functionalized triazine (**5**), the Cu complex **5-Cu**, non-functionalized triazine (**6**), and 4,4'-biphenyldicarbonitrile (**3**) and 1,2,4,5-tetracyanobenzene (**7**) monomers for CTF synthesis. The gray lines indicate the maxima of the three peaks obtained for the deconvolution of **CTF-10** N*1s* line (BE = 398.7, 399.6, and 400.9 eV).

compounds as they represent the structural units of **CTF-1** and **CTF-10** (Scheme 5.1). 1,3,5-triazine (**6**) without any substituents was also measured for comparison. To have a reference for non-reacted nitrile groups, we have

also investigated **3** and 1,2,4,5-tetracyanobenzene (**7**) with XPS. Measurements of other nitrile-containing monomers reported in this work were not possible due to their low adhesion towards the supporting material (carbon tape) and higher volatility in high vacuum conditions.

The results show that the exact position of the N*1s* line from triazinic species strongly depends on the nature of the substituents of the ring (Figure 5.2). While the non-substituted triazine (**6**) is characterized by a peak with BE = 400.3 eV, substitution of hydrogen atoms for electron-donating phenyl rings in the triazine ring (**4**) shifts the peak to significantly lower binding energy, 397.9 eV. When pyridinic groups are present (compound **5),** two different nitrogen species in XPS can be expected. However, in the N*1s* line of **5** only one peak, shifted to higher binding energy (398.7 eV), is observed. Full width at half-maximum (FWHM) of this peak is the same as for **4** (FWHM = 1.3 eV). Thus, **5** represents a fully conjugated aromatic system where the nitrogen moieties in the triazine unit and pyridine rings result in electronically similar species, and likely the peak at 398.7 eV is a superposition of pyridinic and triazinic species with very close binding energy. Taking into account that pyridine and triazine are 6-membered nitrogen-containing aromatic heterocycles with each nitrogen atom contributing only one electron into the *π*-aromatic ring, we further denote this peak as N6 peak.

To investigate how metal coordination affects the N*1s* XPS spectra of CTFs, we also prepared the Cu complexes of **4** and **5** (denoted as **4-Cu** and **5-Cu**, respectively). Mixing of **4** with $Cu(MeCN)_4PF_6$ in solution does not result in any color change and the position of the N*1s* peak does not shift. In contrast, mixing of a Cu salt with **5** leads to rapid color change of the solution to dark red, and the N6 peak in the N*1s* spectrum of the resulting complex clearly shifts to higher binding energy (399.5 eV). Thus, the 1,3,5-triazinic groups within the CTF structure have poor coordinating properties for transitional metal ions, but polydentate pyridine-triazine species are advantageous for metal coordination.

Discrimination between the N6 and unreacted nitrile species with XPS turns out to be more complicated. N*1s* XPS spectrum of **7** shows a single peak at 399.65 eV, that overlaps with the coordinated N6 peak. However, the C*1s* XPS spectrum of **7** shows an intense peak at 286.8 eV, that can be used for distinguishing (Figure 5.3). In case of **3** the nitrile peak appears in N*1s* XPS spectrum at 399.0 eV, that is located in between coordinated and non-coordinated N6 species, making it difficult to identify. Thus, in most of cases

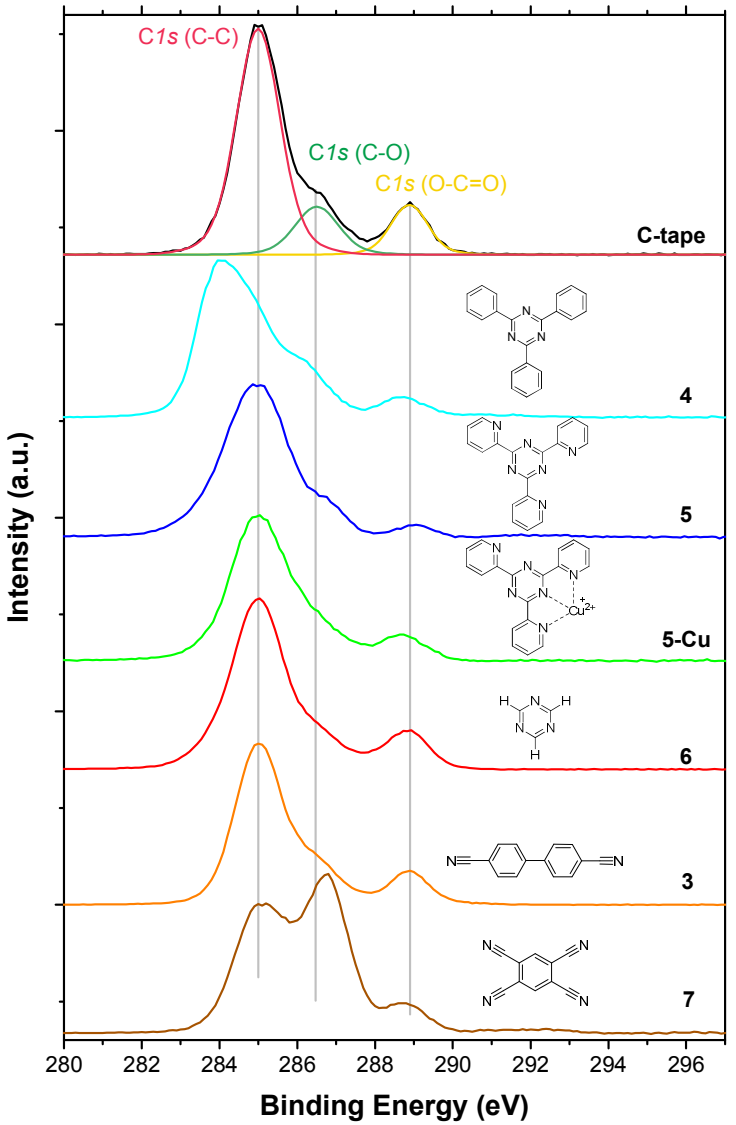

Figure 5.3. C*1s* XPS spectra of carbon tape support and of the model compounds: phenyl substituted triazine (**4**), pyridine functionalized triazine (**5**), the Cu complex **5-Cu**, non-functionalized triazine (**6**), 4,4'-biphenyldicarbonitrile (**3**) and 1,2,4,5-tetracyanobenzene (**7**) monomers for CTF synthesis. The grey lines indicate the maxima of the three peaks obtained from the deconvolution of C-tape C*1s* line (BE = 285, 286.4, and 288.9 eV).

the free nitrile peak in the N*1s* line will be hidden by N6 peaks, so the fraction of unreacted nitriles could be estimated only from the peak at approx. 287 eV in the C*1s* line.

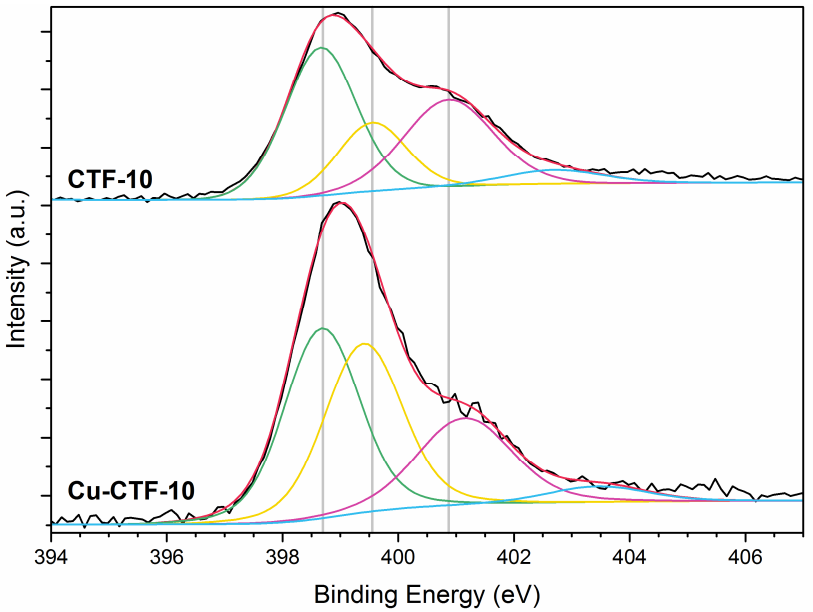

Figure 5.4. Deconvoluted N*1s* XPS spectra of **CTF-10** and **Cu-CTF-10**. The gray lines indicate the maxima of the three peaks obtained for the deconvolution of **CTF-10** N*1s* line (BE = 398.7, 399.6, and 400.9 eV).

Using the peak positions from model compounds, we deconvoluted the N*1s* line of samples **CTF-10** and Cu coordinated to this framework (**Cu-CTF-10,** Fig. 5.4). Fitting resulted in four peaks (398.7, 399.5 ± 0.1, 401.0 ± 0.1 and 403.0 ± 0.2 eV) attributed to free N6 species, coordinated N6 species, products of partial CTF decomposition and oxidized N-O species, respectively. Including several peaks for decomposition products was making the fitting too ambiguous, so we decided to use one broader peak (FWHM ≈ 1.7–2.0 eV) at ≈ 401 eV for all species arising from CTF degradation. The increased intensity of the peak at 399.5 eV demonstrates that metal coordination contributes to this peak and proves the applicability of the proposed deconvolution model. Using this model, we investigate the influence of monomer composition, synthesis temperature and trimerization catalyst in CTFs materials.

5.3.1. Coordination properties of the monomer during synthesis

CTF-10 is a microporous material and it is possible to introduce mesoporosity either by (i) increasing the synthesis temperature or by

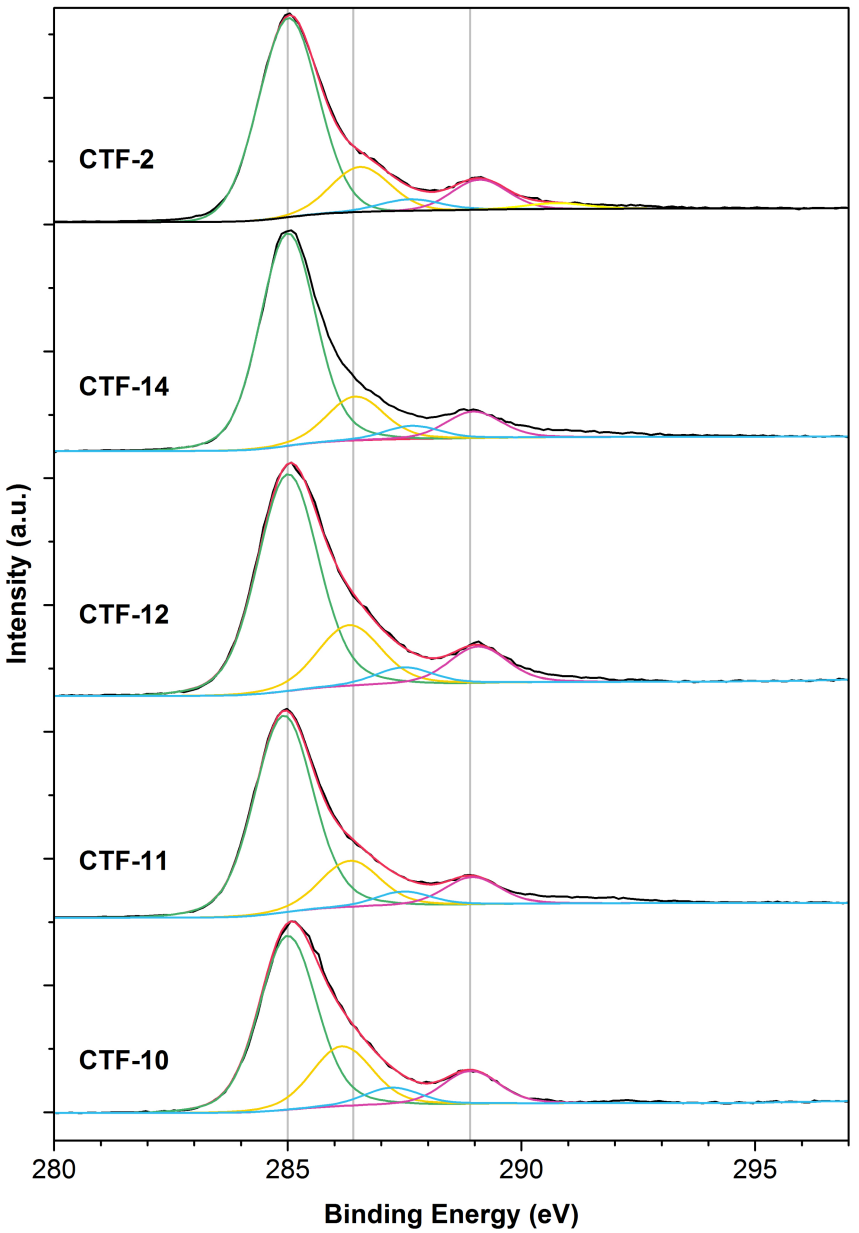

Figure 5.5. C*1s* XPS spectra for CTFs prepared from mixtures of monomers **2** and **3** with different ratios. Nomenclature according to Table 5.1.

(ii) introducing different monomers with distinct topologies (*e.g.* 4,4'-biphenyldicarbonitrile, **3**) to the reaction mixture.[11-12, 14, 16] To analyze the impact of the monomer ratio during synthesis and how this reflects on the CTF XPS N*1s* line, we prepared a series of CTFs with different monomer ratios (**2** to **3**) in the reaction mixture – 1:1, 1:2 and 1:4 ratios,

denoted as **CTF-11**, **CTF-12** and **CTF-14**, respectively (see Table 5.1). The CTF obtained only from monomer **3** was also prepared for comparison (denoted as **CTF-02**).

XPS C*1s* spectra of CTF samples (Figure 5.5) were fitted using four peaks with binding energies of 285.0 eV (adventitious carbon/C-C bonds), 286.4 ± 0.2 eV (C-O groups), 287.5 ± 0.2 eV (C≡N groups) and 289.0 ± 0.1 eV (O-C=O groups). The ratio of C≡N to C-O peak areas was nearly constant, and the C≡N peak area was around 5% of C*1s* line for all CTFs (Table 5.4).

According to Zn*2p* XPS data, all CTF samples contain residual amounts of zinc (see Table 5.5). This observation is supported by the results of elemental analysis for selected samples (2.87 wt% of Zn in **CTF-10**, 0.3 wt% of Zn in **CTF-12**). Content of zinc roughly correlates with the content of nitrogen for all samples, thus, coordinated N6 species are expected to be present in all CTFs.

The XPS N*1s* spectra for these CTF series are shown in Fig. 5.6a. When using a greater number of equivalents of **3,** a relative decrease of the total amount of N6 species in CTFs and an increased ratio of free to coordinated N6 species is observed (Figure 5.6b). Although there is a difference in the N6 peak position in **4** and **5** and the same shift can be expected when increasing equivalents of **3**, the N6 peak shows a negligible shift among all samples, including **CTF-02.** This suggests that the electron donation of each biphenyl unit in the CTFs structure is lower compared to that in **4**, where the phenyl rings are connected to only one triazine unit.

According to N_2 adsorption measurements (Fig. 5.6b, Fig 5.17), a higher loading of **3** significantly increases the surface area and mesoporosity of CTFs. Fig. 5.6 shows that these changes are accompanied by an increase of the CTF decomposition products peak in the N*1s* XPS spectra. Thus, biphenyl groups of **3** favor the reactions of CTF decomposition (Scheme 5.2), and the increase of porosity is achieved at the expenses of the total number of sites available for coordination within the structure. However, it is not clear whether the framework decomposition or the bigger size of **3** has a greater effect on the CTF porous structure.

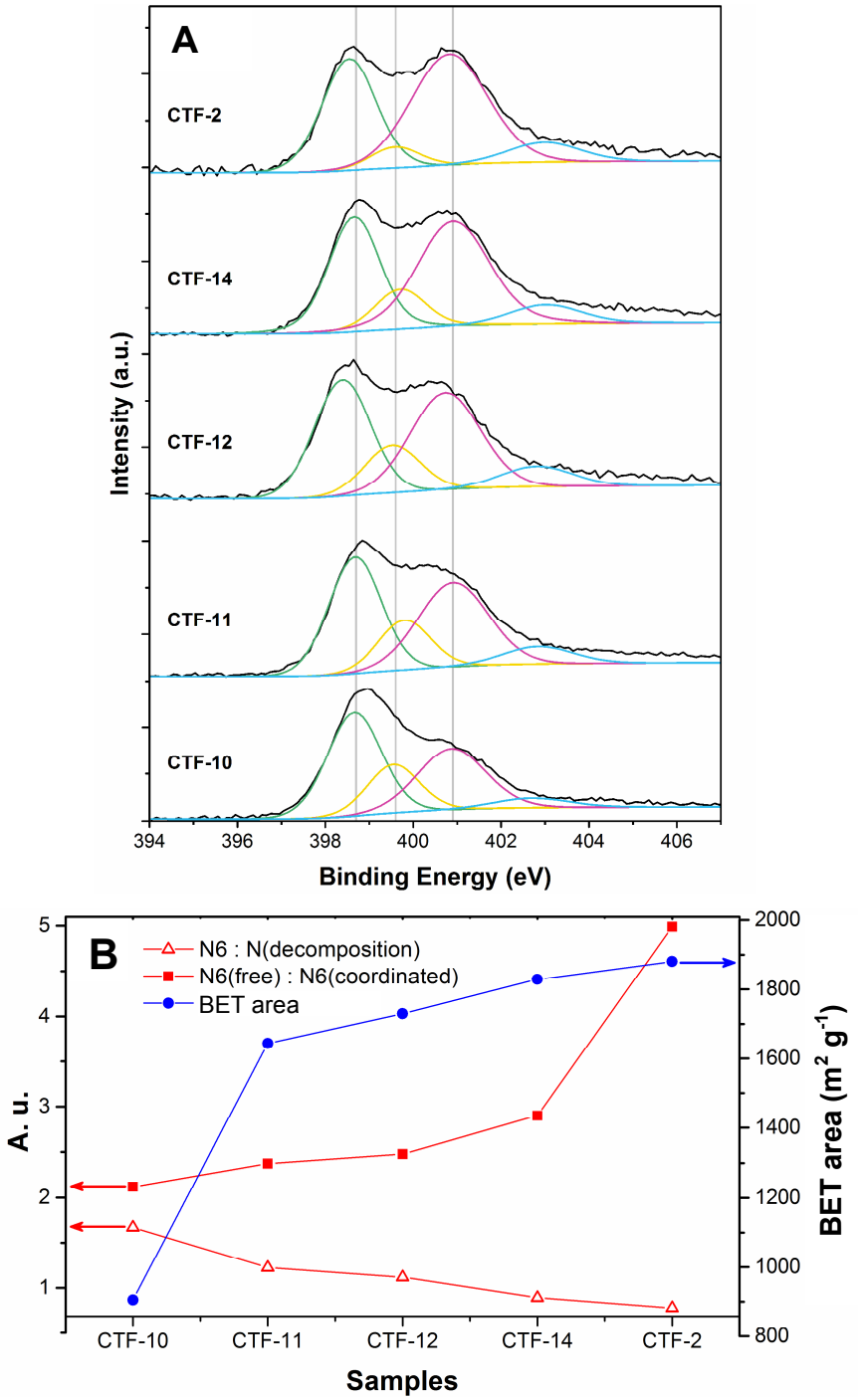

Figure 5.6. a) N*1s* XPS spectra and b) evolution of BET area, ratio of N6 to decomposition nitrogen species and ratio of free N6 to coordinated N6 species for CTFs prepared from mixtures of monomers **2** and **3** with different ratios. Nomenclature according to Table 5.1.

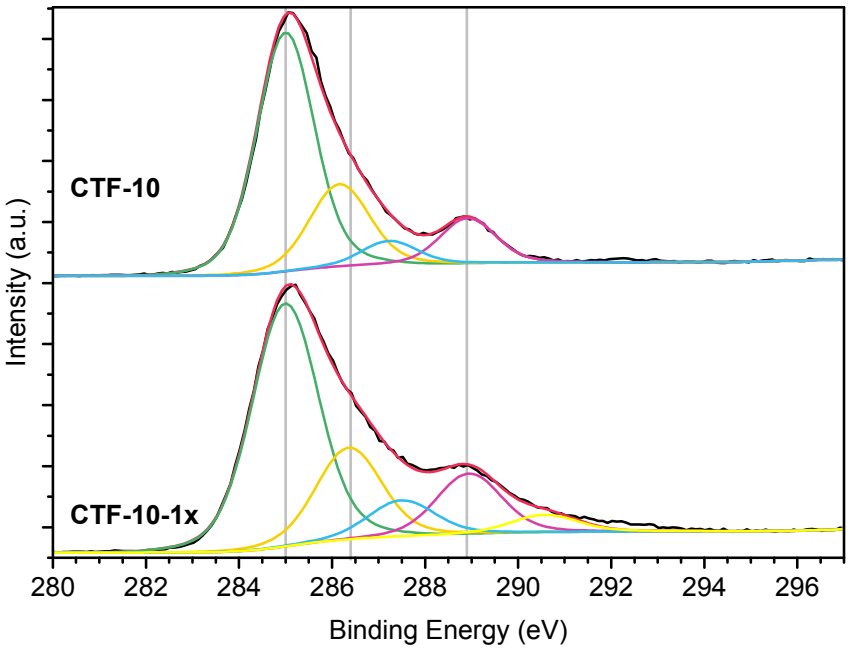

Figure 5.7. C*1s* XPS spectra of **CTF-10** and **CTF-10-1x**.

5.3.2. Influence of the catalyst amount

It was shown for **CTF-1**, that decomposition of CTFs depends strongly on the amount of catalyst used for the synthesis. For that framework the most crystalline sample was prepared with the ratio of monomer : $ZnCl_2$ = 1:1.[18] However, in case of **CTF-10** the optimal amount of catalyst can be different due to the presence of coordinating pyridinic groups within the framework. In order to investigate this, we have prepared **CTF-10** with 1:1 catalyst loading (further denoted as **CTF-10-1x**). Comparison of C*1s* XPS spectra (Fig. 5.7) shows that **CTF-10-1x** has higher content of free C≡N groups than **CTF-10** (8.1% and 5.7% of the total C*1s* line area, respectively). The ratio of N6 species to decomposition products, obtained from deconvolution of N*1s* XPS spectra (Fig. 5.8), was found equal to 1.94 and 1.41 for **CTF-10** and **CTF-10-1x**, respectively. This indicates that reactions of CTF decomposition take place both in case of 1:1 and 5:1 ratios of $ZnCl_2$:monomer, but for a 1:1 loading the CTF synthesis is not complete and still a lot of free nitrile groups are present after synthesis. Thus, the optimal amount of $ZnCl_2$ catalyst for **CTF-10** synthesis is different from equimolar, probably due to the presence of coordinating pyridinic sites in the monomer structure.

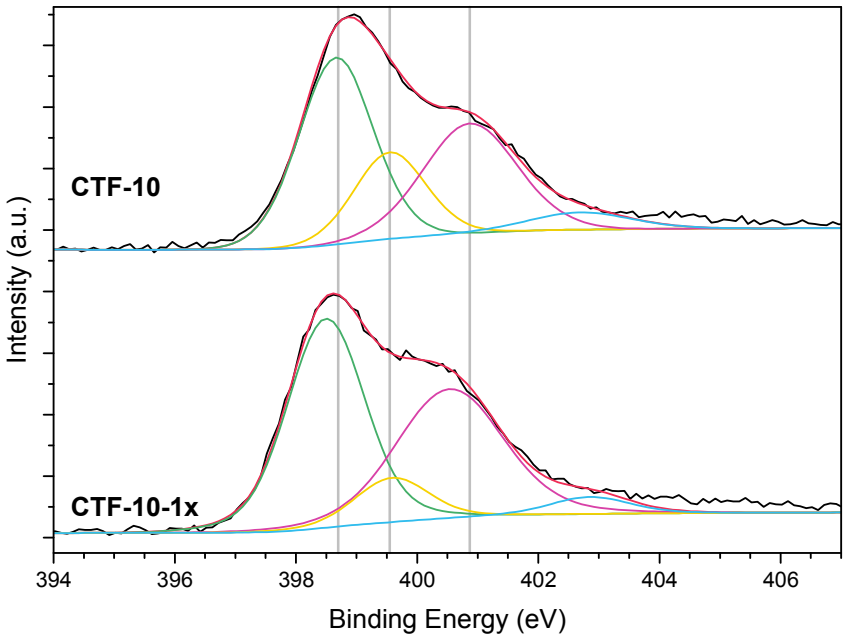

Figure 5.8. N*1s* XPS spectra of **CTF-10** and **CTF-10-1x.**

5.3.3. Influence of the reaction time

In order to investigate how CTF properties depend on the reaction time we have run the synthesis of **CTF-12** for 10 h and for 48 h (these samples are further denoted as **CTF-12-10h** and **CTF-12**, respectively). N_2 adsorption measurements (Fig. 5.19) show that **CTF-12** has higher BET area, but the micropore volume is the same for both samples, indicating that the porosity of **CTF-12** increases only due to the framework decomposition. This is supported by the C*1s* XPS spectra (Fig. 5.9), where the content of unreacted C≡N groups is close for both samples, meaning that nitrile trimerization reaction is complete after 10 h. N*1s* XPS spectra (Fig. 5.10) show the same ratio of N6 to decomposition species for both samples, but the total content of nitrogen decreases with increasing reaction time**.** This indicates that decomposition of CTF at 500 °C mainly occurs via formation of C-C bonds with elimination of nitrogen in a form of volatile N-containing compounds (HCN, NCCN, *etc.*).

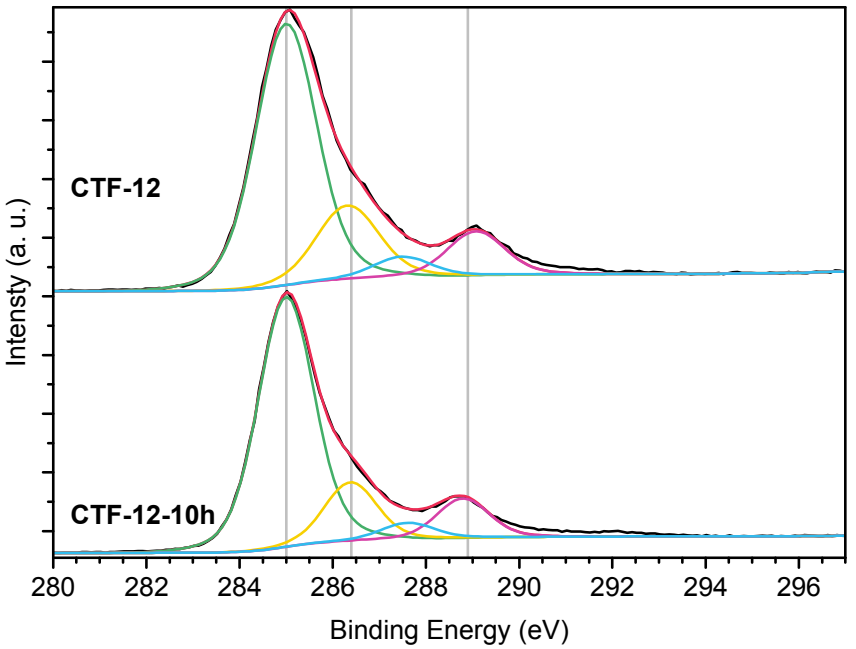

Figure 5.9. C*1s* XPS spectra of **CTF-12** and **CTF-12-10h.**

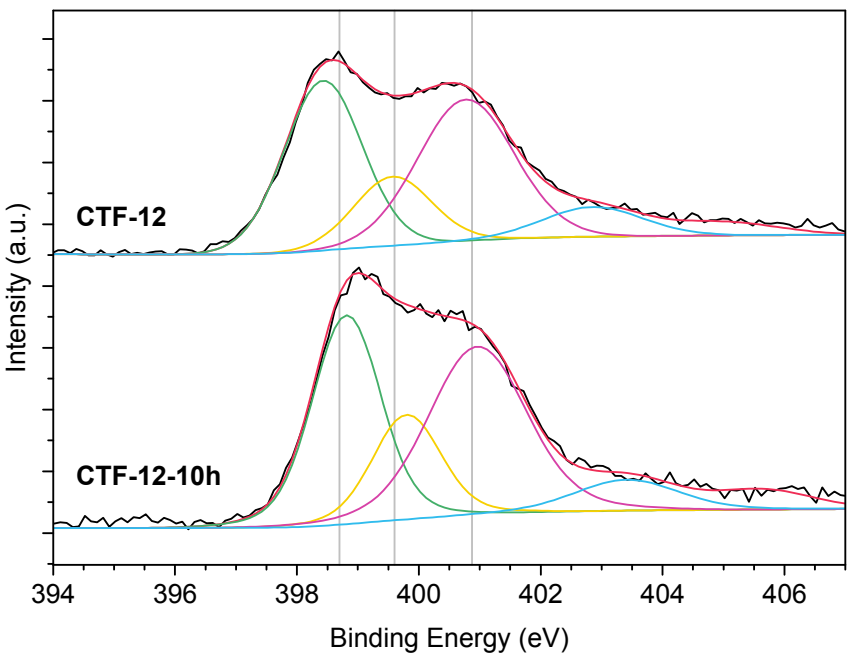

Figure 5.10. N*1s* XPS spectra of **CTF-12** and **CTF-12-10h.**

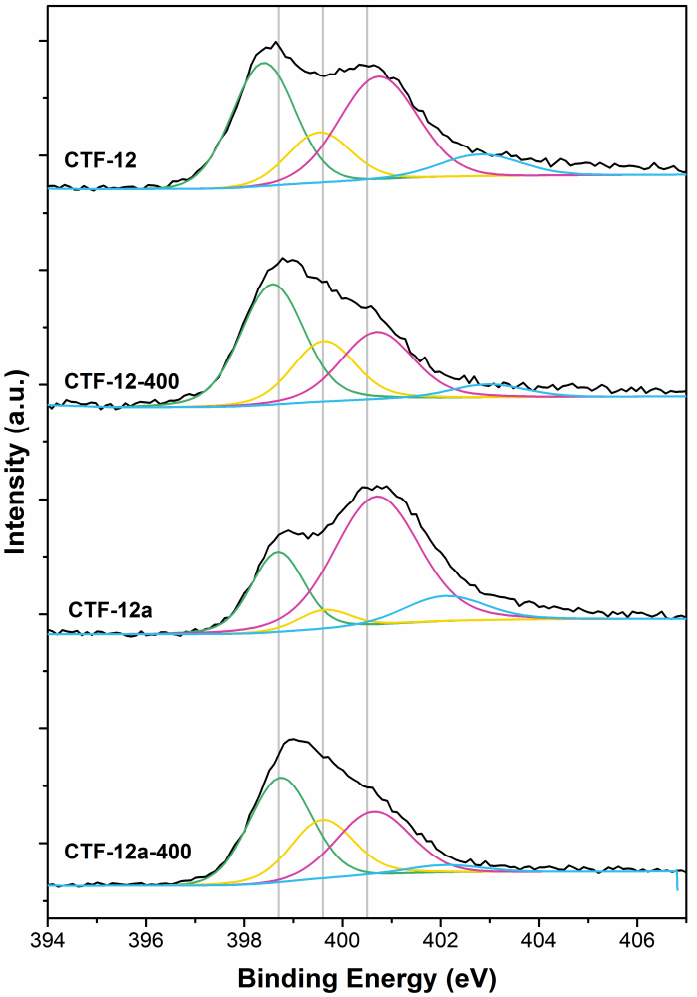

Figure 5.11. N*1s* XPS spectra of **CTF-12**, **CTF-12-400**, **CTF-12a**, and **CTF-12a-400.**

5.3.4. Influence of synthesis temperature

The increase of synthesis temperature from 400 °C in **CTF-12-400** to 500 °C in **CTF-12** leads to an increase of decomposition products that accounts for more than half of the total amount of nitrogen species (Fig. 5.11). Total nitrogen content (Table 5.5) and C*1s* line shape (Fig. 5.12) do not change at higher temperature. N_2 adsorption measurements (Fig. 5.19) show that the micropore volume remains unchanged, but the mesopore volume becomes 3 times higher in **CTF-12** compared to **CTF-12-400**. This proves that the mesoporosity of CTFs originates from thermal decomposition of the framework and correlates with the higher intensity of the decomposition product peak in the XPS N*1s* line.

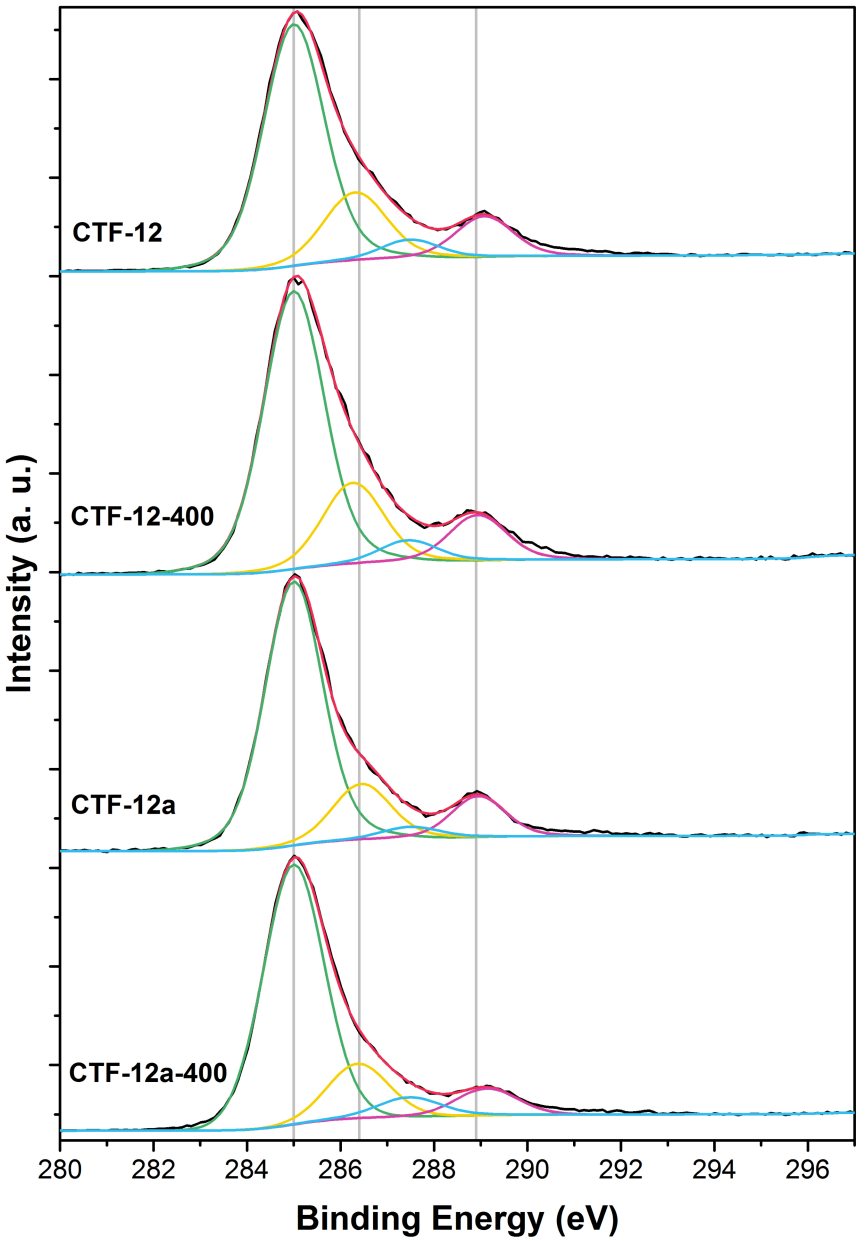

Figure 5.12. C*1s* XPS spectra of **CTF-12, CTF-12-400, CTF-12a,** and **CTF-12a-400**.

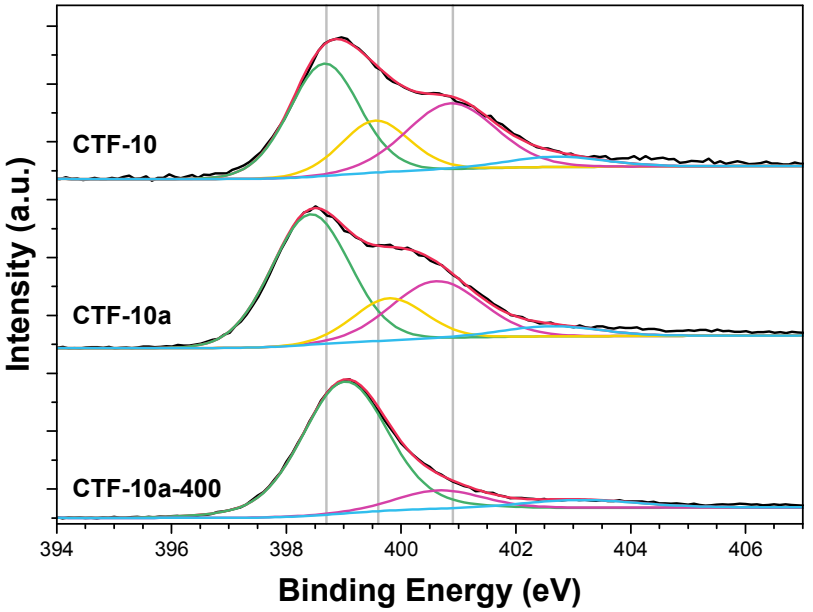

Figure 5.13. N*1s* XPS spectra of **CTF-10, CTF-10a** and **CTF-10a-400**.

5.3.5. Influence of monomer structure

To understand the role of the monomer structure during CTF synthesis we have prepared **CTF-10a** using an isomer of **2** – 2,4-pyridinedicarbonitrile (**2a**, see Table 5.1). This monomer has only one of the two nitrile groups near the pyridinic nitrogen. The second nitrile group is located far from the pyridinic nitrogen, so it is expected to be closer in reactivity to the nitrile groups of **1** and **3**. Having two different nitrile groups, a two-step reaction mechanism, where the trimerization rate of nitriles in *ortho*-position to the pyridinic nitrogen can be faster to that in *para*-position, can be expected. As it was already discussed above, close proximity of nitrile groups to the pyridinic N atom in **2** should promote the synthesis of CTF and potentially the decomposition reactions. The N*1s* line of the sample synthesized at 400 °C (**CTF-10a-400**) shows one main peak with BE = 398.9 eV and a negligible amount of decomposition products (Fig. 5.13). Binding energy of 398.9 eV matches perfectly with the values observed for **3**, that contains free nitrile groups. Increase of the free C≡N peak is also observed in C*1s* XPS line (Fig. 5.14). Adsorption measurements show that **CTF-10a-400** has no porosity. Thus, this suggests that when using **2a** only oligomers are formed rather than an extended CTF framework. This also confirms that the nitrile groups in *ortho* and *para* position of the pyridine ring have significantly different reactivity in trimerization reaction.

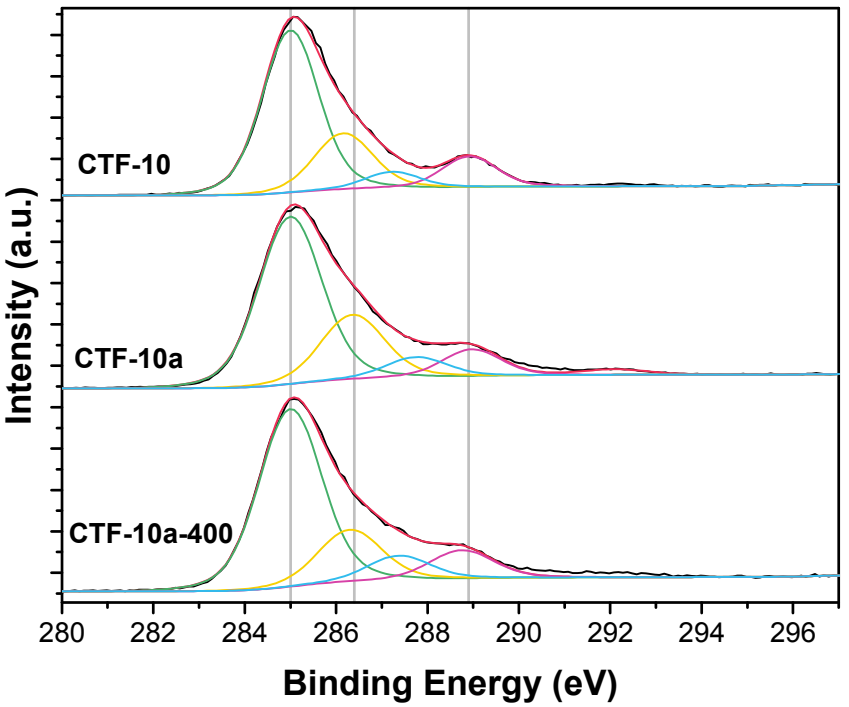

Figure 5.14. C*1s* XPS spectra of **CTF-10, CTF-10a**, and **CTF-10a-400**.

Use of **2a** for synthesis of **CTF-12a-400** leads to lower surface area and mesopore volume compared to **CTF-12-400**. N*1s* XPS spectra for these two samples are very similar (Fig. 5.11), but C*1s* XPS spectra show increase of C≡N peak in case of **CTF-12a-400** (Fig. 5.12). On the contrary, **CTF-12a**, prepared at 500 °C, has a higher mesoporosity and surface area than **CTF-12**. XPS characterization of **CTF-12a** demonstrates that it has a significantly lower concentration of N6 species and higher concentration of framework decomposition products in the N*1s* line than **CTF-12**.

Use of **2a** instead of **2** for CTF synthesis hampers the framework formation at 400 °C and promotes the decomposition reactions at 500 °C. This shows that uniform activation of nitrile groups within the monomer is critical for the formation of the framework and proves that the formation of Zn-monomer complexes has an important structure-directing role.

5.3.6. Influence of the catalyst nature

Complexation of Zn to the monomer **2** promotes the activation of the nitrile groups and the CTF formation. The use of a Lewis acid that is able to form a

Table 5.2. Properties of some inorganic Lewis acids.

Lewis acid	Melting T, °C	Standard oxidation potential ($M^{n+} + ne = M^0$)
$ZnCl_2$	290	-0.7628
CuCl	426	0.521
$SnCl_2$	247	-0.14

more stable complex with **2** than $ZnCl_2$, can be beneficial for the synthesis procedure. The use of CuCl as catalyst for CTF synthesis is attractive as it forms much stronger complexes with **2** than $ZnCl_2$.[31] A drawback of using CuCl is its higher melting temperature and higher oxidation potential compared to $ZnCl_2$. Another promising catalyst for CTF synthesis is $SnCl_2$ because has lower melting temperature than $ZnCl_2$ and has an intermediate oxidation potential compared to CuCl and $ZnCl_2$ (Table 5.2).

Fig. 5.20 represents N_2 adsorption isotherms for **CTF-10** samples prepared at 500 °C using $ZnCl_2$, CuCl and $SnCl_2$ as trimerization catalysts (denoted as **CTF-10(Zn)**, **CTF-10(Cu)** and **CTF-10(Sn)**, respectively). **CTF-10(Cu)** is significantly more porous than **CTF-10(Zn)** and even exhibits some mesoporosity. Comparison of XPS N*1s* spectra (Fig. 5.15) shows that **CTF-10(Cu)** and **CTF-10(Sn)** have a smaller fraction of N6 species and relatively higher content of framework decomposition products compared to **CTF-10(Zn)**. This means, that the increased porosity of **CTF-10(Cu)** is a consequence of the partial decomposition of the framework. Interestingly, the sealed ampoule that was used for the **CTF-10(Cu)** synthesis was coated with a thin layer of metallic copper after 48 h of reaction, indicating the reduction of CuCl during synthesis. On the contrary, when using $SnCl_2$ the surface area decreases. Quantification of XPS data shows that tin to nitrogen ratio in **CTF-10(Sn)** is significantly higher than zinc to nitrogen ratio in **CTF-10(Zn)** and copper to nitrogen ratio in **CTF-10(Cu)** (0.20, 0,05 and 0,02, respectively), suggesting that the pores of **CTF-10(Sn)** can be partially blocked by fully encapsulated residuals of the catalyst.

The use of Lewis acids other than $ZnCl_2$ as catalysts for CTF synthesis can be beneficial for the one-step introduction of the desired metal (*e.g.* copper) into the structure of CTF. However, under ionothermal conditions many metal salts can easily oxidize organics, thus promoting decomposition of the framework and an increase in mesoporosity.

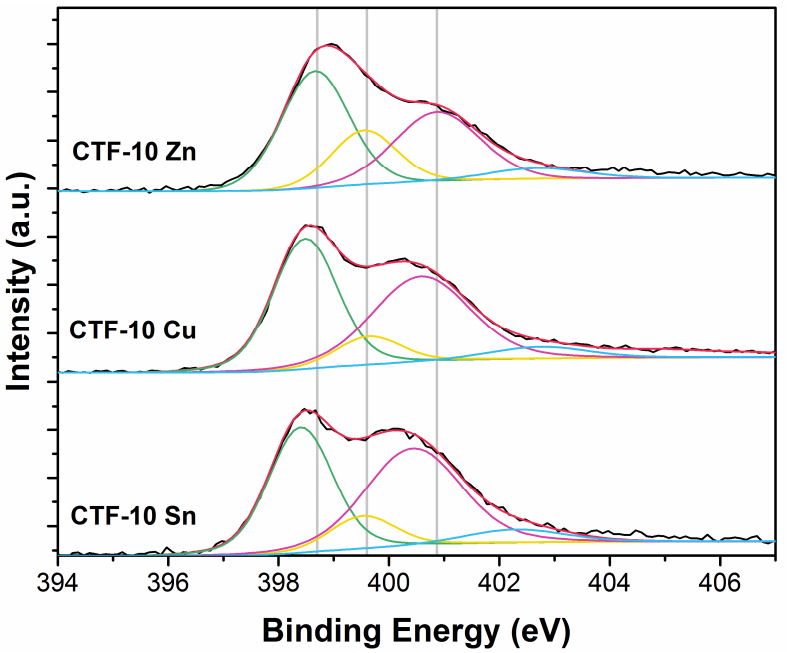

Figure 5.15. N*1s* XPS spectra of CTF samples prepared from **2** at 500 °C using $ZnCl_2$, CuCl and $SnCl_2$ as trimerization catalysts.

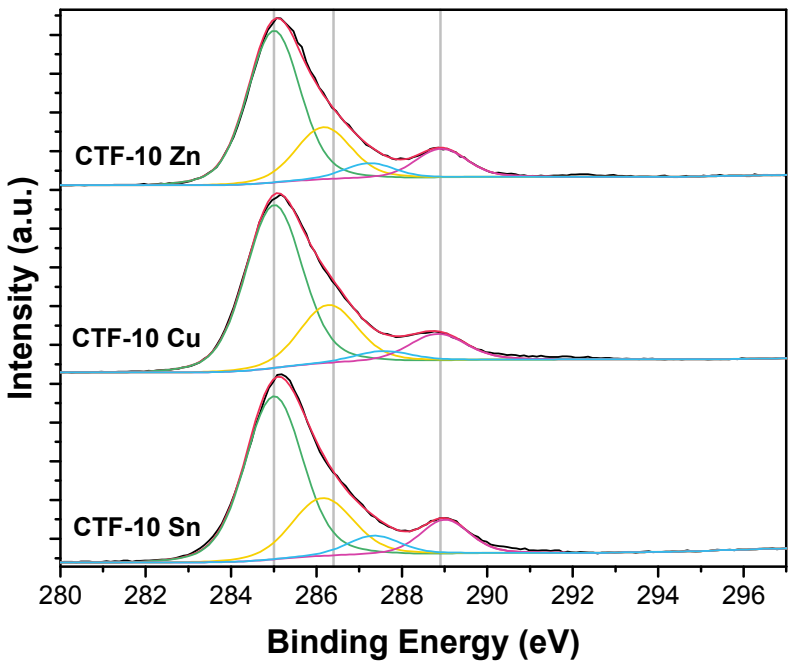

Figure 5.16. C*1s* XPS spectra of CTF samples prepared from **2** at 500 °C using $ZnCl_2$, CuCl and $SnCl_2$ as trimerization catalysts.

5.4. Conclusions

Synthesis of CTFs proceeds through a delicate interplay between framework formation *via* nitrile trimerization and framework decomposition through C-C coupling. By combining the results of a thorough XPS study with the textural properties of CTFs synthesized under different conditions, we show that decomposition of CTFs increases the surface area and mesoporosity of the material, but decreases the relative amount of N6 nitrogen species, suitable for coordination of metal ions. Increase of synthesis time and temperature and use of oxidizing compounds as trimerization catalysts promote the decomposition reactions. Use of monomers that form more stable complexes with Lewis acids favors the CTF formation and reduces the rate of framework decomposition.

5.5. Appendix

Table 5.3. Parameters of N*1s* line deconvolution for the samples reported in this work.

Sample	Free N6 peak			Coordinated N6 peak			Decomposition products			N-O species		
	BE, eV	FWHM, eV	%at	BE, eV	FWHM, eV	%at	BE, eV	FWHM, eV	%at	BE, eV	FWHM, eV	%at
CTF-10	398.66	1.5	43.1	399.55	1.45	19.3	400.87	1.90	32.1	402.69	1.98	5.4
CTF-10-1x	398.5	1.51	46.7	399.59	1.44	9.4	400.54	2.08	39.9	402.85	1.54	3.9
CTF-10a	398.42	1.61	52.8	399.79	1.46	15.5	400.62	1.84	26.6	402.62	1.97	5.1
CTF-10a-400	399.10[a]	1.76	81.5				400.75	1.76	11.7	403.20	2.4	6.8
CTF-11	398.68	1.46	39.4	399.8	1.44	16.6	400.91	1.94	37.9	403.02	1.65	6.2
CTF-12	398.43	1.55	37.6	399.76	1.54	15.2	400.77	1.92	38.7	402.85	1.98	8.4
CTF-12-10h	398.82	1.33	35.4	399.83	1.33	1.79	400.99	1.9	39.2	403.33	2.0	7.5
CTF-12a	398.70	1.26	24.5	399.64	1.26	5.9	400.71	2.03	63.7	402.86	1.52	5.9
CTF-12-400	398.59	1.52	44.5	399.64	1.50	22.0	400.72	1.73	28.2	402.99	1.80	5.3
CTF-12a-400	398.74	1.54	42.2	399.59	1.5	24.5	400.63	1.81	29.9	402.10	1.76	3.3
CTF-14	398.66	1.37	35.0	399.71	1.37	12.1	400.91	1.92	44.9	403.02	1.90	8.0
CTF-02	398.53	1.43	36.4	399.69	1.34	7.3	400.86	1.99	48.2	403.11	1.95	8.1
CTF-10(Cu)	398.56	1.32	41.6	399.71	1.39	9.5	400.63	2.08	43.2	402.81	2.08	5.8
CTF-10(Sn)	398.31	1.37	38.9	399.44	1.39	10.2	400.34	2.03	44.8	402.21	2.09	6.0
Cu-CTF-10	398.68	1.53	38.4	399.40	1.58	35.2	401.14	1.94	22.3	403.46	1.98	4.1
3	398.99[a]	1.32	100									
4	397.95	1.26	100									
4+Cu				397.92	1.3	100						
5	398.65	1.28	100									
5+Cu				399.52	1.86	100						
6	400.29	1.89	100									
7	399.65[a]	1.21	100									

[a] This peak corresponds to unreacted C≡N groups

Table 5.4. Parameters of C*1s* line deconvolution for the samples reported in this work.

Sample	C-C peak			C-O peak			C≡N peak			O-C=O peak		
	BE, eV	FWHM, eV	%at.	BE, eV	FWHM, eV	%at.	BE, eV	FWHM, eV	%at.	BE, eV	FWHM, eV	%at.
CTF-10	285.0	1.45	61.2	286.16	1.51	21.9	287.23	1.4	5.7	288.92	1.4	11.2
CTF-10-1x	285.0	1.68	54.6	286.36	1.66	20.3	287.49	1.68	8.1	288.94	1.64	13.2
CTF-10a	285.0	1.62	60.7	286.36	1.63	23.4	287.75	1.58	7.0	288.97	1.51	8.9
CTF-10a-400	285.0	1.62	62.9	286.3	1.64	18.6	287.37	1.62	8.5	288.75	1.64	10.0
CTF-11	285.0	1.49	67.8	286.42	1.49	15.9	287.57	1.38	4.4	289.03	1.38	8.7
CTF-12	285.0	1.54	65.9	286.32	1.58	18.9	287.49	1.45	4.8	289.07	1.45	10.4
CTF-12-10h	285.0	1.42	70.1	286.38	1.32	15.3	287.61	1.34	4.3	288.79	1.32	10.3
CTF-12a	285.0	1.46	74.2	286.45	1.46	15.6	287.51	1.46	3.2	288.95	1.36	7.0
CTF-12-400	285.0	1.53	65.9	286.26	1.53	19.2	287.45	1.45	4.8	288.93	1.45	10.2
CTF-12a-400	285.0	1.59	71.9	286.37	1.59	15.0	287.47	1.59	5.7	289.13	1.59	7.4
CTF-14	285.0	1.4	69.9	286.45	1.43	14.8	287.67	1.4	4.3	288.97	1.39	8.6
CTF-02	285.0	1.55	68.8	286.54	1.53	15.3	287.61	1.53	4.2	289.09	1.43	9.6
CTF-10(Cu)	285.0	1.57	63.2	286.28	1.57	22.6	287.56	1.57	3.9	288.83	1.57	10.2
CTF-10(Sn)	285.0	1.59	60.52	286.14	1.68	22.7	287.34	1.45	6.3	289.0	1.33	10.5
Cu-CTF-10	285.0	1.42	36.8	285.74	1.43	38.5	287.1	1.59	14.9	289.21	1.66	9.9
3	285.0	1.43	70.9	286.5	1.32	15.5	287.55	1.15	1.4	288.87	1.15	12.2
4[a]	285.0	1.3	27.0	286.22	1.32	16.2				288.68	1.42	7.2
4+Cu[b]	285.0	1.28	13.9	286.2	1.36	15.7				288.72	1.73	4.2
5[c]	285.0	1.62	72.0	286.68	1.33	11.8				289.05	0.86	3.4
5+Cu	285.0	1.69	76.8	286.51	1.54	13.3				288.74	1.34	9.9
6	285.0	1.54	74.3	286.57	1.44	11.7				288.8	1.34	13.9
7	285.0	1.51	70.9	285.81	1.2	1.4	286.8	1.34	15.5	288.8	1.22	12.2
C-tape	285.0	1.33	71.6	286.5	1.33	15.2				288.88	1.12	13.2

[a] Not shown in the table: peak at 284.0 eV (49.6 %at., FWHM = 1.34 eV), corresponding to sp^2 C-C bonds.

[b] Not shown in the table: peak at 283.9 eV (62.2 %at., FWHM = 1.29 eV), corresponding to sp^2 C-C bonds.

[c] Not shown in the table: peak at 283.7 eV (12.9 %at., FWHM = 1.57 eV), corresponding to sp^2 C-C bonds.

Table 5.5. Elemental composition of samples, calculated from XPS analysis data.

Sample	C, %at.	O, %at.	Zn, %at.	N, %at.	Cu, %at.	Sn, %at.
CTF-10	77.66	14.13	0.35	7.86		
CTF-10-1x	77.71	13.49	0.16	8.64		
CTF-10a	75.53	12.06	0.00	12.42		
CTF-10a-400	74.41	10.38	0.42	14.78		
CTF-11	82.11	9.63	0.15	8.12		
CTF-12	82.81	13.07	0.56	3.56		
CTF-12-10h	80.26	14.12	0.44	5.17		
CTF-12a	79.18	17.24	0.10	3.47		
CTF-12-400	83.19	13.53	0.05	3.23		
CTF-12a-400	83.11	11.19	0.17	5.54		
CTF-14	85.97	9.76	0.07	4.20		
CTF-02	87.20	10.45	0.05	2.30		
CTF-10(Cu)	75.97	10.84		12.87	0.32	
CTF-10(Sn)	76.56	15.70		6.45		1.29
Cu-CTF-10	72.27	12.91	0.17	12.82	1.83	
3	80.87	17.47		1.65		
4	88.07	5.95		5.97		
4+Cu	86.68	5.19		7.85	0.29	
5	77.65	8.34		14.01		
5+Cu	79.30	14.35		5.80	0.55	
6	78.42	20.61		0.97		
7	76.86	10.87		12.27		
C-tape	80.12	19.88				

Table 5.6. Theoretical composition of **CTF-10, CTF-12, CTF-12a, CTF-02,** and comparison with the real nitrogen content of CTFs from the elemental analysis (Mikroanalytisches Laboratorium Kolbe).

	Theoretical composition			Elemental analysis	XPS
	C, wt%	H, wt%	N, wt%	N, wt%	N, wt%
CTF-10	65.1	2.3	32.5	20.83	8.52
CTF-12	78.2	3.6	18.2	9.98	3.86
CTF-12a	78.2	3.6	18.2	10.0	3.79
CTF-02	82.3	3.9	13.7	6.72	2.58

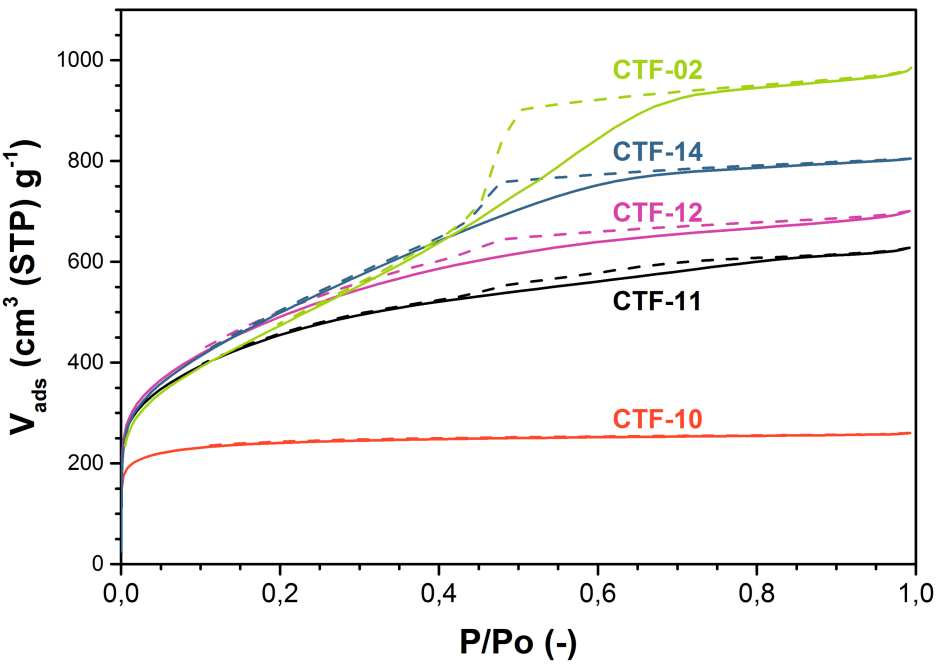

Figure 5.17. N_2 adsorption isotherms at 77 K of CTFs prepared from mixtures of monomers **2** and **3** with different ratios (solid line – adsorption, dashed line – desorption). Nomenclature according to Table 5.1.

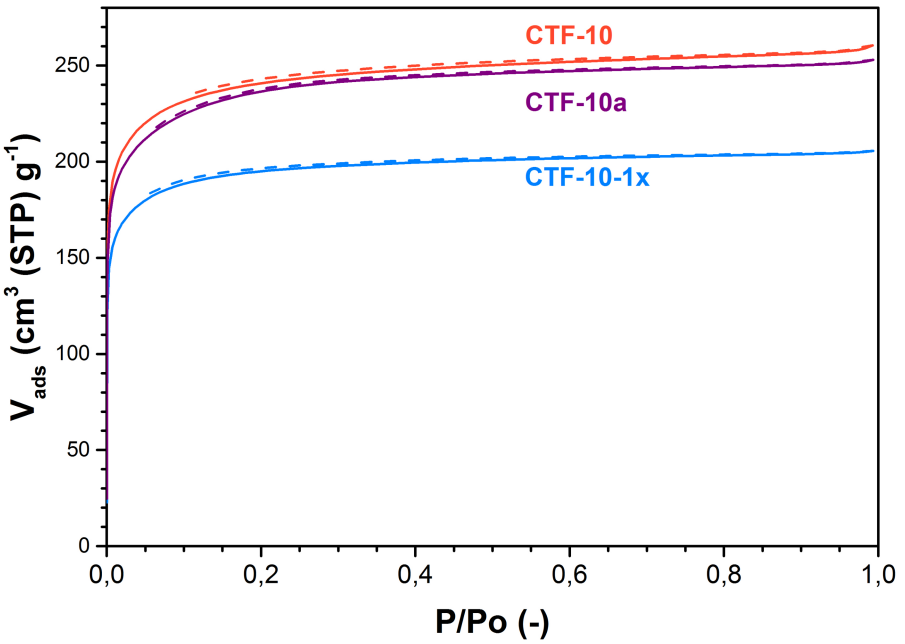

Figure 5.18. N_2 adsorption isotherms at 77 K of **CTF-10**, **CTF-10-1x**, and **CTF-10a** (solid line – adsorption, dashed line – desorption). Nomenclature according to Table 5.1.

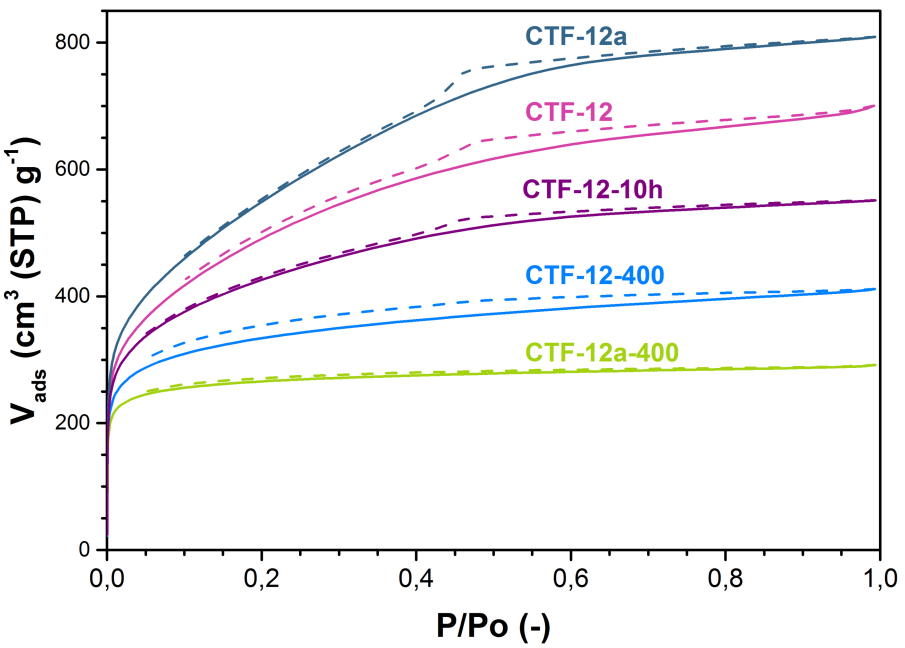

Figure 5.19. N_2 adsorption isotherms at 77 K of **CTF-12**, **CTF-12-400**, **CTF-12-10h, CTF-12a**, and **CTF-12a-400** (solid line – adsorption, dashed line – desorption). Nomenclature according to Table 5.1.

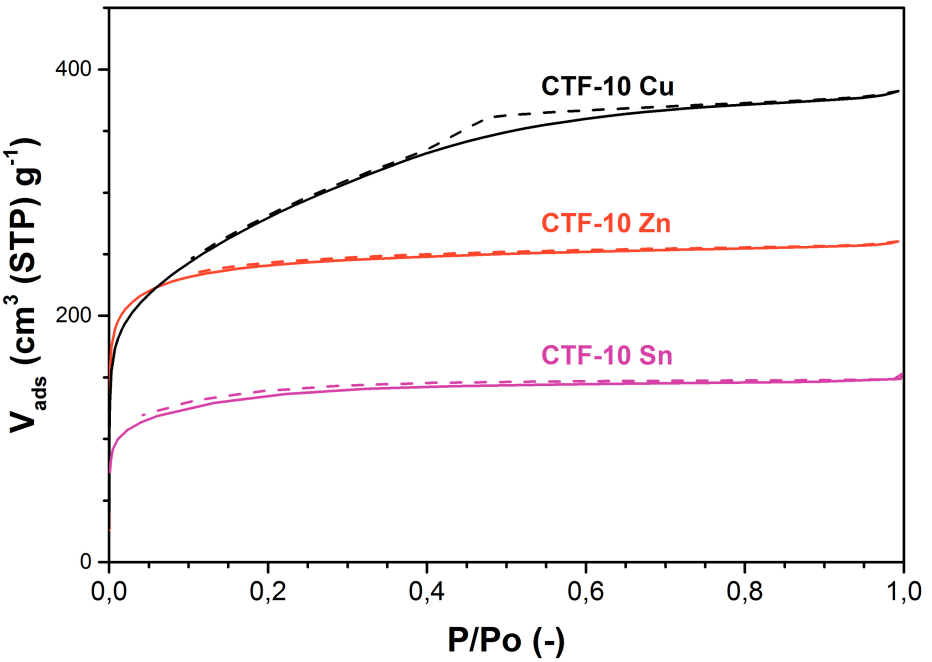

Figure 5.20. N_2 adsorption isotherms at 77 K of **CTF-10**, **CTF-10(Cu)**, and **CTF-10(Sn)** (solid line – adsorption, dashed line – desorption). Nomenclature according to Table 5.1.

5.6. References

1. Qiu, S.; Ben, T., *Porous Polymers: Design, Synthesis and Applications*. The Royal Society of Chemistry: Thomas Graham House, Science Park, Milton Road, Cambridge CB4 0WF, UK, **2015**.
2. Zhu, G.; Ren, H., *POROUS ORGANIC FRAMEWORKS Design, Synthesis and Their Advanced Applications*. Springer Berlin Heidelberg: **2015**.
3. Kuhn, P.; Antonietti, M.; Thomas, A., Porous, covalent triazine-based frameworks prepared by ionothermal synthesis. *Angewandte Chemie - International Edition* **2008,** *47* (18), 3450-3453.
4. Zhu, X.; Tian, C.; Mahurin, S. M.; Chai, S.-H.; Wang, C.; Brown, S.; Veith, G. M.; Luo, H.; Liu, H.; Dai, S., A Superacid-Catalyzed Synthesis of Porous Membranes Based on Triazine Frameworks for CO2 Separation. *Journal of the American Chemical Society* **2012,** *134* (25), 10478-10484.
5. Ren, S.; Bojdys, M. J.; Dawson, R.; Laybourn, A.; Khimyak, Y. Z.; Adams, D. J.; Cooper, A. I., Porous, fluorescent, covalent triazine-based frameworks via room-temperature and microwave-assisted synthesis. *Advanced Materials* **2012,** *24* (17), 2357-2361.
6. Miller, G. H. NITRILE TRIMERIZATION PROCESS. **1972**.
7. Meier, C. B.; Sprick, R. S.; Monti, A.; Guiglion, P.; Lee, J.-S. M.; Zwijnenburg, M. A.; Cooper, A. I., Structure-property relationships for covalent triazine-based frameworks: The effect of spacer length on photocatalytic hydrogen evolution from water. *Polymer*.
8. Byun, J.; Patel, H. A.; Thirion, D.; Yavuz, C. T., Reversible water capture by a charged metal-free porous polymer. *Polymer (United Kingdom)* **2017,** *126*, 308-313.
9. Palkovits, R.; Antonietti, M.; Kuhn, P.; Thomas, A.; Schüth, F., Solid catalysts for the selective low-temperature oxidation of methane to methanol. *Angewandte Chemie - International Edition* **2009,** *48* (37), 6909-6912.
10. Kamiya, K.; Kamai, R.; Hashimoto, K.; Nakanishi, S., Platinum-modified covalent triazine frameworks hybridized with carbon nanoparticles as methanol-tolerant oxygen reduction electrocatalysts. *Nature Communications* **2014,** *5*.
11. Bavykina, A. V.; Goesten, M. G.; Kapteijn, F.; Makkee, M.; Gascon, J., Efficient production of hydrogen from formic acid using a Covalent Triazine Framework supported molecular catalyst. *ChemSusChem* **2015,** *8* (5), 809-812.
12. Rozhko, E.; Bavykina, A.; Osadchii, D.; Makkee, M.; Gascon, J., Covalent organic frameworks as supports for a molecular Ni based ethylene oligomerization catalyst for the synthesis of long chain olefins. *Journal of Catalysis* **2017,** *345*, 270-280.

13. Yoshioka, T.; Iwase, K.; Nakanishi, S.; Hashimoto, K.; Kamiya, K., Electrocatalytic Reduction of Nitrate to Nitrous Oxide by a Copper-Modified Covalent Triazine Framework. *The Journal of Physical Chemistry C* **2016,** *120* (29), 15729-15734.

14. Dey, S.; Bhunia, A.; Breitzke, H.; Groszewicz, P. B.; Buntkowsky, G.; Janiak, C., Two linkers are better than one: enhancing CO2 capture and separation with porous covalent triazine-based frameworks from mixed nitrile linkers. *Journal of Materials Chemistry A* **2017,** *5* (7), 3609-3620.

15. Hug, S.; Stegbauer, L.; Oh, H.; Hirscher, M.; Lotsch, B. V., Nitrogen-Rich Covalent Triazine Frameworks as High-Performance Platforms for Selective Carbon Capture and Storage. *Chemistry of Materials* **2015,** *27* (23), 8001-8010.

16. Kuhn, P.; Forget, A.; Hartmann, J.; Thomas, A.; Antonietti, M., Template-free tuning of nanopores in carbonaceous polymers through Ionothermal synthesis. *Advanced Materials* **2009,** *21* (8), 897-901.

17. Kuhn, P.; Forget, A.; Su, D.; Thomas, A.; Antonietti, M., From microporous regular frameworks to mesoporous materials with ultrahigh surface area: Dynamic reorganization of porous polymer networks. *Journal of the American Chemical Society* **2008,** *130* (40), 13333-13337.

18. Kuhn, P.; Thomas, A.; Antonietti, M., Toward tailorable porous organic polymer networks: A high-temperature dynamic polymerization scheme based on aromatic nitriles. *Macromolecules* **2009,** *42* (1), 319-326.

19. Konovalov, A. I.; Kiselev, V. D., Diels - Alder reaction: Effect of internal and external factors on the reactivity of diene - dienophile systems. *Russian Chemical Bulletin* **2003,** *52* (2), 293-311.

20. Schwinghammer, K.; Hug, S.; Mesch, M. B.; Senker, J.; Lotsch, B. V., Phenyl-triazine oligomers for light-driven hydrogen evolution. *Energy and Environmental Science* **2015,** *8* (11), 3345-3353.

21. Kuecken, S.; Schmidt, J.; Zhi, L.; Thomas, A., Conversion of amorphous polymer networks to covalent organic frameworks under ionothermal conditions: A facile synthesis route for covalent triazine frameworks. *Journal of Materials Chemistry A* **2015,** *3* (48), 24422-24427.

22. Soorholtz, M.; Jones, L. C.; Samuelis, D.; Weidenthaler, C.; White, R. J.; Titirici, M. M.; Cullen, D. A.; Zimmermann, T.; Antonietti, M.; Maier, J.; Palkovits, R.; Chmelka, B. F.; Schüth, F., Local Platinum Environments in a Solid Analogue of the Molecular Periana Catalyst. *ACS Catalysis* **2016,** *6* (4), 2332-2340.

23. Gammon, W. J.; Kraft, O.; Reilly, A. C.; Holloway, B. C., Experimental comparison of N(1s) X-ray photoelectron spectroscopy binding energies of hard and elastic amorphous carbon nitride films with reference organic compounds. *Carbon* **2003,** *41* (10), 1917-1923.

24. Kapteijn, F.; Moulijn, J. A.; Matzner, S.; Boehm, H. P., Development of nitrogen functionality in model chars during gasification in CO 2 and O 2. *Carbon* **1999,** *37* (7), 1143-1150.

25. Stańczyk, K.; Dziembaj, R.; Piwowarska, Z.; Witkowski, S., Transformation of nitrogen structures in carbonization of model compounds determined by XPS. *Carbon* **1995,** *33* (10), 1383-1392.

26. Pels, J. R.; Kapteijn, F.; Moulijn, J. A.; Zhu, Q.; Thomas, K. M., Evolution of nitrogen functionalities in carbonaceous materials during pyrolysis. *Carbon* **1995,** *33* (11), 1641-1653.

27. Arrigo, R.; Hävecker, M.; Schlögl, R.; Su, D. S., Dynamic surface rearrangement and thermal stability of nitrogen functional groups on carbon nanotubes. *Chem. Commun.* **2008,** (40), 4891-4893.

28. Friedel Ortega, K.; Arrigo, R.; Frank, B.; Schlögl, R.; Trunschke, A., Acid-Base Properties of N-Doped Carbon Nanotubes: A Combined Temperature-Programmed Desorption, X-ray Photoelectron Spectroscopy, and 2-Propanol Reaction Investigation. *Chemistry of Materials* **2016,** *28* (19), 6826-6839.

29. Beamson, G.; Briggs, D., *High Resolution XPS of Organic Polymers: The Scienta ESCA300 Database*. Wiley: **1992**.

30. Tanuma, S.; Powell, C. J.; Penn, D. R., Calculations of electron inelastic mean free paths. V. Data for 14 organic compounds over the 50–2000 eV range. *Surface and Interface Analysis* **1994,** *21* (3), 165-176.

31. Smith, R. M.; Martell, A. E.; Standards, N. I. o.; Technology, *NIST critically selected stability constants of metal complexes database*. National Institute of Standards & Technology: **1998**.

6.1. Summary

This dissertation is devoted to the attractive and rapidly developing field of heterogeneous catalysts with isolated metal sites. The following research questions served as the source of inspiration for it:

- How to design a catalyst with isolated metal sites?
- How to synthesize and develop a catalyst with isolated metal sites?
- How to characterize a catalyst with isolated metal sites?

In the first part of this dissertation (Chapters 2-3) the route for design, synthesis, characterization and further modification of heterogeneous catalysts with isolated sites is described, using the development of a catalyst for direct conversion of methane to methanol as an example. The second part (Chapters 4-5) investigates the applicability of X-ray based analysis techniques (primarily X-ray photoelectron spectroscopy (XPS) and X-ray absorption spectroscopy (XAS)) for the characterization of such catalysts. A literature review and introduction to both parts is presented in Chapter 1.

The first part of introductory **Chapter 1** describes in brief the scope of previous works and the main research challenges in developing the process for the direct methane-to-methanol conversion. Significant research efforts in this area have been focused so far on developing catalysts for activation of the C-H bond in methane, which is one of the most stable bonds in organic chemistry. However, other equally important challenges in this process are the activation and regeneration of the oxidant, the removal of methanol from the active site and protection of methanol from overoxidation, and the regeneration of the active catalyst site after the reaction cycle. Based on the literature review, the features of the successful catalyst for mild methane oxidation are formulated – it should be a heterogeneous catalyst with isolated active sites on a porous hydrophobic support, and stable under the applied reaction conditions.

In **Chapter 2** the design and development of a catalyst for mild methane oxidation based on metal organic frameworks (MOFs) is presented. Due to their tuneable porosity and functionalization, MOFs can potentially meet the requirements for the mild methane oxidation catalyst formulated in Chapter 1. The use of electrochemical synthesis allows introducing isolated Fe sites into MIL-53(Al) framework in a broad range of concentrations (0.1-5.5 wt%) without formation of iron oxide nanoparticles, which was not possible by

using conventional hydrothermal ion exchange. Electrochemically-synthesized MIL-53(Al,Fe) catalysts were tested for methane oxidation under mild aqueous reaction conditions (60 °C, 30 bar CH_4) using H_2O_2 as oxidant. Under such conditions MIL-53(Al,Fe) catalysts were active in methane oxidation, producing mainly methanol and methyl hydroperoxide with minor formation of overoxidation products (formic acid, CO_2), with TOFs in the order of 90 h^{-1} and selectivities to oxygenates of *ca.* 80%. The catalyst was recyclable at least up to 5 catalytic runs. Characterization of MIL-53(Al,Fe) catalysts with Mössbauer spectroscopy, electron paramagnetic resonance (EPR), and X-ray absorption spectroscopy (XAS) showed that iron in these samples is mainly present as monomeric and dimeric antiferromagnetically-coupled sites, incorporated in the structure of MIL-53(Al) framework. Periodic density functional theory (DFT) calculations proved the stability of such species and allowed proposing a reaction mechanism of methane oxidation over isolated Fe-sites in the MIL-53 framework.

Possible approaches for further modification of MIL-53(Al,Fe) catalyst are described in **Chapter 3**. Different approaches, including synthesis of MOF catalysts with different metal centres or different organic linkers, as well as including different additives in the reaction media, are discussed. Electrochemical introduction of Cr, Co, and Cu in MIL-53(Al) instead of Fe was tried. IR characterization showed, however, that only Cr got incorporated in the structure of the MOF. MIL-53(Al,Cr) catalysts demonstrated an activity and selectivity for the methane-to-methanol conversion comparable or even higher than in case of MIL-53(Al,Fe). However, MIL-53(Al,Cr) showed a lower stability with significant leaching of Cr already after the first (batch-wise) run, indicating that catalytic activity in this case is mainly attributed to leached chromium species in solution. Introduction of linkers with additional functional groups leads to a significantly lower porosity of the MOF and can block the active site, thus minimizing the possible positive effect of such modification. Introduction of the radical scavenger Na_2SO_3 into the reaction mixture leads to a higher methane conversion, but with a poor selectivity towards methanol, producing CO_2 as the main product. This effect could possibly be explained by the formation of highly reactive peroxosulfuric acids in solution.

In addition, heterogeneous catalysts based on purely organic covalent triazine frameworks (CTFs) with coordinated metal sites were also investigated for the mild methane oxidation with H_2O_2. However, due to low-

spin state of metal sites in N-rich coordination environment of CTFs the samples showed only a low activity in methane conversion.

In **Chapter 4** the applicability of X-ray photoelectron spectroscopy (XPS) for characterization of carbon-based heterogeneous catalysts is investigated. In three Case studies three different types of materials (carbon nanotubes, nitrogen-doped amorphous carbons with cobalt sites, and a nitrogen-containing polymer with nickel sites) are investigated. In case of nanotubes, exposing only carbon and oxygen on their surface, XPS can provide informative insight in the nature of their surface species. However, in case of more complex systems, where C, N, O, and transition metals are present, it becomes very difficult to distinguish species with similar values of binding energies. In order to be able to distinguish metal oxide particles and dispersed metal ions the use of element-specific local structural methods such as X-ray absorption spectroscopy (XAS) is highly beneficial.

Chapter 5 presents an in-depth XPS investigation of the influence of synthesis parameters on the properties of covalent triazine framework (CTF) materials. Series of CTF samples were prepared at different temperature, reaction time, using different monomers, different amounts of catalyst for CTF synthesis ($ZnCl_2$) as well as with other catalysts. XPS characterization of these samples, combined with characterization of their textural properties, shows that a higher synthesis temperature leads to a higher decomposition of the CTF framework due to side reactions during its synthesis. Decomposition increases the porosity of CTFs but decreases the amount of nitrogen sites in the structure, suitable for coordination of transition metals. Shorter reaction times lead to higher nitrogen content in the samples. Also an excess of $ZnCl_2$ is required to complete the synthesis of CTF. Catalysts for CTF synthesis that are more easily reducible than $ZnCl_2$ (*e.g.* CuCl, $SnCl_2$) promote the decomposition of the framework. On the other hand, it is demonstrated that the use of monomers that form more stable complexes with the catalyst decreases the rate of framework decomposition.

Overall, the results presented in this dissertation demonstrate how a rational combination of characterization methods can advance the design and optimization of heterogeneous catalysts. The significant role in this research was given to X-ray based characterization techniques. However, other types of characterization methods (*e.g.* electron microscopy, techniques based on vibrational transitions or on magnetic resonance, *etc.*) also play an indispensable role and provided crucial additional information for this research.

6.2. Samenvatting

Dit proefschrift is gericht op het interessante en zich snel ontwikkelende veld binnen de heterogene katalyse, namelijk de katalyse over atomair gedispergeerde ('geïsoleerde') actieve plaatsen. De volgende onderzoeksvragen dienden hierbij als leidraad:

- Hoe ontwerpen we een katalysator met atomair gedispergeerde ('geïsoleerde') actieve plaatsen?
- Hoe synthetiseren en ontwikkelen we zo'n katalysator?
- Hoe karakteriseren we zo'n katalysator?

Het eerste deel van dit proefschrift (Hoofdstukken 2 en 3) beschrijft aan de hand van de ontwikkeling van een katalysator voor de directe omzetting van methaan naar methanol de route voor het ontwerp, synthese, karakterisering en verdere modificatie van heterogene katalysatoren met geïsoleerde actieve plaatsen. In het tweede deel (Hoofdstukken 4 en 5) wordt de toepasbaarheid onderzocht van analysetechnieken gebaseerd op röntgenstraling (voornamelijk X-ray photoelectron spectroscopy (XPS) and X-ray absorption spectroscopy (XAS)) voor de karakterisering van deze katalysatoren. Aan de hand van een literatuurstudie wordt in Hoofdstuk 1 een inleiding tot beide delen gepresenteerd.

Inleidend **Hoofdstuk 1** beschrijft in het kort de strekking van voorgaand onderzoek en de belangrijkste onderzoeksuitdagingen bij het ontwikkelen van het proces voor de directe methaan-naar-methanolomzetting. Aanzienlijke onderzoeksinspanningen op dit gebied zijn tot nu toe gericht op het ontwikkelen van katalysatoren voor activering van de C-H binding in methaan, één van de meest stabiele bindingen in de organische chemie. Andere, even belangrijke uitdagingen in dit proces zijn echter de activering en regeneratie van het oxidatiemiddel, de verwijdering van methanol van de actieve plaats en bescherming van methanol tegen overoxidatie en de regeneratie van de actieve katalysatorsite na de reactiecyclus.

Op basis van de literatuurstudie worden de kenmerken van de succesvolle katalysator voor milde methaanoxidatie geformuleerd - het moet een heterogene katalysator zijn met geïsoleerde actieve plaatsen op een poreuze hydrofobe drager en stabiel onder de toegepaste reactieomstandigheden.

In **Hoofdstuk 2** wordt het ontwerp en de ontwikkeling van een katalysator voor milde methaanoxidatie op basis van metal-organic frameworks (MOF's)

gepresenteerd. Vanwege hun instelbare porositeit en mogelijkheden tot functionalisering, kunnen MOF's mogelijk voldoen aan de vereisten gesteld aan de milde methaanoxidatiekatalysator zoals geformuleerd in hoofdstuk 1.

Het gebruik van elektrochemische synthese maakt het mogelijk geïsoleerde Fe-sites in het MIL-53(Al)-framework te introduceren over een breed concentratiebereik (0,1 - 5,5 gew.%) zonder vorming van ijzeroxide-nanodeeltjes, wat niet mogelijk was met behulp van conventionele hydrothermale ionwisseling.

Elektrochemisch gesynthetiseerde MIL-53(Al,Fe)-katalysatoren werden getest op methaanoxidatie onder milde waterige reactieomstandigheden (60 °C, 30 bar CH_4) met H_2O_2 als oxidant. Onder dergelijke condities waren MIL-53(Al,Fe)-katalysatoren actief voor methaanoxidatie, waarbij ze voornamelijk methanol en methyl-hydroperoxide produceerden met een minimale vorming van overoxidatieproducten (mierenzuur, CO_2), met TOF's in de orde van 90 h^{-1} en selectiviteit voor zuurstofhoudende producten van *ca*. 80%. De katalysator kon minimaal 5 keer worden hergebruikt.

Karakterisering van MIL-53(Al,Fe) katalysatoren met Mössbauer spectroscopie, elektron paramagnetische resonantie (EPR) en röntgenabsorptiespectroscopie (XAS) toonde aan dat ijzer in deze monsters voornamelijk aanwezig is als monomere en dimere antiferromagnetisch-gekoppelde sites, ingebouwd in MIL-53(Al) framework. Periodic density functional theory (DFT) berekeningen bewezen de stabiliteit van dergelijke plaatsen en suggereerden een reactiemechanisme voor methaanoxidatie over geïsoleerde Fe-plaatsen in het MIL-53-framework.

Mogelijke opties voor verdere modificatie van de MIL-53(Al,Fe)-katalysator worden beschreven in **Hoofdstuk 3**. Verschillende benaderingen zijn besproken, waaronder synthese van MOF-katalysatoren met verschillende metaalcentra of verschillende organische linkers, evenals gebruik van verschillende additieven in de reactiemedia. Elektrochemische introductie van Cr, Co en Cu in MIL-53(Al) in plaats van Fe werd geprobeerd. IR-karakterisering toonde echter aan dat alleen Cr werd opgenomen in de structuur van de MOF.

MIL-53(Al,Cr)-katalysatoren vertoonden een activiteit en selectiviteit voor de methaan-naar-methanolomzetting vergelijkbaar of zelfs hoger dan MIL-53(Al,Fe). MIL-53(Al,Cr) vertoonde echter al na de eerste (ladingsgewijze) run een lagere stabiliteit en een significante uitloging van Cr; de katalytische activiteit wordt in dit geval hoofdzakelijk toegeschreven aan uitgeloogde chroomspecies in oplossing.

Introductie van linkers met extra functionele groepen leidt tot een aanzienlijk lagere porositeit van de MOF en kan de actieve site blokkeren, waardoor het mogelijk positieve effect van een dergelijke modificatie wordt geminimaliseerd. Introductie van de radicaalvanger Na_2SO_3 in het reactiemengsel leidt tot een hogere methaanomzetting, maar met een slechte selectiviteit voor methanol, waarbij CO_2 als het hoofdproduct wordt gevormd. Dit effect kan mogelijk worden verklaard door de vorming van zeer reactieve peroxosulfuurzuren in oplossing.

Bovendien werden heterogene katalysatoren op basis van zuiver organische covalent triazine frameworks (CTF's) met daaraan gecoördineerde metalen als actieve sites ook onderzocht op de milde methaanoxidatie met H_2O_2. Vanwege de lage spin-toestand van de metal-sites in een N-rijke coördinatieomgeving van CTF's vertoonden de monsters echter slechts een lage activiteit voor de methaanomzetting.

In **Hoofdstuk 4** wordt de toepasbaarheid van röntgenfoto-elektron spectroscopie (XPS) voor karakterisering van op koolstofdrager gebaseerde heterogene katalysatoren onderzocht. In drie casestudies worden drie verschillende soorten materialen (carbon nanotubes, met stikstof gedoteerde amorfe koolstoffen met actieve kobalt sites en een stikstofhoudend polymeer met nikkel sites) onderzocht. In het geval van nanotubes die alleen koolstof en zuurstof op hun oppervlak exposeren, kan XPS informatie geven over de aard van hun oppervlaktespecies. In het geval van meer complexe systemen, waar C, N, O en overgangsmetalen aanwezig zijn, wordt het echter erg moeilijk om species met vergelijkbare bindingsenergieën te onderscheiden. Om metaaloxidedeeltjes en gedispergeerde metaalionen te kunnen onderscheiden, kunnen veel beter elementspecifieke lokaal-structuurgevoelige methoden zoals röntgen-absorptiespectroscopie (XAS) gebruikt worden.

Hoofdstuk 5 presenteert een diepgaand XPS-onderzoek naar de invloed van syntheseparameters op de eigenschappen van covalent triazine framework (CTF)-materialen. Series CTF-monsters werden bereid bij verschillende temperatuur, reactietijd, verschillende monomeren, met verschillende hoeveelheden katalysator voor CTF-synthese ($ZnCl_2$), evenals het gebruik van andere katalysatoren. XPS-karakterisering van deze monsters, gecombineerd met karakterisering van hun textuureigenschappen, toont aan dat een hogere synthesetemperatuur leidt tot een hogere ontleding van het CTF-framework als gevolg van nevenreacties tijdens de synthese. Ontleding verhoogt de porositeit van CTF's maar vermindert de hoeveelheid stikstof in de structuur geschikt voor

coördinatie van overgangsmetalen. Kortere reactietijden leiden tot een hoger stikstofgehalte in de monsters.

Ook is een overmaat $ZnCl_2$ nodig om de synthese van CTF te completeren. Katalysatoren voor CTF-synthese die makkelijker reduceerbaar zijn dan $ZnCl_2$ (bijv. CuCl, $SnCl_2$) bevorderen de ontleding van het framework. Anderzijds is aangetoond dat het gebruik van monomeren die stabielere complexen vormen met de katalysator de snelheid van de framework-ontleding vermindert.

Al met al laten de resultaten in dit proefschrift zien hoe een rationele combinatie van karakteriseringsmethoden het ontwerp en de optimalisatie van heterogene katalysatoren kan bevorderen. Een belangrijke rol in dit onderzoek was weggelegd voor op röntgenstraling gebaseerde karakteriseringstechnieken. Andere typen karakteriseringsmethoden (bijvoorbeeld elektronenmicroscopie, technieken op basis van vibratiespectrocopie of magnetische resonantie, enz.) spelen echter ook een onmisbare rol en hebben cruciale aanvullende informatie voor dit onderzoek opgeleverd.

7. List of publications and presentations

Publications related to this thesis

1. **D. Y. Osadchii**,* A. I. Olivos Suarez,* Á. Szécsényi, G. Li, M. A. Nasalevich, I. A. Dugulan, P. S. Crespo, E. J. M. Hensen, S. L. Veber, M. V. Fedin, G. Sankar, E. A. Pidko, J. Gascon, Isolated Fe sites in Metal Organic Framework catalyze the direct conversion of methane to methanol. *ACS Catal. (2018), 8, 6, 5542-5548.*
2. X. Sun, A. I. Olivos Suarez, **D. Osadchii,** M. J. V. Romero, F. Kapteijn, J. Gascon, Single Cobalt Sites in Mesoporous N-Doped Carbon Matrix for Selective Catalytic Hydrogenation of Nitroarenes. *J. Catal. (2018), 357, 20-28.*
3. **D. Y. Osadchii**, A. I. Olivos Suarez, A. V. Bavykina, J. Gascon, Revisiting nitrogen species in Covalent Triazine Frameworks. *Langmuir (2017), 33, 50, 14278-14285.*
4. X. Sun, A. I. Olivos Suarez, L. Oar-Arteta, E. Rozhko, **D. Osadchii**, A. Bavykina, F. Kapteijn, J. Gascon, Metal–Organic Framework Mediated Cobalt/Nitrogen-Doped Carbon Hybrids as Efficient and Chemoselective Catalysts for the Hydrogenation of Nitroarenes. *ChemCatChem (2017), 9, 10, 1854-1862.*
5. E. Rozhko, A. Bavykina, **D. Osadchii**, M. Makkee, J. Gascon, Covalent organic frameworks as supports for a molecular Ni based ethylene oligomerization catalyst for the synthesis of long chain olefins. *J. Catal. (2017), 345, 270-280.*

* Denotes equal contribution from both authors.

Other publications

6. X. Sun, H. Jansma, T. Miyama, R. D. Sanjeewa Aluthge, K. Shinmei, N. Yagihashi, H. Nishiyama, **D. Osadchii,** B. van der Linden, M. Makkee, Unveiling the structure sensitivity for direct conversion of syngas to C2-oxygenates with a multicomponent-promoted Rh catalyst. *Catal. Lett. (2020), 150, 2, 482-492.*
7. X. Sun, R. Wang, S. Ould-Chikh, **D. Osadchii,** G. Li, A. Aguilar, J.-L. Hazemann, F. Kapteijn, J. Gascon, Structure-Activity Relationships in Metal Organic Framework Derived Mesoporous Nitrogen-doped Carbon Containing Atomically Dispersed Iron Sites for CO_2 Electrochemical Reduction. *J. Catal. (2019), 378, 320-330.*

8. R. Wang, H. Haspel, A. Pustovarenko, A. Dikhtiarenko, A. Russkikh, G. Shterk, **D. Osadchii**, S. Ould-Chikh, M. Ma, W. A. Smith, K. Takanabe, F. Kapteijn, J. Gascon, Maximizing Ag Utilization in High-Rate CO_2 Electrochemical Reduction with a Coordination Polymer-Mediated Gas Diffusion Electrode. *ACS Energy Lett. (2019), 4, 8, 2024-2031.*
9. X. Wang, M. Shan, X. Liu, M. Wang, C. M. Doherty, **D. Osadchii**, F. Kapteijn, High-performance Polybenzimidazole Membranes for Helium Extraction from Natural Gas. *ACS App. Mater. Interf. (2019), 11, 22, 20098-20103.*
10. M. J. Valero-Romero, J. G. Santaclara, L. Oar-Arteta, L. van Koppen, **D. Y. Osadchii**, J. Gascon, F. Kapteijn, Photocatalytic properties of TiO_2 and Fe-doped TiO_2 prepared by metal organic framework-mediated synthesis. *Chem. Eng. J. (2019), 360, 75-88.*
11. A. Iglesias-Juez, S. Castellanos, M. Monte, G. Agostini, **D. Osadchii**, M. A. Nasalevich, J. G. Santaclara, A. I. Olivos Suarez, S. L. Veber, M. V. Fedin, J. Gascon, Illuminating the nature and behaviour of the active centre: the key for photocatalytic H_2 production in Co@NH_2-MIL-125(Ti). *J. Mater. Chem. A (2018), 6, 36, 17318-17322.*
12. R. Wang, X. Sun, S. Ould-Chikh, **D. Osadchii**, F. Bai, F. Kapteijn, J. Gascon, Metal-organic framework-mediated N-doped carbon material for CO_2 electrochemical reduction. *ACS App. Mater. Interf. (2018), 10, 17, 14751-14758.*
13. J. G. Santaclara, A. I. Olivos Suarez, A. Gonzalez-Nelson, **D. Osadchii**, M. A. Nasalevich, M. A. Van Der Veen, F. Kapteijn, A. M. Sheveleva, S. L. Veber, M. V. Fedin, A. T. Murray, C. H. Hendon, A. Walsh, J. Gascon, Revisiting the incorporation of Ti(IV) in UiO-type metal-organic frameworks: metal exchange versus grafting and their implications on photocatalysis. *Chem. Mater. (2017), 29, 21, 8963-8967.*
14. A. V. Bavykina, A. I. Olivos Suarez, **D. Osadchii**, R. Valecha, R. Franz, M. Makkee, F. Kapteijn, J. Gascon, Facile Method for the Preparation of Covalent Triazine Framework coated Monoliths as Catalyst Support: Applications in C1 Catalysis. *ACS App. Mater. Interf. (2017), 9, 31, 26060-26065.*
15. F. R. Fortea-Pérez, M. Mon, J. Ferrando-Soria, M. Boronat, A. Leyva-Pérez, A. Corma, J. M. Herrera, **D. Osadchii**, J. Gascon, D.

Armentano, E. Pardo, The MOF-driven synthesis of supported palladium clusters with catalytic activity for carbene-mediated chemistry. *Nature Materials (2017), 16, 7, 760-766.*

16. R. V. Gulyaev, **D. Yu. Osadchii**, S. V. Koscheev, A. I. Boronin, Films of the $Pd_xCe_{1-x}O_2$ solid solution as a model object for the XPS study of the surface chemistry of Pd/CeO_2 catalysts. *J. Struct. Chem. (2015), 56, 3, 566-575.*
17. D. I. Potemkin, E. Y. Semitut, Y. V. Shubin, P. E. Plyusnin, P. V. Snytnikov, E. V. Makotchenko, **D. Y. Osadchii**, D. A. Svintsitskiy, S. A. Venyaminov, S. V. Korenev, V. A. Sobyanin, Silica, alumina and ceria supported Au-Cu nanoparticles prepared via the decomposition of $[Au(en)_2]_2[Cu(C_2O_4)_2]_3 \cdot 8H_2O$ single-source precursor: Synthesis, characterization and catalytic performance in CO PROX. *Catal. Today (2014), 235, 103-111.*
18. R. V. Gulyaev, E. M. Slavinskaya, S. A. Novopashin, D. V. Smovzh, A. V. Zaikovskii, **D. Osadchii**, O. A. Bulavchenko, S. V. Korenev, A. I. Boronin, Highly active $PdCeO_x$ composite catalysts for low-temperature CO oxidation, prepared by plasma-arc synthesis. *App. Catal. B: Environmental (2014), 147, 132-143.*

Conference presentations related to this thesis

1. Design of Cr- and Fe-containing MOF catalysts for mild methane oxidation. *The Netherlands' Catalysis and Chemistry Conference (NCCC) XX,* Noordwijkerhout, the Netherlands, March **2019 (oral)**.
2. Designing Metal-Organic Framework Catalysts For the Mild Oxidation of Methane. *2nd European Conference on Metal Organic Frameworks and Porous Polymers (EuroMOF2017),* Delft, the Netherlands, October **2017 (poster)**.
3. Designing Metal-Organic Framework Catalysts For the Mild Oxidation of Methane. *8th World Congress on Oxidation Catalysis*, Krakow, Poland, October **2017 (oral)**.
4. Metal-Organic Frameworks as Catalysts for Mild Methane Oxidation. *13th European Congress on Catalysis (EUROPACAT 2017)*, Florence, Italy, August **2017 (oral)**.
5. Design of iron-containing MOF catalysts for mild methane oxidation. *The Netherlands' Catalysis and Chemistry Conference (NCCC) XVIII,* Noordwijkerhout, the Netherlands, March **2017 (poster)**.

6. Spectroscopic Characterization of Covalent Triazine Frameworks: on the Nature of Nitrogen Species for Metal Incorporation. *5th International Conference on Metal-Organic Frameworks & Open Framework Compounds (MOF2016)*, San Diego, USA, September **2016 (poster)**.
7. Investigation of active sites in MOF catalysts for mild methane oxidation. *The Netherlands' Catalysis and Chemistry Conference (NCCC) XVII,* Noordwijkerhout, the Netherlands, March **2016 (poster)**.
8. Synthesis of copper-based catalysts for mild methane oxidation. *The Netherlands' Catalysis and Chemistry Conference (NCCC) XVI,* Noordwijkerhout, the Netherlands, March **2015 (poster)**.
9. Copper-Based MOF Catalysts for Mild Methane Oxidation. *2nd Annual Event of the Delft Process Technology Institute (DPTI)*, Rotterdam, the Netherlands, November **2014 (poster)**.

Acknowledgements

Every adventure has a beginning and an end. The PhD journey could be compared to a river – some parts of its course can be fierce and vigorous, in other the flow is stable and the riverbed is safe, some have lots of deep ends and underwater stones, in other parts it slows down and almost looks like a swamp, or even goes underground. But finally, this moment comes – and it enters the ocean. The boat that enabled this journey might have changed a lot from the moment it sailed off – but it still carries the same name and the sailor still holds the helm firmly. The ocean and new adventures are awaiting – so it's time for a sailor to look back and acknowledge those who were part of this journey.

Of course, first of all I would like to thank people that made this journey possible – Jorge and Freek. Jorge, thank you for all your input into this project, for all discussions and enthusiasm, giving freedom to my research but also shaping it with direction, focus and timing when necessary. Freek, I cannot thank you enough for your advice and support in the final steps of this journey, for all priceless experience you have to share, for high professionalism and dignity you have always demonstrated.

Two more professors made a significant impact on the course of this journey. Evgeny, thanks for all bright discussions and suggestions, computational and mental support, as well as for the concept of "visual spectroscopy" in research. Michiel, I am grateful for the opportunity to work together on my postdoctoral project. Performing research on a real industry-requested project, on the topic and with the equipment I never dealt with before was an invaluable experience and, in certain sense, a real school of life for me as a scientist and as a person. Thank you for the motivation and for our long conversations, full of very useful knowledge.

I would like to especially thank all people who make things work – our technicians and secretaries of the Catalysis Engineering team.

Harrie, thanks for your help in solving myriads of issues with high pressure setups, for organizing the moving and starting up of the Industrial Catalysis lab. All the best in many korfball seasons to come! Bart (from CE), thank you for your wise and positive attitude as well as for your ability to tackle and solve practically any problem with the equipment. Willy, thank you for your enthusiastic help with a plethora of adsorption measurements I had to perform. Liliana, the pyrolysis oil was difficult to handle from any point of view, but you managed to develop reliable methods for its analysis – thank you for this help (as well as for all nice chats and parties). Bart (from

MECS), your LabView experience and passion for XPS brings us a lot of topics for discussion every time we meet – thanks for all your help with making Microflow alive and keeping XPS in good shape. Ben and Duco, thanks for the jokes and practical tips as well as rapid technical support when needed. Els, lots of thanks for your considerate and friendly help with all bureaucracy and arrangements. Caroline, thank you for the help with organizing the delivery of all those sometimes hazardous packages I had to send. Alex, thanks for making the electronics working and for all incredible stories!

Alma – my mentor and my friend, indispensable member of the "team awesome" – thank you for being part of this project, for all your help and support, energy and motivation, and for all adventures we had during these years. I have learnt a lot from you, and hope we are still going to have quite some talks/drinks/boardgame evenings together in the future. Team of the office 0.420 – Nastya, Canan, Francesc – thanks for all the fun, wild dances, science and non-sense talks we had there. And, of course, for my style transformation before my Go/No Go – seems it is going to stay with me forever (well, at least part of it). Team of CE PhD starters-2014 – Eduardo, Jara (and Elmar!), Anahid, Damla – thanks for being next to me along (part of) this journey, for all shared victories and frustrations, parties and travels. "Never give up for science" poster and postcards from "you-know-who", the ultimately best Friday drinks ever and all the variety of games from "Imadzhinarium" to "Ha-ha-ha" are among the most unforgettable experiences of these years. Jara, thanks for inventing Oschadi and all other misspelled versions of my surname (and also for learning the correct one). Anahid, hope one day I will know more words in Persian than just the names of seasons (or at least will learn these four properly). Edu, good luck with dragons and breakthrough experiments!

"Russian team" (or Russian-speaking team, or Post-Soviet team) of CE – Maxim, Nastya, Irina, Alla, Alexey, Alyona, also Dmitriy and Leonid – thanks for keeping the proper spirit within the group, generating tons of bilingual humour and making happen all those nice occasions we had here together. Maxim, thank you for the guidance on survival in the Netherlands and at the synchrotron. Nastya, thank you for helping, motivating and challenging me throughout the four years of my PhD. Ira, thanks for the great list "to eat in Petersburg", we have to visit this city couple of times more to really check them all out. Alla, thank you for amazing borsch and for waking me up during the night beamline measurements. Alexey, thanks for jokes and discussions on practically everything, as well as for your energy to organize

events (hope we will still have chance to beat you in Eclipse). Of course, thanks as well to people from Eindhoven who slowly but surely move to Delft – Georgy, Evgeny, Elena, Andrey (who is still on the way). Good luck with making science below the sea level ;)

“Spanish team” – Edu, Jara, Maria Jose, Beatriz, Lide, Sonia, Pablo, Mario, Jose Luis – thanks for all those wonderful sangrias, risottos, tortillas, chorizos et cetera you were supplying our group with, as well as the relaxing and cheerful atmosphere. Team of the old building survivors – Xiaohui, Harrie, Robert, Rob, Emmanuel, Alex – thanks for the efforts to keep each other sane in that slowly decaying environment. Xiaohui, thanks for insightful discussions on comparison of Europe and Asia as well as for productive collaborations. Robert, спасибо за сало и удачи в дальнейшем изучении великого и могучего русского языка! Rob, good luck with all your future travels!

Monique, Abrar, Tim, Yixiao, Filipe, Ina, Meixia, Riming, Sumit, Martin, Rupali, Xinlei, Xuerui, Chuncheng, Guanna, Stefano, Adrian, Davide, Srinidhi, Han and all other members of CE I might forget – thanks for your contribution to the life and well-being of the group! With many of you I have performed experiments together, analysed XPS or EXAFS and discussed various scientific questions. I am proud that in a number of cases it resulted in co-authored publications. Although they joined the group only recently, people from ICIQ already make a strong positive influence on the atmosphere in the group – thank you Atsushi, Sorin, Donato, Lingjun, and members of Building 67 “Die Hard” team (Atul and Nat) for this!

Matvey, Sergey, Alena – thanks for EPR measurement sessions (quite exhausting sometimes) and for brilliant simulations and interpretation of data. Iulian, thank you for the extensive Mössbauer characterization of my samples at the Reactor Institute, which became an important part of this thesis. Sankar, thanks for the express EXAFS training in London.

I would also like to thank students who contributed to the research I was performing. Dmitriy, Elias, Annemiek – your help was very valuable, and working with you was a nice and important experience for me.

I am grateful to the Group of Supported Metal-Oxide Catalysts Characterization from the Boreskov Institute of Catalysis for the knowledge of XPS and catalysis I gained from there. Andrey Ivanovich, Roma, Dima, Lida, Andrey, Sergey Valentinovich – all the best in your research!

Дорогая моя семья, спасибо вам за то, что поддерживали и верили в меня, несмотря ни на что. Мама и папа, с каждым годом я всё больше убеждаюсь в том, что вырос в семье настоящих героев, которым всё по

плечу – а значит, и мне тоже.) Спасибо за заботу и за то, что вы вложили в меня. Горжусь вами, и безмерно благодарен за всё! Лариса Владимировна, ваш живой и неукротимый дух способствовал завершению этой диссертации – спасибо за всю деятельную помощь!)

My partner in crime, моя Маришка. Наша невероятная история движется по своей удивительной траектории, и я счастлив, что ты рядом со мной в эти фантастические минуты. Держись крепче, любимая – дальше будет ещё интереснее)

It was a long trip, but now this book is close to its end, and the next one is about to start. Hope to see you all in the next chapter!

Dima

About the author

Dmitrii Y. (Yurievich) Osadchii was born on July 5th, 1991, in Novosibirsk, USSR. In June 2008 he graduated with *Cum Laude* from Gymnasium 15 in his home city and started studying chemistry at the Faculty of Natural Sciences at Novosibirsk State University (NSU) the same year. While studying at the university, he decided to specialize in catalysis. For his graduation project Dmitrii joined the Group of Supported Metal-Oxide Catalysts Characterization at the Boreskov Institute of Catalysis, where he investigated the electronic and geometric structure of Pd/CeO_2 catalysts for low-temperature CO oxidation under supervision of Prof.dr. Andrei I. Boronin.

Dmitrii graduated from NSU in June 2013, and in February 2014 he started his PhD on development of mild methane oxidation catalyst under supervision of Prof.dr. Jorge Gascon and Prof.dr. Freek Kapteijn at the Catalysis Engineering team at Delft University of Technology. The results of his research within this project can be found in this dissertation. During his PhD Dmitrii supervised BSc and MSc internship projects and gained experience in teaching, working as a teaching assistant in Chemical Reactor Engineering course for Bachelor students at TU Delft.

In June 2018 Dmitrii started his postdoctoral research project on upgrading of waste tire pyrolysis oil at Delft University of Technology under supervision of Dr.ir. Michiel Makkee.